Constraints on chalcophile element recycling in subduction zones from Selenium isotope systematics

Dissertation
der Mathematisch-Naturwissenschaftlichen Fakultät
der Eberhard Karls Universität Tübingen
zur Erlangung des Grades eines
Doktors der Naturwissenschaften
(Dr. rer. nat.)

vorgelegt von
M.Sc. Timon Kurzawa
aus Schmallenberg

Tübingen
2019

Gedruckt mit der Genehmigung der Mathematisch-Naturwissenschaftlichen Fakultät der Eberhard Karls Universität Tübingen.

Tag der mündlichen Prüfung: 07.06.2019

Dekan: Prof. Dr. Wolfgang Rosenstiel
1. Gutachter: Dr. Stephan König
2. Gutachter: Prof. Dr. Ronny Schönberg

Ich erkläre hiermit, dass ich die zur Promotion eingereichte Arbeit mit dem Titel „Constraints on chalcophile element recycling in subduction zones from Selenium isotope systematics“ selbstständig verfasst, nur die angegebenen Quellen und Hilfsmittel benutzt und wörtlich oder inhaltlich übernommene Stellen (alternativ: Zitate) als solche gekennzeichnet habe. Ich erkläre, dass die Richtlinien zur Sicherung guter wissenschaftlicher Praxis der Universität Tübingen (Beschluss des Senats vom 25.05.2000) beachtet wurden. Ich versichere an Eides statt, dass diese Angaben wahr sind und, dass ich nichts verschwiegen habe. Mir ist bekannt, dass die falsche Angabe einer Versicherung an Eides statt mit Freiheitsstrafe bis zu drei Jahren oder mit Geldstrafe bestraft wird.

Ort, Datum Unterschrift

Tübingen,

Abstract

In this cumulative dissertation isotope systematics of the redox-sensitive, chalcophile and moderately volatile element selenium (Se) are used to place further constraints on the recycling of chalcogens in subduction zones. Investigation of Se isotope compositions of low nanogram (ng)-level geological samples is challenging. This is both due to difficulties regarding chemical Se purification from sample matrices and instrumental challenges during mass spectrometric analysis. As a result, only few Se isotope data exist so far for relatively Se-poor samples, such as subduction-related rocks. In comparison, crustal materials such as sediments have several magnitudes higher Se concentrations. Particularly sediments were thus already subject to several Se isotope investigations regarding the mechanisms and the timing of Earth`s atmospheric oxygenation. In contrast, little if any work has been dedicated to employ the versatile Se isotopes to study the connection between Earth`s surface and interior evolution. By assessing the chalcophile element cycle in subduction zones using Se isotopes, this dissertation takes first steps to close this gap.

Given the analytical challenges of Se isotope analyses and the fact that former instruments used to determine Se isotope ratios of igneous rocks (i.e. Micromass IsoProbe – Rouxel et al., 2002, 2004) have become commercially unavailable, a new method is thus required. The first chapter of this dissertation comprises detailed descriptions and advantages of the method developed for the purpose of this study. The presented method allows to use a ThermoFisher Scientific® Neptune*Plus*™ for accurate and precise determination of Se isotope ratios. This involves a double spike to account for isotope fractionation and a hydride generator system for efficient sample introduction. Injection of methane to the plasma source results in two-to three-fold Se signal increase and background signal suppression by a factor of two. This method now allows a systematic investigation of low ng-level geological materials.

In the second chapter, the first Se isotope data on island arc lavas from the Mariana arc system are provided. The Se isotope signature of submarine Mariana lavas from the arc and back-arc regions is not affected by degassing and, unlike the elemental Se budget of these lavas, is not affected by magmatic differentiation processes. Hence, the $\delta^{82/76}$Se of submarine arc lavas may retain its source signature. This signature is likely enriched by melt-like and fluid-like subduction components derived from the subducting Pacific crust and overlying sedimentary cover. The Mariana samples show a tendency to become isotopically lighter from the back-arc to arc(-like) lavas, possibly reflecting a decreasing chromatographic effect of the overlying mantle wedge and increasing influence of a fluid-induced signature. Addition of a sediment melt-like subduction component seems to buffer this fluid signature as observed in Mariana arc samples. The large Se isotope compositional range of Mariana lavas is due to the complex contributions of subduction components, but are on average isotopically lighter than the Mariana pre-subduction mantle. Potential slab-derived contributions may be traced back to subduction recycling of isotopically light

Se input such as altered sulfide-bearing oceanic crust and modern sediments. Subduction recycling of Se may also have had an impact on the secular Se isotope composition of the Earth’s upper mantle given that a considerable shift to lower $\delta^{82/76}$Se average values in sediments has been identified due to the Neoproterozoic Oxygenation Event. Future studies might help to better understand the interplay between Earth`s atmospheric oxygenation, Se recycling and isotopic evolution of the mantle through geological time.

In the third chapter, new Se isotope data for prograde metamorphic rocks are presented and used to investigate the processes affecting the behavior of chalcophile elements within subducting oceanic crust. Therefore, eclogites, serpentinized peridotites and a metapelite from the Raspas complex, SW Ecuador, were studied. These rocks were subducted to depths of ~60 km and subsequently exhumed as a coherent package. Eclogites have previously been identified to be derived from typical N-type mid-ocean-ridge basalts (N-MORB) that were subject to hydrothermal seafloor alteration. This is also inferred from isotopically light Se isotope compositions that overlaps with those of typical hydrothermally altered basalts. Eclogites influenced by extensive fluid-mobile element enrichment, as identified by low Ce/Pb, Ce/Rb and Ce/Cs, are characterized by heavy Se isotope compositions that approach those of serpentinized peridotites and metapelites. It is thus proposed that, dehydration of subducted oceanic crust and serpentinites leads to fluid release and scavenging of chalcophile elements. Potential sources are hydrothermal sulfides within hydrothermally altered basalt that destabilize during prograde subduction metamorphism. Extensive interaction of slab lithologies with fluids bears the potential to relocate and re-distribute dissolved chalcophile elements within the slab. Further, this provides a realistic mechanism for element transfer to the overlying sub-arc mantle. This could, in principle, explain the Se isotope signature of Mariana lavas (*Chapter* 2).

The results of the three chapters of this dissertation provide evidence that Se isotope systematics are a powerful tool to unravel the link between the behavior of sulfides within subducting oceanic crust and the subduction-related chalcophile element cycle. It is further anticipated that new constraints can be placed on the evolution of Earth`s mantle–crust–atmosphere system throughout geological history from the perspective of this novel redox-sensitive and chalcophile isotope system.

Zusammenfassung

In dieser kumulativen Dissertation wird die Isotopensystematik des redox-sensitiven, chalkophilen und moderat volatilen Elements Selen (Se) benutzt, um das Subduktions-Recycling der Chalkogene tiefergehend zu untersuchen. Bis dato ist die Analyse der Se-Isotopenzusammensetzung von geologischen Proben, die Se-Konzentrationen im ng pro g Bereich aufweisen, eine analytische Herausforderung. Dies liegt an der schwierigen chemischen Aufreinigung von Selen aus Probenmatrizen und instrumentellen Herausforderungen bei der massenspektrometrischen Messung. Daher gibt es nur wenige Datensätze für geologische Probenmaterialien, die niedrige Se-Konzentrationen aufweisen, wie etwa Proben aus dem Erdmantel. Für krustale Proben, wie zum Beispiel Sedimente, die einige Größenordnungen höhere Se Konzentrationen aufweisen, gibt es weitaus mehr Daten. Insbesondere Sedimente waren bereits Forschungsgrundlage mehrerer Studien, die sich das redox-sensitive Verhalten von Se zu Nutze machten, um die Mechanismen und den Zeitpunkt der Sauerstoffanreicherung in der Erdatmosphäre zu untersuchen. Im Gengenteil dazu gibt es, wenn überhaupt nur wenige Arbeiten, die die vielseitige Se-Isotopensystematik genutzt haben, um die Verbindung von Erdoberfläche und der Evolution des Erdinneren zu untersuchen. Diese Dissertation soll einen ersten Anteil an der Schließung dieser Wissenslücke leisten, indem potentielles Recycling von Se in Subduktionszonen untersucht wird.

Aufgrund der analytischen Herausforderungen und der Tatsache, dass die Analysegeräte die bei früheren Studien verwendet wurden nicht mehr käuflich zu erwerben sind (z.B.: Micromass IsoProbe – Rouxel et al., 2002, 2004), war es notwendig eine neue Messmethode zu entwickeln. Das erste Kapitel dieser Dissertation beinhaltet detaillierte Beschreibungen und Vorzüge der entwickelten Methode. Für die genaue und präzise Messung von Isotopenzusammensetzungen wird ein Neptune*Plus*™ Massenspektrometer der Firma ThermoFisher Scientific® verwendet. Der verwendete ‘double spike’ erlaubt die Korrektur möglicher Isotopenfraktionierungen und ein Hydrid-Generator (HG) begünstigt die Probeneinleitung. Die Zufuhr von Methan in das Plasma bedingt eine zwei- bis dreifache Steigerung des Se-Signals bei gleichzeitiger Unterdrückung der Untergrundsignale um einen Faktor zwei. Die Methode ermöglicht nun die systematische Untersuchung von Gesteinsproben mit Se-Konzentrationen im Nanogramm-Bereich.

Das zweite Kapitel stellt die ersten Se-Isotopendaten für Inselbogenvulkanite vom Marianen Inselbogen bereit. Die Se-Isotopensignaturen von submarinen Marianen Laven aus dem back-arc Becken und des Inselbogens sind nicht von Entgasung und anders als die Se-Konzentrationen dieser Gesteine, nicht von magmatischen Differenzierungsprozessen beeinflusst. Daher könnte die Se-Isotopenzusammensetzung der submarinen Laven der Isotopensignatur der Mantelquelle entsprechen. Die Se-Isotopensignatur ist wahrscheinlich durch Schmelz- und Fluidkomponenten angereichert worden, die von der subduzierten Pazifischen Platte und aufliegenden Sedimenten stammen. Die Proben zeigen eine Tendenz hin zu leichteren

Se-Isotopenzusammensetzungen ausgehend von den Proben des back-arc Beckens hin zu den arc-typischen Proben. Dies liegt vermutlich in einem abnehmenden chromatographischen Effekt des Mantelkeils und daher zunehmender Fluid-Signatur begründet. Das Zuführen einer Sediment-Schmelze im Fall der arc-Proben scheint diese Fluid-Signatur abzuschwächen. Die Se-Isotopensignatur der Marianen Laven zeigt aufgrund der komplexen Beimengungen der verschiedenen Subduktionskomponenten eine große Spannbreite. Insgesamt betrachtet ist diese Signatur deutlich verschieden von der des Prä-Subduktionsmantels. Der Eintrag von isotopisch leichtem Selen mittels Subduktionskomponenten kann vermutlich auf das Recycling von alterierter, Sulfid-führender ozeanischer Kruste und von modernen Sedimenten zurückgeführt werden. Subduktions-Recycling könnte einen Einfluss auf die zeitliche Se-Isotopenzusammensetzung des (Oberen) Erdmantels gehabt haben, die auf der Verschiebung der Se-Isotopenszusammensetzung von Sedimenten hin zu isotopisch leichteren Signaturen seit der neoproterozoischen Sauerstoffanreicherung der Erdatmosphäre beruht. Ein Ziel zukünftiger Selen-Studien sollte es sein, mögliche Beziehungen zwischen atmosphärischem Sauerstoffanstieg, Se Recycling und der isotopischen Evolution des Erdmantels über die Erdgeschichte hinweg zu identifizieren.

Das dritte Kapitel präsentiert erste Se-Isotopendaten für metamorphe Gesteine, die genutzt wurden, um die Prozesse die das Verhalten chalkophiler Elemente in subduzierter ozeanischer Kruste beeinflussen, zu untersuchen. Dazu wurde eine vom Raspas Komplex, SW Ecuador, stammende Probensuite genutzt, die Eklogite, serpentinisierte Peridotite und einen Metapelit umfasst. Diese Gesteine wurden bis in eine Tiefe von ~60 km subduziert und wurden anschließend als strukturell-zusammengehörendes Paket exhumiert. Die Gesteine, die während der Metamorphose zu Eklogiten wurden, stellen typische Mittelozeanische Rückenbasalte (N-MORB) dar, die vor ihrer Versenkung in den Erdmantel unterschiedlich stark von hydrothermaler Alteration beeinflusst wurden. Dies wurde während dieser Studie anhand von leichten Se-Isotopensignaturen bestätigt, die typisch für hydrothermal alterierte Basalte sind. Zusätzlich zeigen Eklogite, die eine starke Anreicherung fluid-mobiler Elemente aufweisen (niedrige Ce/Pb, Ce/Rb und Ce/Cs Verhältnisse), die schwersten Se-Isotopensignaturen, die denen von serpentinisierten Peridotiten und Metapeliten ähneln. Es kann davon ausgegangen werden, dass durch Dehydration von subduzierter ozeanischer Kruste und Serpentiniten freigesetzte Fluide in der Lage sind chalkophile Elemente zu mobilisieren. Potentielle Quellen für diese sind vermutlich hydrothermale Sulfide innerhalb alterierter ozeanischer Kruste, die im Zuge sich verändernder Druck- und Temperaturbedingungen instabil werden. Intensive Interaktion von Gesteinen und Fluiden hat vermutlich das Potential gelöste chalkophile Elemente innerhalb der subduzierten Kruste umzuverteilen und darüber hinaus in den Mantelkeil abzuführen, wobei letzteres die Se-Isotopensignatur der Marianen Laven erklären könnte (*Chapter* 2).

Die Ergebnisse der drei Kapitel dieser Dissertation zeigen, dass die Isotopensystematik des redox-sensitiven und chalkophilen Elements Se ein mächtiges Werkzeug darstellt, um die Zusammenhänge zwischen dem Verhalten von Sulfiden innerhalb subduzierter ozeanischer Kruste und dem Subduktions-Recycling der Chalkogene zu entschlüsseln. Die Se-Isotopensystematik kann genutzt werden, um die Evolution des Mantel–Kruste–Atmosphäre–Systems der Erde über die Erdgeschichte hinweg, nachzuvollziehen.

List of publications and author contributions

Chapter 1

Title	A method for Se isotope analysis of low ng-level geological samples via double spike and hydride generation MC-ICP-MS
Authors	Timon Kurzawa, Stephan König, Jabrane Labidi, Aierken Yierpan, Ronny Schoenberg
Status	published 2017 in *Chemical Geology 466, 219–228*
Declaration	contribution by author
Position in list of authors	1
Scientific ideas	30%
Data generation	90%
Interpretation	70%
Writing	75%

Chapter 2

Title	The role of subduction recycling on the Se isotope signature of the mantle: Constraints from Mariana arc lavas
Authors	Timon Kurzawa, Stephan König, Jeffrey C. Alt, Aierken Yierpan, Ronny Schoenberg
Status	published 2019 in *Chemical Geology 513, 239–249*
Declaration	contribution by author
Position in list of authors	1
Scientific ideas	70%
Data generation	90%
Interpretation	70%
Writing	85%

Chapter 3

Title	Sulfide breakdown, within-slab redistribution and chalcophile element recycling in subduction zones: Evidence from Se isotope systematics of HP-LT rocks from the Raspas Complex, SW Ecuador
Authors	Timon Kurzawa, Stephan König, Timm John, Ronny Schoenberg
Status	In preparation to be submitted to *Geology*

Declaration	contribution by author
Position in list of authors	1
Scientific ideas	70%
Data generation	95%
Interpretation	75%
Writing	90%

Table of contents

Introduction

Selenium (Se) is a chalcophile, moderately volatile as well as a redox-sensitive element with a total of six stable isotopes (^{74}Se, ^{76}Se, ^{77}Se, ^{78}Se, ^{80}Se and ^{82}Se, the latter is considered stable due to its long half-life). The concentration of Se within the silicate Earth (crust and mantle) is higher than expected from metal-silicate partitioning experiments (Rose-Weston et al., 2009), which has been interpreted to be the result of addition of Se, and other elements (e.g. the highly siderophile elements, HSEs), via meteoritic material (late veneer hypothesis; Kimura et al., 1974) following core-mantle differentiation.

Due to its geochemical characteristics, Se progressively attracted attention in the geoscience community over the past decades. Several studies investigated the Se elemental and isotope systematics of various materials to constrain Earth's (i) volatile origin (e.g. König et al., 2014; Wang and Becker, 2013), and (ii) atmospheric evolution as well as global Se cycle (Kipp et al., 2017; Mitchell et al., 2016; Pogge von Strandmann et al., 2015; Stüeken et al., 2015a; Stüeken et al., 2015b), the (iii) elemental distribution and isotope composition of terrestrial and extraterrestrial materials (Dreibus et al., 1995; Johnson, 2004; König et al., 2012; Labidi et al., 2018; Layton-Matthews et al., 2013; Lissner et al., 2014; Lorand et al., 2003; Marchesi et al., 2013; Marin et al., 2001; Rouxel et al., 2004; Rouxel et al., 2002; Schilling et al., 2011; Vollstaedt et al., 2016; Wang et al., 2013) and (iv) Se isotope fractionation during redox processes (Clark and Johnson, 2010; Johnson and Bullen, 2003; König et al., 2019; Mitchell et al., 2013; Schilling et al., 2013; Wen and Carignan, 2011; Zhu et al., 2014). Whether Se elemental systematics in mantle rocks can be extrapolated to trace an exact late veneer component or are too obscured due to metasomatic processes, remains a matter of debate (König et al., 2014; König et al., 2015; Wang and Becker, 2015). Hence, Se isotope investigations are a new approach that might help to resolve this issue. They might further be of great value when investigating the role of subduction recycling with respect to Se and other chalcophile elements.

Subduction of oceanic lithosphere represents the key geological process responsible for crustal recycling and generation of continental crust via subduction-related magmatism (Fig. A). Increasing pressure (P) and temperature (T) during subduction of crustal material including continental and marine sediments lead to metamorphic reactions that ultimately result in dehydration and liberation of fluids. These fluids serve as transport medium for fluid-mobile elements, such as the large ion lithophile elements, LILE), cause element enrichments in the overlying mantle wedge and trigger melting as it lowers the solidus of the mantle peridotite (Green, 1973; Schmidt and Poli, 2003). Island arc lavas show pronounced enrichments in fluid-mobile elements (e.g. Perfit et al., 1980) and can thus be considered as the complementary output for these elements in subduction zones. However, in addition to fluids, sediment- and/or slab-derived melts may also contribute to the geochemical budget of island arc lavas (i.e. Mariana arc lavas; Elliott et al. (1997)) an thus emphasize the complexity of subduction zone recycling. Although, recycling of S and other chalcophile elements in subduction zones was the focus of previous studies (e.g. Alt et al., 1993; Evans et al., 2014; Noll Jr et al., 1996; Timm et al., 2012), many aspects remain poorly constrained. In view of this, Se elemental and isotope systematics may provide valuable new insights that improve our understanding of the evolution of the Earth's crust–mantle system, the origin and evolution of volatiles, as well as provide insights into the formation of economically valuable ore deposits.

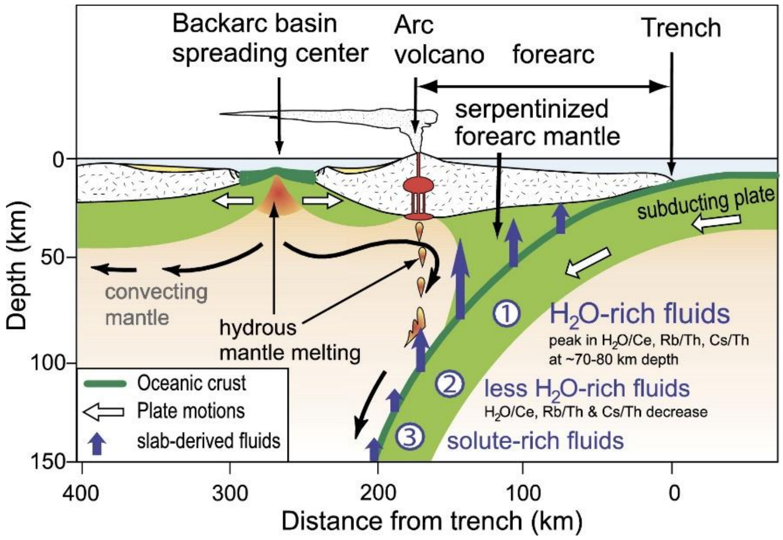

Figure A (from Ribeiro et al., 2015). Schematic illustration of a subduction zone with its structural units. The sketch shows continuous dehydration of oceanic crust due at various depths (blue arrows) and melt generation in the sub-arc mantle that leads to arc magmatism. Black arrows indicate mantle flow in the overlying mantle.

Selenium isotope studies on igneous rocks are rare with the exception of a pioneering study by Rouxel et al. (2002), who investigated different terrestrial igneous rocks and iron meteorites to define the Se isotope composition of a bulk Earth reservoir. The scarcity of available Se isotope data on igneous rocks is mainly due to low Se concentrations in mantle rocks that are at least one order of magnitude lower compared to those of sedimentary materials (ng g^{-1} vs µg g^{-1}), hence challenging Se purification and accurate Se isotope analysis.

This dissertation is part of the ERC project "O2RIGIN – From the origin of Earth`s volatiles to atmospheric oxygenation". This project aims to identify the link between exogenic and endogenic processes of our planet, which resulted in the redox contrast between the Earth`s interior and surface. Within the project, the aim of this PhD study was to constrain the behavior of Se in subduction zones in order to place constraints on chalcophile element recycling and potential re-distribution among different terrestrial reservoirs, i.e. crust and mantle. For this, well-characterized samples of the Mariana Island arc, SW Pacific, and prograde metamorphic rocks from the Raspas formation, SW, Ecuador were analyzed. This required an analytical method capable to yield accurate and precise Se isotope data of low ng-level geological materials such as mantle-derived melts and their derivates.

Chapter 1 provides a newly developed method to determine precise and accurate Se isotope compositions of low ng-level geological samples via the double spike approach using a hydride generator (HG) introduction system connected to a multi-collector inductively plasma coupled mass spectrometer (MC-ICP-MS). This became essential because (i) the majority of igneous samples are characterized by low Se concentrations compared to several magnitude higher surface materials such as sedimentary rocks and (ii) former instruments that were used to determine Se isotope ratios on igneous rocks, such as the NuPlasma (Mitchell et al., 2012, Schilling et al., 2011 Zhu et al. 2014) or the Micromass IsoProbe (i.e. Rouxel et al., 2002, 2004) are commercially not available anymore. The method described in this chapter employs a ThermoFisher Scientific Neptune*Plus* that, however, bears the disadvantage of relatively high background signals (i.e. compared to Rouxel et al., 2002) on interference masses, such as m/z 74, 77, 78, 80 and 82 when analyzing low-ng (<15 ng) Se solutions (i.e. Rouxel et al., 2002). This problem has been overcome because of very efficient suppression of interference levels by methane addition (see also Floor et al., 2011), which renders Se isotope ratio determinations on low-ng solutions in low-mass resolution mode possible. This approach now allows a systematic Se isotope investigation of many planetary reservoirs such as the Earth's mantle as well as mantle-derived melts such as island arc and mid-ocean ridge lavas with low Se concentrations (<200 ng g^{-1}). In addition to Se isotope and concentration determination, concentrations of Te can also be obtained following a method described by Yierpan et al. (2018), which can be used to assess potential fractionation of Se/Te during processes relevant for adequate Se isotope interpretation.

Chapter 2 presents a combined Se isotope and Se-Te elemental study of subduction-derived lavas from the Mariana arc system. The aim of this case study was to decipher the role of different subduction components (fluids and melts) on the Se isotope composition of arc lavas as well as to understand the elemental behavior of Se-Te in subduction zones. It can be shown that overall larger Se isotope variability with a tendency to lighter compositions of lavas compared to the Mariana pre-subduction mantle can be explained by subduction recycling of Se-bearing slab lithologies. This might also have potential implications for the Se isotope evolution of the crust–mantle system throughout geological time.

Chapter 3 comprises an investigation of Se isotope and Se–Te elemental systematics of prograde metamorphic rocks from the Raspas Complex of SW Ecuador. This study was conducted to identify potential sources of Se within the subducted slab that might explain the observed larger isotopic variability of subduction-related lavas compared to a given pre-subduction wedge (Chapter 2). In addition, within-slab processes responsible for the liberation of chalcophile elements were investigated. The analyzed samples resemble metamorphosed oceanic crust (eclogites), abyssal mantle (serpentinized peridotites) and sediments (metapelite) that were subducted to depths of ~60 km and subsequently exhumed without significant retrograde overprint. This sample suite constitutes a paramount example for a structurally pristine but extensively metamorphosed slice of oceanic lithosphere and therefore might provide valuable insights into processes during subduction zone metamorphism. Our results indicate, that eclogites to some extent preserve the Se isotope composition of their precursor rocks – hydrothermally altered mid-ocean-ridge basalts – and are thus a likely source of isotopically light Se that is transferred to the source region of arc magmas during prograde subduction. Striking correlations of LILE as well as fluid-mobile elements and Se isotope compositions suggest that, fluids liberated from serpentinites and/or metapelites play an important role in the mobilization of Se and other chalcophile elements from slab lithologies. This likely is facilitated by destabilization, decomposition, re-distribution and recrystallization of hydrothermal sulfides during temperature and pressure increase during prograde metamorphism.

Chapter 1: A method for Se isotope analysis of low ng-level geological samples via double spike and hydride generation MC-ICP-MS

Abstract

The isotopic signature of the chalcophile, redox-sensitive and moderately volatile element Se in geological materials may offer valuable new insights into the origin and evolution of volatiles in planetary systems. Here, we report a new method for Se isotope determination of low Se containing samples relevant to the Earth's mantle reservoir. We present a method that combines a double spike and hydride generation sample introduction system with a ThermoFisher Scientific® Neptune*Plus*™ MC-ICP-MS. The measurement routine takes advantage of methane injection in the instrument source during measurement, resulting in enhanced Se signals and suppression of polyatomic interferences. Purification of Se from natural samples was simplified by employing conventional ion exchange chromatography procedures. An external reproducibility of 0.15‰ (2σ) on $\delta^{82/76}$Se values for measurements performed on natural samples with Se abundances down to ~5 ng is obtained. We demonstrate that our technique allows the determination of Se isotope signatures of low Se-bearing geological materials with complex matrices such as mafic igneous rocks, which is essential to extend the Se isotopic investigation to Se-depleted planetary reservoirs such as the Earth's mantle.

1.1 Introduction

Selenium (Se) is a redox-sensitive element with the valence states -II, 0, +IV, +VI and a total of six stable isotopes (^{74}Se, ^{76}Se, ^{77}Se, ^{78}Se, ^{80}Se and ^{82}Se). The potential for Se isotopes to study low-temperature redox processes on the Earth's surface has been shown in various studies (Clark and Johnson, 2010; Ellis et al., 2003; Johnson and Bullen, 2003; Johnson and Bullen, 2004; Johnson et al., 2000; Johnson et al., 1999; Mitchell et al., 2013; Rouxel et al., 2004; Rouxel et al., 2002; Schilling et al., 2014; Schilling et al., 2011; Schilling et al., 2013; Shore, 2011; Wen and Carignan, 2011; Zhu et al., 2014). In addition, Earth's atmospheric redox evolution has more recently been studied by examining the redox state of the oceans using Se isotopes in the ancient sedimentary record (e.g. Kipp et al., 2017; Mitchell et al., 2016; Pogge von Strandmann et al., 2015; Stüeken et al., 2015a; Wen et al., 2014, and references therein). Moreover, Se isotope systematics have been evaluated as a possible tracer for the volatile evolution of meteoritic material and planetary reservoirs (Vollstaedt et al., 2016a; Vollstaedt et al., 2016b). To this end low Se containing planetary reservoirs such as the Earth's mantle need to be more firmly constrained and require new Se isotopic data which need to be placed in context of its elemental behavior.

In the Earth's mantle, Se is an ultra-trace element, with typical Se content <100 ng g^{-1} in lherzolites (Lorand and Alard, 2010). Although small fractions of Se can be present in silicates (Tamari et al., 1990), Se mostly is concentrated in micrometric sulfides and is accordingly considered chalcophile (Hattori et al., 2002; König et al., 2014; Lorand et al., 2013; Luguet et al., 2004). In contrast to the highly siderophile elements (HSE, Os, Ir, Ru, Rh, Pt, Pd, Re, Au), studies involving Se in mantle-derived rocks are still relatively rare (Alard et al., 2011; Lorand and Alard, 2010; Lorand et al., 2003; Lorand et al., 2004; Morgan, 1986), although more recent high-precision isotope dilution studies on Se in fertile and depleted peridotites and pyroxenites have emerged (König et al., 2015a; König et al., 2014; König et al., 2012; Wang and Becker, 2013; Wang et al., 2013). These are complemented by geochemical and experimental studies on Se behavior during mantle melting (Brenan, 2015; Lissner et al., 2014; Marchesi et al., 2013).

The Se concentration in the Earth's mantle is estimated to be ~80 ng g^{-1} (McDonough and Sun, 1995; Wang and Becker, 2013). When normalized to a CI chondrite, the Se depletion degree is ~0.0037 × CI (Palme and O'Neill, 2003; Vollstaedt et al., 2016a), similar to but somewhat lower than what is observed for the HSEs (Becker et al., 2006). These elements altogether show a roughly chondritic pattern and an excess abundance in the Earth's mantle compared to those predicted following core-mantle differentiation (Lorand et al., 2008; Morgan et al., 2001; Walker, 2009). This is widely explained by late accretion of chondritic material (e.g. Kimura et al., 1974; Mann et al., 2012; Walker, 2009) shortly after core-mantle differentiation.

Due to its volatile character, Se links late accretion with the origin of other volatiles such as e.g. S, Te, Zn but also highly volatile components like H_2O, C, or N_2 (McDonough and Sun, 1995; Wang and Becker, 2013). Understanding the origin and evolution of Se in the Earth's mantle-crust-atmosphere system may thus help to constrain the origin of volatile components on Earth. However, it remains controversial whether the Se systematics in mantle rocks allow description of late accreted components (Wang and Becker, 2013), or metasomatic processes in the mantle (König et al., 2014; König et al., 2015b; Wang and Becker, 2015). A new perspective provided by the isotopic signature of Se may help in this context. Yet analyses remain challenging because igneous rocks contain orders of magnitudes lower Se concentrations in the range of 10 to 200 ng g^{-1} (König et al., 2014; Lissner et al., 2014) compared to sediments with µg g^{-1} levels of Se. Hence, an analytical technique is needed to precisely and accurately determine the Se isotope ratio of low abundance geological materials including igneous rocks such as basalts. Here we present a method for Se isotope measurements of such samples with Se concentrations of few tens of nanograms, using a double spike technique and a hydride generation introduction system on a Neptune*Plus*™ MC-ICP-MS.

1.2 Materials and analytical techniques

1.2.1 Reagents and materials

All sample digestions, chemical purifications and instrumental measurements were performed at the ISO-5 (US FED standards class 100) clean-room facilities of the Isotope Geochemistry Group at the University of Tübingen, Germany. De-ionized water was further purified with a Merck Millipore Milli-Q™ system to 18.2 MΩ × cm at 25 °C. All acids used during digestion, sample preparation and measurements were distilled from MERCK Millipore Emsure™ grade HNO_3 (65 %) and HCl (37 %) with Savillex™ DST-1000 Acid Purification Systems and diluted to required molarities to ±0.03 mol L^{-1} as checked by titration. Eichrom® ion exchange resins, beakers, vials for centrifugation and analysis were pre-cleaned with multi-step HCl-HNO_3 treatments.

Two Se standard solutions with different Se isotopic compositions were used. The Se standard reference material SRM-3149 (Lot.-#: 100901; 10.042 ± 0.051 mg g^{-1}) was purchased from the National Institute of Standards and Technology (NIST). NIST SRM-3149 is now widely used as δ-zero reference material for Se isotope measurements (Carignan and Wen, 2007). The second standard solution used in our study is MH-495, previously used as an in-house Se solution at the University of Urbana, Illinois and generously provided by T. M. Johnson (Johnson and Bullen, 2004; Johnson et al., 1999). This standard solution was created from reagent-grade Se^0 pellets at the University of California at Davis by Mitchell Herbel (Johnson et al., 1999) and shows a $\delta^{82/76}$Se isotope ratio lower than the reference value for NIST SRM-3149 by −3.04 ± 0.50 ‰ (2σ, n = 2) (Carignan and Wen, 2007) to −3.44 ± 0.06 ‰ (2σ, n = 5) (Zhu et al., 2014).

For comparison to previously published Se isotope results we chose the two US Geological Survey (USGS) shale reference materials SGR-1 and SCo-1 (e.g. Pogge von Strandmann et al., 2014; Rouxel et al., 2002). These shales have relatively high Se concentrations (SGR-1: 3.50 ± 0.28 µg g^{-1}; SCo-1: 0.89 ± 0.06 µg g^{-1}) (Gladney and Roelandts, 1988) and comparison to other studies is possible (Kipp et al., 2017; Mitchell et al., 2012; Pogge von Strandmann et al., 2014; Rouxel et al., 2002; Schilling et al., 2011; Stüeken et al., 2013; Stüeken et al., 2015b; Stüeken et al., 2015c; Vollstaedt et al., 2016a). We also selected the USGS BCR-2 (~77.8 ± 6.4 ng g^{-1}, 2σ, n=5) (Lissner et al., 2014), which has a factor 50 lower Se concentration compared to the USGS shales, can be compared to data reported by Rouxel et al. (2002) and is suitable as a geological reference to terrestrial basalts.

1.2.2 Sample digestion and Se purification

Between 10 and 1000 mg of sample powder were weighted into quartz glass vessels (15, 50 or 90 mL) and mixed with an adequate amount of the ^{77}Se–^{74}Se double spike solution. We report accuracy tests where variable amount of in-house standard solution MH-495 was additionally admixed to some samples (section 3.2). Depending on the sample weight 2.5 to 7.5 ml inverse aqua regia (3:1

M ratio; conc. HNO_3 : conc. HCl) were added, the vessels were subsequently sealed with Teflon-tape and placed in a high-pressure asher (HPA-S, Anton Paar, Graz). During digestion for 16 h at 220 °C and 100 bar, Se was extracted from the sample material and equilibrated with the Se double-spike.

Several studies emphasize Se loss in the presence of HCl while evaporating at temperatures exceeding 80 to 85 °C (Layton-Matthews et al., 2006; Pogge von Strandmann et al., 2014; Rouxel et al., 2002; Stüeken et al., 2013; Wang et al., 2013). This is because of the formation of volatile Se-species (e.g. Stüeken et al., 2013; Vollstaedt et al., 2016a). Special care was taken during subsequent chemical purification: Se solutions were dried down without exceeding 65 °C and re-dissolved in concentrated HCl to convert all Se^{VI} to Se^{IV} (Elwaer and Hintelmann, 2008; Pogge von Strandmann et al., 2014).

Previous studies have demonstrated that the purification of Se from a sample matrix can be challenging in terms of quantitative recoveries from ion exchange resins and a potentially associated mass-dependent fractionation (e.g. Pogge von Strandmann et al., 2014). Thiol cotton fibre (TCF) or powder (TCP) is one way to separate Se from its sample matrix. This method allows recovering ≥98% of the initial Se (Elwaer and Hintelmann, 2008; Rouxel et al., 2002) and has been used for routine determination of Se concentrations of rock reference materials at low ng levels (e.g. König et al., 2012; Marin et al., 2001; Yu et al., 1983). The relatively high Se yield and the additional advantage of a simultaneous Te purification is considered a good choice for concentration analysis (Yu et al., 1983). The use of TCF/TCP can lead to the formation of insoluble salts and organic-derived interferences on Se masses (Pogge von Strandmann et al., 2014). Thus, TCF-/TCP-handled samples require careful treatment with HNO_3 and H_2O_2 (König et al., 2012; Pogge von Strandmann et al., 2014; Rouxel et al., 2002). In order to test the instrumental capabilities we here describe a simpler technique adapted from Fehr et al. (2004) and Wang et al. (2013). This involves the combination of conventional ion exchange chromatography procedures with hydride generation. The following procedure has been optimized for Se purification and yields.

First, the dried samples obtained after a first evaporation were dissolved with 4 mL 6 mol L^{-1} HCl and centrifuged at 5000 rpm for 10 min. Before loading the sample solutions onto Spectra/Chrom® Disposable MiniColumns containing 3 mL of Eichrom® AG1-X8 anion resin (100–200 mesh), the resin was washed with 3 ml of 1 mol L^{-1} HNO_3 twice and conditioned with 2 × 3 mL 6 mol L^{-1} HCl. While Fe was retained as $FeCl_4^-$ by the resin, Se was not adsorbed but collected together with other matrix elements in 12 mL 6 mol L^{-1} HCl. The collected Se-containing solutions were evaporated to dryness at $T \leq 65$ °C. The dried down solutions were then taken up in 4 ml 0.06 mol L^{-1} HNO_3 for purification by cation exchange chromatography using Spectra/Chrom® Disposable MiniColumns containing 3 mL of Eichrom® AG50W-X8 resin (100–200 mesh) (e.g. Wang et al., 2013). The cation exchange resin was washed with 6 mol L^{-1} HCl and

H_2O and conditioned with 6 mL 0.06 mol L^{-1} HNO_3 before loading the samples. Se was collected in 12 mL 0.06 mol L^{-1} HNO_3 while other matrix elements were retained on the resin under these conditions. The solutions containing Se were again dried at T ≤65 °C on a hotplate, re-dissolved in 2 mol L^{-1} HCl and heated in closed beakers on a hotplate at 80 °C for several hours to achieve complete reduction of Se^{VI} to Se^{IV} (Elwaer and Hintelmann, 2008; Pogge von Strandmann et al., 2014). Typically, our total procedural blanks remain below detection limit and only in some cases show up to 1 ng, likely mirroring randomly suboptimal HPA-S glass vial treatment. While this still represents only <1 % of bulk Se for most samples analyzed here, multiple replicate digestions of all samples were performed in order to verify results with different blank levels including for lower Se containing samples. Although blanks are generally too low to determine an isotopic composition, high reproducibility for various blank levels confirms that blanks are negligible.

1.2.3 The role of the double spike

Metallic selenium enriched in ^{77}Se and ^{74}Se tracer material in metal form was obtained from ISOFLEX. Upon dissolution in 2 mol L^{-1} HNO_3, a double spike solution with a composition of ~52% ^{74}Se and ~47% ^{77}Se was prepared taking the error propagation calculations after Rudge et al. (2009) into account. After dilution, the normality of nitric acid in the double-spike solution was 0.1 mol L^{-1}. Other Se isotopes account for <1% of the double spike solution as shown in Table 1.1, which also gives a comparison to double spike compositions used in other studies. Provided that sample and spike are well equilibrated prior to chemical purification, double spike methods have already been demonstrated to be suitable for Se stable isotope analyses (Clark and Johnson, 2010; Johnson et al., 1999; Pogge von Strandmann et al., 2014; Vollstaedt et al., 2016a; Zhu et al., 2008).

The spike was calibrated against the NIST SRM-3149 Se solution. Various proportions of spike-sample ratios (f_{spike} from 0.1 to 0.9, n = 9) were tested. To increase the small volumes of NIST SRM-3149 and double spike, an additional 2 mL of 2 mol L−1 were added. To achieve equilibration the mixtures were heated at 80 °C in a closed beaker for a minimum of 2 h. The mixtures were then dried down at 65 °C and re-dissolved in 2 mol L−1 HCl, again heated at 80 °C for 2 h to ensure that all Se is reduced and finally measured. All measured mixtures of f_{spike} varying from 0.1 to 0.8 give $\delta^{82/76}$Se within our long-term reproducibility for NIST SRM-3149 of 0.00 ± 0.11‰ (2σ, n = 350, Tab. A.1.5) (filled circles in Fig. 1.1a). Note that the mixture with the lowest $f_{spike} = 0.1$ has a significantly larger internal uncertainty (2 s.e error bars in Fig. 1.1a) and the mixture with the highest $f_{spike} = 0.9$ is outside of the external reproducibility of 0.11 ‰ given by all other mixtures with f_{spike} between 0.2 and 0.8. This provides a lower and upper limit of acceptable double spike-sample ratios. Within the wide range of f_{spike} between 0.2 and 0.8 the ^{74}Se–^{77}Se double spike used in this study thus allows for accurate Se isotope measurements. A systematic shift to heavier $\delta^{82/76}$Se of 0.18 ± 0.10‰ (2σ, n = 7) is observed for mixtures that were not allowed to equilibrate as described above (open circles in Fig. 1.1a), but directly dried down after mixing. This may be due to preferential loss of light Se isotopes during evaporation, even at temperatures below 65 °C, prior to full equilibration of standard and spike Se and emphasizes that careful treatment is crucial.

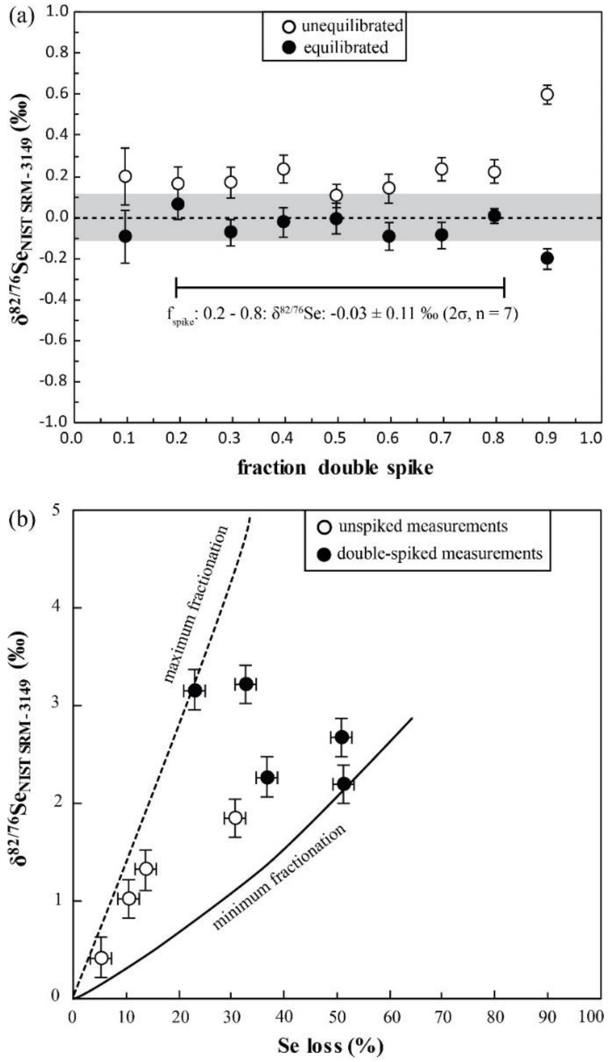

Figure 1.1 (a) Measured $\delta^{82/76}Se_{NIST\ SRM\text{-}3149}$ as a function of various proportions of double spike (filled circles). The results indicate that even significantly underspiked (f_{spike} = 0.2) or overspiked (f_{spike} = 0.8) standards yield accurate data. Grey box represents the long-term average for $\delta^{82/76}Se_{NIST\ SRM\text{-}3149}$ of 0.00 ± 0.11‰ (2σ, n=350). Unfilled circles show measured $\delta^{82/76}Se_{NIST\ SRM\text{-}3149}$ for unequilibrated mixtures of standard and double spike Se, resulting in isotopic shift towards heavier values of 0.10 to 0.60‰. Error bars are internal errors (2 s.e.) for each measurement. For measurement data see Tab. A.1.1 (b) $\delta^{82/76}Se_{NIST\ SRM\text{-}3149}$ as a function of evaporative loss of light Se isotopes. Results indicate unpredictable loss-induced fractionation between solution and vapor even at 65 °C and thus illustrate the requirement for double spike use in our experimental set up. Unfilled circles represent data from SSB measurements. Filled circles represent double spike measurements (section 1.2.3). Uncertainty on data is 0.20‰ (2σ). See section 1.2.3 for details. Measurement data provided in Tab. A.1.2.

Based on the above observation, we further tested the possibility of Se isotope fractionation during partial Se loss by evaporation from solutions with HCl. For this, NIST SRM-3149 solutions were dried down at 65 °C without spike addition. The Se isotope measurements were then performed with two different analytical approaches, one involving the sample-standard bracketing (SSB) (Stüeken et al., 2013) and the other the double spike measuring method (e.g. Pogge von Strandmann et al., 2014; Vollstaedt et al., 2016a). For the SSB approach a 50 ng mL^{-1} NIST SRM-3149 Se solution was used as the bracketing standard, yielding ^{82}Se voltages of roughly 1.5V (using an amplifier resistor of 10^{11} Ω). Sample solutions were then prepared to match the signal intensity of the standard within 10% intensity. Samples and standards were measured for 100 cycles each having an integration time of 4.194 s. Over the measurement session, Se in-house solution (MH-495) was measured versus the NIST SRM-3149 standard solution. These solutions were taken directly out the main batch and were not dried. SSB measurements yielded average $\delta^{82/76}$Se of −3.25 ± 0.03‰ (2σ, n = 4), indistinguishable from our double-spike value (MH-495: −3.27 ± 0.13 ‰, 2σ, n = 100, Tab. A.1.4) (see section 3.1). For the SSB approach, four solutions were processed and Se losses varying between 5 and 30% yielded $\delta^{82/76}$Se values ranging between 0.43 ± 0.31‰ and 1.85 ± 0.31‰ (Fig. 1.1b, open circles) (Tab. A.1.2). For the double spike measuring approach, five NIST SRM-3149 solutions were doped with an adequate amount of the double spike after evaporation and prior to mass spectrometric determinations, which were performed on ~15 ng mL^{-1} Se solutions. Evaporative Se losses between 23 and 51 % with $\delta^{82/76}$Se values ranging between 2.20 ± 0.20‰ and 3.20 ± 0.20‰ were determined by the double spike measurements (Fig. 1.1b, filled circles).

The data of our two experiments cannot be explained by a single unidirectional fractionation process as they do not fit a single Rayleigh evaporation function. The data rather indicate Rayleigh distillations with variable isotopic fractionations $\Delta_{\text{vapor-solution}}$ ranging between 3 and 12‰ (Fig. 1.1b). If the theoretical fractionation associated with evaporation corresponds to the square root of the evaporated molecule masses (Richter, 2004; Young et al., 2002), the inferred fractionations seem consistent with evaporation of pure $SeCl_2$ (fractionation $\Delta_{\text{vapor-solution}}$ of ~13‰) and pure $SeCl_6$ (fractionation $\Delta_{\text{vapor-solution}}$ of ~7‰). Future studies are needed to evaluate the exact speciation of evaporated selenium species. The origin of evaporative loss of Se remains unclear, but our experiments clearly demonstrate a significant loss of preferentially isotopically light Se during evaporation of pure reference materials. However, the double spike approach inherently corrects for such chemistry-induced fractionations.

1.2.4 Mass spectrometry (MC-ICP-MS)

1.2.4.1 Instrumental parameters and set up

Isotope measurements were conducted on a ThermoFisher Scientific® Neptune*Plus*™ multi-collector inductively coupled plasma mass spectrometer linked with a CETAC® HGX 200 hydride generator, an ESI MP2-6 peristaltic pump and an ESI SC-µ DX autosampler. To obtain the highest Se sensitivity at high front vacuum a nickel skimmer cone (H-cone) and a Ni-Jet sample cone were employed. Daily tuning included the gas flows and torch positions. Typical parameters and settings are listed in Table 1.2. Measured masses include interference monitors for hydrides and argon dimers as generated in the plasma (Table 1.3). Signal intensities given in V were obtained using amplifier resistors of 10^{11} Ω.

1.2.4.2 Hydride generation

One of the major advantages of a hydride introduction system is the efficient transport of Se into the plasma under dry conditions (Johnson and Bullen, 2004). The hydride generator serves as Se signal booster and as a purification device, because exclusively hydride-forming elements (e.g. Se, As, Ge) are effectively transferred to the plasma (Clark and Johnson, 2008). A sodium borohydride solution is prepared by adding 1 g of $NaBH_4$ (analysis grade) to 250 mL of 18.2 MΩ-grade water. To stabilize the solution, 1 g of sodium hydroxide monohydrate is added. In our setup, constant flows of 2 mol L^{-1} HCl and sodium borohydride (NaBH4; 0.4% (m/m)) are mixed in a coil which results in a steady production of hydrides throughout an entire measurement session. To this constant hydride-generating mixture the sample is then additionally introduced in 2 mol L^{-1} HCl and H_2Se is formed according to reaction (1) that can be ionized efficiently.

$$4\ H_2SeO_{3(aq)} + 3\ HCl_{(aq)} + 3\ NaBH_{4(aq)} \rightarrow 4\ H_2Se_{(g)} + 3\ H_3BO_{3(aq)} + 3\ H_2O + 3NaCl_{(aq)} \qquad (1)$$

Residual non-hydride forming matrix elements that remain in the sample solution after chemical purification are fully excluded via a gas/liquid separator while hydrides are carried to the plasma in an argon flux (Fig. 1.2). In addition to argon for the plasma and to act as the sample carrier gas, we also introduced methane because it enhances the sensitivity for Se as shown in previous studies (e.g. Floor et al., 2011). In our instrumental setup, an increase of the Se signal by a factor two to three was achieved.

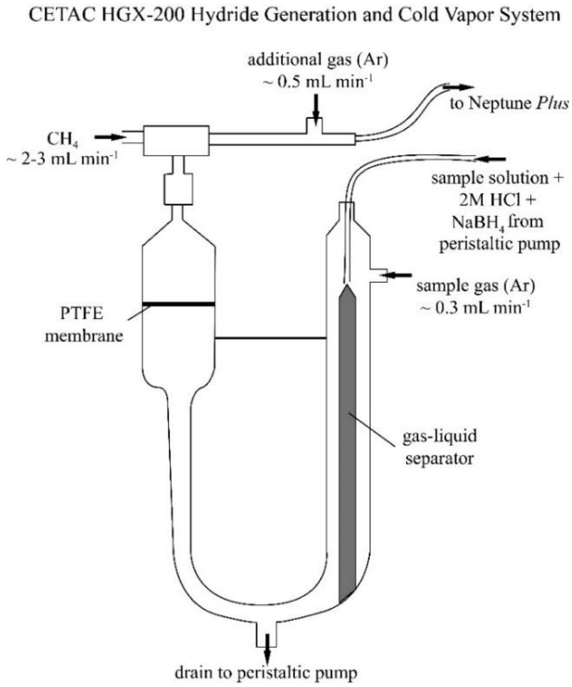

Figure 1.2 Schematic set up of the hydride generator system.

1.2.4.3 Analyses, interference corrections and double spike deconvolution

Instrument parameters were optimized for high Se signal intensities and low Argon dimers before each measurement session. Typical signals on ^{82}Se of a 15 ng mL^{-1} solution with the operating conditions summarized in Table 1.2 are 0.5 V. Each measurement consists of 40 cycles with 4.194 s integration time. Washout time was generally set to 4 min. All measurements of standards and samples were bracketed by background (on-peak zero) measurements of the same batch of pure 2 mol L^{-1} HCl in which standards and samples were taken up. On-peak zeros were subtracted from measured intensities of standards and samples. Measurements of NIST SRM-3149 standard solutions were performed between each sample to assess potential instrumental drift. Additionally, standard solution MH-495 was measured after every 5th sample. Following acquisition of isotope signal intensities the data was further reduced offline. A major issue of stable Se isotope measurements are the numerous single-mass polyatomic isobaric interferences that typically form in plasma source mass spectrometers in the mass range of Se isotopes and interference monitors (Table 1.3). These spectral interferences can be divided into (i) plasma induced, (ii) plasma and analyte matrix induced and (iii) analyte and sample matrix induced.

The subtraction of on-peak zero signals determined on pure analyte matrix solutions (i.e. 2 mol L^{-1} HCl) from sample signals adequately accounts for the small interferences of Kr and ArCl. On-peak zero subtraction, however, does not allow accurate correction of the large ArAr interferences due to the considerable fluctuations in the plasma energy between and within sample runs. We typically observe ^{40}Ar^{40}Ar^{+} signals of 20–25 V, with variations of this signal from scan to scan of ±0.15 V due to plasma fluctuations. We therefore employed a two-step strategy for accurate correction of Ar dimer interferences:

(1) We admixed methane to the sample Ar gas carrying the SeH_2 from the hydride generator to the plasma torch (Fig. 1.2). Enhancement of Se signal and suppression of polyatomic interferences by methane addition for Se concentration and isotope ratio measurements has been described in previous studies (Fliegel et al., 2011; Floor et al., 2011; Guo et al., 2013). We indeed observed an approximately two- to three-fold increase in Se signal intensities and a decrease in Ar dimer intensities by a factor of two with an addition of 2.0–3.5 mL min^{-1} methane to the instrument. This significantly suppressed Ar dimer signals allowed more accurate on-peak zero corrections of polyatomic Ar interferences. Furthermore, hydride interferences (ArArH^{+}, SeH^{+}, GeH^{+}, BrH^{+}, AsH^{+}) dropped to negligible levels by methane addition making subsequent correction of hydrides after on-peak zero subtraction unnecessary.

(2) We employed a secondary correction for Ar dimer interferences as described by Elwaer and Hintelmann (2008), which takes plasma energy fluctuations into account. We used the ^{82}Se signal to predict the ^{80}Se signal of the samples by artificially fractionating the ^{82}Se/^{80}Se ratio using the samples' instrumental mass bias. Assuming IUPAC Se isotope composition (Berglund and

Wieser, 2011) the ^{80}Se signal of the sample is estimated and subtracted from the signal measured at m/z = 80 to estimate the excess or deficit in ^{40}Ar^{40}Ar^{+} compared to the on-peak zero measurement. Signals of the minor Ar dimers (i.e. ^{36}Ar^{36}Ar$^{+,}$ ^{38}Ar^{36}Ar^{+}, ^{38}Ar^{38}Ar^{+}, ^{40}Ar^{36}Ar^{+} and ^{40}Ar^{38}Ar^{+}) are then determined relative to the calculated ^{40}Ar^{40}Ar^{+} signal considering the relative abundance of Ar isotopes (Berglund and Wieser, 2011). For measurements on 15 ng mL^{-1} sample solutions this correction improves the external 2σ reproducibility on $\delta^{82/76}$Se values by 20 to 30%. We tested the necessity to artificially fractionate Ar isotope ratios to account for the instrumental mass bias. We assumed that at a first order, Ar and Se are subject to equal isotope fractionations in the instrument plasma, which per se is not entirely correct. Since this artificial fractionation of Ar isotope ratios only resulted in shifts of 0.001 to 0.002‰ for both sample and standard solutions. This therefore means that the possible occurrence of Ar isotopic fractionation in the plasma has a negligible effect on our Se isotope data correction. Consequently, for routine measurements, possible Ar isotopic fractionations were ignored. The calculated ArAr interferences were arithmetically subtracted from measured Se signal intensities.

The iterative double spike deconvolution calculations used first by Compston and Oversby (1969) for Pb isotopes were applied to correct the measured Se isotope data with the exception that exponential rather than linear law was used as a proxy for the instrumental mass bias. Apart from the two spike isotopes ^{74}Se and ^{77}Se, ^{78}Se and ^{82}Se were used for the deconvolution. All isobaric interferences (e.g. Ge correction, see below) and the fluctuations of Ar dimers were iteratively converged within the double spike deconvolution for accurate corrections. The double spike deconvolution yields three types of information: (i) an exponential fractionation factor (per amu) for the instrumental mass bias, which might also include a mass-dependent Se isotope fractionation during chemical purification of the sample. (ii) An exponential fractionation (per amu) for the samples' natural mass-dependent fractionation compared to NIST SMR-3149 against which the double spike was calibrated. From this factor the samples' natural Se isotope ratios are calculated and can be reported in the δ-notation as the per mil difference in these ratios compared to that of the isotopically certified reference material NIST SRM-3149. The samples' natural isotope ratios are calculated according to eq. (2) and can be converted to any ratio per amu as a function of the exact masses of ^{82}Se, ^{78}Se and ^{76}Se (Young et al., 2002). (iii) The spike-to-sample ratio from which, knowing the Se concentration of the double spike, an accurate Se concentration for the sample can be calculated.

$$\delta^{82/78}\text{Se} = [(^{82}\text{Se}/^{78}\text{Se})_{\text{sample}}/(^{82}\text{Se}/^{78}\text{Se})_{\text{NIST SRM-3149}} - 1] \times 1000 \qquad (2)$$

1.2.4.4 Accuracy of isobaric interference correction of ^{74}Ge on ^{74}Se

Germanium like Se forms hydrides (GeH_4) leading to isobaric interferences of ^{74}Ge on ^{74}Se and ^{76}Ge on ^{76}Se during mass spectrometric analyses. We observed the Ge correction to be unnecessary if the measured Ge/Se ratio is smaller than 0.0001 when measuring 15 ng mL^{-1} sample solutions: below this threshold, Ge signals are below 0.5 mV on mass 72 and appear to be indistinguishable from background noise. Correcting for this signal only adds uncertainty to the internal precision of the $\delta^{82/76}$Se value without significantly changing it. At Ge/Se ratios above this threshold value, the canonical ^{72}Ge/^{74}Ge ratio of 0.7521 (Berglund and Wieser, 2011) was artificially fractionated using the instrumental mass bias determined for Se to correct ^{74}Se from the isobaric interference of ^{74}Ge. However, the instrumental mass bias for Se also includes the mass-dependent Se isotope fractionation induced by the chemical purification when Se recovery is incomplete.

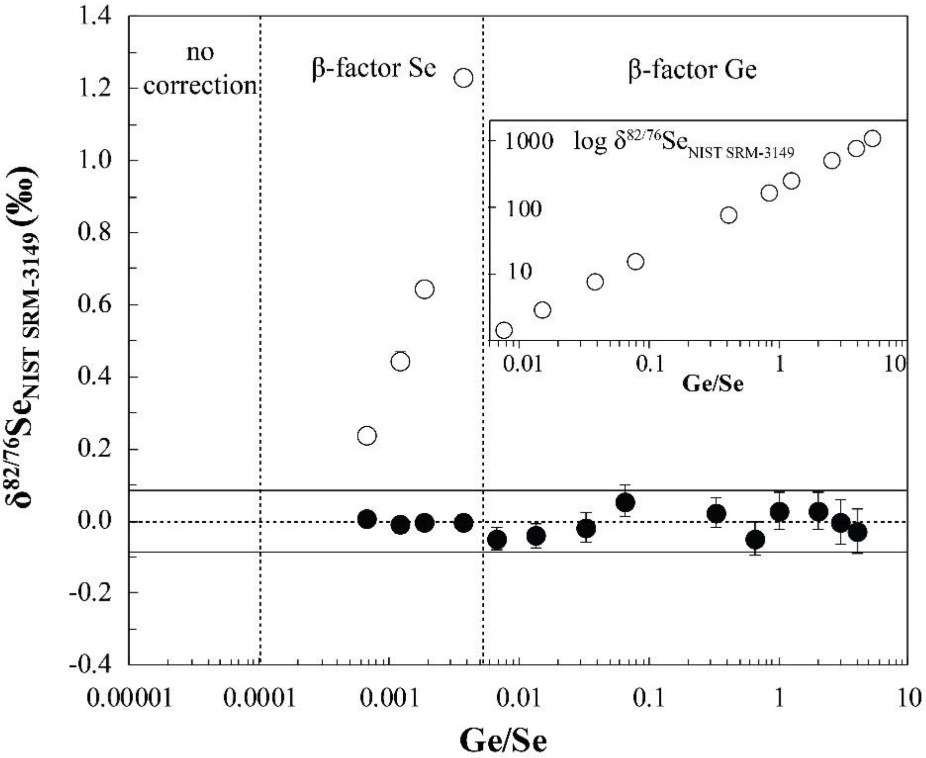

Figure 1.3 Results of measurements of Se standard solution NIST SRM-3149 doped with different amounts of Ge. The constant range of $\delta^{82/76}$Se shows efficient correction even for Ge/Se ratios of up to 4. Grey bar represents 2σ (0.08‰) of obtained $\delta^{82/76}$Se$_{\text{NIST SRM-3149}}$ data, whereas error bars are in-run errors (2 s.e.) of single measurements. Dashed lines indicate threshold values for correction with Se or Ge mass bias, respectively. Unfilled symbols indicate uncorrected $\delta^{82/76}$Se$_{\text{NIST SRM-3149}}$ (uncorrected data for Ge/Se >0.0056 given in logarithmic scale as isotopic shift is >1.3 to 1006‰).

Furthermore, the chemically induced mass-dependent isotope fractionation of Ge is likely different from that of Se. As a result, this correction is only applied to Ge/Se ratios <0.0056. We set this value as it still yields accurate data for Se mass bias corrected data. Above this upper threshold value for the Ge/Se ratio (see. Fig. 1.3) for 15 ng mL^{-1} measurement solutions, signal intensities of ^{72}Ge and ^{73}Ge become large enough (>2 mV on mass 72) to accurately determine the mass-dependent instrumental mass bias and chemical fractionation of Ge assuming a canonical ^{72}Ge/^{73}Ge of 0.2823 (Berglund and Wieser, 2011). To test the accuracy of our Ge interference correction method, 15 ng mL^{-1} NIST SRM-3149 solutions were mixed with different amounts of a pure Ge in-house standard solution, similar to a previous approach described by Pogge von Strandmann et al. (2014). As illustrated in Fig. 1.3 the values of the Ge-doped NIST SRM-3149 solutions perfectly lie within the external reproducibility for this standard of 0.00 ± 0.11‰ to Ge/Se ratios of up to 4 (see Tab. A.1.3), showing that this method accurately corrects any Ge interference.

1.3 Results and discussion

1.3.1 Se isotope measurements of matrix-free standard solutions

Background or "on-peak zero" (OPZ) corrections have been used in Se isotope analytical studies to account for plasma and other instrumental interferences (e.g. Johnson, 2004; Rouxel et al., 2002; Zhu et al., 2008). Previously performed scans on an Element 2 ICP-MS at high resolution (m/Δm = ~10,000, 5–95% peak edge width) resolved Se and ArAr peaks and observed constant voltage on ArAr peaks regardless of whether Se was introduced in the plasma (Pogge von Strandmann et al., 2014). This was argued to justify the use of OPZ correction. We performed Se isotopic measurements while using the OPZ correction on our MC-ICP-MS in low (LR) and medium resolution (MR) mode (m/Δm = ~2000 vs. MR: m/Δm = ~7000, respectively, 5–95% peak edge width). The MR measurements allow crude resolution of Se and ArAr peaks but yielded indistinguishable isotope results than in LR mode. This confirms the validity of the OPZ correction and demonstrates that measurements in LR produce precise and accurate data as previously suggested (Pogge von Strandmann et al., 2014).

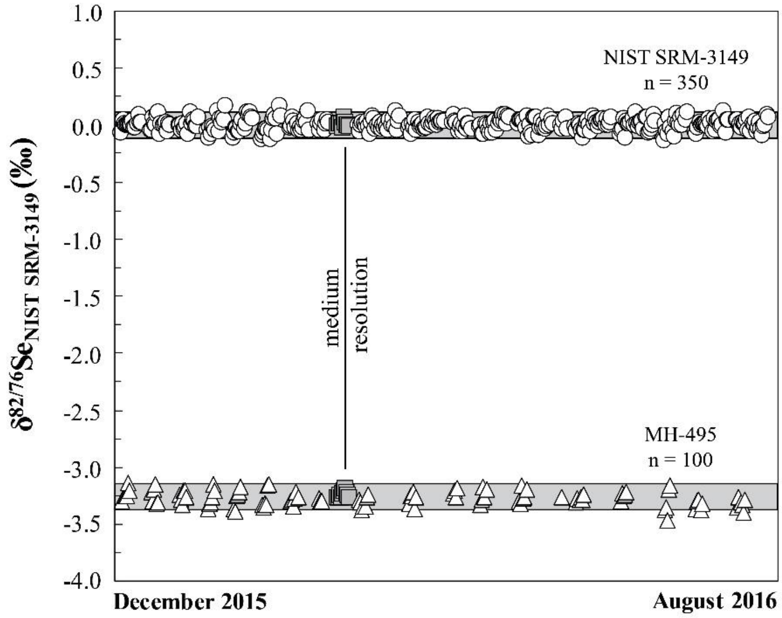

Figure 1.4 Long-term reproducibility of NIST SRM-3149 ($\delta^{82/76}Se_{NIST\ SRM\text{-}3149}$: 0.00 ± 0.11‰, n = 350, Tab A.1.5) and MH-495 ($\delta^{82/76}Se_{NIST\ SRM\text{-}3149}$: −3.27 ± 0.13‰; n = 100; Tab.A.1.4). Grey bars represent 2σ uncertainties. Measurements in MR yield indistinguishable data compared to data acquired in LR, showing that LR measurements are sufficient for precise and accurate Se isotope data acquisition.

Over a period of over 6 months that included LR and MR measurements, a long-term average and reproducibility for MH-495 of $\delta^{82/76}$Se = −3.27 ± 0.13‰ (2σ, n=100) is obtained (Fig. 1.4). This is consistent with recently published values following double-spike measurements (−3.44 ± 0.06‰; 2σ, n=5) (Zhu et al., 2014) and within uncertainty of an earlier study using standard-sample bracketing measurements (−3.04 ± 0.50‰, 2σ, n=2) (Carignan and Wen, 2007).

1.3.2 Accuracy tests

Despite a quantitative removal of matrix elements by ion exchange chromatography and hydride generation, potential matrix effects may not be always ruled out because droplets from excess liquid could occasionally pass the PTFE-membrane of the hydride generation system. Although negligible voltages were observed on the masses of chloride (^{35}Cl and ^{37}Cl), the likely main constituent of such droplets, we tested the effect of variable matrix/Se ratios by adapting a standard addition method employed previously (Nielsen et al., 2004; Schumann et al., 1992; Tipper et al., 2008). Increasing amounts of MH-495 were admixed to constant amounts of NIST SRM-3149, homogenized (see section 2.3), re-dissolved and measured. Unresolved polyatomic interferences from the carrier solutions and/or gases would lead to samples arbitrarily plotting off a two-component mixing line. Here we show that mixtures remain within uncertainty of 0.20‰ (2σ) (Fig. 1.5a), which argues against the contribution of unresolved interferences.

In addition, we performed accuracy tests involving USGS reference material SGR-1. Increasing amounts of SGR-1 (20 to 40 mg or 70 to 140 ng total Se) were mixed to given amounts of standard solution MH-495. Measured and calculated Se isotope compositions remain within uncertainty of 0.20 ‰ (2σ) and confirm that potential matrix-induced interferences are negligible (Fig. 1.5b).

1.3.3 Exploring the minimum Se required for accurate isotope measurements

A major goal is to determine Se isotope compositions of samples with low Se concentrations such as basalts (<200 ng g^{-1}, see below). Before this is attempted, the minimum Se required for measurement was evaluated in a first step by analyzing 1 mL solutions of 50 to 3 ng per mL of MH-495 standard solution (filled circles in Fig. 1.6). Measured signals on ^{82}Se ranged from 0.1 to 1.5 V and showed no correlation with $\delta^{82/76}$Se of MH-495. It is however observed that the uncertainties vary with signal intensities: Solutions with a minimum of 15 ng mL^{-1} concentrations and >0.5 V on mass ^{82}Se (lowest abundant mass measured) show internal errors of 0.04 ‰ (2 s.e., n=6) and yield an external reproducibility of 0.09 ‰ (2σ, n=6). Solutions between 15 and 7.5 ng mL^{-1} show a higher internal error of up to 0.08‰ (2 s.e., n=5) and the external reproducibility increases to 0.12‰ (2σ, n=5). When the ^{82}Se signal is below 0.18 V, equivalent to solutions below 7.5 ng mL^{-1}, the internal error increases to 0.12‰ (2 s.e., n=7) and the external reproducibility becomes >0.20‰ (2σ, n=7). Hence, the external reproducibility systematically changes at a concentration of approximately 7.5 ng mL^{-1}. While it is desirable to measure sample solutions with higher than 15 ng total Se, we show the instrumental capability to yield 0.24‰ (2σ, n = 7) external reproducibility for down to 3 ng total Se. This is similar to results of a previous study by Zhu et al. (2008) using a different set up.

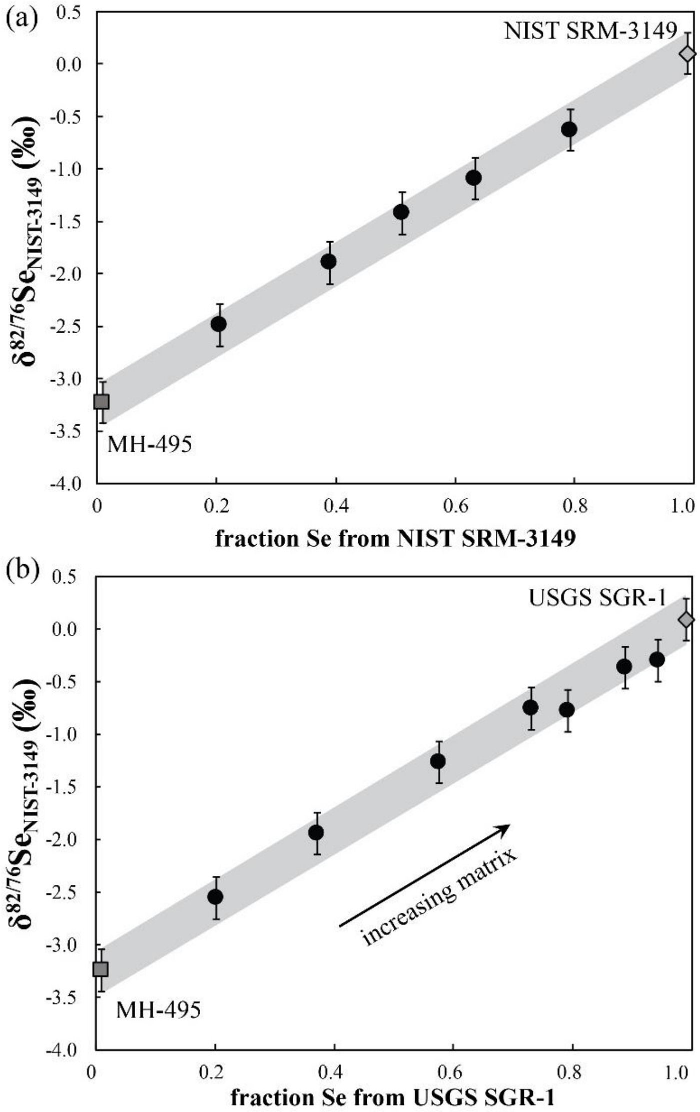

Figure 1.5 Results for Se isotope measurements of mixtures between (a) standard solutions MH-495 and NIST SRM-3149 and (b) increasing amounts of sample SGR-1 (20 to 40 mg or 70 to 140 ng total Se) and constant amounts of standard solution MH-495. Doped solutions fall on a mixing line between endmembers within maximum uncertainty of 0.20‰ (2σ), indicating no bias despite increasing matrix over total Se and potential emergence of interferences above background. Endmember data taken from same measurement session. For individual measurement data see Tab. A.1.6 and Tab. A.1.7.

Analogue to measurements of various amounts of MH-495 we performed tests with USGS reference material SGR-1 (unfilled circles in Fig. 1.6). This involved the digestion of 100 mg SGR-1 (equivalent to ~350 ng total Se, section 2.2) and dilution to various concentrations (from 50 ng mL^{-1} to 5 ng mL^{-1}). As for standard solution MH-495, the internal errors and the external reproducibility depend on signal intensities. Again, total Se contents with a minimum of 15 ng mL^{-1} yield internal errors of 0.04‰ (2 s.e., n=4) and an external reproducibility of 0.06‰ (2σ, n=4), whereas down to 7.5 ng mL^{-1} total Se analyzed yield internal errors of 0.07‰ (2 s.e., n=4) and an external reproducibility of 0.14 ‰ (2σ, n=4). Below 7.5 ng mL^{-1} the ^{82}Se signal intensities are <0.18 V and the internal error increases to 0.10 ‰ (2 s.e., n=6) and the external reproducibility is >0.14‰. This reproducibility obtained with a NeptunePlus™ instrument is similar to that previously reported for other instruments where similarly small quantities were analyzed (5 ng total Se analyzed with 0.25 ‰ (2σ) on $\delta^{82/76}Se$ on a Micromass IsoProbe by Rouxel et al. (2002) and on a NuPlasma by Zhu et al. (2008) (4 ng total Se analyzed with 0.10‰ (2σ) for standard solutions MH-495 and NIST SRM-3149 and 0.15–0.20 ‰ (2σ) for natural samples).

Measurements of USGS reference shales (SGR-1 and SCo-1) allow comparison to previous studies (Kipp et al., 2017; Mitchell et al., 2012; Pogge von Strandmann et al., 2014; Pogge von Strandmann et al., 2015; Rouxel et al., 2002; Schilling et al., 2011; Stüeken et al., 2013; Stüeken et al., 2015b; Stüeken et al., 2015c; Vollstaedt et al., 2016a) and have relatively high Se abundances (SGR-1: 3.50 ± 0.28 µg g^{-1}; SCo-1: 0.89 ± 0.06 µg g^{-1}) (Gladney and Roelandts, 1988).

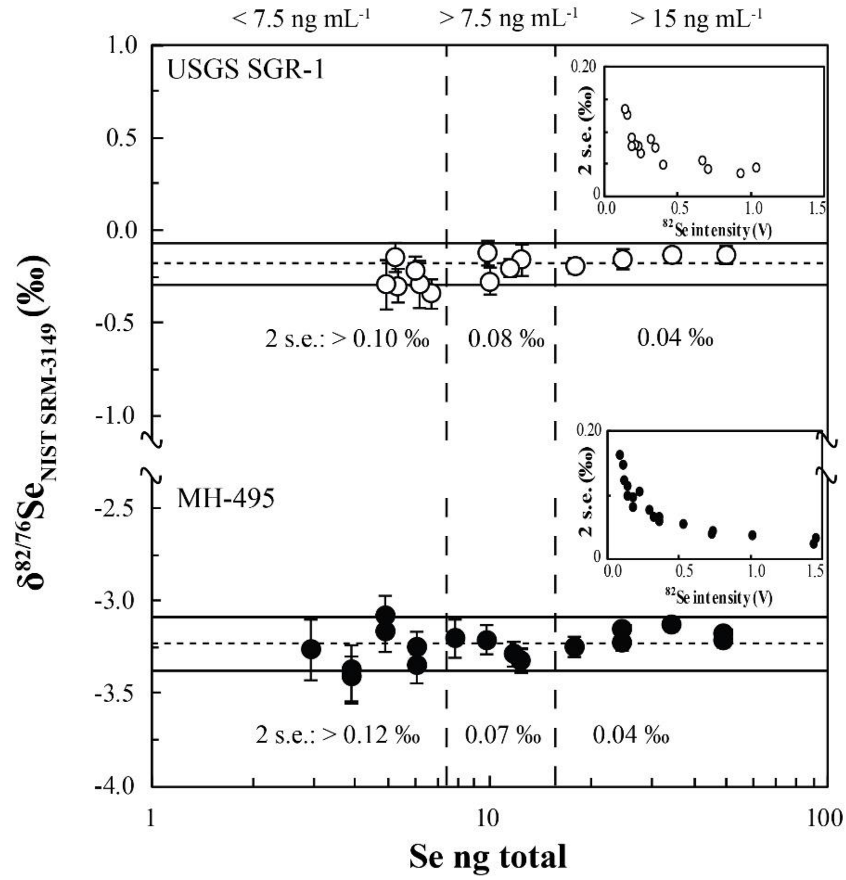

Figure 1.6 Results and signal-dependent external reproducibility for measurements of various dilutions of the MH-495 standard solution (filled circles) and 100 mg digested USGS rock reference material SGR-1 (unfilled circles). Error bars represent 2 standard errors (2 s.e.) of the individual measurements. Black dashed horizontal lines represent average value of dilutions >7.5 ng mL^{-1} as these are characterized by decent internal errors. Black solid horizontal lines are 2σ uncertainties. Vertical dashed lines divide dilutions into <7.5 ng mL^{-1}, 7.5–15 ng mL^{-1} and >15 ng mL^{-1}, which are characterized by different internal errors (2 s.e) and external reproducibility (see section 1.3.3). For individual measurement data see Tab. A.1.8.

Both our obtained concentrations (SGR-1: 3.76 ± 0.32 µg g^{-1}, 2σ, n=9; SCo-1: 0.84 ± 0.06 µg g^{-1}, 2σ, n=5) and isotopic compositions (SGR-1: −0.08 ± 0.20‰, 2σ, n=9; SCo-1:

−0.18 ± 0.22 ‰, 2σ, n=5) are within error of most previous studies (see Fig. 1.7) (Kipp et al., 2017; Mitchell et al., 2012; Pogge von Strandmann et al., 2014; Rouxel et al., 2002; Savard et al., 2009; Schilling et al., 2011; Stüeken et al., 2013; Stüeken et al., 2015b; Stüeken et al., 2015c; Vollstaedt et al., 2016a) and demonstrate full homogenization of sample with double spike Se. The USGS SGR-1 batch (USGS SGR-1, Split 25, Position 8) used in this study may be affected by heterogeneity. This may explain better reproducibility for repeated isotope measurements on diluted solutions from the same sample digestion, compared to solutions from separately digested material. Therefore, our values for samples (Fig. 1.7 and Tab. 1.4) that were obtained from separately digested material in different measurement sessions over a period of 9 months provide a long-term external reproducibility.

1.3.4 Selenium measurements of samples with concentrations in the ng g^{-1} range

In order to test our method on low Se containing samples with a matrix relevant to mantle derived rocks, USGS reference basalt BCR-2 is suitable (78 ± 3.2 ng g^{-1}, 1σ, n=5) (Lissner et al., 2014). For this we weighted, double-spiked and digested 300 mg of BCR-2 (equivalent to ca. 25 ng total Se). Our batch of BCR-2 (3223) yields a Se concentration of 71 ± 4 ng g^{-1} (1σ, n=3, Tab. 1.4), which is within uncertainty to published concentrations (Lissner et al., 2014). The isotopic data acquired is based on measurements of 1 mL sample solution containing ca. 15 ng total Se. Our measurement yields $\delta^{82/76}$Se of 0.18 ± 0.03‰ (2σ, n=3). This value is also within uncertainty to 0.24 ± 0.25‰ (2σ, n=n. g.) reported by Rouxel et al. (2002). It is important to note that the isotopic composition obtained is unlikely to represent a mantle reference value as mantle processes are not entirely understood yet. The pioneering study by Rouxel et al. (2002) reported a large variety of different geological materials. It is also noteworthy that accurate stable Se isotope measurements down to the lower ng level have been reported by (Zhu et al., 2008). Both groups however reported Se isotope data from analysis on different instruments compared to a Neptune*Plus*™.

While Zhu et al. (2008) and further colleagues of Prof. T. Johnson at the Department of Geology, University of Illinois at Urbana-Champaign (e.g. Mitchell et al., 2012; Schilling et al., 2011) analyzed Se isotopes on a NuPlasma, Rouxel et al. (2002) used a Micromass IsoProbe plasma source instrument with collision/reaction cell technology, which suppressed the formation of polyatomic interferences down to insignificant levels. However, neither this instrument nor another MC-ICP-MS with collision/reaction cell technology is commercially available at the present. The ThermoFisher Scientific® Neptune*Plus*™ used in this study could be used in medium- or high-mass resolution mode,

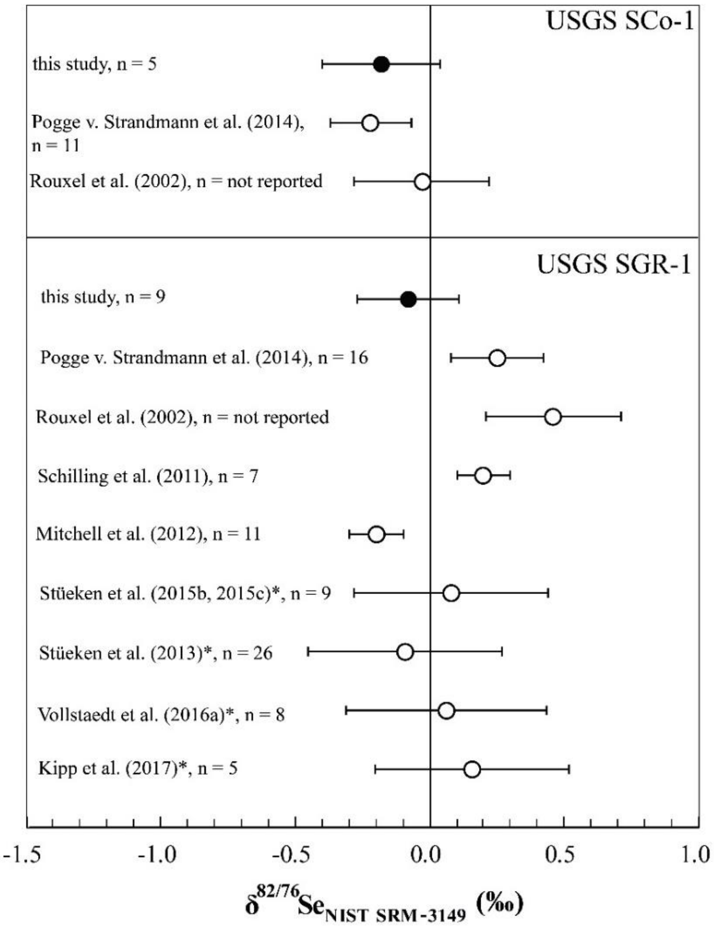

Figure 1.7 Compiled Se isotope data for USGS shales SCo-1 and SGR-1. Filled symbols represent results from this study, combining 5 analytical sessions over a period of 9 months (SCo-1: −0.18 ± 0.22‰, n=5; SGR-1: −0.08 ± 0.19‰, n=11), providing a long-term external reproducibility for data obtained in our study. Unfilled symbols are data taken from the literature. All error bars indicate 2σ analytical reproducibility; errors where converted to 2σ where data was given in 1σ (e.g. Stüeken et al., 2013, 2015b, 2015c; Kipp et al., 2017). * = Data reported as $\delta^{82/78}$Se was converted to $\delta^{82/76}$Se.

as a strategy to resolve polyatomic interferences from monoatomic ion beams at a given m/z ratio (Weyer and Schwieters, 2003).

Unfortunately, this technique clips the ion beam leading to a significant decrease in ion beam intensity to 15 % for medium- and to 8 % for high-mass resolution compared to the normal low-mass resolution measurement mode. In medium- or high-resolution modes, it is thus impossible to obtain accurate Se isotope compositions on analytes with lower than 15 ng total Se, even with the efficient sample introduction to the plasma promoted by a hydride generator. At a low-mass resolution measurement mode on the Neptune*Plus*™ MC-ICP-MS, however, background signals mainly from Ar dimers are in the range of tens of mV at m/z of 74, 77, 78 and 82 and are very large (20–25 V) at m/z of 80 (i.e. $^{40}Ar/^{40}Ar^+$) using amplifier resistors of 10^{11} Ω. In comparison, Rouxel et al. (2002) only report background levels on their Micromass Isoprobe at m/z = 80 to be <1 mV (using a 10^{11} Ω amplifier resistor). Here, we report the first Se measurement method on the ThermoFisher Scientific® Neptune*Plus*™ MC-ICP-MS that minimizes the problem of major polyatomic interferences on Se isotope masses by introducing methane. Together with a hydride generation system, this additionally increases the Se signal and thus enables the measurement of materials with Se concentrations in the range of 15 ng with a 2σ reproducibility of ca. 0.10‰ and of 5 ng with a reproducibility of 0.20 ‰. This is significant because it allows a systematic Se isotope investigation of many planetary reservoirs such as the Earth's mantle, which is characterized by low Se concentrations (peridotites: ~1–150 ng g^{-1}, König et al., 2014; MORB: 120–200 ng g^{-1}, Lissner et al., 2014) as well as different sulfides and minerals (e.g. mantle sulfides range from 20 to 280 µg g^{-1} Se (e.g. Hattori et al., 2002).

1.4 Conclusions

(1) The method presented here allows to employ a ThermoFisher Scientific® Neptune*Plus*™ for the accurate determination of Se isotope ratios. The method is based on a double spike to account for fractionation induced during all stages of sample preparation and combines hydride generation with the introduction of methane, which results in a two- to three-fold Se signal increase and background suppression by a factor of two.

(2) Accurate Se isotope measurements with a reproducibility of <0.10‰ (2σ) on $\delta^{82/76}$Se are obtained on 1 mL sample solution with a total of 15 ng Se. With lower Se quantities down to 5 ng mL^{-1} a reproducibility of 0.20‰ (2σ) is obtained on $\delta^{82/76}$Se.

(3) Our analytical approach for Se isotope analysis pushes the boundary for the investigation of geological materials and single minerals with low Se concentrations (200 ng g^{-1} down to tens of ng g^{-1}) and thus allows investigating Se-depleted planetary reservoirs such as the terrestrial mantle and other high-temperature environments by employing a commercially available instrument, the ThermoFisher Scientific® Neptune*Plus*™ MC-ICP-MS. As a first result we report a $\delta^{82/76}$Se value of 0.18 ± 0.03‰ (2σ; n=3) for the USGS reference basalt BCR-2. This value should not be regarded as mantle reference value as processes in the Earth's mantle that might produce Se isotopic fractionations cannot be ruled out.

Chapter 2: The role of subduction recycling on the selenium isotope signature of the mantle: Constrains from Mariana arc lavas

Abstract

Investigating the isotope systematics and behavior of selenium in subduction zones provides valuable insights into mechanisms that contribute to chalcophile and moderately volatile element distribution between terrestrial reservoirs. In this study, we present high-precision Se isotope and Se–Te elemental data on subduction zone lavas from the Mariana arc system. Our results indicate that Se–Te concentrations are unaffected by submarine degassing but are affected by magmatic differentiation. In contrast, Se isotopes of submarine lavas are unaffected by both magmatic differentiation and degassing and thus may preserve their magmatic source signature. Compared to the average Se isotope composition previously obtained for mantle-derived samples ($\delta^{82/76}$Se=0.23±0.12‰, 2 s.d., n=5), suitable to represent the Mariana pre-subduction wedge, Mariana lavas show a larger overall range ($\delta^{82/76}$Se from 0.03 to −0.33‰, n=21) with a clear tendency towards lighter Se isotope compositions. The variable Se isotope signatures within the Mariana suite can further be attributed to different slab-derived fluid and melt-like subduction components. This provides evidence for a significant role of subduction recycling of hydrothermal sulfide-containing altered oceanic crust and pelagic sediments with possible implications for the Se isotope evolution of the crust-mantle system throughout geological time.

2.1 Introduction

Constraining the behavior of elements in subduction zones provides valuable insights into their distribution and (re)cycling between surface and igneous reservoirs throughout Earth's evolution. The distribution of the chalcophile and moderately volatile elements sulfur (S), selenium (Se) and tellurium (Te) are of particular interest because they provide insights into Earth's volatile origin and evolution (König et al., 2014; Wang and Becker, 2013). Selenium and Te are ultra-trace elements with two orders of magnitude lower abundances in Earth's mantle compared to CI chondrites. Their abundances however, are still higher than expected from metal-silicate partitioning experiments (Rose-Weston et al., 2009), which predict S, Se and Te to be very effectively scavenged from Earth's mantle into its core during metal core formation. This may be reconciled with a late accretion of chondritic material (late veneer hypothesis; e.g. Kimura et al., 1974) following core-mantle differentiation. The relative abundances of S–Se–Te in mantle rocks believed to represent the primitive upper mantle (PUM) signature are near-chondritic, which was interpreted as evidence for replenishment of Earth's mantle by accretion of chondritic late veneer material (Wang and Becker, 2013). However, this interpretation conflicts with the non-chondritic sulfur isotopic composition of the Earth's mantle (Labidi et al., 2013), which has been attributed to partial incorporation of S into the Earth's core and thus substantial pre-Late Veneer existence of volatiles (Labidi et al., 2016). Alternatively, the observed near-chondritic Se/Te ratios in fertile peridotites might be the result of refertilization and thus represent secondary magmatic processes (Harvey et al., 2015; König et al., 2014; Lorand and Alard, 2010; Luguet et al., 2015). The fertile peridotite signature for adequate representation of a PUM model composition remains therefore controversially debated (König et al., 2015a; König et al., 2014; König et al., 2015b; Wang and Becker, 2013; Wang and Becker, 2015).

Investigation of the Se isotopic composition of the Earth's mantle offers a novel approach to investigate the origin and evolution of volatiles. This requires firm constraints on the Se isotopic composition of the different terrestrial reservoirs. Within this scope, the role of subduction zone processes on the Se isotope composition of the mantle is relevant because of large concentration and isotope differences between Earth's mantle and crust (Jenner, 2017; Jenner et al., 2012; Lissner et al., 2014; Rouxel et al., 2002; Yierpan et al., 2018). As in mid-ocean ridge settings, Se elemental signatures of subduction zone lavas are affected by sulfide segregation during magma differentiation (Brenan, 2015; Hamlyn et al., 1985; Jenner, 2017; Lissner et al., 2014) and these processes must therefore be considered in order to adequately interpret the Se isotope composition of arc lavas. Due to the different partitioning behavior of Se and Te in sulfides (i.e. partitioning into distinct sulfide phases), Se–Te systematics are a valuable tracer of the relative influence of the different sulfide populations involved during magmatic differentiation and partial melting (Brenan, 2015; Yierpan et al., 2019). Interpretation of the Se isotope composition of subduction zone lavas therefore benefits significantly from combined Se isotope and Se–Te elemental investigations. Recently, Kurzawa et al. (2017) and Yierpan et al. (2018) presented refined analytical techniques for both chemical purification and high-precision analyses of Se–Te concentrations and Se isotope compositions on samples with low total amounts of Se and Te. These analytical advancements provide the potential to investigate the Se isotope signature of low ng Se-bearing silicate rocks in the context of their Se–Te elemental signatures. This helps to evaluate the different petrogenetic processes involved in mantle melt evolution and ultimately to decipher the role of subduction recycling on the Se isotope composition of the mantle.

Studies on V, Fe and Tl isotopes (Prytulak et al., 2013; Prytulak et al., 2017; Williams et al., 2018) have been conducted on samples from the Mariana arc system to (i) investigate the oxygen fugacity of the mantle source (using V isotopes), to (ii) explore the interplay of sulfide saturation and segregation as well as crystal fractionation on the isotope composition of arc lavas (Fe and V isotopes) and to (iii) trace subduction zone inputs (using Tl isotopes). These studies concluded that Fe and V isotope signatures of magmatic rocks cannot directly be used as redox proxies without considering the influence of magmatic processes such as partial melting and differentiation. Yet, the timing of sulfide saturation and magnetite crystallization and associated isotope fractionations could be constrained.

In this study we focus on a suite of well-characterized, submarine arc lavas dredged from the Mariana subduction system (Fig. 2.1), which already have been the focus of a pioneering work on S isotopes (Alt et al., 1993). This suite may hence provide the geochemical background for first Se isotope constraints on chalcophile element recycling in subduction zones.

2.2 Geodynamic and geochemical context of sample materials

The Mariana arc-basin magmatic system (herein referred to as the Mariana system) extends over a distance of 2800 km (N–S) and constitutes the southern extension of the Izu-Bonin-Mariana subduction zone. The Mariana system is the result of westward subduction of the Pacific Plate along the Mariana trench beneath the Philippine Sea Plate initiated in the early Eocene (e.g. Stern and Bloomer, 1992; Stern et al., 2003). It can be subdivided into the Mariana island arc, which is an arcuate alignment of ~40 subaerial and submarine volcanoes, and the Mariana trough, an actively spreading back-arc basin (e.g. Pearce et al., 2005).

A total of 21 glassy samples from the submarine Mariana arc and trough sections (Fig. 2.1) were analyzed in this study. Among these are 12 samples from the active Mariana arc. These samples were either dredged (Fukujin, Eifuku and S. Daikoku) or collected by submersible (Kasuga) at collection depths of ~800-2900 mbsl (Alt et al., 1993). Additionally, 9 samples from two trough localities (18°N and 22°N) were analyzed, that were obtained by submersible or dredging at collection depths of ~2800–3700 mbsl. The samples are mainly basalts, basaltic andesites and andesites (Alt et al., 1993). Samples were petrographically classified into three groups: (i) 'glass', (ii) 'glassy' and (iii) 'microcrystalline' (see Alt et al., 1993). Some materials analyzed here have previously been analyzed including for S, Sr and Nd isotopes and major and trace element systematics (Alt et al., 1993 and references therein). These studies showed that back-arc lavas from 22°N and a single trough rock from 18°N (1846-9; Alt et al. (1993)) carry a strong arc signature, as inferred from trace element and Sr–Nd–Pb isotope systematics, which can be explained by addition of an arc component to a MORB mantle (e.g. Stern et al., 1990). Based on this observation, we suggest the subdivision of the following groups among the samples analyzed: back-arc samples at 18°N, arc-like samples at 22°N (and sample 1846-9 from 18°N) (where the back-arc basin intersects the arc) and arc samples from submarine volcanoes (Kasuga, Fukujin, Eifuku, S.Daikoku). These subdivisions also account for different subduction components that comprise shallow, deep and total slab-derived contributions as expressed by Ba/Th, Th/Yb and Ba/Yb, respectively (Pearce et al., 2005). The shallow subduction contribution results from early dehydration of the slab and migration of fluids from the slab-mantle interface into the sub-arc mantle wedge (arc and back-arc). Deep subduction additions are explained as sediment-derived melt-like components (mainly arc). The flux of subduction components in not limited to vertical transport but also includes lateral transport (Stolper and Newman, 1994 and references therein). In previous studies, the sub-arc mantle wedge has been interpreted to act as chromatographic column diluting the subduction input in arc-distal areas. However, assessing these mechanisms in these arc-distal areas is not the aim of this study and we rather focus on how the different and variable subduction components influence the Se isotope systematics of arc-related melts.

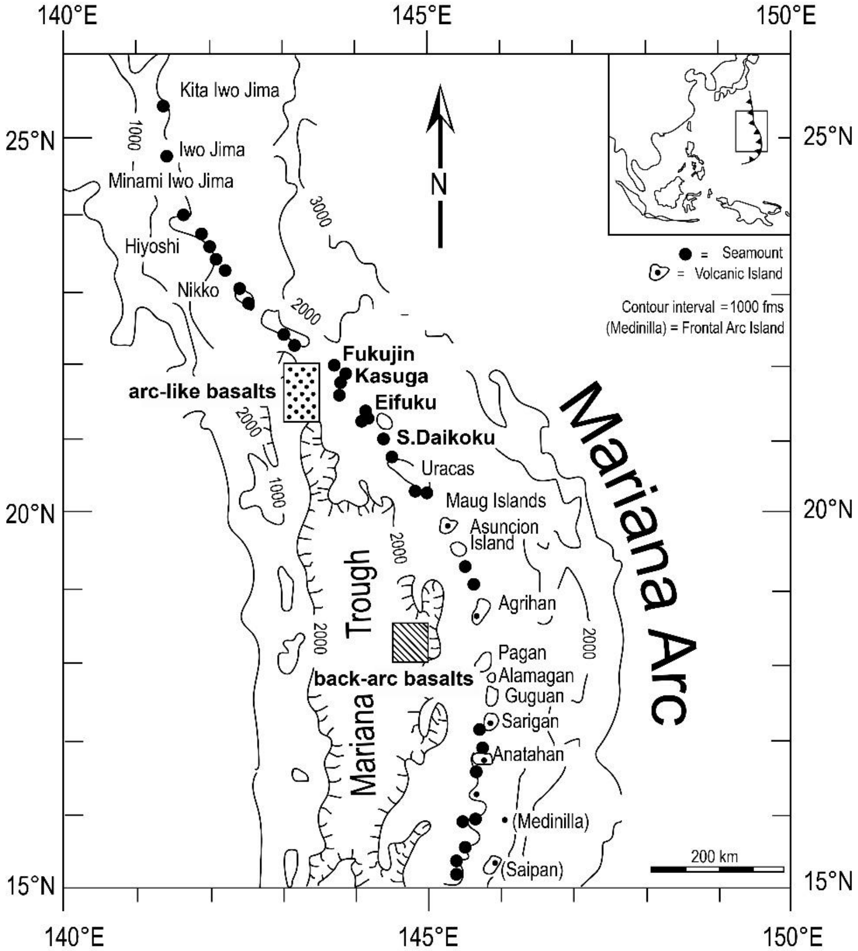

Figure 2.1 Locality map for the Mariana arc system and locations of samples. Analyzed samples are from submarine seamounts (bold labels) and from two back-arc regions (shaded rectangular boxes). Modified after Alt et al. (1993 and references therein).

2.3 Analytical techniques

2.3.1 Reagents, materials, major- and trace element analyses

Glass free of coatings and alteration was carefully handpicked from each sample, followed by multiple washing steps in dilute HCl and distilled water and were finally ground to powder (Alt et al., 1993). Sulfur concentrations of these samples were already published by Alt et al. (1993). In addition to Se isotope measurements and Se–Te concentration analyses, selected samples were also analyzed for major and trace element concentrations. All analyses were performed in the ISO-5 (US FED standards class 100) clean-room facilities of the Isotope Geochemistry at the University of Tübingen, Germany. All reagents used during digestion, sample preparation and measurements were distilled from MERCK Millipore Emsure™ grade HCl (37%) and HNO_3 (65%) using Savillex™ DST-1000 Acid Purification Systems. Reagents were diluted to required molarities to ±0.03 mol L^{-1} as checked by titration. Ion exchange resins, beakers, pipette tips and centrifuge vials were pre-cleaned with multi-step HCl and HNO_3 treatments. A Merck Millipore Milli-Q™ system was employed to further purify de-ionized water to 18.2 MΩ·cm at 25 °C.

Previously determined major element data was complemented and trace elements were measured for the entire Mariana sample suite (Alt et al., 1993) during this study using a ThermoFisher Scientific iCAP Qc quadrupole ICP-MS housed at the Isotope Geochemistry Laboratory at the University of Tübingen following the analytical procedure by Albut et al. (2018). Due to limited sample material, all major and trace element concentrations of samples were determined together with rock reference materials AGV-2 (for major element data, n=2, Tab. A.2.1) and BHVO-2 and BIR-1a (for trace element data, n=2 and 1, respectively, Tab. A.2.2). Analytical precision for most analyzed trace elements is better than 2% r.s.d. except for Be, As, W and U with analytical precisions better than 5% r.s.d. Obtained trace element concentrations of rock reference materials match those reported by Jochum et al. (2016) (see Supplemental Information). For major element analysis, 0.1 g of homogenized sample material was fused together with 0.5 g of Spectromelt® to produce a fused glass bead, which was subsequently dissolved in 0.45 mol L^{-1} HNO_3 in a Teflon beaker agitated in an ultrasonic bath and diluted by addition of an internal standard solution before final measurement. For determination of trace element concentrations, 0.02 g homogenized powder of each sample were weighted into Teflon beakers and digested at 120°C in a mixture of concentrated HF and HNO_3 (5:1, v/v). After dry down, the samples were taken up in 6 mol L^{-1} HCl and heated in closed beakers to break up existing fluoride complexes. The sample solutions were again evaporated to dryness, converted to nitrite form and subsequently diluted with an internal standard solution before final measurement.

2.3.2 Se concentration analyses

Pre-determination of Se concentration of an unknown sample is required in order to know the amount of double spike to be added to the sample for precise Se isotope analysis with ideal double spike-sample ratio of ~1:1 (Kurzawa et al., 2017). For the pre-determination of Se concentrations via isotope dilution, we followed the procedure described by Yierpan et al. (2018). For this, we weighed 0.02 g sample material (equivalent to 2 ng total Se assuming a Se concentration of 100 ng g^{-1}) in Teflon beakers, added an adequate amount of ^{74}Se–^{77}Se double spike and digested the mix with an acid mixture of 5:1 (v/v) conc. HF : conc. HNO_3 in closed Teflon beakers at 85°C. The digested samples were then dried at 65°C followed by conversion, heating and dry down steps (see Yierpan et al., 2018) in 6 mol L^{-1} HCl before Fe was removed by means of anion exchange chromatography. Fe-free cuts were then diluted to 0.5-1 ng mL^{-1} Se and finally measured on the iCAP Qc ICP-MS using hydride generation following the protocol of Yierpan et al. (2018).

2.3.3 Se isotope and Te concentration analyses

Chemical purification of Se and Te for subsequent Se isotope and Se–Te concentration analyses was achieved following the protocol by Yierpan et al. (2018) as it allows to simultaneously purify Se and Te from a single sample digest with high yields. Briefly, this involves weighing sample material equivalent to ~30 ng Se (exact Te amount uncritical) into conventional perfluoralkoxy (PFA) beakers, adding adequate amounts of ^{74}Se–^{77}Se double spike (1:1; sample Se : double spike Se) and ^{125}Te single spike (exact single spike amount less critical) and digesting the sample-spike mixtures in an acid mixture of 5:1 (v/v) conc. HF : conc. HNO_3 in closed beakers on a hotplate at 85°C for 48 hours. Se and Te were purified from sample solutions by a two-step ion exchange chromatography. In a first step, we employed an anion exchange column to remove Fe and collect purified Te. In a second step, Se was purified using a cation exchange column to remove remaining cations. Te concentrations were then determined by hydride generator quadrupole ICP-MS on the iCAP Qc instrument and Se isotopes and concentrations were measured by hydride generation multi-collector ICP-MS on the ThermoFisher Scientific Neptune*Plus*™ instrument of the Isotope Geochemistry laboratory, University of Tübingen. Typical signals on ^{82}Se (using an amplifier resistor of 10^{11} Ω) on a 30 ng mL^{-1} Se solution with operating parameters similar to those reported by Kurzawa et al. (2017) generally are 0.8-0.9 V. During Te concentration measurements on the iCAP Qc ICP-MS using similar operating parameters to those of Yierpan et al. (2018), ~55000cps on ^{126}Te were obtained for a Te standard solution of 0.5 ng mL^{-1}. Se isotopes and Te concentrations of samples were determined at similar signal intensities compared to those of standard solutions. For detailed descriptions of analytical techniques employed see Kurzawa et al. (2017) and Yierpan et al. (2018). All Se isotope compositions obtained during this study are reported relative to the NIST-3149 Se reference solution. Measurements of the inter-laboratory standard solution MH-495 yielded an average value of $\delta^{82/76}$Se of −3.25±0.08‰ (2s.d., n=26, 30 ng mL^{-1} solutions, see Tab. A.2.3), in agreement with previous studies (Kurzawa et al., 2017; Labidi et al., 2018; Yierpan et al., 2018 and references therein; Yierpan et al., 2019). The external reproducibility for sample materials was derived from two multiple digested samples (arc-like 1881-4; Kasuga 1880-3 (K2)) during different measurement sessions and is 0.10‰ (2 s.d., n=3 and n=6, respectively; see Tab. A.2.4). All samples were measured together with the international rock reference material USGS BHVO-2 that has been published by Yierpan et al. (2018). Further, we provide Se isotope and Se–Te concentration data for the international rock reference materials JB-2 and JB-3 (Geological Survey of Japan) (Tab. A.2.5 and A.2.6). Obtained Se–Te concentrations are in agreement with data reported in the literature (see Supplemental Information). Long-term analytical reproducibility for both Se and Te concentration determinations are ~3% r.s.d. The main advantage of the procedure by Yierpan et al. (2018) followed here is that it yields very low blanks. Accurate isotopic compositions of procedural blanks cannot be determined because blank levels are always insignificant (at background level; e.g., ~0.05 and 0.01 ng for Se and Te, respectively; see Yierpan et al., 2019). However, Kurzawa et al. (2017) showed high accuracy for low Se-containing solutions with various blank levels (up to 1 ng) that confirms a negligible blank contribution for a given isotopic composition.

2.4 Results

2.4.1 Major and trace elements

All samples show 48 to 61 wt.% SiO_2 and 2 to 9 wt.% MgO (Tab. 2.1; Tab. A.2.7) and are classified as basalts, basaltic andesites, andesites. Relative to the back-arc samples (MgO between 5 to 9 wt.%) and with the exception of the Kasuga samples, the arc samples are more differentiated showing MgO contents of 2 to 4 wt.%. The Kasuga samples are more primitive as indicated by lower SiO_2 and higher MgO contents of <55 wt.% and >5 wt.%, respectively. The samples from S.Daikoku, Eifuku, Fukujin and both back-arc localities follow the tholeiitic fractionation trend whereas samples from Kasuga follow calc-alkaline to shoshonitic fractionation trends (Alt et al., 1993). In terms of major element composition samples from both back-arc localities (18°N and 22°N) are indistinguishable from each other. Our new trace element data are in accordance with previous observations (Stern et al., 2003 and references therein) in that primitive mantle normalized trace element diagrams (after Palme and O'Neill, 2014) for the Mariana arc and trough samples all show marked enrichments in large ion lithophile elements and light rare earth elements such as Rb, Ba, U, K, Pb ,Sr, La and Ce, show arc-typical relative depletions in high field strength elements (HFSE) (e.g. Nb, Ta, Zr, Hf) and relatively low heavy rare earth element concentrations (e.g. Tb, Er, Yb) (Fig. A.1). They share these characteristics with other arc volcanic rocks from the Mariana arc (e.g. Elliott et al., 1997). In addition, our new trace element data are in agreement with the previous observation (section 2.2 and references therein, e.g. Pearce et al., 2005) that the back-arc samples are dominated by slab-derived fluid enrichment (elevated Ba/Th compared to primitive mantle) and the arc samples additionally contain a marked sediment-melt subduction component (similar Ba/Th but higher Th/Yb and Ba/Yb than the back-arc suite).

2.4.2 S–Se–Te concentrations

The arc samples exhibit S contents in the range of 10 to 200 µg/g. Compared to those, back-arc and arc-like samples are characterized by higher S contents between 200-930 µg/g (Alt et al., 1993). Selenium concentrations of back-arc samples are on average 153±55 ng g^{-1} (1 s.d., n=4), similar to those from arc-like samples with an average of 138±42 ng g^{-1} (1 s.d., n=5) (Fig. 4a). In contrast, the arc samples show lower Se contents with an average of 111±32 ng g^{-1} (1 s.d., n=12) (Table 1) and can vary significantly between volcanoes and even within one individual volcano (e.g. Kasuga). Sulfur/Selenium ratios of back-arc and arc-like samples range from 2190 to 8230 and 1450 to 5110, respectively (Fig. 2.3d). The arc samples show generally lower S/Se ratios in the range of 120 to 1680 (Fig. 2.3d).

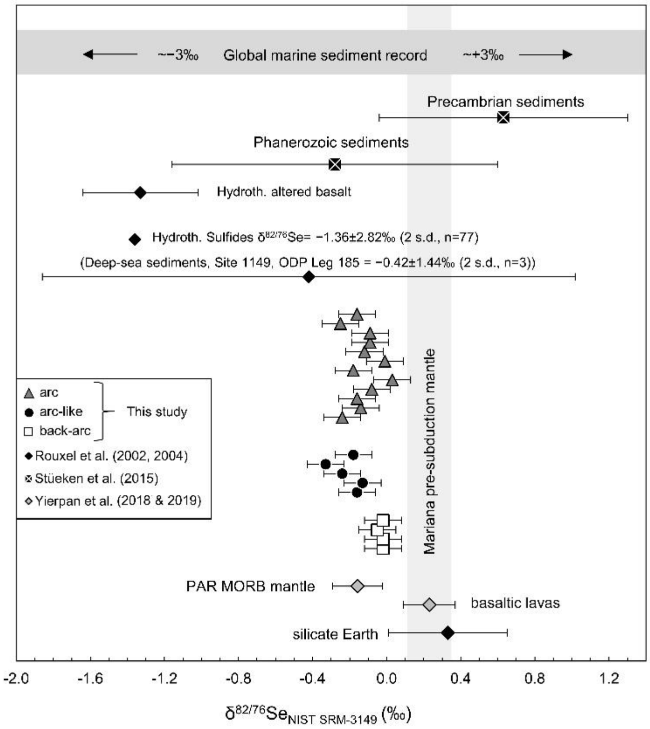

Figure 2.2 Compilation of Se isotope compositions of Mariana lavas analyzed in this study and literature data. Data for deep-sea sediments, hydrothermal sulfides, hydrothermally altered basalts and the silicate Earth from Rouxel et al., (2002) are averaged values. Additional data for hydrothermal sulfides from Rouxel et al. (2004). Silicate Earth value by Rouxel et al. (2002) comprises a peridotite (PCC-1) and five basalts (BHVO-1, BCR-1, BE-N and BR). ‘basaltic lavas’ (BHVO-2, BCR-2, BIR-1a, BE-N) from Yierpan et al. (2018). The vertical grey box indicates range of the Mariana pre-subduction mantle value that comprises basalts without any subduction-related origin measured by Yierpan et al. (2018) and the peridotite analyzed by Rouxel et al., (2002). PAR mantle represented by Pacific Antarctic Ridge MORBs (n=27) from Yierpan et al. (2019). Average values for Phanerozoic and Precambrian sediments from Stüeken et al. (2015). Range of global marine sediments from Mitchell et al., (2016) and references therein. All error bars given as 2 s.d. uncertainty, for details see Section 2.3.3. No error bars displayed for hydrothermal sulfides as uncertainties exceed the diagram range (instead values are given).

Tellurium concentrations of back-arc and arc-like samples show average concentrations of 4.0±2.3 ng g^{-1} (1 s.d., n=4) and 2.4±1.5 ng g^{-1} (1 s.d., n=5), respectively (Fig. 2.4b). The arc samples are characterized by Te concentrations with an average of 2.1±2.0 ng g^{-1} (1 s.d., n=12). The Te concentrations of some arc samples (n=5, e.g. back-arc sample 1846-9) analyzed by Yi et al. (2000) are in good agreement with those obtained in this study. The Se–Te ratios are controlled by variable Te concentrations and are most variable within the arc samples ranging from 14 to 481. It is noteworthy, that the Se/Te ratios of the Kasuga volcano are among the lowest of all arc samples with typical Se/Te between 14 and 31. Two samples from Fukujin are characterized by very low Te concentrations (<1 ng g^{-1}; see Tab. 2.1) and thus have the highest Se/Te ratios (393 and 481, respectively).

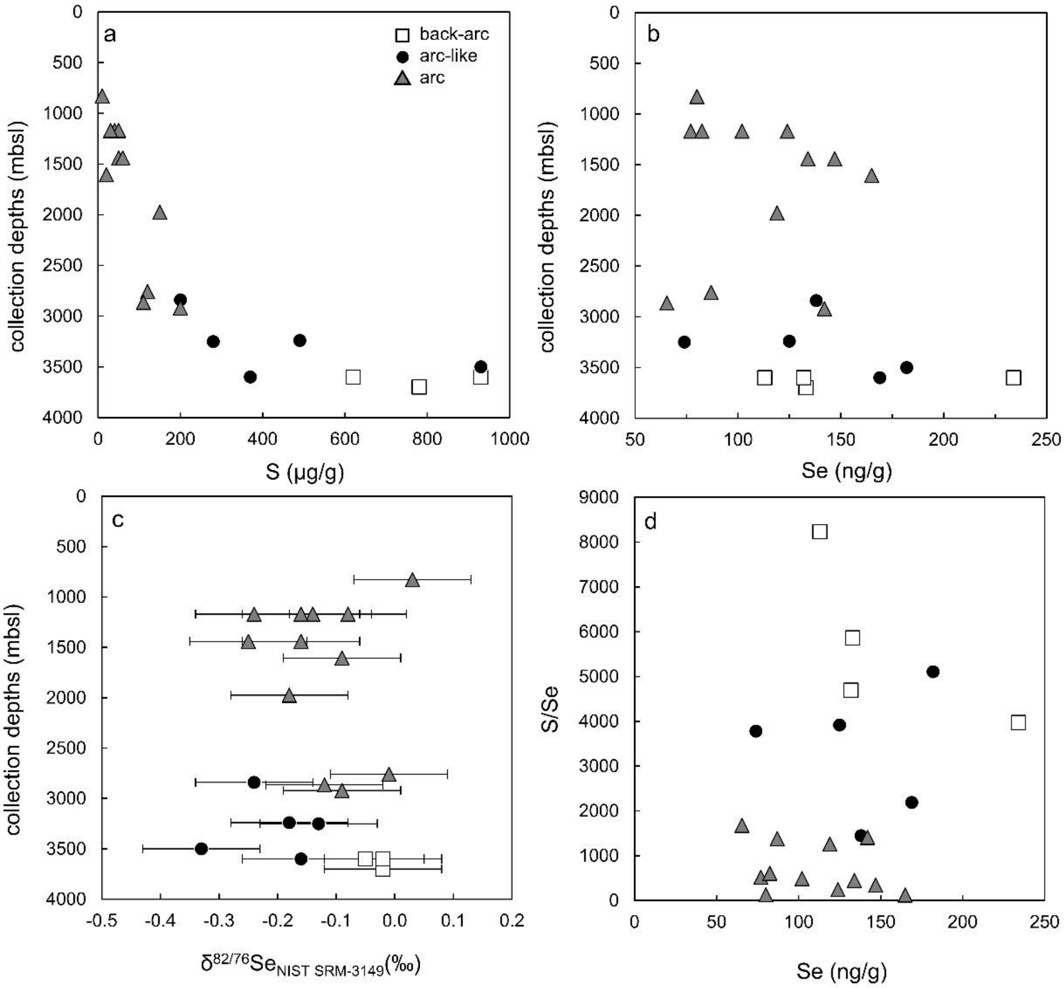

Figure 2.3 (a) Apparent covariation of collection depth and S concentrations, (b) no indication of eruption-related degassing of Se. (c) No covariation of collection depth and Se isotope composition, (d) S/Se vs. Se concentrations indicating S/Se not controlled by Se concentrations. All error bars given as 2 s.d.

2.4.3 Se isotope composition

The average $\delta^{82/76}$Se of the back-arc samples is −0.03±0.03‰ (2 s.d., n=4) whereas the average $\delta^{82/76}$Se of the arc-like samples is −0.21±0.16‰ (2 s.d., n=5) (Fig. 2 and 5a). The arc samples exhibit Se isotopic compositions that average at −0.13±0.17‰ (2 s.d., n=12) (Fig. 2.2 and 2.5a). The Se isotope compositions of the samples are not related to silicate differentiation as inferred from the absence of covariation of MgO and $\delta^{82/76}$Se (Fig. 2.5a). Furthermore, the $\delta^{82/76}$Se of the samples are unrelated to the collection depths (Fig. 2.3b).

Interestingly, the back-arc samples are isotopically heavier than the arc and arc-like samples, which overlap in their Se isotope composition with recent Se isotope data of MORBs from the Pacific Antarctic Ridge (PAR; Yierpan et al. (2019)). However, it is very important to note that, Mariana samples originate from a different mantle domain than Pacific-type MORBs. Volpe et al. (1990) concluded from Sr, Nd and Pb isotope ratios of Mariana Trough basalts (equivalent to back-arc samples analyzed in this study), that the mantle beneath the back-arc region of the Mariana arc is isotopically similar to average Indian-type MORB. Most likely, this also applies to the mantle wedge beneath the Mariana arc, similar to complex dynamics revealed for other SW Pacific arcs (e.g. König et al., 2007; Schuth et al., 2011). In contrast, PAR basalts originate from the Pacific mantle domain that is isotopically depleted compared to the Indian mantle domain (Ito et al., 1987). Thus, the Indian mantle domain resembles an enriched mantle reservoir compared to the Pacific mantle domain, which precludes a direct comparison of the PAR data and our Mariana data.

Given the absence of literature $\delta^{82/76}$Se data for the Indian mantle domain, the Mariana pre-subduction wedge may be best represented by melts that originate from enriched reservoirs that are isotopically heavier as indicated also by the heavier back-arc compared to arc lavas analyzed here (Fig. 2.2). Hence, a suitable Mariana pre-subduction background is provided by the most recent data of worldwide, non-subduction-related basalts (BHVO-2, BCR-2, BIR-1a and BE-N) by Yierpan et al. (2018) and the reported peridotite (PCC-1) value of Rouxel et al. (2002), which yield an average $\delta^{82/76}$Se of 0.23±0.12‰ (2 s.d., n=5, Tab. A.2.9). Compared to this value, all Mariana samples, including for the back-arc, show isotopically lighter Se isotope compositions (Fig. 2.2). Note, that especially the arc and arc-like samples display a greater variability in their $\delta^{82/76}$Se (e.g. Fig. 2.2) compared to the more homogeneous and slightly isotopically heavier back-arc lavas. We conducted *t*-tests to evaluate the statistical significance of the different averages of the distinct sample suites relative to the pre-subduction mantle. The three obtained two-tailed P values for the back-arc, the arc-like and the arc samples each relative to the pre-subduction mantle equal $t(7)=4.18$, $p=0.0042$, $t(8)=4.92$, $p=0.0012$ and $t(15)=4.27$, $p=0.0007$, which are all statistically very significant.

2.5 Discussion

2.5.1 No effect of degassing on Se isotope signatures of submarine Mariana lavas

Previous work on Mariana arc lavas showed heavier S isotope signatures compared to the mantle, which was suggested to mirror recycling of subducted sediments (Alt et al., 1993). A trend of decreasing S contents (Fig. 2.3a) and low S concentrations in highly vesicular Mariana lavas suggests that partial extrusive degassing of S can occur in submarine environments despite the great pressures of overlying water columns (Alt et al., 1993; Davis et al., 1991). Considerable differences in S concentrations of lavas erupted under submarine conditions may result from partial eruptive degassing, the degree of crystal fractionation, different conditions and percentages of partial melting and variations in source conditions (Davis et al., 1991). An assessment of these processes and their role on S isotope compositions is beyond the scope of this study. Importantly, Se contents and Se isotope compositions of our samples do not systematically change with water depths (Fig. 2.3b, c), nor do Se contents correlate with Se isotope compositions (Fig. 2.5b). Moreover, Se concentrations of our samples are independent from S as inferred from a lack of covariation between these elements

(Fig. 2.3d) in contrast to a correlation of S/Se ratios controlled by S (not shown). Therefore, irrespective of the process affecting S, we rule out Se loss and Se isotope fractionation due to eruption-related degassing.

Recently, Jenner et al. (2010) reported similar Se concentrations in volcanic rocks derived from the Manus back-arc basin (north-east of Papua New Guinea) compared to MORB and concluded, that the Se contents remain unchanged during eruption associated degassing, which is in accordance with our conclusion. The decoupling of Se from S in terms of their degassing potential might be due to the fact that Se becomes oxidized only at elevated fO_2, or Eh, compared to S as earlier proposed by Jenner et al. (2010 and references therein). This implies that Se is retained whereas S (oxidized at given Eh) is lost.

2.5.2 Magmatic differentiation

Although submarine Mariana arc lavas from the shallowest depths contain the lowest S contents (Table 1), back-arc lavas from rather constant and great depths (>3000 mbsl) also show very variable S contents (~200-1000 µg/g). This suggests that a process unrelated to changing water column pressure (such as potential degassing and magmatic differentiation) also affected the S contents of the lavas. Since all our samples show MgO contents between ~9 and 2 wt.% (Tab. 1) the effect of magmatic differentiation and potential sulfide segregation needs to be considered when interpreting chalcophile element concentrations and in particular potential Se isotope variations.

Geochemical evidence for sulfide segregation stems from trends of chalcophile element concentrations (Cu, Se and Te) and V/Sc versus MgO (Fig. 2.4) (Jenner, 2017 and references therein). Before ~7 wt.% MgO the concentrations of Se, Te (and some Cu) increase, followed by a drop in concentrations (Fig. 2.4a-c). A different phase than sulfide has to account for the observed changes in Se–Te–Cu concentrations, because the melt is under-saturated in sulfides at this stage of melt differentiation (Jenner et al., 2015; Jenner et al., 2010). In the case of the platinum group elements (PGEs), a Pt-rich alloy has been identified to be the most likely source of PGE depletion during early stages of fractional crystallization before the magnetite crisis and segregation of sulfides (Jenner et al., 2015; Park et al., 2013). Thus, it is likely that Se and (especially) Te are concentrated in alloys (e.g. tellurides; König et al., 2015a) that crystallize from sulfide under-saturated melts.

From ~6 to ~3 wt.% MgO, Se and Cu concentrations increase whereas Te concentrations still decrease, which might be due to incorporation of Te into Pt-Te-alloys (Fig. 2.4b). Note, that the observed trend seen for Cu concentrations (Fig. 2.4c) is also evident from Cu data reported in the literature (Jenner et al., 2015; Williams et al., 2018). At ~3 wt.% MgO and contents of Cu, Se and Te in the melt show a pronounced scatter, possibly related to appearance of sulfides, which are not fully segregating (previously inferred by Williams et al., 2018).

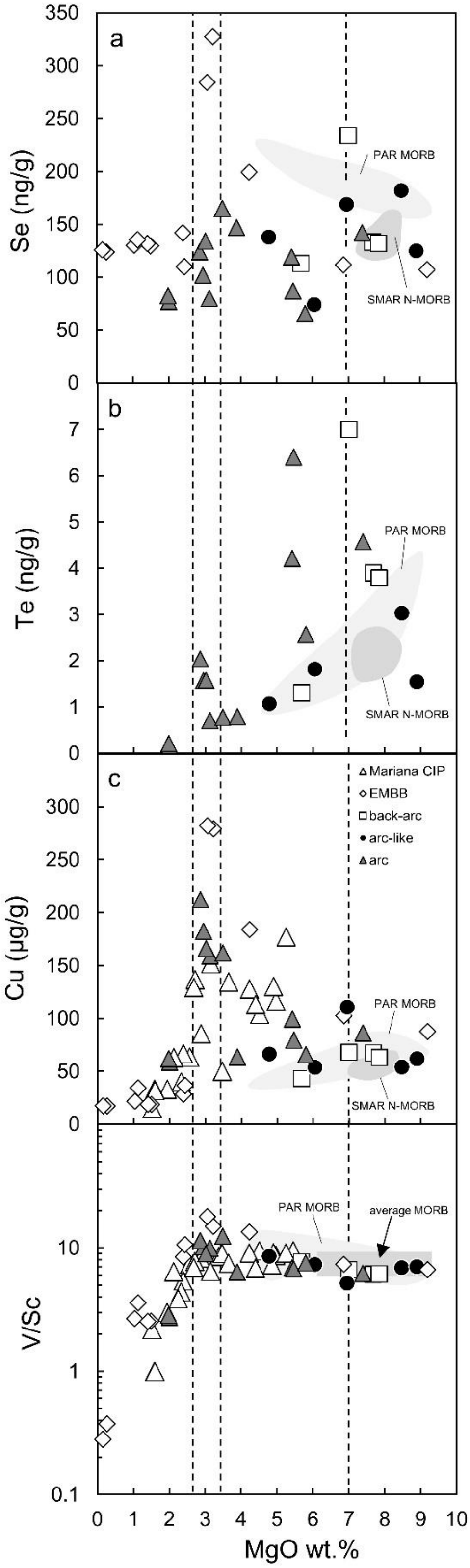

Figure 2.4 (a) Se, (b) Te and (c) Cu concentrations vs. MgO content show variation of chalcophile element concentrations as a function of their bulk partition coefficients during magmatic differentiation. (d) V/Sc ratio vs. MgO content, indicates V partitioning into magnetite and onset of the 'magnetite crisis' at ~3–4 wt.% MgO. Data for the Eastern Manus back-arc basin (EMBB) from Jenner et al., (2015 and references therein). PAR MORB data (light grey fields) from Yierpan et al. (2019). SMAR N-MORB (dark grey fields) data from Lissner et al. (2014). Copper concentration data of samples from the Central Island
Province (CIP) of the Mariana system from Williams et al. (2018). Dashed vertical lines represent important stages during magmatic differentiation, see text for interpretation of the data.

At 2.8 wt.% MgO, magnetite appears on the liquidus as inferred from the onset of decreasing V/Sc that is accompanied with a decrease in the $Fe^{3+}/\sum Fe$ ratio leading to a decline in fO_2 (Jenner et al., 2010). At this stage sulfide becomes saturated in the melt and finally segregates, thus scavenging Se, Te and Cu, albeit to different extents (more pronounced decrease of Cu and Te contents compared to Se; Fig. 2.4). This is related to a lower sulfide-silicate melt partition coefficient of Se compared to Cu.

Whereas the exact processes responsible for the unsystematic variations in Cu, Se and Te concentrations remain to be constrained, it is important to investigate potential correlations between Se concentrations and an index of differentiation, such as MgO, with Se isotope variations. Previous studies (Prytulak et al., 2017; Williams et al., 2018) involving Mariana arc lavas showed that for both V and Fe, significant isotope fractionation is induced as a consequence of magnetite fractionation and sulfide segregation, respectively. Both studies identified heavier isotope compositions following the 'magnetite-crisis' at ~2.8 wt.% MgO, consistent with preferential scavenging of isotopically light V and Fe into magnetite and sulfide phases.

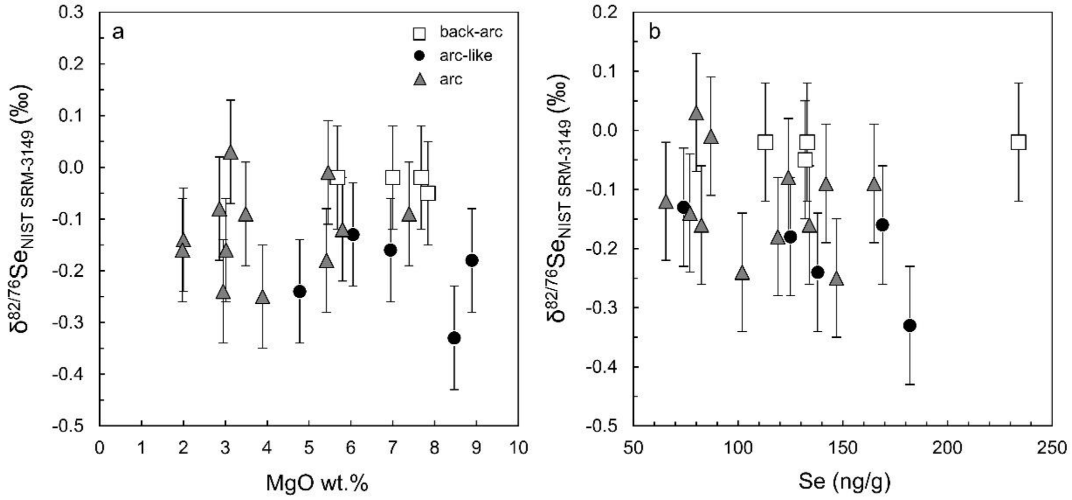

Figure 2.5 (a) Se isotope compositions of Mariana lavas vs. MgO contents shows no covariation with index of alteration indicating absence of isotope fractionation during magmatic differentiation. (b) Se isotope composition of Mariana lavas vs. Se concentrations indicates no isotope fractionation during magmatic differentiation (i.e. sulfide segregation, alloy fractionation; see text for details).

Such a link between sulfide saturation and Se isotope fractionation is not observed in our study. No trend between the Se isotope composition and MgO or Se is seen (Fig. 2.5a,b), which suggests that magmatic differentiation processes significantly affect both Se and other chalcophile element contents of the samples analyzed (Fig. 2.4), but do not result in Se isotope fractionation. This is in agreement with observations and conclusions based on a dry magmatic suite from the PAR (Yierpan et al., 2019). As neither degassing nor magmatic differentiation affect the Se isotope compositions of our samples, the isotopic variations among Mariana samples, particularly systematic differences between back-arc and arc samples are most likely related to their respective source composition.

2.5.3 Different subduction components and their influence on the Se isotope composition of arc lavas

The $\delta^{82/76}$Se signatures of Mariana lavas show a relatively large range and overall lower values compared to a rather confined range for the Mariana pre-subduction mantle, represented by basaltic melts and peridotite from intraplate and ridge settings, but without any subduction-related origin. Thus, $\delta^{82/76}$Se signatures of Mariana lavas seem indeed intrinsic to their subduction zone origin (Fig. 2.2). The Se isotope compositions of the Mariana lavas represent that of their mantle sources in contrast to their elemental budget that is compromised by magmatic differentiation (see section 2.5.2). Se isotopes of Mariana lavas may thus trace the slab-derived contribution and be related to potential recycling of Se in subduction zones. Although the Mariana system is highly complex, the natures of subduction components (i.e. fluid-like and melt-like components, see sections 2.2 and 2.4.1) added to the sub-arc mantle are broadly classified via different incompatible trace element systematics (Pearce et al., 2005). Any covariations between these proxies of subduction components and Se isotope compositions could therefore help to assess potential subduction recycling of Se. Slab-derived fluids and sediment melts may influence the Se isotope compositions of Mariana lavas to different extents. Figure 2.6a shows variable Ba/Th and Th/Yb ratios indicating that Mariana arc lavas are affected by both subduction components as has been documented in the literature (e.g. Elliott et al., 1997). Figure 2.6b shows the Se isotope compositions of all Mariana samples relative to Ba/Th, indicating slab-derived fluid enrichments (termed shallow subduction component by Pearce et al. (2005)). It can be observed that Mariana lavas all show lower $\delta^{82/76}$Se at somewhat higher Ba/Th compared to the Mariana pre-subduction mantle albeit some scatter exists in the dataset (Fig. 2.6b). Slab-derived sediment melts were termed deep subduction component by Pearce et al. (2005) and are indicated for instance by elevated Th/Yb in arc samples. Interestingly, these arc samples also extend to slightly heavier Se isotope compositions relative to slab-fluid dominated back-arc and arc-like samples (Fig. 2.6c). The influence of a sediment melt on the arc samples is also expressed by high La/Sm ratios (Elliott, 2003), which indeed show a positive trend with $\delta^{82/76}$Se but no trend with indicators for magmatic differentiation such as MgO contents (Fig. A.2).

Although back-arc and arc-like samples mostly overlap in their relatively low Th/Yb, they can be distinguished based on their respective $\delta^{82/76}$Se (Fig. 2.6c). In particular, the back-arc samples with their highest relative $\delta^{82/76}$Se do not match the tendencies observed for the other sample suites, which could be attributed to their rather distinct origin within the subduction zone. Indeed, the location of the back-arc samples lies ~350 km away from that of the arc-like samples (Fig. 2.1). In contrast, arc and arc-like samples originate from relatively restricted areas, respectively. These two groups however share the same subtle tendency between $\delta^{82/76}$Se and Th/Yb (Fig. 2.6c), which is in agreement with a strong arc signature previously found in back-arc lavas from 22°N (see section 2.2; Stern et al., 1990). The back-arc samples fall off this trend, possibly reflecting a different source due to the remote setting. It seems clear however, that all samples experienced slab fluid addition revealed by increased Ba/Th and offset to lower $\delta^{82/76}$Se compared to the pre-subduction mantle. Again, the distinction between shallow and deep subduction contribution based on Ba–Th–Yb systematics and the observation that sediment melts are more dominant in the arc samples compared to the back-arc samples is entirely based on a previous classification (Pearce et al., 2005). Reasons for a similar shallow and less pronounced deep subduction signature in back-arc lavas may be a chromatographic effect and dilution by back-arc melts (Stolper and Newman, 1994). Overall, it seems that shallow slab fluids can explain lower $\delta^{82/76}$Se, whereas deep-derived sediment melts may carry a heavier Se isotope signature that raises the $\delta^{82/76}$Se again (i.e. buffer the initial slab-fluid signature). Hence, slab-derived fluids and sediment melts (Fig. 2.6a, Ba/Th vs. Th/Yb) may shift $\delta^{82/76}$Se in arc lavas to opposing directions, where the relative proportion of these subduction components ultimately determines the direction of tendencies among suites. As a result, the total subduction addition, expressed by Ba/Yb (Fig. 2.6d), may be the best approximation of a net recycling signature (Pearce et al., 2005) that seems to produce lower overall $\delta^{82/76}$Se compared to the Mariana pre-subduction mantle. Further studies that examine in more detail the effects of different types of subduction components are clearly required.

Moreover, it remains to be investigated if and how a net contribution of subduction components to arc lavas relate to the Se isotope signature of the subduction input. In the case of S, the heavier δ^{34}S of Mariana lavas compared to the mantle has been linked to recycling of subducted sediments (Alt et al., 1993). Sediments in addition to altered oceanic crust containing hydrothermal sulfides indeed show variable Se isotope compositions (e.g. Mitchell et al., 2016; Rouxel et al., 2004; Rouxel et al., 2002). Therefore, it is necessary to assess if recycling of these materials might in principle account for the Se isotope compositions observed in subduction zone magmas.

2.5.4 Recycling of subducted surface material as possible source for Se isotope variability in Mariana arc lavas

Marine sediments have been the focus of numerous Se isotope studies (e.g. Mitchell et al., 2016 and references therein). So far, available data from the literature comprises shales of various ages (Archean to present day) and depositional environments (open marine and marine basins) with distinct conditions (euxinic, anoxic, suboxic and oxic) (Mitchell et al., 2016). Stüeken et al. (2015) identified a statistically significant shift in the Se isotope composition from predominantly positive (0.63±0.67‰; 2 s.d., n=169) to negative (−0.28±0.88‰; 2 s.d., n=240) $\delta^{82/76}$Se values from Precambrian to Phanerozoic samples (Fig. 2.2; see also Fig. 3a in Stüeken et al., 2015). Taken together, the Se isotope compositions of all these samples combined with other published $\delta^{82/76}$Se data (e.g. Mitchell et al., 2016) are in the range of −3 to +3‰ (Fig. 2.2; see also Mitchell et al., 2016). This suggests that not the entire Se isotope variation of all hitherto analyzed sediments

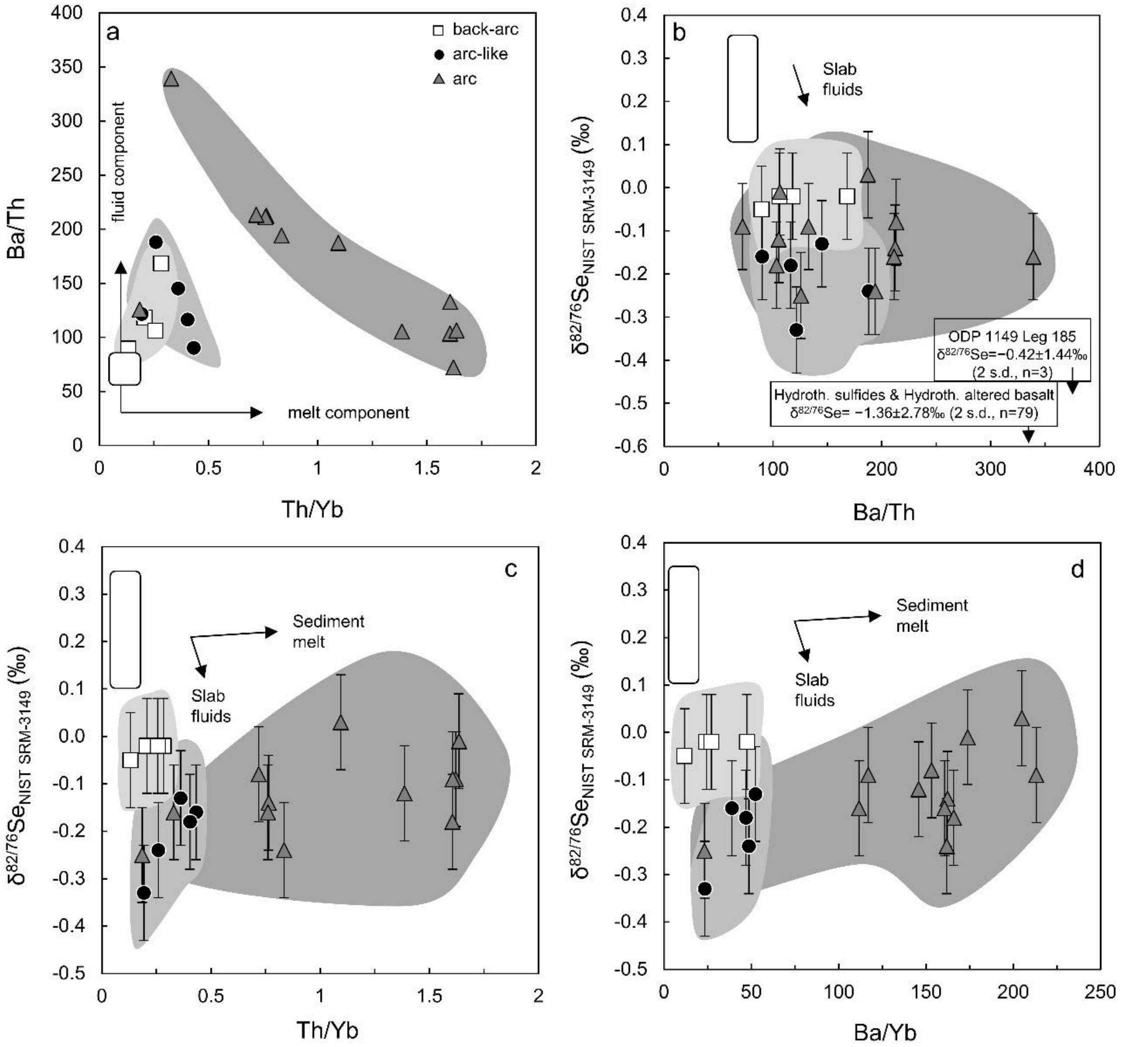

Figure 2.6 (a) Ba/Th vs. Th/Yb indicating different proportions of slab-derived components. Se isotope composition vs. (b) Ba/Th and (c) Th/Yb indicating the influence of slab-derived fluid and melt-like components. (d) Se isotope composition vs. Ba/Yb demonstrates Se isotope composition as function of total subduction addition. See Section 5.3 for details. Labelled boxes in (b) point to Se isotope compositions of deep-sea sediments (ODP 1149 Leg 185), hydrothermally altered basalt and hydrothermal sulfides analyzed by Rouxel et al., (2002, 2004). White box indicates Mariana pre-subduction mantle wedge value (0.23 ± 0.12‰, 2 s.d., n=5, Tab. A.2.9) represented by non-subduction-related mantle melts (basalts, Yierpan et al., 2018; peridotite, Rouxel et al., 2002) and. Ba/Th, Th/Yb and Ba/Yb ratios for the (sub-arc) mantle taken from Gale et al. (2013). All error bars given as 2 s.d.

qualify as endmembers to constrain potential sediment recycling in a modern subduction zone system. Instead, a narrower isotopic range of only modern sediments can be considered to begin with. In addition to age, the depositional setting may also be critical. Isotope fractionations in low-temperature environments can be large as inferred from laboratory experiments (Johnson and Bullen, 2004) and the wide range of reported $\delta^{82/76}$Se of sediments (e.g. Mitchell et al., 2016; Rouxel et al., 2002; Stüeken et al., 2015). Even these modern surface Se isotope variations exceed that identified in Mariana lavas by far but all show average $\delta^{82/76}$Se that are distinctly negative (Fig. 2.2). Thus, subduction recycling of surface material may indeed account for the isotopic offset of Mariana lavas compared to the Mariana pre-subduction mantle range.

Deep-sea sediments of the uppermost stratigraphic section from Site 1149 ODP 129, which are subducted beneath the Izu-Bonin-Arc as part of the Izu-Bonin-Mariana subduction system, have been analyzed for Se isotopes (Rouxel et al., 2002). These sediments have an average Se isotope composition of −0.42±1.44‰ (2 s.d., n=3, Rouxel et al., 2002), in agreement with input of, on average, isotopically light Se during subduction. However, in addition to pelagic sediments, subducted volcaniclastic turbidites have been identified as another major source of melt-like subduction components affecting the geochemistry of arc lavas in the northern part of the Mariana arc (Tollstrup and Gill, 2005). Moreover, isotopically light, hydrothermally altered basalt may also contribute to an isotopically light subduction input (−1.33±0.31‰, 2 s.d., n=2; Rouxel et al., 2002). Overall, although the proportion of altered versus unaltered oceanic crust to a net subduction input is difficult to constrain, the role of subducted sulfides needs to be considered.

Due to its chalcophile behavior Se is predominantly hosted by sulfides both in the mantle and slab (e.g. Guo et al., 1999; Hattori et al., 2002; König et al., 2015a; König et al., 2014). Thus, hydrothermal sulfides may constitute important subduction input material and published data show an average Se isotope composition of −1.36±2.82‰ (2 s.d., n=77; Rouxel et al., 2004; Rouxel et al., 2002) with the most extreme values up to −4.75‰ (Tab. A.2.10). This is in agreement with recent analyses of hydrothermal pyrite minerals, albeit from a continental setting, showing a record of $\delta^{82/76}$Se ranging from −4.48±0.09‰ to −0.39±0.09‰ (2 s.d., n=10) with an average of −2.73±0.09‰, altogether confirming the pronounced, isotopically light hydrothermal sulfide signatures for Se (König et al., 2019). Hydrothermal sulfides together with pelagic clays may be among the first phases to destabilize during subduction and therefore significantly contribute to slab-derived fluid signatures. The importance of sulfides in the recycling of chalcophile elements is supported by the observation of migrating S-bearing fluids up the subduction interface after liberation of sulfide from sediments and altered basalt at shallower depth (Mottl et al., 2004). It has further been suggested that S is released from magmatic sulfides in sediments and the oceanic crust itself by extensive recrystallization during high-pressure metamorphism (Li et al., 2016), possibly amplifying Se recycling. However, some S enters deeper parts of the subduction zone as indicated by sulfide inclusions in garnets from eclogites that grew during prograde metamorphism (Li et al., 2016). This sulfur might be liberated by subduction components that contribute to enrichment of the deeper sub-arc mantle wedge. In summary, the complex combination of pelagic and volcaniclastic sediments, altered and unaltered oceanic crust and sulfides altogether could account for the relatively lighter Se isotope signatures of Mariana lavas compared to the pre-subduction mantle (Fig. 2.2).

A pronounced shift in the average Se isotope composition of marine sediments before and after ca. 550 Ma ($\Delta_{\text{Precambrian−Phanerozoic}} \approx 0.91‰$; Stüeken et al. (2015)) was recently reported. This shift was interpreted to be the result of increased oxidative weathering and more pronounced continental mobilization of Se following Earth's second atmospheric oxygen increase ca. 550 Ma ago (Neoproterozoic Oxygenation Event, NOE). Progressive subduction of this isotopically lighter average Se isotope input may have had an impact on the secular Se isotope composition of the Earth's upper mantle after ca. 550 Ma, possibly mirroring the NOE. Such a link between stepwise atmospheric oxygenation and mantle evolution has previously been invoked for redox-sensitive uranium isotope systematics (Andersen et al., 2015). Subduction recycling of Se may not only produce larger and systematic Se isotope variations in Mariana lavas compared to the Mariana pre-subduction mantle but also, make Se isotopes a tool to investigate links between Earth's interior and atmospheric oxygenation throughout geological history.

2.6 Conclusions

The first case study involving stable Se isotopes in arc and back-arc lavas provides significant new insights into the systematics of this chalcophile and moderately volatile element in subduction zones. The Se isotope signature of submarine Mariana lavas is not affected by degassing and, unlike the elemental Se budget, not affected by magmatic differentiation. Therefore, the $\delta^{82/76}$Se of submarine arc lavas may retain its source signature. This signature is likely enriched by melt-like and fluid-like subduction components derived from the subducting Pacific crust and overlying sedimentary cover. Mariana samples show a tendency to become isotopically lighter from the back-arc to arc(-like) lavas, possibly reflecting a decreasing chromatographic effect of the overlying mantle wedge and increasing influence of a fluid signature. Addition of a sediment melt-like subduction component seems to buffer this fluid-induced signature as observed in Mariana arc samples. Due to these complex contributions of subduction components, Se isotope compositions of Mariana lavas show a larger range and are overall lighter than the pre-subduction mantle range that comprises peridotite and non-subduction related worldwide mantle melts. Possible slab-derived contributions may be traced back to subduction recycling of isotopically light Se input such as modern sediments and altered sulfide-bearing oceanic crust. Subduction recycling of Se may also have had an impact on the secular Se isotope composition of the Earth's upper mantle, because of a considerable shift to lighter average $\delta^{82/76}$Se in sediments that was attributed to the Neoproterozoic Oxygenation Event ca. 550 Ma ago. Further work on Se isotope systematics in arc lavas should therefore be dedicated to the different roles of variable subduction components and the possible links between atmospheric oxygenation, Se recycling and isotopic evolution of the mantle through geological time.

Chapter 3: Sulfide breakdown, within-slab redistribution and chalcophile element recycling in subduction zones: Evidence from Se isotope systematics of HP-LT rocks from the Raspas Complex, SW Ecuador

Abstract

The selenium (Se) isotope systematics may provide valuable insights into the behavior of Se in subduction zones and its recycling potential. In this study, we present Se–Te elemental and Se isotope data on prograde metamorphic rocks from the Raspas complex, SW Ecuador. These well-characterized samples allow significant constraints on the mechanisms of Se cycling in subduction zones. Eclogites derived from metamorphism of normal-type mid-ocean-ridge basalts (N-type MORB) during subduction, partly preserve their light Se isotope composition ($\delta^{82/76}$Se up to −1.89 ‰) of their precursor rocks that was imprinted during hydrothermal seafloor alteration. Striking correlations of fluid-mobile element enrichments and progressively heavier Se isotope compositions are observed. Eclogites with high Ce/Pb (and Ce/Rb, and Ce/Cs) that overlap that of typical MORB, show the lightest Se isotope compositions, whereas samples which experienced extensive fluid-mobile element enrichment (low Ce/Pb, Ce/Rb and Ce/Cs) due to fluid–rock interaction are characterized by heavy Se isotope compositions that approach those of serpentinized peridotites and metapelites. We propose that, fluids released from subducted oceanic crust and serpentinites by dehydration results in scavenging of chalcophile elements from destabilizing hydrothermal sulfides within hydrothermally altered basalt that transforms to eclogite during prograde subduction metamorphism. Extensive fluid–rock interaction (‘flushing’) of slab lithologies bears the potential to re-distribute dissolved chalcophile elements within the slab and further provides a realistic means for element transfer to the overlying sub-arc mantle. This, together with recently found isotopically light Se isotope compositions of subduction-related lavas, provides evidence for recycling Se (and likely other chalcophile elements) in subduction zones.

3.1 Introduction

Subduction of oceanic lithosphere is a key mechanism for crust-mantle recycling on Earth. Investigating the behavior and recycling of elements in subduction zones provides valuable information on their distribution between the Earth’s reservoirs. Understanding the behavior of the moderately volatile and chalcophile elements selenium (Se) and tellurium (Te) may contribute to constrain their potential as proxies for the origin and evolution of Earth’s volatiles (König et al., 2014; Wang and Becker, 2013) and economically valuable ore deposits (Hedenquist and Lowenstern, 1994; Jenner et al., 2015; Jenner et al., 2010; Richards, 2015; Sillitoe, 1972; Timm et al., 2012; Wilkinson, 2013) at convergent continental margins. The recycling potential of S and chalcophile elements, such as Se and Copper (Cu), has been the focus of several studies over the past decades (e.g. Alt et al., 1993; Evans et al., 2014; Liu et al., 2015; Timm et al., 2012). In the case of Cu, Stolper and Newman (1994) inferred from high Cu concentrations of Mariana arc lavas (compared to those of the back-arc region), that Cu might have been derived from the subducted slab. Other studies inferred that elevated Cu concentrations might be controlled by the solubility of S in the magma or by the thickness of the overriding plate (Chiaradia, 2014; De Hoog et al., 2001a). Recently, Jenner (2017) postulated that Cu, Au, Ag and Se might be trapped in magmatic sulfides in the lower oceanic crust prior to subduction and therefore escape subduction zone recycling as they are most likely transferred back into the mantle. On the contrary, chalcophile and siderophile elements that are hosted in the upper oceanic crust however might show a greater recycling potential (Jenner, 2017).

Regarding S, it was found that arc lavas generally show heavy $\delta^{34}S$ compositions, which are distinctly different from those of the Earth's mantle. It has been suggested that these heavy isotope signatures are derived from sedimentary S, which is mobilized via subduction components and metasomatizes the sub-arc mantle (Alt et al., 1993; De Hoog et al., 2001b; Imai et al., 1993; Ueda and Sakai, 1984; Woodhead et al., 1987). However, some sulfur might also be transported into the Earth's mantle as inferred from sulfide inclusions in eclogitic diamonds (e.g. Chaussidon et al., 1987). Another mechanism to explain heavy $\delta^{34}S$ signatures of arc lavas has recently been postulated by (Lee et al., 2018). These authors concluded that primitive arc cumulates are similar in their S isotope composition to that of the Earth's mantle and that more evolved cumulates overlap in their S isotope composition with those of seawater-derived sulfates. Thus, magma interaction with pre-arc crust, enriched in metasediments, metabasalts and seawater altered oceanic crust might be viable mechanism to produce the observed S isotope systematics. However, several studies that investigated melt inclusions (De Hoog et al., 2001a; Métrich et al., 1999) identified the S enrichment of the arc lava source region; likely by slab-derived sulfur fluxing into the overlying mantle wedge. Evans et al. (2014) investigated sulfur isotope systematics of eclogite-hosted sulfides and concluded that the subducted slab can experience sulfur addition in high fluid flux domains. This bears the potential of remineralization, metamorphism and re-liberation of sulfur. Moreover, loss of sulfur to ascending fluids by devolatilization likely results in sulfur loss to the subduction channel and mantle wedge. This scenario is best described as a "leaky loop" (Evans et al., 2014). Most likely, this scenario also resembles a conceivable mechanism for Se recycling in subduction zones, because Se often is regarded as geochemical twin of S.

The Se isotope systematics may contribute to study chalcophile element recycling in subduction zones from a new perspective, as Se substitutes S in sulfides (e.g. Guo et al., 1999; Hattori et al., 2002; Lorand and Alard, 2001) and because hydrothermal sulfides show high Se concentrations and on average light Se isotope compositions (Rouxel et al., 2004; Rouxel et al., 2002). It has been recently shown that the Se isotope composition of Mariana lavas are more variable than ambient mantle but with overall lighter values relative to the Mariana pre-subduction wedge (Kurzawa et al., 2019). This was interpreted to be due to sub-arc mantle wedge refertilization by, on average, isotopically light Se-bearing subduction components derived from subducted deep-sea sediments and sulfide-bearing altered oceanic crust. This may be reconciled with increasing pressure (*P*) and temperature (*T*) conditions during subduction, which cause metamorphic reactions within the subducted material associated with dehydration and transport of fluid-mobile elements across the slab-mantle wedge interface (e.g. Hermann et al., 2006; Schmidt and Poli, 2003). However, the exact mechanisms that lead to Se distribution and slab-mantle wedge transfer including processes that occur within the uppermost lithospheric mantle, the oceanic crust and overlying deep-sea sediments (oceanic and/or terrigenous) remain inconclusive.

Here we provide the first Se isotope data for a coherent suite of prograde high-pressure/low-temperature (H*P*/L*T)* metamorphic rocks from the Raspas Complex, SW Ecuador. This suite resembles a paramount example for a structurally pristine but extensively metamorphosed slice of oceanic lithosphere obducted onto continental crust. We aim to constrain the influence of subduction metamorphism on the Se isotope composition of different sections of obducted and metamorphosed oceanic lithosphere (eclogites, serpentinized peridotites and metapelites) and to reconcile our observations with Se isotope systematics of Mariana lavas to improve our understanding of chalcophile element recycling across subduction zones.

3.2 Geological setting and sample materials

The Ecuadorian continental margin constitutes part of the Andean subduction zone where the Nazca plate subducts beneath the South American Plate. Between the Late Jurassic and the Eocene times, various terranes of oceanic origin have been accreted and amalgamated during subduction of oceanic lithosphere (Arculus et al., 1999; Bosch et al., 2002; John et al., 2010 and references therein). Tectonically, Ecuador can be subdivided into two parts that are separated by a major suture zone dividing the eastern margin of the inter-Andean valley and the western foot of the Cordillera Real (Gabriele et al., 2003). The eastern part is of continental origin and thought to resemble the active continental margin during the end of the Jurassic (~140 Ma) (Gabriele et al., 2003). In contrast, the western domain comprises magmatic bodies of oceanic origin that were added during different subduction-accretion events since the Early Cretaceous (Gabriele et al., 2003 and references therein). Although the Andean subduction zone currently constitutes the worldwide longest, uninterrupted and almost linear subduction zone, the occurrence of exhumed high-pressure/low-temperature (H*P*/L*T*) metamorphic rocks is rather limited (Halama et al., 2013 and references therein). However, HP/LT metamorphic rocks as part of metamorphic terranes occur in SW Ecuador and Colombia (e.g. Bosch et al., 2002; Feininger, 1982). In the case of Ecuador, these metamorphic terranes of various metamorphic ages (Paleozoic to Cretaceous) are grouped together as the El Oro Metamorphic Complex (Gabriele et al., 2003 and references therein), which is sandwiched between continentally derived units (Tahuin Group in the South and Birone Terrane in the North) (Fig. 3.1). One major constituent of the El Oro Metamorphic Complex is the Raspas Complex, which itself comprises two high-pressure/low-temperature formations. The El Toro formation is made up of eclogites-facies, serpentinized peridotites whereas the Raspas formation consists of eclogites, blueschists and garnet-chloritoid-kyanite metapelites (John et al., 2010 and references therein). Recently, the Raspas Complex has been interpreted to resemble a deeply subducted ophiolite complex which was subject to H*P*/L*T* metamorphism during the Early Cretaceous (as derived from K–Ar, Ar–Ar and Lu-Hf dating of mineral separates) (John et al., 2010 and references therein). Based on geochemical data, the El Toro and Raspas formation resemble metamorphosed depleted mid-ocean ridge basalt (MORB) mantle, MOR basalts as well as subducted seamounts of ocean-island basaltic (OIB) origin (John et al., 2010), respectively. During uplift and exhumation, the ophiolite sequence was subject to retrogressive greenschist-facies metamorphism. However, this did not overprint eclogites-facies mineral assemblages. Peak metamorphic conditions for blueschists and eclogites have been derived by geothermobarometry yielding *P*–*T* conditions of 600±20°C and 14–16 kbar (maximum 18-20 kbar) and 600±30°C and 16-18kbar, respectively (see John et al. (2010) for details). The fact that blueschists coexist with eclogites under similar *P*–*T* conditions has been attributed to their bulk compositional differences (OIB vs. MORB protoliths) (John et al., 2010). In summary, metamorphic rocks from the Raspas Complex resemble an exhumed high-pressure/low-temperature ophiolite of oceanic origin that was subducted beneath the South American Plate during Early Cretaceous times.

In this study, we provide the first Se isotope together with Se elemental data for H*P*/L*T* rocks. We focus in this pioneering study on 10 representative and well-characterized samples from the Raspas Complex, that have been thoroughly analyzed including multiple re-digestions. We also provide first high-precision Te concentration data to expand the Te database for future studies. Among the samples are 6 eclogites and 1 metapelite from the Raspas Formation and 3 serpentinized peridotites from the El Toro formation. Most samples have been the focus of previous studies that investigated major- and trace element geochemistry, Sr–Nd, Lu–Hf-geochronology and Li–N–O–isotope systematics, (e.g. Halama et al., 2010; Halama et al., 2011; John et al., 2010) to constrain the geochemical affinity as well as conditions and timing of the H*P*/L*T* metamorphism (e.g. Feininger, 1980; Gabriele et al., 2003; John et al., 2010). For detailed sample descriptions see (John et al., 2010 and references therein). In the following, eclogites from the Raspas formation will be termed MORB-type eclogites because their protoliths have been identified to be typical MOR-basalts.

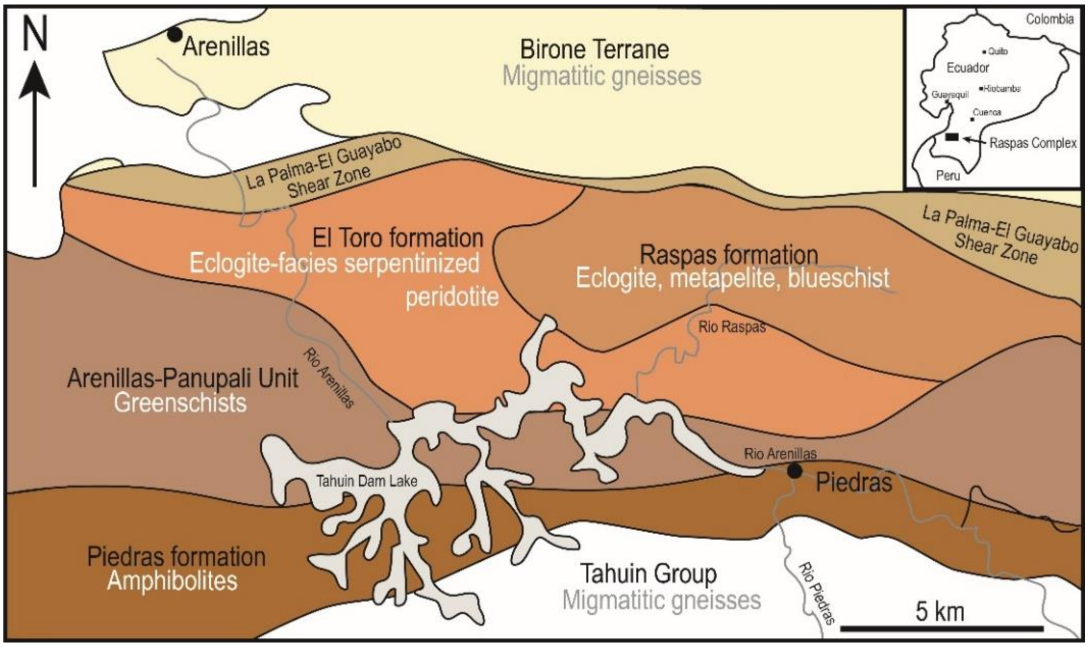

Figure 3.1 Geological map of SW Ecuador showing structural and lithological units of the El Oro Metamorphic Complex (modified after Gabriele (2002)).

3.3 Analytical techniques

3.3.1 Reagents and materials

Sample preparation and measurements involved usage of reagents that were distilled from MERCK Millipore Emsure™ grade HNO_3 (65%) and HCl (37%) using Savillex™ DST-1000 Acid Purification Systems. When necessary, reagents were diluted to required molarities to ±0.03 mol L^{-1} (checked by titration). Before usage, perfluoralkoxy (PFA) beakers, pipette tips, centrifuge vials and ion exchange resins were cleaned with multi-step HNO_3-HCl treatments. De-ionized water was further purified to 18.2 MΩ·cm (at 25°C) using a Merck Millipore Milli-Q™ system. All analyses were performed in the ISO-5 (US FED standards class 100) clean-room facilities of the Isotope Geochemistry Group at the University of Tübingen, Germany.

3.3.2 Selenium isotope and Se–Te elemental analyses

All samples were ground well below 25 µm particle size to provide powder material which can be effectively dissolved via hotplate PFA beaker digestion and, if not fully dissolved in the case of small garnet fragments, provide sufficient surface for near-quantitative dissolution of sulfides as dominant Se hosts. This was also demonstrated by comparison of Se concentrations additionally obtained for selected samples via bomb and high pressure asher digestion (SEC 47-1, SEC 50-1, and USGS BCR-2) techniques as well as multiple hotplate PFA beaker digestions of some samples. Pressure bomb digestions yield Se concentrations, which are not higher but even slightly lower than concentrations obtained from table top digestions (Tab. A.3.1). Slightly lower amounts could be explained by some volatile Se loss during the polytetrafluoroethylene (PTFE) bomb digestion.

However, the minor BCR-2 Se loss corresponds to the difference of Se contents between bomb and table top dissolutions. High-pressure asher digestion of sample SEC 50-1 yields a Se concentration of 87 ng g^{-1}, which is similar to concentrations obtained from table top digestions (section 3.4.2). These results strongly suggest that quantitative dissolution of Se from sample powders, which still might contain small <25 µm garnet fragments, is achieved.

A general pre-determination of Se concentrations from a minor sample powder aliquot identifies precise double spike amounts to be later added to the main powder aliquot for an ideal spike-sample ratio of ~1:1 (Kurzawa et al., 2017). For pre-determination of Se concentrations we followed the procedure described by Yierpan et al. (2018). Briefly, this involves weighting of 0.02 g sample material in perfluoralkoxy (PFA) beakers, adding of an equal amount of ^{74}Se–^{77}Se double spike and digesting the mix using an acid mixture of 5:1 (v/v) conc. HF : conc. HNO_3 in closed beakers at 85°C. The sample solutions were then dried at 65°C followed by multiple conversion, heating and dry down steps (see Yierpan et al., 2018) in 6 mol L^{-1} HCl before Fe was removed by means of anion exchange chromatography. Fe-free cuts were then diluted to 0.5-1 ng mL^{-1} Se and finally measured on the iCAP Qc following the protocol by Yierpan et al. (2018).

For Se isotope and Te concentration analyses we followed the protocol by Yierpan et al. (2018) as it allows to simultaneously purify Se and Te from a single sample digest. This protocol has the advantage that high yields and very low blanks can be obtained. In fact, blank Se isotopic compositions cannot be determined because in these cases signal intensities are generally too low, i.e. below background intensities (≤3 mV on m/z = 82, using a 10^{11} Ω amplifier resistor). For Se–Te element concentration determination by iCAP Qc analysis, blank levels correspond to 0.01 and ~0.05 ng for Te and Se, respectively; see Yierpan et al. (2019). It has also been shown that, even for low Se-containing aliquots a high reproducibility can be achieved, in accordance with insignificant blank contribution to a sample (Kurzawa et al., 2017). Following Se concentration predetermination, the protocol for the Se isotope and Te concentration determination analyses comprises weighing of sample material equivalent to ~30 ng Se (exact Te amount uncritical) into conventional PFA beakers, adding adequate amounts of ^{74}Se-^{77}Se double spike (1:1; sample Se : double spike Se) and ^{125}Te single spike (aiming for Se/Te of ca. 10, exact Te amount uncritical) and digesting the sample-spike mixtures in an acid mixture of 5:1 (v/v) conc. HF : conc. HNO_3 in closed beakers on a hotplate at 85°C for 48 hours. Se and Te were purified from sample solutions by a two-step ion exchange chromatography. In a first step, we employed an anion exchange column to remove Fe and collect purified Te. In a second step, Se was purified using a cation exchange column to remove remaining cations. Te concentrations were then determined by hydride generator quadrupole ICP-MS on the iCAP Qc instrument and Se isotopes and concentrations were then measured by hydride generation multi-collector ICP-MS on the ThermoFisher Scientific Neptune*Plus* instrument of the Isotope Geochemistry laboratory, University of Tübingen. Typical signals on ^{82}Se (using an amplifier resistor of 10^{11} Ω) on a 30 ng mL^{-1} Se solution with operating parameters similar to those reported by Kurzawa et al. (2017) were generally 0.8-0.9 V. With similar operating parameters to those of Yierpan et al. (2018), 30000 cps on ^{126}Te were obtained for a Te standard solution of 0.5 ng mL^{-1}. Se isotopes and Se-Te concentrations of samples were determined at similar signal intensities compared to those of standard solutions. For detailed descriptions of analytical techniques employed see Kurzawa et al. (2017) and Yierpan et al. (2018). All Se isotope compositions obtained during this study are reported relative to the NIST-3149 Se reference solution. Measurements of the inter-laboratory standard solution MH-495 yield an average value of $\delta^{82/76}$Se of −3.26±0.09‰ (2s.d., n=19, 30 ng mL^{-1} solutions, see Tab. A.3.2), in agreement with previous studies (Kurzawa et al., 2019; Kurzawa et al., 2017; Labidi et al., 2018; Yierpan et al., 2018; Yierpan et al., 2019). All samples were measured together with the international rock reference material USGS BCR-2, which yield $\delta^{82/76}$Se of 0.14±0.15‰ (2 s.d., n=4) and Se–Te concentrations of 78 and 2.5 ng g^{-1}, respectively (Table A.3.3). This in agreement with previously published Se isotope composition and Se–Te concentration data (Kurzawa et al., 2017; Yierpan et al., 2018; Yierpan et al., 2019). Long-term analytical reproducibility for both Se and Te concentration determination is ~3% r.s.d. (1 s.d.). In most cases, external reproducibility for sample materials is <0.13‰ (2 s.d., n=4, SEC 43-3), as derived from multiple digested and analyzed sample SEC 43-3 during different measurement sessions (Tab. A.3.4).

3.4 Results

3.4.1 Major and trace elements

Eclogite samples show 44 to 50 wt.% SiO_2, 13.5 to 15.0 wt.% Al_2O_3, 13.3 to 15.5 wt.% Fe_2O_3 and MgO contents between 6 and 10 wt.%, thus possessing tholeiitic bulk compositions (Fig. 3.1). The protolith of the eclogites formed in a mid-ocean-ridge setting as inferred from their average N-MORB-like Th/Yb, Nb/Yb and TiO_2/Yb (see Tab 3.1) and their chondrite-normalized rare earth element (REE) patterns (Fig. 3.3a).

Although displaying a rather wide range for their Nb/La ratio (0.5-1.0), the MORB-like $(La/Sm)_N$ (0.50-0.65; chondrite-normalized after Boynton, 1984) rules out substantial contributions from a subduction component (Fig. 3.4a; see Fig. 5 in John et al., 2010). Further, the Nb/Zr and Hf/Yb ratios of the eclogites are inferred to be representative of shallow melting in a depleted mantle source (Fig. 3.4b; see Fig. 7 in John et al., 2010). In the following, eclogites will be termed MORB-type eclogites, because of their geochemical derivation from typical N-MORBs.

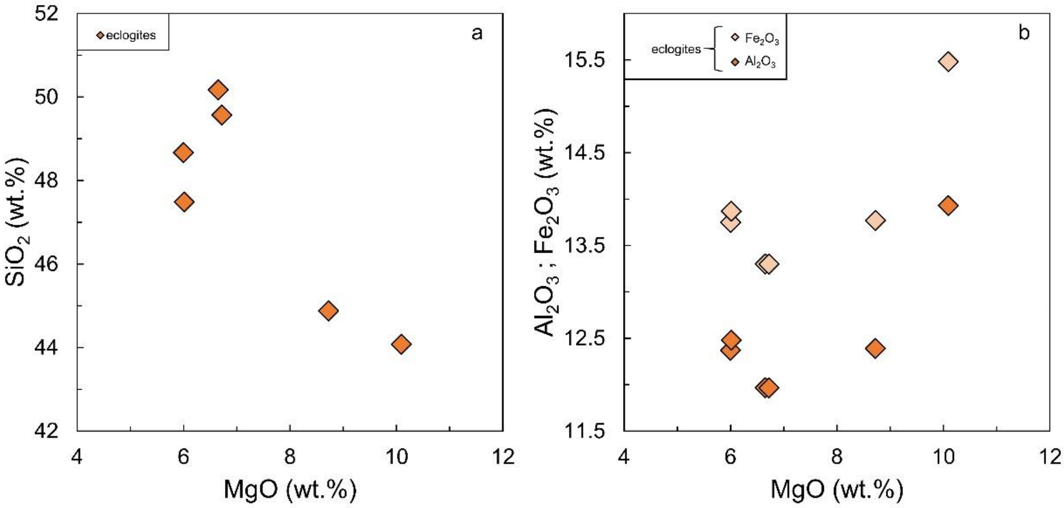

Figure 3.2 Diagrams showing the relationship of **a** SiO_2 and MgO contents and **b** MgO and Al_2O_3 and Fe_2O_3 contents of eclogite samples, respectively.

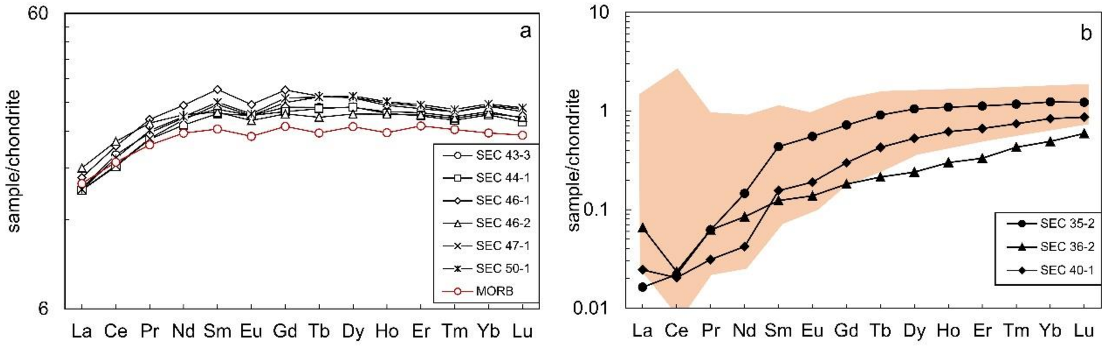

Figure 3.3 Chondrite-normalized rare earth element diagrams (Boynton, 1984) for **a** eclogites analyzed in this study. N-type MORB composition of Hofmann (1988) is shown for comparison. **b** For serpentinized peridotites analyzed during this study. For reasons of geochemical similarity, chondrite-normalized REE data of abyssal peridotites from the Bullard and Vulcan fracture zones are shown, data from Niu (2004).

Samples of serpentinized peridotites show 40 to 41.5 wt.% SiO_2 and overall low TiO_2 (≤0.05 wt.%) and Al_2O_3 (1.34-2.37 wt.%) contents and high MgO contents (37-41 wt.%). According to their trace element systematics (Ni, and Cr concentrations) and chondrite-normalized REE patterns (Fig. 3.3b), the serpentinized peridotite samples are similar to abyssal peridotites and likely represent residues of a depleted mantle source (John et al., 2010 and references therein).

3.4.2 Se–Te concentrations

MORB-type eclogites of the Raspas formation exhibit Se concentrations in the range of 36 to 144 ng g^{-1} (n=5), with the exception of sample SEC 46-1, which shows a pronounced Se depletion (6.40 ng g^{-1}) compared to the other samples. Overall, Se concentrations of the eclogites are generally lower compared to those of their protoliths that resemble typical N-type mid-ocean ridge basalts and are characterized by systematically higher Se concentrations of 140 to 220 ng g^{-1} (Lissner et al., 2014; Yierpan et al., 2019). The Se concentrations are not the result of MORB

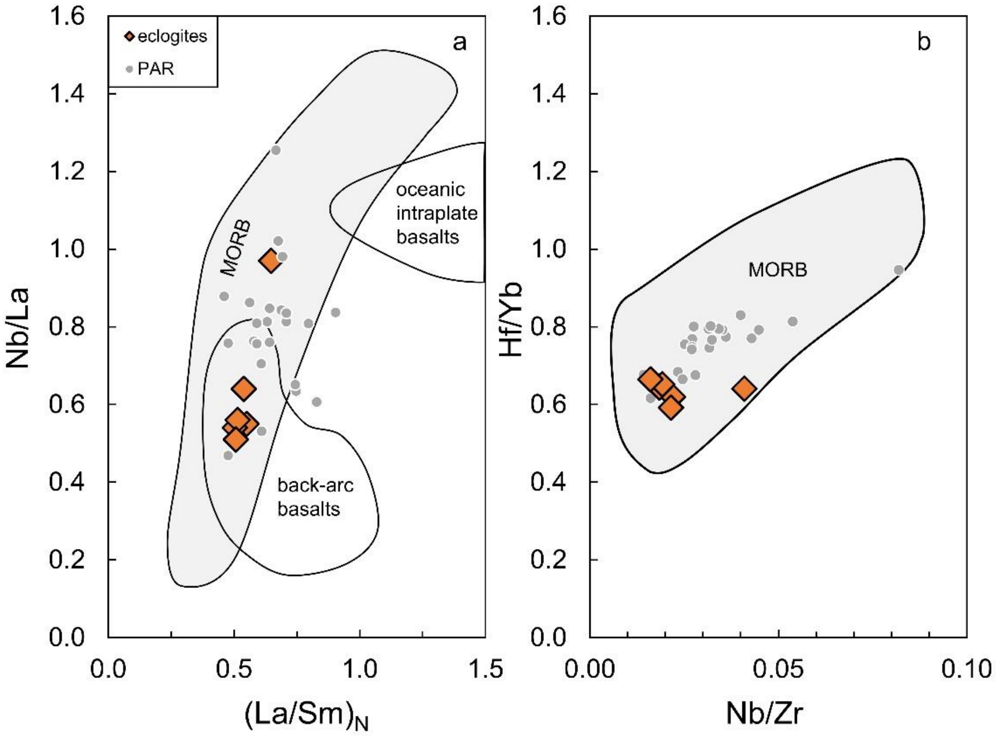

Figure 3.4 a Nb/La vs (La/Sm)$_N$ and **b** Hf/Yb vs Nb/Zr diagrams modified after modified after John et al. (2004) showing geochemical similarity of the eclogites analyzed in this study and normal-type mid-ocean-ridge basalts (MORB). For comparison, MORB data of the Pacific Antarctic Ridge (PAR) by Yierpan et al. (2019) is shown. Fields for MORB, back-arc basalts and oceanic intraplate basalts were graphically extracted from John et al. (2010).

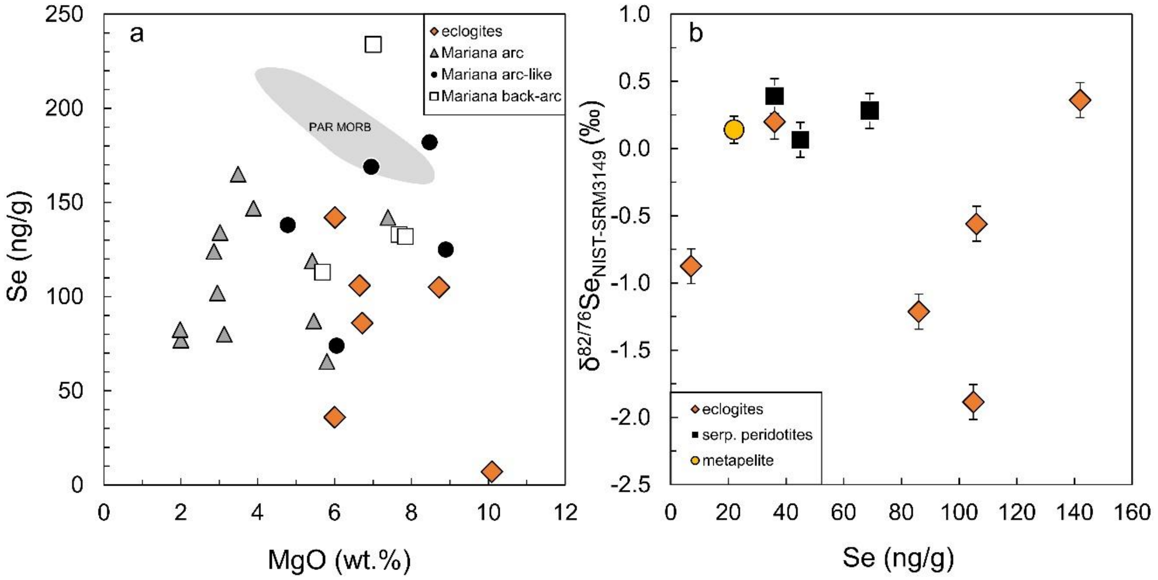

Figure 3.5 a Relationship of Se concentrations and MgO contents of eclogites and serpentinized peridotites. No systematic relation of the two parameters is inferred from the data, indicating limited utility of Se concentration data of these specific rock types likely due to subduction zone processes. For comparison, data from the PAR (Yierpan et al., 2019) and the Mariana arc system (Kurzawa et al., 2019) are shown. **b** Se isotope composition vs Se concentrations showing very variable Se isotope compositions. Note that, samples with the highest Se concentrations already span almost the entire Se isotope composition range of all eclogites. Uncertainty on Se isotope compositions is 0.13 ‰, see section 3.3.2 for details.

differentiation as inferred from the lack of correlation of Se concentrations and the MgO content (Fig. 3.5a), which recently was observed for MORB samples from the Pacific Antarctic Ridge (Yierpan et al., 2019). Tellurium concentrations of the MORB-type eclogites range from 2.15 to 8.55 ng g^{-1} and are thus generally higher than Te concentrations observed for N-type mid-ocean ridge basalts (compare Lissner et al., 2014; Yierpan et al., 2019). The serpentinized peridoitites are characterized by Se concentrations that range from 37 to 68 ng g^{-1} and thus are generally lower than that of the primitive upper mantle (PUM) (~76 ng g^{-1}; Palme and O'Neill, 2014). Tellurium concentrations range from 5.62 to 9.15 ng g^{-1}. Metapelite sample SEC 45-3 shows low Se-Te concentrations of 22 and 4.03 ng g^{-1}, respectively.

3.4.3 Se isotope composition

MORB-type eclogites show very variable $\delta^{82/76}$Se between −1.89 to 0.35‰ (Tab. 3.2), which overlaps with recently reported Se isotope data for N-type MORB from the Pacific Antarctic Ridge (PAR) (Yierpan et al., 2019) but on average is lighter compared to those. The metapelite SEC 45-3 shows a $\delta^{82/76}$Se of 0.14‰ and thus overlaps with the Se isotope composition range of the serpentinized peridotites ($\delta^{82/76}$Se from 0.07 to 0.39‰) (Tab. 3.2). A lack of correlation is observed for $\delta^{82/76}$Se vs. Se concentrations and samples with highest Se contents already span the entire range of Se isotope composition of the dataset (Fig. 3.5b). Positive correlations between Se isotopes and N concentrations and N isotope compositions are less pronounced but can be deduced (Fig. A.3). Samples SEC 44-1 and SEC 47-1 show heavy Se isotope compositions at elevated concentrations of the large ion lithophile elements (LILE) K, Rb, Cs and other fluid-mobile elements (i.e. Pb, and Ba) (Fig. 3.6). Likewise, these samples show higher Li concentrations and lower Ce/Li with sample SEC 47-1 also showing the lightest Li isotope composition among the rather limited Li isotope data of the samples (Fig. 3.7d). Interestingly, $\delta^{82/76}$Se negatively correlates with Ce/Pb (and other immobile element/LILE; Ce/Rb, Ce/Cs, also Ce/N) ratios (i.e. Fig 3.7c), which is the most characteristical feature of the dataset. Figure 3.5c shows that eclogites span the entire range from highest Ce/Pb and lightest Se isotope composition to lowest Ce/Pb and heaviest Se isotope compositions of serpentinized peridotites and the metapelite sample.

3.5 Discussion

3.5.1 Effect of hydrothermal seafloor alteration on Se isotope compositions of subduction input material

The herein analyzed eclogites are influenced by various degrees of low-temperature hydrothermal seafloor alteration as inferred from Sr and O-isotopes (Halama et al., 2011). Additionally, hydrothermal seafloor alteration can be identified by steep trends in Th/U vs. U diagrams (caused by U addition without significant addition of Th), by enrichments in K_2O, Rb, Cs and Pb as well as radiogenic Sr- and unradiogenic Nd isotope compositions (Bebout, 2007; Macgregor and Manton, 1986). The Raspas eclogites analyzed here generally show these features as identified by Halama et al. (2010), see also Fig. A.4). Additional evidence for seafloor alteration has been suggested based on nitrogen (N) elemental and isotopic systematics, because N isotope compositions are shifted towards heavier values that overlap with those of altered oceanic crust from the modern seafloor (Halama et al., 2010). The influence of variable hydrothermal seafloor alteration is further supported by the fact that, eclogites overlap in their Se isotope compositions with those of hydrothermally altered basalt and hydrothermal sulfides (Fig. 3.8). The latter two are characterized by on average light $\delta^{82/76}$Se values of −1.33±0.31‰ (2 s.d., n=2; Rouxel et al., 2002) and −1.36±2.82‰ (2 s.d., n=77; Rouxel et al., 2004; Rouxel et al., 2002), respectively (Tab. A.2.9). The eclogites with the lowest Se isotope composition and the highest Ce/Pb could thus resemble metamorphosed assemblages that preserve at least some Se isotope signatures resulting from hydrothermal alteration.

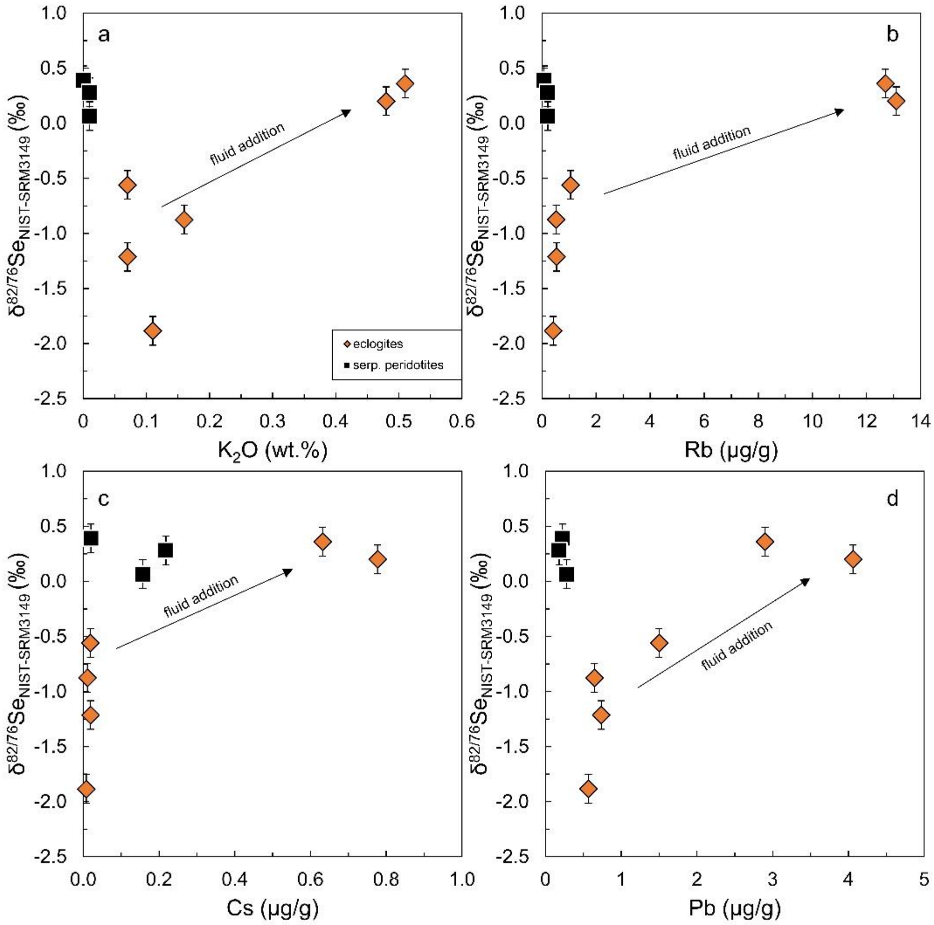

Figure 3.6 Se isotope composition of eclogites and serpentinized peridotites vs **a** K_2O contents, **b** Rb, **c** Cs and **d** Pb concentrations. Samples SEC 44-1 and SEC 47-1 show pronounced enrichments in fluid-mobile elements and moreover display the heaviest Se isotope compositions among all eclogite samples. These samples might represent extensively fluid flushed eclogites (see section 3.5.2 for details). Uncertainty on Se isotope compositions same as in Fig. 3.5.

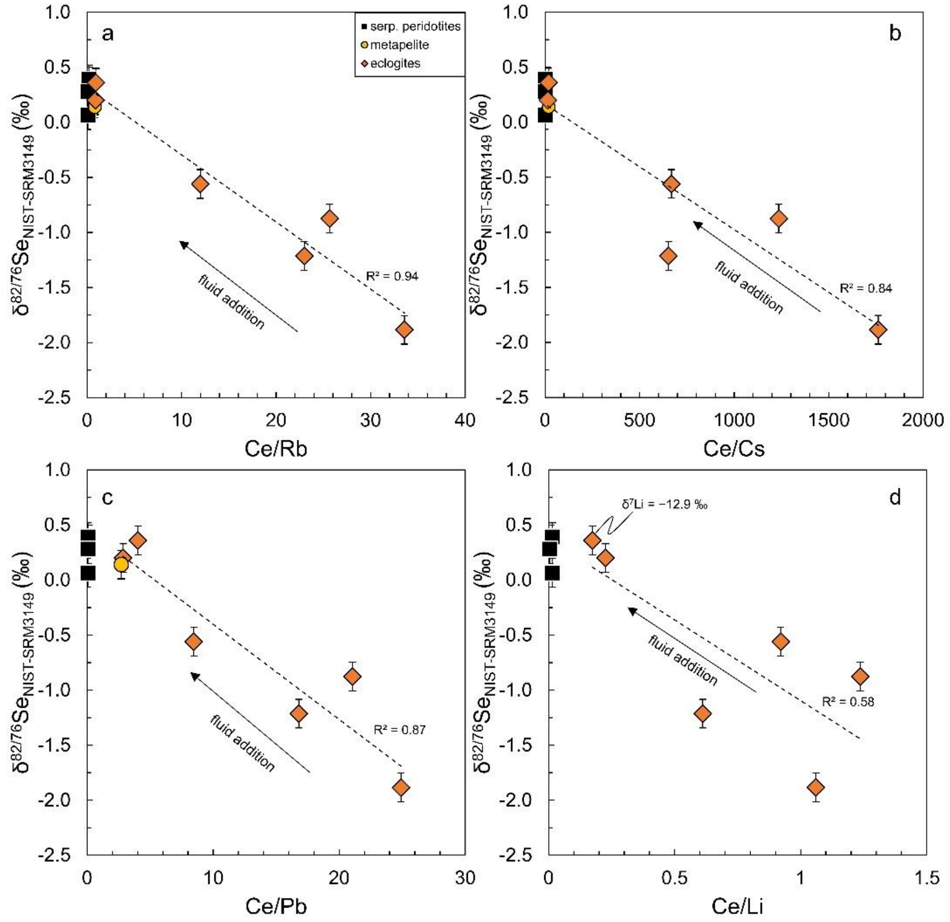

Figure 3.7 Se isotope composition vs. **a** Ce/Rb, **b** Ce/Cs, **c** Ce/Pb and **d** Ce/Li showing strong negative correlations for the eclogite samples, indicating that the process responsible for enrichment of fluid-mobile elements also affected Se isotope compositions. Note that, sample SEC 47-1, which shows the heaviest Se isotope composition among all eclogites, also is characterized by a very negative Li isotope composition, likely being the result of kinetic isotope fraction during diffusive transport of Li through the eclogite body. For details on this matter see Halama et al. (2011). Uncertainty on Se isotope compositions same as in Fig. 3.5. Dashed lines in **a–d** represent linear correlations with correlation coefficient (R^2) of eclogite samples.

However, Se concentrations of the eclogites are very different from those of hydrothermally altered basalt (~60 µg g^{-1}), perhaps indicating that substantial Se loss occurred without affecting the Se isotope compositions of the studied rocks. While this would explain the absence of correlations between Se isotope compositions and Se concentrations, this Se loss might be the result of complex processes within the subduction slab at different depths (see section 3.5.3). At this point this hampers the straightforward use of Se concentrations in eclogites and suggests that Se isotopes may be more suitable to assess the subduction input signature. The proportion of hydrothermally altered crust to the bulk subducted oceanic lithosphere is difficult to constrain, although there is evidence from S isotope systematics of mafic and ultramafic rocks (Ocean Drilling Program Leg 147), which implies partial or even complete hydrothermal alteration of the studied samples (Puchelt et al., 1996). The lithospheric mantle, which was subducted along with the MORB-type eclogites, consists of variably serpentinized peridotites (10 to 95 %), hence demonstrating the effect of serpentinization an hydrothermal seafloor alteration processes. However, if the Se isotope composition of the eclogites would exclusively result from low-temperature hydrothermal seafloor alteration, one would expect a clear correlation between extent of the alteration and Se isotopes or at least consistently very light Se isotope compositions. Yet Se isotopes do not correlate with such indices of alteration (e.g. Sr-isotopes, Fig. A.5). On the contrary, samples characterized by high K_2O, Rb, Cs and Pb contents (Fig. 3.6) and lowest ratios of Ce to any of these elements (Fig. 3.7) display the heaviest Se isotope compositions, in some cases even showing a subtle trend. This leads to the assumption that the process responsible for LILE enrichment also accounts for relative enrichment in heavy Se isotope compositions. It is hence likely that, the LILE enrichment is not exclusively the result of hydrothermal seafloor alteration but indeed is caused by additional processes. The "reversed" correlation between hydrothermal sulfide Se isotope composition and classic proxies for hydrothermal seafloor alteration (Fig. 3.7) may indicate that secondary processes obscured previous correlations between these two and are represented by the heaviest Se isotope endmember signature of our samples.

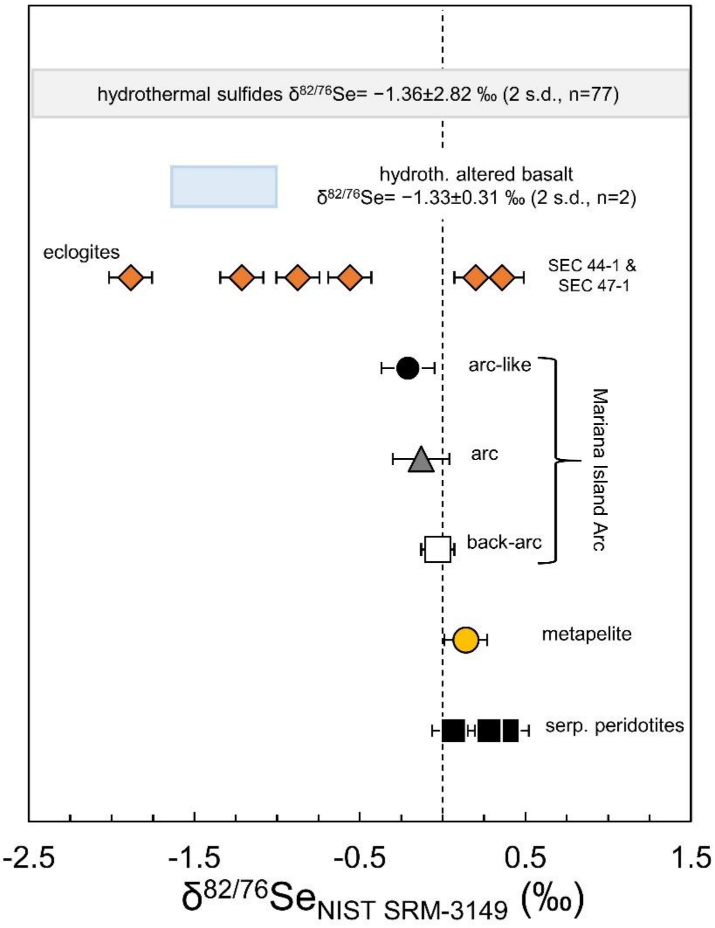

Figure 3.8 Compilation of Se isotope compositions of eclogites, serpentinized peridotites and the metapelite from this study, hydrothermal sulfides (horizontal grey box), hydrothermally altered basalt (horizontal blue box) and lavas from the Mariana Island arc. Data sources are Rouxel et al. (2002), Rouxel et al. (2004) and Kurzawa et al. (2019). All error bars given as 2 s.d. uncertainty, see section 3.3.2. Uncertainty on Se isotope compositions of Raspas samples same as in Fig. 3.5.

Altogether, as previously found for other geochemical and isotopic signatures, Raspas MORB-type eclogites preserve, to some extent, previous hydrothermal alteration-related Se isotope composition during subduction. The samples with the lightest Se isotope composition and highest

Ce/Pb may represent this endmember signature. However, this process likely is not the last one that affected these samples. The other endmember signature (heaviest Se isotope composition and lowest Ce/Pb) needs to be evaluated which might provide clues about the role of superimposed, secondary processes during subduction, such as dehydration of serpentinites, oceanic crust and overlying sedimentary cover.

3.5.2 The role of fluids on the Se isotope signature of the total slab component

The Se isotope composition and Se elemental budget of the eclogites is rather distinct from their protoliths (N-type MORBs) and no correlations of Se concentration (not shown) or Se isotope composition with classic proxies for hydrothermal seafloor alteration are observed (Fig. A.3). It has been suggested that the MORB-type eclogites were influenced by a non-pervasive but variable metasomatic overprint caused by a fluid derived from dehydration of metabasalts that transformed from blueschist into eclogites (Halama et al., 2011). This is indicated by elevated Li contents and distinctly negative δ^7Li values of the eclogites which is best explained by diffusive Li mobility through the eclogite body and kinetic isotope fractionation (Halama et al., 2011). In the case of nitrogen, Halama et al. (2010) found that, N concentrations and isotope compositions overlap with those of altered oceanic crust from the modern seafloor and concluded that, additional batch or Rayleigh devolatilization effects could have been a superimposed mechanism to explain the observed characteristics. Based on correlations of N and trace elements such as Cs, Pb, and Ba and their evident enrichment during subduction zone fluid-rock interaction (Bebout, 2007; John et al., 2004), the authors additionally suggested the possibility that some eclogites (and serpentinized peridotites) might have experienced N addition due to metasomatism during subduction-zone metamorphism derived from a sedimentary or metasedimentary source. The involvement of the latter is also supported by the uniformity of δ^{15}N of the MORB-type eclogites, which has been interpreted to result from isotopic homogenization via fluid-rock and fluid-sediment interaction (Halama et al., 2010). However, serpentinized peridotites, which previously interacted with sediment-derived N, were not ruled out as potential source for the N enrichment. Subduction-related dehydration of altered and serpentinized oceanic mantle, previously enriched in incompatible elements due to serpentinization processes (Scambelluri et al., 2001), has been identified to release large volumes of H_2O and fluid mobile elements. These fluids may have affected the fluid-mobile element budget and Se isotope compositions as well as Se abundances of overlying metamorphic oceanic crust, i.e. that of the MORB-type eclogites.

The eclogites show marked positive correlations of 1/Pb and Ce/Pb, 1/Rb and Ce/Rb, and 1/Cs and Ce/Cs (at fairly constant Ce concentrations) (Fig. A.6), indicating fluid-mobile element addition by a fluid phase. This fluid addition seems to have affected the Se isotope compositions as can be inferred from the negative correlations of $\delta^{82/76}$Se with Ce/Rb, Ce/Cs, Ce/Pb and Ce/Li (Fig. 3.7). On the contrary, Se concentrations do not correlate with any of these trace elements, nor do

Se isotopes correlate with Ce/Se, pointing to the possibility of decoupled Se elemental and Se isotope systematics. This hampers the use of Se concentrations in our suite for unravelling its mobility. On the other hand, Se isotopes prove to be more useful. The MORB-type eclogite with the highest Ce/Pb overlaps with the Ce/Pb of non-subduction related reservoirs (e.g. average MORB, Gale et al. (2013)). This eclogite could be interpreted as a least fluid-influenced endmember, which preserved the most pronounced hydrothermal signature. With increasing fluid addition, the Ce/Pb (and Ce/Rb; Ce/Cs) decrease away from this mantle endmember. Note that, samples SEC 44-1 and SEC 47-1, which show the heaviest Se isotope composition among all eclogites, are characterized by relatively low Ce/Pb, Ce/Rb, Ce/Cs and Ce/Li that approach those of serpentinized peridotites and the metasediment sample. Interestingly, Pb addition by fluids was also recognized in previous studies on eclogites (Zambezi eclogites, John et al., 2004) where it was suggested to be derived from metasediments. Overall, our observations can be reconciled with metasediment-affected serpentinite-derived fluids that increasingly overprint overlying eclogites and thus may lead to both shallow and deeper partial loss of Se, as inferred from overall lower Se concentrations of the eclogites compared to the Se budget of hydrothermally altered basalt. The product is a mixture of isotopically light Se from hydrothermal seafloor alteration and isotopically heavier fluids derived from serpentinite and metasediment dehydration. This would imply that, samples SEC 44-1 and SEC 47-1 were not only significantly affected by fluid flushing but were also entirely overprinted in their Se isotope composition which now resembles that of the serpentinite fluid source(s). The fact that, samples SEC 44-1 and SEC 47-1 display rather distinct Se concentrations (36 an 140 ng g^{-1}, respectively) again substantiates the rather limited use of Se concentrations, mainly because of superimposed processes that affected the protoliths to variable extents prior to subduction. Given that eclogites have been identified to be prone to fluid flushing, they may also provide the isotopic input signature and the source of its recycling into the sub-arc mantle wedge.

3.5.3 Breakdown of low-T sulfides during subduction and transport via slab components

Evidence for progressive devolatilization of the subducting plate is derived from fluid compositions of springs across the Mariana forearc. Mottl et al. (2004) concluded that sulfate is lost at an early stage of subduction, most likely from altered basalt and sediments at shallow depths. This early commencing and continuous low-T sulfide breakdown due to progressive subduction also bears potential for loss of chalcophile elements and might explain the overall lower Se concentrations of the MORB-type eclogites compared to hydrothermally altered basalt. At the same time, our Raspas case study also shows that eclogites may partly preserve a Se isotope composition of their pre-subduction metasomatic overprint, tracing the survival of some low-T sulfides to greater subduction depths. Hence, despite their early breakdown, hydrothermal sulfides therefore remain a significant carrier and source of Se input, like that of other chalcophile elements, into subduction zones. For instance, in the case of a sulfide-bearing H*P* vein within lawsonite eclogites from the Tianshan Orogen, dehydration of oceanic crustal metabasalts and decomposition of hydrothermal sulfides have been suggested to result in Ca, Sr, Pb and S-bearing slab fluids (Li et al., 2013). Sulfide breakdown during deeper subduction has generally been identified to release oxidizing fluids which are able to transport siderophile and chalcophile elements such as Ni, Co, and As (Cruz-Uribe et al., 2018). These fluids may infiltrate the slab-mantle interface and eventually find their way into the sub-arc mantle, hence being incorporated into the arc magma source region (Cruz-Uribe et al., 2018). This indicates the likely role of destabilization and decomposition of sulfides below the sub-arc region, which plays an important role for the Se and other chalcophile element budgets of subduction zone lavas.

The early breakdown of sulfides and their part preservation until deeper subduction need to be reconciled. This may be done by invoking part-retention of sulfides by recrystallization processes within the slab. The presence of typical magmatic sulfide assemblages in eclogites, overall suggests that sulfur is not completely lost during prograde metamorphism (Evans et al., 2014). Based on similar S isotope compositions of hydrothermal sulfides and eclogite-hosted sulfides, Evans et al. (2014) concluded that sulfur may have moved from hydrothermal sulfides to sulfides which grew during subduction zone metamorphism. This would involve dissolution of sulfur in a fluid phase, its transport and recrystallization to form new sulfide minerals. Hydrothermal sulfides are subject to H*P*/L*T* metamorphism, thereby liberating sulfur (Li et al., 2016) and probably also Se but are also affected by extensive recrystallization. Textural evidence for recrystallization of sulfide associated with remobilization of S during metamorphism arises from late position of pyrite in an eclogite sample from New Caledonia (Evans et al., 2014). This implies sulfide destabilization and dissolution of S (and probably Se) into a fluid, which can ascend through the overlying subducting crust or sediments, where it may partly be reincorporated in secondary pyrites (Evans et al., 2014) and may in another part be transported to the overlying mantle wedge. This near-open system sulfur cycling within the slab, associated with breakdown and recrystallization of sulfides (Evans et al., 2014) due to progressive subduction has been termed “leaky loop” Evans et al. (2014). A similar process of Se mobilization and re-precipitation in secondary sulfides would then explain the rather impossible quantification of net Se mobility during subduction. The “leaky loop” hypothesis implies that at least some S, Se and other chalcophile elements are lost from the slab and probably enter the overlying mantle wedge. As for S, a part-retention of Se likely occurs. The breakdown, recrystallization and part preservation of hydrothermal sulfides remains controversial but still seem a valid explanation to reconcile all observations (e.g. Evans et al., 2014; Li et al., 2016).

Several studies showed that, S can be subducted to depths beyond the arc and be entrapped in eclogitic or peridotitic diamonds, as inferred from their variable S isotope composition that can only be explained by the S isotope budget of subducted, sulfide-bearing (metasedimentary) material (e.g. Aulbach et al., 2012; Farquhar et al., 2002; Thomassot et al., 2009). Se concentrations in eclogitic sulfide inclusions in diamonds (mostly pyrrhotite) have been found to vary between several tens to hundreds of µg g^{-1} with a pronounced peak at 50 µg g^{-1} (Bulanova et al., 1996). These concentrations overlap with those of hydrothermal sulfides (Rouxel et al., 2004; Rouxel et al., 2002), although the latter displaying rather more variable sulfide compositions (pyrite, marcasite, chalcopyrite, sphalerite, and bornite/covelite). In general, concentrations of hydrothermal sulfides are higher compared to sulfide inclusions in diamonds, which may indicate that subduction zone metamorphism, recrystallization and destabilization as well as decomposition of hydrothermal sulfides within the slab lead to considerable loss of chalcophile elements from the subducting lithologies. Thomassot et al. (2009) found that, sulfide inclusions in Jwaneng diamonds suggest formation at a specific point in a recrystallization sequence within a subducting slab in the upper mantle, therefore supporting recrystallization processes within the slab at given *P–T*. Altogether, this argues in favor of progressive breakdown of subducted hydrothermal sulfides and recrystallization along with mobilization of S and other chalcophile elements. We speculate that, continuous breakdown and recrystallization of low-T and isotopically light Se-bearing hydrothermal sulfides occurs during subduction of altered oceanic crust. Serpentinite-derived dehydration fluids may then readily scavenge such sulfide along with their isotopically light Se and superimpose or ultimately overprint eclogitic sections in the subduction channel. In extreme cases where abundant dehydration fluids are present, they may even cross the slab-mantle wedge interface. While retaining some recrystallized sulfide in the slab for deeper subduction, this process could at the same time contribute to element enrichment of the overlying mantle wedge and enrich the sources of arc lavas.

3.5.4 Implications for Se isotope recycling into sources of arc magmas

It has been recently suggested that subduction components may significantly contribute to the Se isotope composition of arc lavas (Kurzawa et al., 2019). In particular, Mariana fluid-dominated lavas were shown to be isotopically lighter in Se compared to back-arc lavas and the Mariana pre-subduction wedge. However, uncertainties regarding exact input signatures into the subduction zone, due to isotopically very variable Se compositions of sediments, considerably complicate any conclusive implication regarding the mechanism and extent of Se recycling during subduction. The fact that eclogites analyzed in this study have been shown to preserve their pre-subduction Se isotope composition to variable degrees is one significant new constraint. We can thus postulate that, sulfide-bearing hydrothermally altered basalt, which transforms to eclogite during subduction, resembles an important constituent among the inputs into subduction zones. The metapelite sample from the Raspas Complex yields a heavy Se isotope composition, which at first contradicts with isotopically light Se isotope compositions of deep-sea sediments from the literature (Rouxel et al., 2002). However, the metapelite from this study underwent the same H*P*/L*T* metamorphism and dehydration–recrystallization reactions than the eclogites. At the same time this sample shows lower Ce/Pb than all eclogites, almost within serpentinite values (Fig. 3.7c). Thus, the heavy Se isotope signature might just mirror very pronounced flushing by serpentinite-derived fluids that removed most of the isotopically light Se during breakdown of subducted low-T sulfides. In other words, this metapelite constitutes the complement to the isotopically light input signature of subducting sediments: a squeezed-out and hydrothermal Se-depleted but later rehydrated isotopic endmember. The same could then account for the two isotopically heaviest eclogites, whereas decreasing Se isotope values and increasing Ce/Pb gradually reveal the closest analogue to the pre-subducted hydrothermally altered oceanic crust.

Based on the observations on samples from the Raspas Complex, we suggest the following model to account for preferential light Se isotope compositions recently found in fluid-dominated Mariana lavas: Mid-ocean ridge basalts are affected by hydrothermal seafloor alteration and hydrothermal sulfide accumulation to variable extents but with an average light Se isotope composition. The same, although to smaller degrees with depths, may be the case for abyssal peridotites, which also are subject to serpentinization processes as the slab bends towards the subduction zone (Ranero et al., 2003).

Due to progressive subduction, pressure and temperature increase occurs, which leads to continuous breakdown of distinct phases including hydrothermal sulfides (Fig. 3.9). It is important to stress out, that the extent of breakdown, recrystallization and re-precipitation and/or loss of elements from hydrothermal sulfides has not yet been constrained. Serpentinite-derived fluids may migrate via channelized fluid flow or by pervasive fluid flow (e.g. Ague, 2011; John et al., 2012; John et al., 2004; Plümper et al., 2016; Scambelluri and Philippot, 2001; Zack and John, 2007) (Fig. 3.9), overall bearing the potential to affect the chemical and isotopic composition of other subducted lithologies. Indeed, zoisite veins associated with zoisite eclogites have been identified within the Raspas Complex, most likely resembling fluid pathways and reaction products of intense fluid–rock interaction. As hydrothermal sulfides break down, their light Se isotope budget may also be relocated, gradually leaving isotopically light Se-depleted and increasingly flushed eclogites behind until they almost resemble the signatures of serpentinites. Repeated Se remobilization during flushing and Se removal from the top of the slab produces a continuous array of isotopically light and fluid-poor vs isotopically heavier and fluid-enriched lithologies within the subduction channel. Liberated fluid-mobile and chalcophile elements may eventually be transported into the overlying mantle wedge and potentially fertilize the source region of arc lavas (Fig. 3.9).

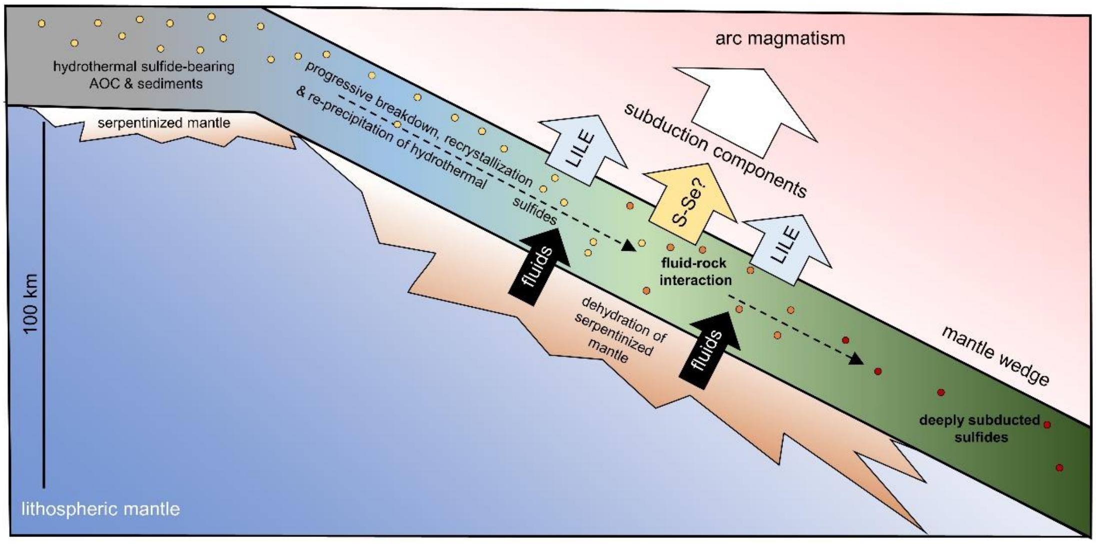

Figure 3.9 Schematic illustration of a subduction zone (not to scale), illustrating potential processes during prograde subduction of hydrothermally altered oceanic crust and underlying serpentinized mantle. Colored circles represent different sulfide minerals that are the result of progressive subduction zone metamorphism, element release and recrystallization. During subduction and changing *P–T* conditions, dehydration reactions (e.g. blueschist to eclogite transformation) take place which facilitate fluid release and liberation of incompatible elements (LILE) via fluid–rock interaction into aqueous fluids. In addition, prograde metamorphism might lead to destabilization and decomposition of hydrothermal sulfides thereby releasing siderophile and chalcophile elements that are re-distributed via fluids within slab lithologies or eventually are fluxed into the overlying mantle wedge, where they may fertilize the source region of arc magmas and induce melting. Sulfides that survive subduction zone metamorphism are transported into the deep mantle as evidenced by sulfide inclusions in diamonds.

This has already been postulated for several siderophile and chalcophile elements such as Cu, Fe, Pb, Mo, Sn, Zn, and Sb (e.g. De Hoog et al., 2001a; König et al., 2016; Noll Jr et al., 1996; Sillitoe, 1972; Stolper and Newman, 1994). Metasediments, which resemble the uppermost part of the subducted package, resemble the ultimate product of flushed slab top that has already lost most (if not all) of its former hydrothermal sulfides with its light Se isotope composition. Isotopically heavier Se may be brought into the sub-arc mantle at greater depths, where isotopically light Se-depleted sediments might be prone to melting. In the absence of slab-melting, Se among S and other chalcophile elements escapes subduction zone recycling by being transported beyond sub-arc depths as evidenced by sulfide inclusions in diamonds.

Interestingly, samples from the Mariana back-arc and arc plot in the Se isotope vs Ce/Pb plot between the mixing line of eclogites and serpentinized peridotites and the Mariana pre-subduction wedge (Fig. 3.10). This may be due to mixing and thus dilution of slab-derived fluid signatures with the mantle wedge that is proportionally higher in volume and isotopically close to zero compared to the fluid component. In other words, the light Se isotope signature of slab fluids is moderated by the chromatographic effect of the mantle wedge. In cases where sediment melts are present, which is the case for some Mariana arc lavas, the overall isotopic composition is even more moderated and some arc lavas may then not show a pronounced fluid-derived, isotopically light Se signature.

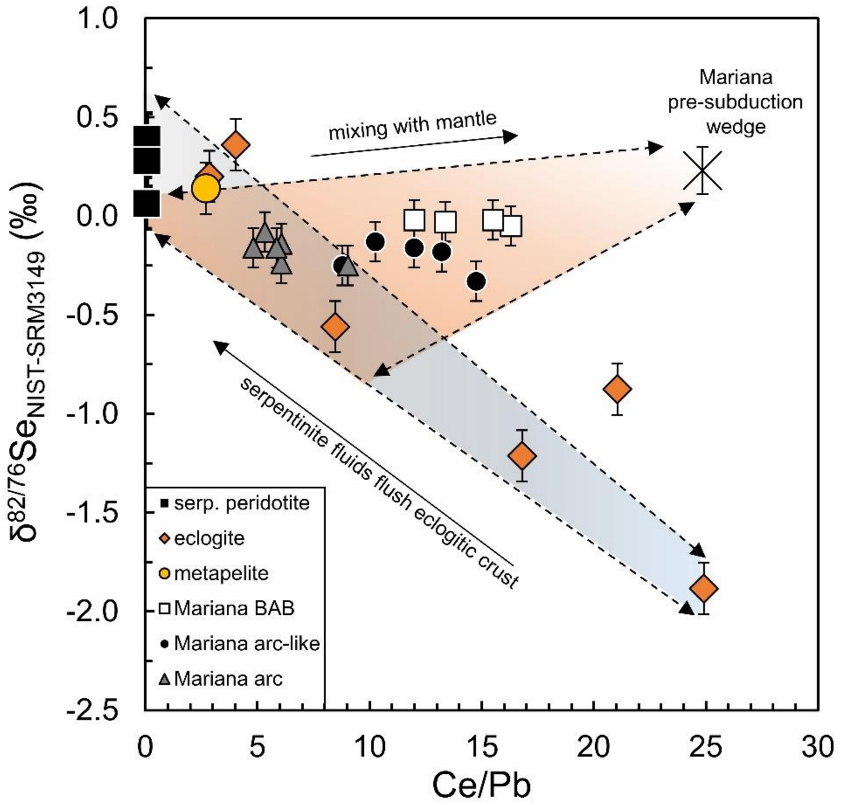

Figure 3.10 Se isotope vs Ce/Pb showing positions of lavas from various setting of the Mariana Island arc (back-arc, arc-like and arc) with variable proportions of subduction components. Se isotope compositions can be explained by mixing of isotopically light Se derived from eclogites whose precursors resemble variably hydrothermally altered basalts with the Mariana pre-subduction wedge. For details on the Mariana pre-subduction wedge, see Kurzawa et al. (2019). Se isotope compositions of Mariana lavas are moderated by the chromatographic effect of the proportionally higher in volume Mariana pre-subduction wedge. Note that, only Mariana arc lavas with relatively small proportions of melt-like subduction components (Th/Yb≤1) have been plotted, because the exact mechanisms involving potential Se transfer via melt-like subduction components is not yet properly constrained. Mariana pre-subduction wedge Ce/Pb from Gale et al. (2013). Data of Mariana lavas from Kurzawa et al. (2019). Uncertainty on Se isotope compositions same as in Fig. 3.5.

3.6 Conclusions

The first Se isotope investigation of prograde metamorphic rocks from the Raspas complex Ecuador allow significant constraints on the mechanisms of Se cycling in subduction zones. MORB-type eclogites partly preserve their very light Se isotope composition ($\delta^{82/76}$Se up to −1.89 ‰) of their precursor rocks that is represented by hydrothermally altered oceanic crust. Striking correlations of fluid-mobile element enrichments and progressively heavier Se isotope compositions are observed. Overall, eclogites with high Ce/Pb (and Ce/Rb, and Ce/Cs) that overlap that of typical MORB, show the lightest Se isotope compositions, whereas samples which experienced extensive fluid-mobile element enrichment (low Ce/Pb, Ce/Rb and Ce/Cs) are characterized by heavy Se isotope compositions that approach those of serpentinized peridotites and metapelites. We postulate that, dehydration of serpentinites and subducted oceanic crust leads to fluid release and scavenging of chalcophile elements from destabilizing hydrothermal sulfides within hydrothermally altered basalt that transforms to eclogite during prograde subduction metamorphism. Flushing of slab lithologies bears the potential to relocate and re-distribute dissolved chalcophile elements within the slab and further provides a reasonable mechanism for element transfer to the sub-arc mantle. This could, in principle, explain recently observed isotopically light Se isotope compositions of Mariana lavas (Kurzawa et al., 2019). As Se isotopes seem very powerful to assess the chalcophile element recycling in subduction zones, further studies should be directed towards investigating subduction metamorphism, sulfide breakdown and recrystallization in the slab and the link between the Se isotope budget of H*P*/L*T* rocks and arc lavas from various settings.

Outlook

The results presented in this dissertation provide evidence for the value of the Se isotope systematic to study subduction zone processes and place constraints on the recycling potential of chalcophile elements between the Earth's reservoirs, i.e. crust and mantle. Although C*hapters 2* and *Chapter* 3 resemble case studies conducted on specific subduction zones (Mariana and Andean subduction zones), a link between prograde subduction and recycling of isotopically variable Se via different subduction components has been identified. However, further studies are needed to attain a common understanding of involved processes and subduction zone recycling in general. In detail, investigation of even more fluid-dominated subduction zones lavas (Tonga subduction zone) may help to assess the sole role of fluids in the course of chalcophile element recycling. Further, the influence of sedimentary Se input (marine vs continental) on the Se isotope composition of the Earth`s mantle should be investigated, given the variable Se isotope composition of sediments linked to redox processes following oxidation of Earth`s atmosphere. The analytical method described in *Chapter* 1 now allows accurate Se isotope analysis of low ng-level Se-bearing geological materials as well as precise determination of the Se isotope composition of micrometric sulfide inclusions (König et al., 2019), with the potential to analyze even sulfide inclusions trapped in diamonds. This might help to further constrain the evolution of chalcophile and moderately volatile element systematics on Earth from the mineral and deep mantle perspective.

Appendix

Figures

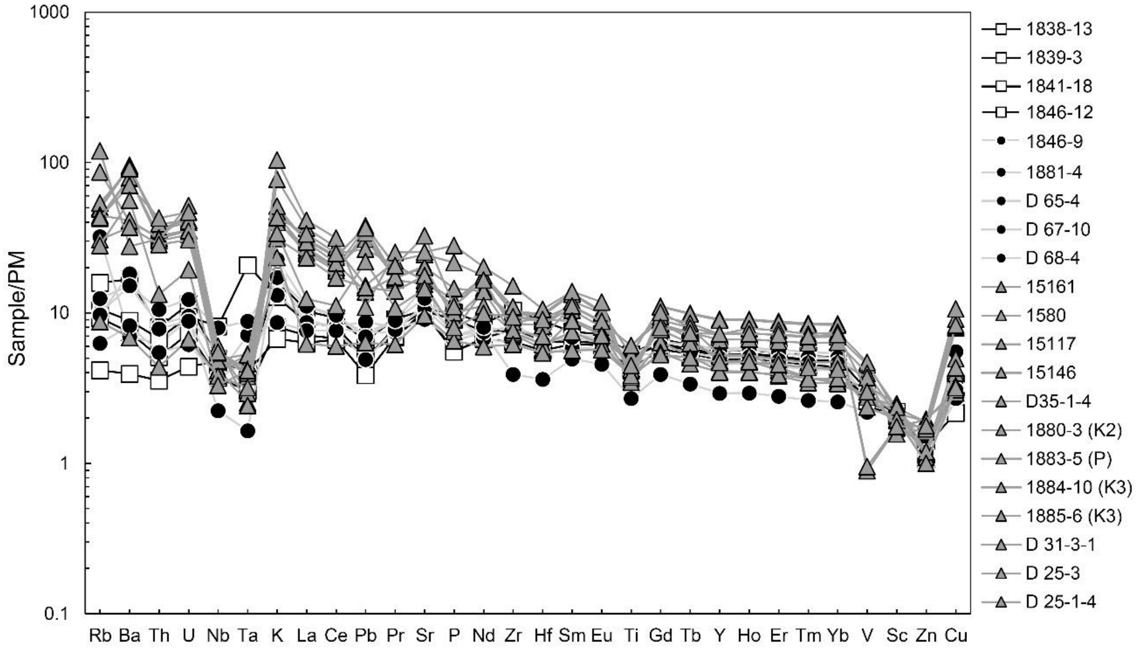

Figure A.1 Extended multi-element diagram for Mariana samples. Element order modified after Williams et al. (2018) and element concentrations normalized to primitive mantle estimates from Palme and O'Neill (2014 and references therein).

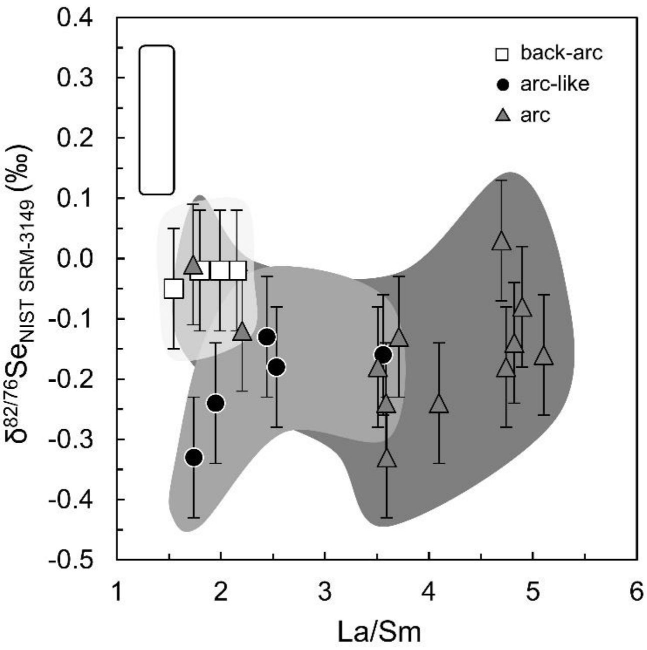

Figure A.2 Se isotope composition vs La/Sm ratio shows evidence for melt-like component in the Mariana arc samples similar to what is inferred from Figure 2.6c and d; Se isotope composition vs Th/Yb and Ba/Yb, respectively.

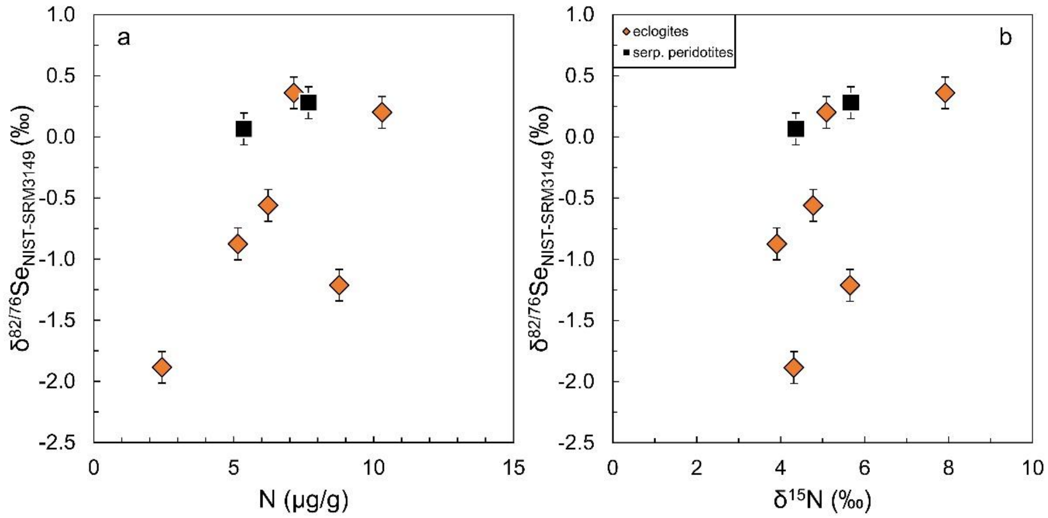

Figure A.3 Positive correlations between **a** Se isotopes and N concentrations and **b** N isotope compositions. Uncertainty on Se isotope compositions same as in Fig. 3.5.

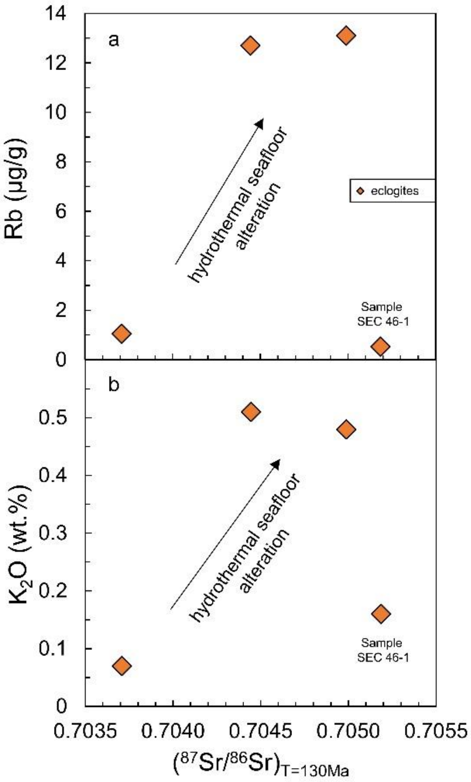

Figure A.4 $(^{87}Sr/^{86}Sr)_{T=130Ma}$ vs **a** Rb and **b** K_2O contents, illustrating the preservation of hydrothermal seafloor alteration systematics of the precursor rocks of the MORB-type eclogites.

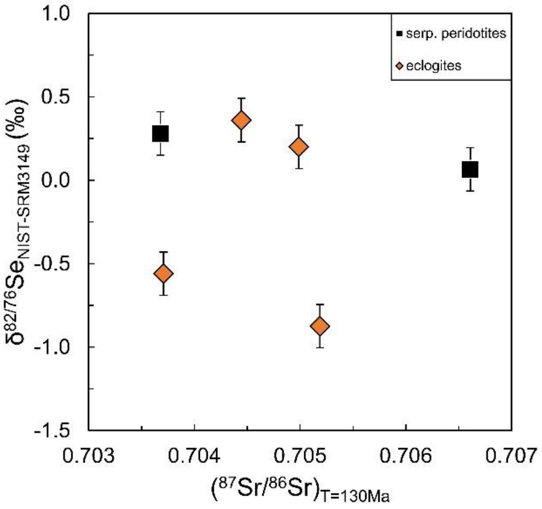

Figure A.5 (^{87}Sr/^{86}Sr)$_{T=130Ma}$ vs Se isotope composition of eclogites showing lacking correlation of Se isotope composition a classic proxy of seafloor alteration. Uncertainty on Se isotope compositions same as in Fig. 3.5.

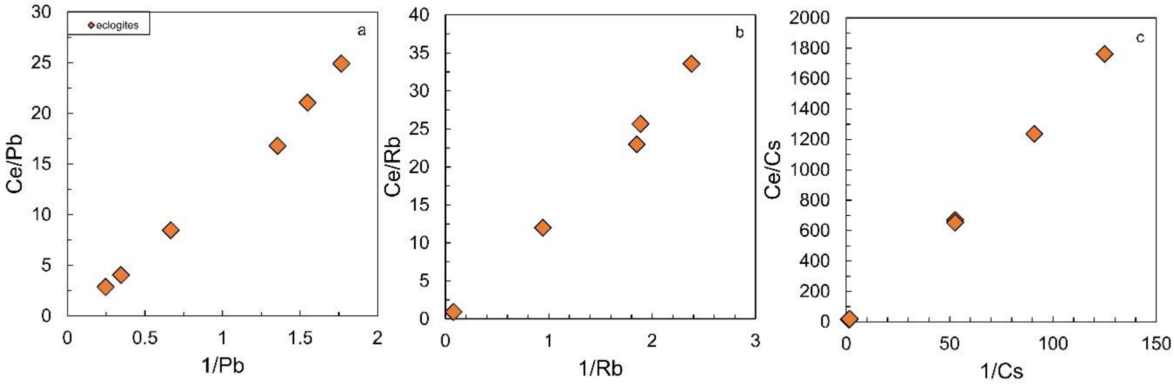

Figure A.6 (^{87}Sr/^{86}Sr)$_{T=130Ma}$ vs Se isotope composition of eclogites showing lacking correlation of Se isotope composition a classic proxy of seafloor alteration. Uncertainty on Se isotope compositions same as in Fig. 3.5.

Tables

Table 1.1
Overview of Se double spike compositions used by different working groups. Bold numbers indicate spike isotopes. Data acquisition at 1: Bristol Isotope Group, School of Earth Sciences, Bristol University, UK. 2: Institute of Geological Sciences, University of Bern, Switzerland. 3: Department of Geology, University of Illinois at Urbana-Champaign, Urbana. 4 (this study): Isotope Geochemistry, University of Tübingen, Germany.

Se masses	74	76	77	78	80	82
Pogge von Strandmann et al. (2014)[1] $^{74\text{-}78\text{-}77\text{-}82}$Se	**45.89%**	-	0.51%	**53.61%**	-	-
Pogge von Strandmann et al. (2014)[1] $^{78\text{-}82\text{-}76\text{-}77}$Se	-	0.14%	-	**15.61%**	-	**84.25%**
Vollstaedt et al. (2016a$^{)2}$ $^{74\text{-}77\text{-}78\text{-}82}$Se	**62.42%**	-	**37.56%**	0.02%	-	0.00%
Zhu et al. (2008)[3]; Schilling et al. (2011)[3]; Mitchell et al. (2012)[3]	**51.20%**	0.09%	**48.57%**	0.09%	0.03%	0.01%
This study[4] $^{74\text{-}77\text{-}78\text{-}82}$Se	**52.29%**	0.53%	**47.12%**	0.04%	0.02%	0.01%
Rudge et al. (2009) ideal composition for $^{74\text{-}77\text{-}78\text{-}82}$Se	**51.75%**		**48.25%**			

Table 1.2
Operating parameters

Parameters	
RF power (W)	1200
Acceleration voltage (V)	-10000
Sample cone	Ni Jet
Skimmer cone	Ni H-type
Ar gas flow rates (L min^{-1})	
Coolant	15
Auxiliary	0.7–1.0
Sample gas	0.24–0.56
Additional gas	0.48–0.56
Methane (mL min^{-1})	2.0–3.5
Analyte matrix	2 mol L^{-1} HCl
NaBH$_4$	0.4% (m/m)
Sample uptake (mL min^{-1})	0.235
conc. sample solution (ng mL^{-1})	≤15
sample solution volume (mL)	1
Cycle integration time (s)	4.194
Number of cycles per analysis	40
Intensity ^{82}Se (V)	0.5

Table 1.3

Measured masses and associated isobaric interferences.

Cups	L4	L3	L2			L1	C		H1	H2	H3	H4
Masses	**72**	**73**	**74**	**75**	**76**	**77**	**78**	**79**	**80**	**81**	**82**	**83**
Selenium			**^{74}Se**		**^{76}Se**	**^{77}Se**	**^{78}Se**		**^{80}Se**		**^{82}Se**	
Abundance (%)			**0.87**		**9.36**	**7.63**	**23.78**		**49.61**		**8.73**	
(i) Plasma induced												
Kr							**^{78}Kr**		**^{80}Kr**		**^{82}Kr**	^{83}Kr
ArAr	^{36}Ar^{36}Ar		**^{38}Ar^{36}Ar**		**^{40}Ar^{36}Ar** **^{38}Ar^{38}Ar**		**^{40}Ar^{38}Ar**		**^{40}Ar^{40}Ar**			
(ii) Plasma and analyte matrix induced												
ArArH		^{36}Ar^{36}ArH		^{38}Ar^{36}ArH		**^{40}Ar^{36}ArH** **^{38}Ar^{38}ArH**		^{40}Ar^{38}ArH		^{40}Ar^{40}ArH		
ArCl		^{38}Ar^{35}Cl ^{36}Ar^{37}Cl		^{40}Ar^{35}Cl ^{38}Ar^{37}Cl		**^{40}Ar^{37}Cl**						
(iii) Analyte and sample matrix induced												
FeO	^{56}Fe^{16}O		**^{58}Fe^{16}O**									
NiO			**^{58}Ni^{16}O**		**^{60}Ni^{16}O**		**^{62}Ni^{16}O**		**^{64}Ni^{16}O**			
ZnO									**^{64}Zn^{16}O**		**^{66}Zn^{16}O**	^{67}Zn^{16}O
Se-H				^{74}SeH		**^{76}SeH**	**^{77}SeH**			^{80}SeH		^{82}SeH
Ge	^{72}Ge	^{73}Ge	**^{74}Ge**		**^{76}Ge**							
Br-H									**^{79}BrH**		**^{81}BrH**	
As-H					**^{75}AsH**							

Table 1.4
Se isotope data for USGS reference materials SGR-1, SCo-1 and BCR-2.

Sample	**Sample type**	**Se (µg g^{-1})**	**δ$^{82/76}$Se (‰)**	**2 s.e (‰)**	**δ$^{82/78}$Se (‰)**	**2 s.e (‰)**
USGS SGR-1	Shale	3.70	0.09	0.04	0.06	0.03
		3.63	-0.08	0.05	-0.05	0.03
		3.49	-0.05	0.05	-0.03	0.03
		3.84	-0.18	0.08	-0.12	0.05
		3.95	-0.17	0.07	-0.11	0.05
		4.03	-0.17	0.07	-0.11	0.05
		3.82	0.04	0.06	0.03	0.04
		3.75	-0.13	0.08	-0.08	0.05
		3.66	-0.16	0.07	-0.10	0.05
	medium resolution	3.72	0.03	0.03	0.02	0.02
	AVERAGE	**3.76**	**-0.08**	**0.06**	**-0.05**	**0.04**
	2 s.d.	**0.32**	**0.20**	**0.03**	**0.13**	**0.02**
USGS SCo-1	Shale	0.88	-0.08	0.07	-0.06	0.04
		0.81	-0.34	0.05	-0.22	0.03
		0.85	-0.15	0.07	-0.10	0.04
		0.86	-0.25	0.08	-0.16	0.05
		0.83	-0.09	0.07	-0.06	0.05
	AVERAGE	**0.84**	**-0.18**	**0.07**	**-0.12**	**0.04**
	2 s.d.	**0.06**	**0.22**	**0.02**	**0.14**	**0.01**
USGS BCR-2	Basalt	0.075	0.19	0.06	0.12	0.04
		0.067	0.16	0.05	0.10	0.03
		0.072	0.19	0.06	0.12	0.04
	AVERAGE	**0.071**	**0.18**	**0.06**	**0.12**	**0.04**
	2 s.d.	**0.008**	**0.03**	**0.01**	**0.02**	**0.01**

Table 2.1 Combined Se isotope compositions and Se-Te concentrations of Mariana samples and international rock reference materials (United States Geological Survey, USGS; Geological Survey of Japan, GSJ).

sample	location	Rock type	SiO_2 wt.%	MgO wt.%	analyses n	$\delta^{82/76}Se$ (‰)	2 s.d.† (‰)	Se (ng/g)	1 s.d. (ng/g)	Te (ng/g)	1 s.d. (ng/g)	Se/Te	S^{π} (µg/g)
15161	arc, Fukujin	andesite	58.0	2.95	1	−0.24	0.10	102	3	1.57	0.05	65	50
1580	arc, Fukujin	andesite	59.7	2.00	1	−0.14	0.10	77	2	0.16	<0.01	481	40
15117	arc, Fukujin	andesite	60.6	1.98	1	−0.16	0.10	83	2	0.21	<0.01	393	50
15146	arc, Fukujin	andesite	56.7	2.86	1	−0.08	0.10	124	4	2.04	0.06	61	30
D35−1−4	arc, Fukujin	andesite	56.0	3.13	2	0.03	0.10	81	2	0.71	0.02	113	10
1880−3 (K2)*	arc, Kasuga	basalt	51.2	5.42	6	−0.18	0.10	119	4	4.21	0.13	28	150
1883−5 (P)	arc, Kasuga	bas. andesite	52.3	5.46	1	−0.01	0.10	87	3	6.40	0.19	14	120
1885−6 (K3)	arc, Kasuga	bas. andesite	54.6	5.80	2	−0.13	0.10	66	2	2.57	0.08	25	110
1884−10 (K3)	arc, Kasuga	basalt	50.3	7.39	2	−0.09	0.10	142	4	4.57	0.14	31	200
D31−3−1	arc, Eifuku	bas. andesite	52.7	3.49	1	−0.09	0.10	165	5	0.78	0.02	212	20
D25−3	arc, S.Daikoku	bas. andesite	54.2	3.89	1	−0.25	0.10	147	4	0.79	0.02	186	50
D25−1−4	arc, S.Daikoku	andesite	57.5	3.02	1	−0.16	0.10	134	4	1.58	0.05	85	60
1838−13	back−arc, 18°N	bas. andesite	52.7	5.68	2	−0.03	0.10	113	3	1.31	0.04	86	930
1839−3	back−arc, 18°N	basalt	48.5	7.68	1	−0.02	0.10	133	4	3.90	0.12	34	780
1841−18	back−arc, 18°N	basalt	50.5	7.84	1	−0.05	0.10	132	4	3.79	0.11	35	620
1846−12	back−arc, 18°N	basalt	50.8	7.00	2	−0.02	0.10	234	7	7.00	0.21	33	930
1846−9	arc−like, 18°N	basalt	49.7	6.95	1	−0.16	0.10	169	5	4.70	0.14	36	370
1881−4*	arc−like, 22°N	bas. andesite	53.0	6.05	3	−0.13	0.10	74	2	1.82	0.05	41	280
D65−4	arc−like, 22°N	bas. andesite	53.9	4.78	2	−0.25	0.10	138	4	1.07	0.03	129	200
D67−10	arc−like, 22°N	basalt	49.8	8.47	1	−0.33	0.10	182	5	3.03	0.09	60	930
D68−4	arc−like, 22°N	basalt	50.4	8.89	1	−0.18	0.10	125	4	1.55	0.05	81	490
USGS BHVO−2**		basalt			1	0.16	0.10	166	5	14.1	0.42	12	
GSJ JB−2		basalt			3	−0.19	0.10	153	5	3.78	0.11	40	
GSJ JB−3		basalt			2	0.16	0.10	67	2	1.03	0.03	65	

Se isotope data reported relative to Se reference solution NIST SRM-3149. *Samples 1881-4 and 1880-3 (K2) were used to assess external reproducibility, see table A.2.4 †Uncertainty on Se isotope compositions is conservatively set to be 0.10 ‰ as derived from multiple digested and analyzed samples during different measurement sessions. **BHVO-2 was analyzed together with Mariana samples and published by Yierpan et al. (2018) with long-term BHVO-2 reproducibility of 0.18±0.10‰ (2 s.d., n=8, multiple analytical sessions over 6 months). Uncertainty on Se-Te concentrations conservatively expressed as 3% relative standard deviation. $^{\pi}$S concentrations from Alt et al. (1993). For reference concentration data of GSJ JB-2 and JB-3 see Tab. A.2.5.and A.2.6. For individual Se isotope data see Tab. A.2.8.

Table 3.1 Major and trace element data of eclogites, serpentinized peridotites and the metapelite sample from the Raspas Complex, SW Ecuador.

Sample	SEC 43-3	SEC 44-1	SEC 46-1	SEC 46-2	SEC 47-1	SEC 50-1
Rock type	Eclogite	Eclogite	Eclogite	Eclogite	Eclogite	Eclogite
Major elements (wt.%)						
SiO_2	50.17	48.67	44.08	44.88	47.49	49.57
TiO_2	1.86	1.91	1.87	2.00	1.94	1.88
Al_2O_3	11.97	12.37	13.93	12.39	12.48	11.97
Fe_2O_3	13.3	13.75	15.48	13.77	13.87	13.30
MnO	0.23	0.19	0.24	0.21	0.23	0.19
MgO	6.65	6.00	10.09	8.72	6.01	6.72
CaO	10.67	10.84	10.87	13.41	11.15	10.48
Na_2O	3.02	3.02	1.69	2.30	2.77	3.04
K_2O	0.07	0.48	0.16	0.11	0.51	0.07
P_2O_5	0.17	0.16	0.11	0.74	0.17	0.17
LOI	0.42	0	0.45	0	0.37	0.81
Total	100.45	99.86	99.75	99.63	99.58	99.85
Trace elements (µg/g)						
Li	13.8	51.4	11.0	13.3	67.3	20.3
Sc	42.6	43.2	44.8	48	42.9	39.6
V	390	389	362	431	358	329
Cr	111	211	253	252	256	144
Co	40.1	45.0	51.9	37.9	45.4	38.4
Ni	53.0	75.9	71.2	59.1	74.2	47.0
Cu	35.3	52.8	79.0	137	69.3	32.9
Zn	106	218	280	277	143	57.4
Ga	18.2	18.4	13.1	10.9	19.0	16.3
Rb	1.06	13.1	0.530	0.420	12.7	0.54
Sr	77.0	66.8	31.6	36.8	103	84.9
Y	46.1	45.1	49.1	46.4	48	50.5
Zr	109	110	102	104	109	119
Nb	2.40	2.03	2.19	4.26	2.09	1.91
Mo			0.130	0.070	0.140	0.130
Sn	0.966	0.743			1.18	
Sb	0.150	0.210	0.200	0.100	0.480	1.20
Cs	0.019	0.777	0.011	0.008	0.632	0.019
Ba	21.2	79.4	6.76	21.1	60.9	121
La	3.75	3.70	4.08	4.40	3.71	3.72
Ce	12.7	11.6	13.6	14.1	11.7	12.4
Pr	2.28	2.17	2.53	2.46	2.18	2.32
Nd	12.6	11.9	13.9	12.9	12.4	12.7
Sm	4.38	4.23	5.11	4.28	4.54	4.62
Eu	1.57	1.57	1.71	1.51	1.57	1.59
Gd	5.90	5.70	6.74	5.60	6.12	6.34
Tb	1.08	1.07	1.18	1.00	1.17	1.17
Dy	7.33	7.35	7.89	6.96	7.92	8.01
Ho	1.58	1.56	1.66	1.55	1.69	1.71
Er	4.59	4.48	4.74	4.52	4.83	4.89
Tm	0.688	0.668	0.713	0.679	0.712	0.727
Yb	4.60	4.49	4.83	4.54	4.80	4.89
Lu	0.674	0.654	0.723	0.678	0.709	0.73
Hf	2.85	2.89	2.86	2.91	3.13	3.25
Ta	0.141	0.129	0.140	0.183	0.146	0.142
W	0.170	0.450			0.300	
Pb	1.50	4.06	0.646	0.566	2.90	0.738
Th	0.208	0.146	0.131	0.170	0.138	0.137
U	0.069	0.184	0.175	0.540	0.194	0.054
Nb/Zr	0.02	0.02	0.02	0.04	0.02	0.02
Hf/Yb	0.62	0.64	0.59	0.64	0.65	0.66
$(La/Sm)_N$*	0.54	0.55	0.50	0.65	0.51	0.51
Ce/Pb	8.47	2.86	21.1	24.9	4.03	16.8
Ce/Rb	12.0	0.9	25.7	33.6	0.9	23.0
Ce/Cs	668	14.9	1236	1763	18.5	653
Ce/Li	0.920	0.226	1.24	1.06	0.174	0.611

Table 3.1 continued

Sample Rock type	SEC 35-2 serp. peridotite	SEC 36-2 serp. peridotite	SEC 40-1 serp. peridotite	SEC 45-3 metapelite
Major elements (wt.%)				
SiO_2	40.49	40.24	41.54	
TiO_2	0.05	0.04	0.03	
Al_2O_3	2.37	1.34	1.69	
Fe_2O_3	8.02	8.23	8.64	
MnO	0.12	0.12	0.13	
MgO	37.26	40.43	40.75	
CaO	2.48	0.28	1.85	
Na_2O	0.07	0.00	0.25	
K_2O	0.01	0.00	0.01	
P_2O_5	0.01	0.01	0.00	
LOI	10.01	10.06	5.67	
Total	100.89	100.75	100.56	
Trace elements (µg/g)				
Li	0.99	1.03	2.76	
Sc	16.8	10.5	11.2	
V	73.6	37.1	51.1	
Cr	2674	2775	2344	
Co	104	100	102	
Ni	1957	2116	2125	
Cu	4.82	2.47	20.3	
Zn	50.3	43.0	42.3	
Ga	2.10	1.56	1.72	
Rb	0.215	0.071	0.200	*63.1*
Sr	3.53	1.51	1.63	
Y	1.58	0.504	0.919	
Zr	9.49	0.294	0.049	
Nb	0.008	0.036	0.034	
Mo	0.190	0.060	0.070	
Sn	0.124	0.084	0.107	
Sb	0.140	3.09	0.030	
Cs	0.157	0.020	0.218	*3.15*
Ba	4.87	3.17	1.32	
La	0.004	0.016	0.006	
Ce	0.014	0.015	0.013	*35.7*
Pr	0.006	0.006	0.003	
Nd	0.069	0.040	0.020	
Sm	0.067	0.019	0.024	
Eu	0.032	0.008	0.011	
Gd	0.147	0.037	0.061	
Tb	0.034	0.008	0.016	
Dy	0.266	0.061	0.134	
Ho	0.062	0.017	0.035	
Er	0.186	0.055	0.110	
Tm	0.030	0.011	0.019	
Yb	0.204	0.081	0.138	
Lu	0.031	0.015	0.022	
Hf	0.238	0.015	0.011	
Ta	0.000	0.002	0.002	
W	0.090	0.060	0.140	
Pb	0.280	0.223	0.179	*14.5*
Th	0.001	0.001	0.001	
U	0.003	0.003	0.001	
Nb/Zr	0.001	0.123	0.685	
Hf/Yb	1.17	0.19	0.08	
$(La/Sm)_N$*	0.04	0.53	0.16	
Ce/Pb	0.050	0.067	0.073	2.68
Ce/Rb	0.065	0.211	0.065	0.783
Ce/Cs	0.089	0.750	0.060	18.1
Ce/Li	0.014	0.015	0.005	

Italic numbers refer to average concentrations and element ratios of metasediments from the Franciscan Complex and the Western Baja Terrane; data from Sadofsky and Bebout (2003); see Tab. A.3.6. *Normalization after Boynton (1984).

Table 3.2 Se isotope composition and Se–Te abundances of eclogites, serpentinized peridotites and the metapelite sample from the Raspas Complex, SW Ecuador.

sample	rock type	$\delta^{82/76}Se_{NIST\ SRM\text{-}3149}$ (‰)	2 s.d. † (‰)	analyses (n)*	Se (ng g^{-1})	Te (ng g^{-1})	analyses (n)#
SEC 43-3	eclogite	*−0.53*	0.13	4	106	2.15	1
SEC 44-1	eclogite	0.20	0.13	1	36	8.55	1
SEC 46-1	eclogite	−0.88	0.13	2	6.40	5.54	1
SEC 46-2	eclogite	−1.89	0.13	2	104	6.33	1
SEC 47-1	eclogite	0.35	0.08	4	144	6.30	2
SEC 50-1	eclogite	−1.21	0.12	4	85	2.63	1
SEC 35-2	serp. peridotite	0.07	0.13	2	46	7.46	1
SEC 36-2	serp. peridotite	0.39	0.13	1	37	5.62	1
SEC 40-1	serp. peridotite	0.30	0.13	2	68	9.15	1
SEC 45-3	metapelite	0.14	0.13	1	22	4.03	1

†For samples with n<4, external reproducibility conservatively is estimated to be 0.13 ‰, as derived from multiple digested and analyzed sample SEC 43-3 during different measurement sessions. *Total number of Se isotope and Se concentration determinations. #Total of individual digestions for combined Se–Te concentration and Se isotope analyses. Uncertainty on Se–Te concentrations conservatively expressed as 3% relative standard deviation. For individual measurement data see Tab. A.3.5.

Table A.1.1
NIST SRM-3149 and various amounts of Se double spike. Well- vs less-well equilibrated standard spike mixtures.

Sample	**Sample type**	**f_{Spike}**	**$\delta^{82/76}$Se (‰)**	**$\delta^{82/78}$Se (‰)**
NIST SRM-3149	reference solution	0.1	**-0.10**	**-0.06**
NIST SRM-3149		0.2	**0.06**	**0.04**
NIST SRM-3149		0.3	**-0.07**	**-0.05**
NIST SRM-3149		0.4	**-0.02**	**-0.01**
NIST SRM-3149		0.5	**-0.01**	**0.00**
NIST SRM-3149		0.6	**-0.09**	**-0.06**
NIST SRM-3149		0.7	**-0.08**	**-0.06**
NIST SRM-3149		0.8	**0.00**	**0.00**
NIST SRM-3149		0.9	**-0.20**	**-0.13**

well equilibrated standard-spike mixtures

Sample	**Sample type**	**f_{Spike}**	**$\delta^{82/76}$Se (‰)**	**$\delta^{82/78}$Se (‰)**
NIST SRM-3149	reference solution	0.1	**0.20**	**0.13**
NIST SRM-3149		0.2	**0.16**	**0.11**
NIST SRM-3149		0.3	**0.17**	**0.11**
NIST SRM-3149		0.4	**0.23**	**0.15**
NIST SRM-3149		0.5	**0.11**	**0.07**
NIST SRM-3149		0.6	**0.14**	**0.09**
NIST SRM-3149		0.7	**0.23**	**0.15**
NIST SRM-3149		0.8	**0.22**	**0.14**
NIST SRM-3149		0.9	**0.59**	**0.39**

less-well equilibrated standard-spike mixtures

Table A.1.2
Results for evaporation experiments involving Se reference solution NIST SRM-3149. SSB: Standard-sample bracketing approach; DS: Double spike approach.

Sample	**Sample type**	**method**	**$\delta^{82/78}$Se (‰)**	**$\delta^{82/76}$Se (‰)**	**loss in %**
NIST SRM-3149	Se reference solution	SSB	**0.28**	**0.43**	5
NIST SRM-3149		SSB	**0.67**	**1.03**	10
NIST SRM-3149		SSB	**0.86**	**1.32**	14
NIST SRM-3149		SSB	**1.20**	**1.85**	31
NIST SRM-3149		DS	**1.74**	**2.68**	51
NIST SRM-3149		DS	**1.43**	**2.20**	37
NIST SRM-3149		DS	**1.48**	**2.28**	51
NIST SRM-3149		DS	**2.09**	**3.22**	33
NIST SRM-3149		DS	**2.05**	**3.15**	23

Table A.1.3

NIST SRM-3149 + various amounts of Ge. Results before and after Ge-correction.

Sample	**Sample type**	**Ge/Se**	**$\delta^{82/76}$Se (‰)**	**$\delta^{82/78}$Se (‰)**	**2 s.e.**	**$\delta^{82/76}$Se (‰)$_{\text{uncorrected}}$**
NIST SRM-3149	Se reference solution	**0.0007**	**0.01**	**0.00**	0.02	**0.24**
NIST SRM-3149		**0.0012**	**-0.01**	**-0.01**	0.02	**0.45**
NIST SRM-3149		**0.0019**	**0.00**	**0.00**	0.02	**0.65**
NIST SRM-3149		**0.0037**	**0.00**	**0.00**	0.02	**1.23**
NIST SRM-3149		**0.0067**	**-0.05**	**-0.03**	0.03	**1.32**
NIST SRM-3149		**0.0133**	**-0.04**	**-0.03**	0.03	**2.57**
NIST SRM-3149		**0.0333**	**-0.02**	**-0.01**	0.04	**6.85**
NIST SRM-3149		**0.0667**	**0.06**	**0.04**	0.04	**13**
NIST SRM-3149		**0.3333**	**0.02**	**0.02**	0.04	**70**
NIST SRM-3149		**1**	**-0.05**	**-0.03**	0.05	**149**
NIST SRM-3149		**1**	**0.03**	**0.02**	0.05	**221**
NIST SRM-3149		**2**	**0.03**	**0.02**	0.05	**464**
NIST SRM-3149		**3**	**0.00**	**0.00**	0.06	**723**
NIST SRM-3149		**4**	**-0.03**	**-0.02**	0.06	**1006**
		AVERAGE	0.00	0.00		
		2 s.d.	0.06	0.04		

Table A.1.4
Long-term reproducibility of in-house Se reference solution MH-495.

Sample	Sample type	Se (µg g^{-1})	$\delta^{82/76}$Se (‰)	$\delta^{82/78}$Se (‰)
MH-495	in-house Se solution	2.08	**-3.29**	**-2.14**
MH-495		2.08	**-3.26**	**-2.11**
MH-495		2.08	**-3.25**	**-2.11**
MH-495		2.08	**-3.25**	**-2.11**
MH-495		2.08	**-3.14**	**-2.04**
MH-495		2.08	**-3.21**	**-2.08**
MH-495		2.08	**-3.21**	**-2.09**
MH-495		2.08	**-3.29**	**-2.14**
MH-495		2.08	**-3.19**	**-2.07**
MH-495		2.08	**-3.15**	**-2.05**
MH-495		2.08	**-3.31**	**-2.15**
MH-495		2.08	**-3.31**	**-2.15**
MH-495		2.08	**-3.24**	**-2.10**
MH-495		2.08	**-3.29**	**-2.13**
MH-495		2.08	**-3.33**	**-2.17**
MH-495		2.08	**-3.20**	**-2.08**
MH-495		2.08	**-3.20**	**-2.08**
MH-495		2.08	**-3.26**	**-2.12**
MH-495		2.08	**-3.37**	**-2.19**
MH-495		2.08	**-3.31**	**-2.15**
MH-495		2.08	**-3.31**	**-2.15**
MH-495		2.08	**-3.27**	**-2.12**
MH-495		2.08	**-3.14**	**-2.04**
MH-495		2.08	**-3.20**	**-2.08**
MH-495		2.08	**-3.37**	**-2.19**
MH-495		2.08	**-3.38**	**-2.20**
MH-495		2.08	**-3.26**	**-2.11**
MH-495		2.08	**-3.24**	**-2.10**
MH-495		2.08	**-3.21**	**-2.09**
MH-495		2.08	**-3.17**	**-2.06**
MH-495		2.08	**-3.33**	**-2.16**
MH-495		2.08	**-3.35**	**-2.17**
MH-495		2.08	**-3.32**	**-2.15**
MH-495		2.08	**-3.33**	**-2.16**
MH-495		2.08	**-3.15**	**-2.05**
MH-495		2.08	**-3.15**	**-2.05**
MH-495		2.08	**-3.30**	**-2.14**
MH-495		2.08	**-3.29**	**-2.14**
MH-495		2.08	**-3.34**	**-2.17**
MH-495		2.08	**-3.28**	**-2.13**
MH-495		2.08	**-3.22**	**-2.09**
MH-495		2.08	**-3.26**	**-2.12**
MH-495		2.08	**-3.27**	**-2.13**
MH-495		2.08	**-3.30**	**-2.14**
MH-495		2.08	**-3.30**	**-2.14**
MH-495		2.08	**-3.29**	**-2.13**
MH-495		2.08	**-3.31**	**-2.15**
MH-495		2.08	**-3.38**	**-2.19**
MH-495		2.08	**-3.34**	**-2.17**
MH-495		2.08	**-3.34**	**-2.17**
MH-495		2.08	**-3.26**	**-2.12**
MH-495		2.08	**-3.23**	**-2.10**
MH-495		2.08	**-3.32**	**-2.15**
MH-495		2.08	**-3.25**	**-2.11**
MH-495		2.08	**-3.25**	**-2.11**
MH-495		2.08	**-3.22**	**-2.09**
MH-495		2.08	**-3.37**	**-2.19**
MH-495		2.08	**-3.26**	**-2.12**
MH-495		2.08	**-3.23**	**-2.10**
MH-495		2.08	**-3.20**	**-2.08**
MH-495		2.08	**-3.27**	**-2.12**
MH-495		2.08	**-3.18**	**-2.07**

Table A.1.4 continued

Sample	Sample type	Se (μg g^{-1})	$\delta^{82/76}$Se (‰)	$\delta^{82/78}$Se (‰)
MH-495		2.08	**-3.32**	**-2.16**
MH-495		2.08	**-3.28**	**-2.13**
MH-495		2.08	**-3.18**	**-2.06**
MH-495		2.08	**-3.26**	**-2.11**
MH-495		0.35	**-3.19**	**-2.07**
MH-495		2.08	**-3.30**	**-2.14**
MH-495		2.08	**-3.32**	**-2.16**
MH-495		2.10	**-3.17**	**-2.06**
MH-495		2.08	**-3.28**	**-2.13**
MH-495		2.08	**-3.26**	**-2.12**
MH-495		2.08	**-3.19**	**-2.07**
MH-495		2.09	**-3.26**	**-2.12**
MH-495		2.09	**-3.31**	**-2.15**
MH-495		2.09	**-3.28**	**-2.13**
MH-495		2.09	**-3.28**	**-2.13**
MH-495		2.09	**-3.26**	**-2.12**
MH-495		2.08	**-3.29**	**-2.13**
MH-495		2.09	**-3.24**	**-2.11**
MH-495		2.09	**-3.29**	**-2.14**
MH-495		2.09	**-3.23**	**-2.10**
MH-495		2.08	**-3.25**	**-2.11**
MH-495		2.09	**-3.24**	**-2.11**
MH-495		2.08	**-3.22**	**-2.09**
MH-495		2.09	**-3.38**	**-2.19**
MH-495		2.09	**-3.36**	**-2.18**
MH-495		2.08	**-3.46**	**-2.25**
MH-495		2.08	**-3.20**	**-2.08**
MH-495		2.09	**-3.16**	**-2.05**
MH-495		2.07	**-3.36**	**-2.18**
MH-495		2.07	**-3.29**	**-2.14**
MH-495		2.07	**-3.28**	**-2.13**
MH-495		2.07	**-3.37**	**-2.19**
MH-495		2.07	**-3.32**	**-2.16**
MH-495		2.07	**-3.35**	**-2.17**
MH-495		2.07	**-3.26**	**-2.12**
MH-495		2.07	**-3.30**	**-2.15**
MH-495		2.07	**-3.33**	**-2.16**
MH-495		2.07	**-3.39**	**-2.20**
MH-495		2.07	**-3.29**	**-2.14**
		AVERAGE	-3.27	-2.12
		2 s.d.	0.13	0.08

Sample	Sample type	Se (μg g^{-1})	$\delta^{82/76}$Se (‰)	$\delta^{82/78}$Se (‰)
MH-495	MR	2.03	-3.25	-2.11
MH-495		2.03	-3.27	-2.13
MH-495		2.03	-3.25	-2.11
MH-495		2.03	-3.27	-2.13
MH-495		2.03	-3.23	-2.10
MH-495		2.03	-3.23	-2.10
MH-495		2.03	-3.23	-2.10
MH-495		2.03	-3.23	-2.10
MH-495		2.03	-3.24	-2.10
MH-495		2.03	-3.26	-2.12
		AVERAGE	-3.25	-2.11
		2 s.d.	0.03	0.02

Table A.1.5
Long-term reproducibility of Se reference solution NIST SRM-3149.

Sample	**Sample type**	**Se (µg g^{-1})**	**$\delta^{82/76}$Se (‰)**	**$\delta^{82/78}$Se (‰)**
NIST SRM-3149	Se reference solution	2.196	**-0.08**	**-0.05**
NIST SRM-3149		2.196	**0.04**	**0.02**
NIST SRM-3149		2.195	**0.00**	**0.00**
NIST SRM-3149		2.195	**-0.01**	**-0.01**
NIST SRM-3149		2.194	**-0.01**	**-0.01**
NIST SRM-3149		2.194	**-0.01**	**0.00**
NIST SRM-3149		2.194	**-0.01**	**-0.01**
NIST SRM-3149		2.194	**0.00**	**0.00**
NIST SRM-3149		2.194	**0.03**	**0.02**
NIST SRM-3149		2.194	**-0.03**	**-0.02**
NIST SRM-3149		2.195	**-0.03**	**-0.02**
NIST SRM-3149		2.195	**0.00**	**0.00**
NIST SRM-3149		2.195	**0.08**	**0.05**
NIST SRM-3149		2.196	**0.01**	**0.01**
NIST SRM-3149		2.196	**0.02**	**0.01**
NIST SRM-3149		2.196	**-0.05**	**-0.03**
NIST SRM-3149		2.196	**-0.05**	**-0.03**
NIST SRM-3149		2.196	**0.06**	**0.04**
NIST SRM-3149		2.196	**0.00**	**0.00**
NIST SRM-3149		2.197	**-0.01**	**0.00**
NIST SRM-3149		2.197	**0.08**	**0.05**
NIST SRM-3149		2.196	**0.10**	**0.07**
NIST SRM-3149		2.196	**-0.09**	**-0.06**
NIST SRM-3149		2.196	**0.00**	**0.00**
NIST SRM-3149		2.196	**-0.01**	**-0.01**
NIST SRM-3149		2.196	**0.00**	**0.00**
NIST SRM-3149		2.196	**0.01**	**0.01**
NIST SRM-3149		2.196	**-0.06**	**-0.04**
NIST SRM-3149		2.194	**0.00**	**0.00**
NIST SRM-3149		2.195	**0.00**	**0.00**
NIST SRM-3149		2.198	**0.00**	**0.00**
NIST SRM-3149		2.198	**-0.01**	**0.00**
NIST SRM-3149		2.198	**-0.05**	**-0.03**
NIST SRM-3149		2.198	**0.00**	**0.00**
NIST SRM-3149		2.198	**-0.04**	**-0.03**
NIST SRM-3149		2.198	**-0.03**	**-0.02**
NIST SRM-3149		2.198	**0.00**	**0.00**
NIST SRM-3149		2.198	**-0.09**	**-0.06**
NIST SRM-3149		2.195	**0.11**	**0.07**
NIST SRM-3149		2.198	**0.01**	**0.01**
NIST SRM-3149		2.198	**0.04**	**0.03**
NIST SRM-3149		2.198	**0.03**	**0.02**
NIST SRM-3149		2.200	**-0.02**	**-0.01**
NIST SRM-3149		2.198	**-0.02**	**-0.01**
NIST SRM-3149		2.198	**0.06**	**0.04**
NIST SRM-3149		2.198	**-0.06**	**-0.04**
NIST SRM-3149		2.198	**-0.12**	**-0.08**
NIST SRM-3149		2.198	**-0.03**	**-0.02**
NIST SRM-3149		2.197	**-0.09**	**-0.06**
NIST SRM-3149		2.197	**-0.02**	**-0.01**
NIST SRM-3149		2.197	**-0.02**	**-0.02**
NIST SRM-3149		2.198	**-0.05**	**-0.03**
NIST SRM-3149		2.198	**0.11**	**0.07**
NIST SRM-3149		2.198	**-0.06**	**-0.04**
NIST SRM-3149		2.198	**0.05**	**0.03**
NIST SRM-3149		2.198	**0.01**	**0.01**
NIST SRM-3149		2.198	**0.06**	**0.04**
NIST SRM-3149		2.197	**0.04**	**0.03**
NIST SRM-3149		2.198	**0.16**	**0.11**
NIST SRM-3149		2.198	**-0.12**	**-0.08**
NIST SRM-3149		2.198	**-0.07**	**-0.05**
NIST SRM-3149		2.198	**-0.03**	**-0.02**

Table A.1.5 continued

Sample	Sample type	Se (μg g^{-1})	$\delta^{82/76}$Se (‰)	$\delta^{82/78}$Se (‰)
NIST SRM-3149		2.197	**-0.03**	**-0.02**
NIST SRM-3149		2.198	**-0.07**	**-0.04**
NIST SRM-3149		2.198	**-0.07**	**-0.04**
NIST SRM-3149		2.198	**0.00**	**0.00**
NIST SRM-3149		2.198	**0.04**	**0.03**
NIST SRM-3149		2.198	**-0.04**	**-0.03**
NIST SRM-3149		2.198	**0.00**	**0.00**
NIST SRM-3149		2.198	**0.10**	**0.07**
NIST SRM-3149		2.198	**0.08**	**0.05**
NIST SRM-3149		2.198	**0.10**	**0.07**
NIST SRM-3149		2.198	**0.06**	**0.04**
NIST SRM-3149		2.198	**0.04**	**0.03**
NIST SRM-3149		2.196	**-0.13**	**-0.09**
NIST SRM-3149		2.196	**-0.10**	**-0.07**
NIST SRM-3149		2.196	**-0.08**	**-0.05**
NIST SRM-3149		2.195	**-0.04**	**-0.03**
NIST SRM-3149		2.197	**-0.05**	**-0.03**
NIST SRM-3149		2.194	**-0.05**	**-0.03**
NIST SRM-3149		2.194	**-0.13**	**-0.08**
NIST SRM-3149		2.195	**-0.05**	**-0.03**
NIST SRM-3149		2.196	**0.05**	**0.03**
NIST SRM-3149		2.196	**0.08**	**0.05**
NIST SRM-3149		2.195	**0.05**	**0.03**
NIST SRM-3149		2.195	**-0.09**	**-0.06**
NIST SRM-3149		2.213	**0.29**	**0.19**
NIST SRM-3149		2.190	**0.16**	**0.10**
NIST SRM-3149		2.193	**0.08**	**0.05**
NIST SRM-3149		2.195	**-0.02**	**-0.02**
NIST SRM-3149		2.196	**-0.02**	**-0.01**
NIST SRM-3149		2.196	**0.06**	**0.04**
NIST SRM-3149		2.196	**0.02**	**0.01**
NIST SRM-3149		2.196	**-0.03**	**-0.02**
NIST SRM-3149		2.196	**0.01**	**0.01**
NIST SRM-3149		2.196	**-0.05**	**-0.03**
NIST SRM-3149		2.196	**-0.03**	**-0.02**
NIST SRM-3149		2.196	**-0.05**	**-0.03**
NIST SRM-3149		2.196	**-0.03**	**-0.02**
NIST SRM-3149		2.196	**0.02**	**0.02**
NIST SRM-3149		2.196	**0.04**	**0.03**
NIST SRM-3149		2.196	**0.01**	**0.01**
NIST SRM-3149		2.196	**0.11**	**0.07**
NIST SRM-3149		2.196	**-0.05**	**-0.03**
NIST SRM-3149		2.194	**0.00**	**0.00**
NIST SRM-3149		2.196	**-0.05**	**-0.04**
NIST SRM-3149		2.196	**0.01**	**0.01**
NIST SRM-3149		2.196	**0.03**	**0.02**
NIST SRM-3149		2.196	**-0.05**	**-0.04**
NIST SRM-3149		2.196	**0.01**	**0.01**
NIST SRM-3149		2.196	**0.03**	**0.02**
NIST SRM-3149		2.196	**0.02**	**0.01**
NIST SRM-3149		2.196	**-0.01**	**-0.01**
NIST SRM-3149		2.196	**-0.07**	**-0.04**
NIST SRM-3149		2.196	**0.00**	**0.00**
NIST SRM-3149		2.196	**0.02**	**0.01**
NIST SRM-3149		2.196	**0.01**	**0.00**
NIST SRM-3149		2.196	**-0.02**	**-0.01**
NIST SRM-3149		8.557	**0.03**	**0.02**
NIST SRM-3149		3.868	**-0.02**	**-0.01**
NIST SRM-3149		0.165	**-0.09**	**-0.06**
NIST SRM-3149		1.994	**0.01**	**0.01**
NIST SRM-3149		2.192	**0.07**	**0.05**
NIST SRM-3149		2.194	**0.05**	**0.03**

Table A.1.5 continued

Sample	Sample type	Se (µg g^{-1})	$\delta^{82/76}$Se (‰)	$\delta^{82/78}$Se (‰)
NIST SRM-3149		2.195	**-0.05**	**-0.03**
NIST SRM-3149		2.194	**-0.01**	**0.00**
NIST SRM-3149		2.195	**-0.03**	**-0.02**
NIST SRM-3149		2.195	**0.01**	**0.01**
NIST SRM-3149		2.195	**-0.05**	**-0.03**
NIST SRM-3149		2.195	**-0.01**	**0.00**
NIST SRM-3149		2.195	**-0.03**	**-0.02**
NIST SRM-3149		2.195	**0.01**	**0.01**
NIST SRM-3149		2.195	**-0.03**	**-0.02**
NIST SRM-3149		2.195	**-0.05**	**-0.03**
NIST SRM-3149		2.195	**0.04**	**0.03**
NIST SRM-3149		2.195	**-0.01**	**-0.01**
NIST SRM-3149		2.195	**0.05**	**0.03**
NIST SRM-3149		2.195	**-0.02**	**-0.02**
NIST SRM-3149		2.195	**0.11**	**0.07**
NIST SRM-3149		2.195	**-0.05**	**-0.03**
NIST SRM-3149		2.195	**0.03**	**0.02**
NIST SRM-3149		2.196	**0.08**	**0.05**
NIST SRM-3149		2.196	**-0.03**	**-0.02**
NIST SRM-3149		2.196	**-0.01**	**-0.01**
NIST SRM-3149		2.196	**-0.09**	**-0.06**
NIST SRM-3149		2.196	**0.00**	**0.00**
NIST SRM-3149		2.196	**-0.03**	**-0.02**
NIST SRM-3149		2.196	**0.04**	**0.02**
NIST SRM-3149		2.196	**-0.06**	**-0.04**
NIST SRM-3149		2.196	**0.01**	**0.01**
NIST SRM-3149		2.196	**-0.02**	**-0.01**
NIST SRM-3149		2.196	**-0.01**	**-0.01**
NIST SRM-3149		2.196	**0.00**	**0.00**
NIST SRM-3149		2.197	**-0.04**	**-0.02**
NIST SRM-3149		2.196	**-0.03**	**-0.02**
NIST SRM-3149		2.196	**-0.03**	**-0.02**
NIST SRM-3149		2.196	**0.06**	**0.04**
NIST SRM-3149		2.196	**0.00**	**0.00**
NIST SRM-3149		2.196	**-0.01**	**-0.01**
NIST SRM-3149		2.196	**0.02**	**0.01**
NIST SRM-3149		2.196	**0.05**	**0.03**
NIST SRM-3149		2.196	**0.03**	**0.02**
NIST SRM-3149		2.196	**-0.01**	**-0.01**
NIST SRM-3149		2.067	**0.05**	**0.03**
NIST SRM-3149		2.196	**0.02**	**0.01**
NIST SRM-3149		2.196	**0.03**	**0.02**
NIST SRM-3149		2.196	**0.03**	**0.02**
NIST SRM-3149		2.196	**0.03**	**0.02**
NIST SRM-3149		2.195	**0.02**	**0.01**
NIST SRM-3149		2.195	**0.08**	**0.05**
NIST SRM-3149		2.196	**0.03**	**0.02**
NIST SRM-3149		2.196	**0.02**	**0.01**
NIST SRM-3149		2.196	**-0.06**	**-0.04**
NIST SRM-3149		2.195	**-0.02**	**-0.01**
NIST SRM-3149		2.196	**0.00**	**0.00**
NIST SRM-3149		2.196	**-0.06**	**-0.04**
NIST SRM-3149		2.196	**-0.02**	**-0.01**
NIST SRM-3149		2.196	**0.08**	**0.05**
NIST SRM-3149		2.196	**-0.04**	**-0.02**
NIST SRM-3149		2.196	**0.01**	**0.01**
NIST SRM-3149		2.196	**0.00**	**0.00**
NIST SRM-3149		2.195	**-0.04**	**-0.03**
NIST SRM-3149		2.196	**-0.02**	**-0.01**
NIST SRM-3149		2.196	**-0.01**	**-0.01**
NIST SRM-3149		2.196	**-0.08**	**-0.05**
NIST SRM-3149		2.196	**-0.09**	**-0.06**

Table A.1.5 continued

Sample	Sample type	Se (µg g^{-1})	$\delta^{82/76}$Se (‰)	$\delta^{82/78}$Se (‰)
NIST SRM-3149		2.196	**0.00**	**0.00**
NIST SRM-3149		2.196	**0.00**	**0.00**
NIST SRM-3149		2.196	**-0.05**	**-0.03**
NIST SRM-3149		2.196	**-0.07**	**-0.05**
NIST SRM-3149		2.196	**0.00**	**0.00**
NIST SRM-3149		2.196	**-0.07**	**-0.05**
NIST SRM-3149		2.196	**0.01**	**0.01**
NIST SRM-3149		2.196	**0.02**	**0.01**
NIST SRM-3149		2.195	**-0.05**	**-0.03**
NIST SRM-3149		2.196	**0.01**	**0.00**
NIST SRM-3149		2.196	**0.04**	**0.03**
NIST SRM-3149		2.196	**0.03**	**0.02**
NIST SRM-3149		2.196	**0.09**	**0.06**
NIST SRM-3149		2.196	**0.02**	**0.01**
NIST SRM-3149		2.196	**0.08**	**0.05**
NIST SRM-3149		2.196	**0.00**	**0.00**
NIST SRM-3149		2.195	**0.08**	**0.05**
NIST SRM-3149		2.195	**0.06**	**0.04**
NIST SRM-3149		2.195	**0.01**	**0.00**
NIST SRM-3149		2.195	**0.04**	**0.03**
NIST SRM-3149		2.187	**0.04**	**0.03**
NIST SRM-3149		2.195	**0.04**	**0.02**
NIST SRM-3149		2.009	**0.02**	**0.02**
NIST SRM-3149		2.208	**-0.03**	**-0.02**
NIST SRM-3149		2.175	**0.07**	**0.05**
NIST SRM-3149		2.191	**-0.11**	**-0.07**
NIST SRM-3149		2.205	**0.00**	**0.00**
NIST SRM-3149		2.201	**-0.08**	**-0.05**
NIST SRM-3149		2.197	**-0.10**	**-0.06**
NIST SRM-3149		2.213	**0.06**	**0.04**
NIST SRM-3149		2.213	**0.06**	**0.04**
NIST SRM-3149		2.213	**0.06**	**0.04**
NIST SRM-3149		2.171	**-0.10**	**-0.06**
NIST SRM-3149		2.188	**-0.03**	**-0.02**
NIST SRM-3149		2.191	**0.03**	**0.02**
NIST SRM-3149		2.198	**-0.03**	**-0.02**
NIST SRM-3149		2.201	**0.01**	**0.01**
NIST SRM-3149		2.198	**-0.04**	**-0.03**
NIST SRM-3149		2.193	**-0.01**	**-0.01**
NIST SRM-3149		2.193	**0.07**	**0.04**
NIST SRM-3149		2.195	**-0.01**	**-0.01**
NIST SRM-3149		2.196	**0.03**	**0.02**
NIST SRM-3149		2.197	**0.00**	**0.00**
NIST SRM-3149		2.201	**0.00**	**0.00**
NIST SRM-3149		2.200	**-0.04**	**-0.03**
NIST SRM-3149		2.201	**0.03**	**0.02**
NIST SRM-3149		2.201	**0.06**	**0.04**
NIST SRM-3149		2.201	**-0.04**	**-0.03**
NIST SRM-3149		2.209	**-0.02**	**-0.01**
NIST SRM-3149		2.209	**-0.06**	**-0.04**
NIST SRM-3149		2.208	**0.01**	**0.00**
NIST SRM-3149		2.208	**0.00**	**0.00**
NIST SRM-3149		2.208	**-0.06**	**-0.04**
NIST SRM-3149		2.208	**-0.12**	**-0.08**
NIST SRM-3149		2.208	**-0.05**	**-0.03**
NIST SRM-3149		2.208	**-0.06**	**-0.04**
NIST SRM-3149		2.208	**0.02**	**0.01**
NIST SRM-3149		2.208	**0.04**	**0.02**
NIST SRM-3149		2.208	**-0.01**	**0.00**
NIST SRM-3149		2.208	**-0.06**	**-0.04**
NIST SRM-3149		2.209	**0.07**	**0.04**
NIST SRM-3149		2.208	**0.00**	**0.00**

Table A.1.5 continued

Sample	Sample type	Se (µg g^{-1})	δ$^{82/76}$Se (‰)	δ$^{82/78}$Se (‰)
NIST SRM-3149		2.209	**0.05**	**0.03**
NIST SRM-3149		2.208	**0.01**	**0.01**
NIST SRM-3149		2.208	**-0.01**	**-0.01**
NIST SRM-3149		2.208	**0.01**	**0.01**
NIST SRM-3149		2.208	**0.04**	**0.03**
NIST SRM-3149		2.208	**0.03**	**0.02**
NIST SRM-3149		2.208	**0.05**	**0.03**
NIST SRM-3149		2.208	**-0.01**	**-0.01**
NIST SRM-3149		2.208	**0.05**	**0.03**
NIST SRM-3149		2.209	**0.00**	**0.00**
NIST SRM-3149		2.209	**0.02**	**0.01**
NIST SRM-3149		2.208	**0.07**	**0.04**
NIST SRM-3149		2.208	**-0.08**	**-0.05**
NIST SRM-3149		2.208	**-0.06**	**-0.04**
NIST SRM-3149		2.208	**-0.04**	**-0.02**
NIST SRM-3149		2.208	**0.05**	**0.03**
NIST SRM-3149		2.208	**-0.12**	**-0.08**
NIST SRM-3149		2.208	**0.02**	**0.01**
NIST SRM-3149		2.208	**0.01**	**0.00**
NIST SRM-3149		2.208	**0.00**	**0.00**
NIST SRM-3149		2.208	**0.01**	**0.01**
NIST SRM-3149		2.208	**0.05**	**0.03**
NIST SRM-3149		2.209	**0.00**	**0.00**
NIST SRM-3149		2.202	**0.11**	**0.07**
NIST SRM-3149		2.203	**0.01**	**0.00**
NIST SRM-3149		2.208	**-0.02**	**-0.01**
NIST SRM-3149		2.208	**0.02**	**0.01**
NIST SRM-3149		2.208	**0.03**	**0.02**
NIST SRM-3149		2.209	**0.03**	**0.02**
NIST SRM-3149		2.208	**-0.04**	**-0.03**
NIST SRM-3149		2.208	**0.06**	**0.04**
NIST SRM-3149		2.208	**0.06**	**0.04**
NIST SRM-3149		2.209	**-0.07**	**-0.05**
NIST SRM-3149		2.208	**-0.07**	**-0.04**
NIST SRM-3149		2.208	**-0.05**	**-0.03**
NIST SRM-3149		2.208	**-0.01**	**0.00**
NIST SRM-3149		2.208	**0.08**	**0.05**
NIST SRM-3149		2.208	**0.03**	**0.02**
NIST SRM-3149		2.208	**-0.14**	**-0.09**
NIST SRM-3149		2.208	**0.01**	**0.01**
NIST SRM-3149		2.208	**-0.06**	**-0.04**
NIST SRM-3149		2.208	**-0.09**	**-0.06**
NIST SRM-3149		2.208	**0.06**	**0.04**
NIST SRM-3149		2.209	**-0.03**	**-0.02**
NIST SRM-3149		2.209	**-0.07**	**-0.04**
NIST SRM-3149		2.208	**-0.10**	**-0.07**
NIST SRM-3149		2.208	**0.03**	**0.02**
NIST SRM-3149		2.208	**0.09**	**0.06**
NIST SRM-3149		2.208	**0.02**	**0.01**
NIST SRM-3149		2.208	**-0.01**	**0.00**
NIST SRM-3149		2.208	**0.06**	**0.04**
NIST SRM-3149		2.208	**0.00**	**0.00**
NIST SRM-3149		2.208	**0.08**	**0.05**
NIST SRM-3149		2.208	**0.04**	**0.03**
NIST SRM-3149		2.208	**0.11**	**0.07**
NIST SRM-3149		2.208	**-0.06**	**-0.04**
NIST SRM-3149		2.208	**-0.09**	**-0.06**
NIST SRM-3149		2.209	**-0.03**	**-0.02**
NIST SRM-3149		2.206	**0.01**	**0.01**
NIST SRM-3149		2.209	**-0.01**	**-0.01**
NIST SRM-3149		2.209	**0.00**	**0.00**
NIST SRM-3149		2.208	**0.00**	**0.00**

Table A.1.5 continued

Sample	**Sample type**	**Se (μg g^{-1})**	**$\delta^{82/76}$Se (‰)**	**$\delta^{82/78}$Se (‰)**
NIST SRM-3149		2.209	**0.00**	**0.00**
NIST SRM-3149		2.209	**0.00**	**0.00**
NIST SRM-3149		2.208	**-0.02**	**-0.01**
NIST SRM-3149		2.209	**0.04**	**0.03**
NIST SRM-3149		2.209	**0.02**	**0.01**
NIST SRM-3149		2.208	**-0.07**	**-0.04**
NIST SRM-3149		2.209	**0.05**	**0.03**
NIST SRM-3149		2.209	**-0.05**	**-0.03**
NIST SRM-3149		2.209	**0.03**	**0.02**
NIST SRM-3149		2.209	**0.04**	**0.02**
NIST SRM-3149		2.208	**0.04**	**0.03**
NIST SRM-3149		2.209	**-0.02**	**-0.01**
NIST SRM-3149		2.209	**0.00**	**0.00**
NIST SRM-3149		2.209	**0.12**	**0.08**
NIST SRM-3149		2.208	**-0.08**	**-0.05**
NIST SRM-3149		2.209	**0.04**	**0.02**
NIST SRM-3149		2.208	**0.04**	**0.03**
NIST SRM-3149		2.208	**0.04**	**0.02**
NIST SRM-3149		2.208	**0.04**	**0.02**
NIST SRM-3149		2.208	**0.01**	**0.00**
NIST SRM-3149		2.208	**-0.03**	**-0.02**
NIST SRM-3149		2.208	**0.01**	**0.01**
NIST SRM-3149		2.208	**0.01**	**0.01**
NIST SRM-3149		2.208	**0.00**	**0.00**
NIST SRM-3149		2.208	**0.04**	**0.03**
NIST SRM-3149		2.208	**-0.05**	**-0.03**
NIST SRM-3149		2.208	**0.06**	**0.04**
NIST SRM-3149		2.208	**-0.07**	**-0.04**
NIST SRM-3149		2.208	**0.00**	**0.00**
NIST SRM-3149		2.208	**0.00**	**0.00**
NIST SRM-3149		2.208	**0.03**	**0.02**
NIST SRM-3149		2.208	**-0.06**	**-0.04**
NIST SRM-3149		2.208	**-0.02**	**-0.02**
NIST SRM-3149		2.208	**0.01**	**0.01**
NIST SRM-3149		2.208	**-0.04**	**-0.03**
NIST SRM-3149		2.209	**-0.09**	**-0.06**
NIST SRM-3149		2.209	**-0.02**	**-0.01**
NIST SRM-3149		2.208	**-0.01**	**-0.01**
NIST SRM-3149		2.209	**0.08**	**0.05**
NIST SRM-3149		2.209	**0.07**	**0.04**
		AVERAGE	0.00	0.00
		2 s.d.	0.11	0.07

Sample	**Sample type**	**Se (μg g^{-1})**	**$\delta^{82/76}$Se (‰)**	**$\delta^{82/78}$Se (‰)**
NIST SRM-3149	MR	2.194	-0.02	-0.01
NIST SRM-3149		2.194	0.00	0.00
NIST SRM-3149		2.194	0.00	0.00
NIST SRM-3149		2.194	0.00	0.00
NIST SRM-3149		2.194	-0.03	-0.02
NIST SRM-3149		2.194	0.06	0.04
NIST SRM-3149		2.194	0.02	0.01
NIST SRM-3149		2.194	-0.01	-0.01
NIST SRM-3149		2.194	-0.01	-0.01
NIST SRM-3149		2.194	-0.02	-0.01
		AVERAGE	0.00	0.00
		2 s.d.	0.05	0.03

Table A.1.6
Results for mixtures of USGS SGR-1 and in-house Se reference MH-495.

Sample	Sample type	$f_{\text{Se USGS SGR-1}}$	$\delta^{82/76}$Se (‰)	$\delta^{82/78}$Se (‰)
USGS SGR-1 + MH-495	shale + in-house Se reference	0.94	**-0.30**	**-0.20**
USGS SGR-1 + MH-495		0.89	**-0.37**	**-0.24**
USGS SGR-1 + MH-495		0.79	**-0.78**	**-0.50**
USGS SGR-1 + MH-495		0.73	**-0.76**	**-0.49**
USGS SGR-1 + MH-495		0.57	**-1.27**	**-0.82**
USGS SGR-1 + MH-495		0.37	**-1.94**	**-1.26**
USGS SGR-1 + MH-495		0.20	**-2.55**	**-1.66**
MH-495	in-house Se reference	0.00	**-3.24**	**-2.11**
USGS SGR-1	shale	1.00	**0.09**	**0.06**

Table A.1.7
Results for mixtures of MH-495 and NIST SRM-3149.

Sample	Sample type	$f_{\text{Se NIST SRM-3149}}$	$\delta^{82/76}$Se (‰)	δ82/78Se (‰)
NIST SRM-3149 + MH-495	in-house Se reference + Se reference	0.79	**-0.64**	**-0.41**
NIST SRM-3149 + MH-495		0.63	**-1.10**	**-0.71**
NIST SRM-3149 + MH-495		0.51	**-1.43**	**-0.93**
NIST SRM-3149 + MH-495		0.39	**-1.90**	**-1.23**
NIST SRM-3149 + MH-495		0.21	**-2.49**	**-1.62**
MH-495	in-house Se reference	0.00	**-3.23**	**-2.10**
NIST SRM-3149	Se reference	1.00	**0.10**	**0.06**

Table A.1.8
Se isotope data for dilutions of MH-495 and USGS SGR-1.

Sample	**Sample type**	**ng mL^{-1} measured**	**δ$^{82/76}$Se (‰)**	**2 s.e. (‰)**	**^{82}Se (V)**
MH-495	in-house Se reference	50	-3.19	0.033	1.477
MH-495		50	-3.23	0.025	1.462
MH-495		35	-3.15	0.038	1.030
MH-495		25	-3.17	0.044	0.736
MH-495		25	-3.24	0.040	0.727
MH-495		18	-3.26	0.055	0.528
		AVERAGE	**-3.21**	**0.04**	
		2 S.D.	**0.09**		
MH-495		13	-3.34	0.067	0.363
MH-495		13	-3.34	0.061	0.360
MH-495		12	-3.30	0.066	0.325
MH-495		10	-3.22	0.078	0.294
MH-495		8	-3.22	0.107	0.222
		AVERAGE	**-3.29**	**0.08**	
		2 S.D.	**0.12**		
MH-495		6	-3.37	0.083	0.182
MH-495		6	-3.27	0.099	0.181
MH-495		5	-3.09	0.114	0.139
MH-495		5	-3.18	0.100	0.140
MH-495		4	-3.39	0.149	0.109
MH-495		4	-3.43	0.125	0.119
MH-495		3	-3.28	0.163	0.088
		AVERAGE	**-3.29**	**0.12**	
		2 S.D.	**0.24**		

Sample	**Sample type**	**ng mL^{-1} measured**	**δ$^{82/76}$Se (‰)**	**2 s.e. (‰)**	**^{82}Se (V)**
USGS SGR-1	shale	50	-0.14	0.043	1.027
USGS SGR-1		35	-0.14	0.035	0.921
USGS SGR-1		25	-0.17	0.054	0.666
USGS SGR-1		*18*	*-0.20*	*0.042*	*0.702*
		AVERAGE	**-0.17**	**0.04**	
		2 S.D.	**0.06**		
USGS SGR-1		13	-0.17	0.088	0.314
USGS SGR-1		*12*	*-0.22*	*0.049*	*0.398*
USGS SGR-1		10	-0.13	0.065	0.246
USGS SGR-1		*10*	*-0.29*	*0.074*	*0.345*
		AVERAGE	**-0.20**	**0.07**	
		2 S.D.	**0.14**		
USGS SGR-1		7	-0.36	0.077	0.232
USGS SGR-1		*6*	*-0.31*	*0.125*	*0.150*
USGS SGR-1		6	-0.23	0.080	0.210
USGS SGR-1		5	-0.31	0.090	0.184
USGS SGR-1		5	-0.16	0.077	0.181
USGS SGR-1		5	-0.31	0.134	0.137
		AVERAGE	**-0.28**	**0.10**	
		2 S.D.	**0.14**		

Data in italics from additional measurement session. Signal intensities obtained on amplifier resistor of 10^{11} Ω.

Table A.2.1 Major element data for USGS reference material AGV-2 acquired during this study and data from USGS.

sample *Major elements (wt.%)*	AGV-2 (n=2)	AGV-2 recommended♦
SiO_2	58.3	59.3
TiO_2	1.04	1.05
Al_2O_3	16.9	16.9
FeO_T	7.13	6.69
MnO	0.09	0.10
MgO	1.46	1.79
CaO	5.27	5.20
Na_2O	4.11	4.19
K_2O	2.45	2.88
P_2O_5	0.28	0.48
Total	97.0	99.9
LOI		1.30

♦United States Geological Survey, Certificate of Analysis, Andesite, AGV-2

Table A.2.2 Trace element data for USGS BHVO-2 and BIR-1 acquired during this study and recommended data from GeoReM.

	BHVO-2 (n=2) (µg/g)	BHVO-2 recommended* (µg/g)	BIR-1 (n=1) (µg/g)	BIR-1 recommended* (µg/g)
Li	4.5	4.5	3.15	3.12
Be	1.1	1.0	0.09	0.09
Sc	32.5	32.1	45.18	43.81
V	316.1	314.8	323.65	318.80
Cr	300.5	299.1	409.23	408.00
Co	45.4	45.3	53.49	52.80
Ni	118.4	117.9	170.19	166.10
Cu	126.3	125.5	117.64	116.20
Zn	104.1	102.4	70.99	67.36
Ga	20.9	21.1	15.47	15.27
Rb	9.1	9.2	0.19	0.20
Sr	394.9	394.9	108.97	108.70
Y	24.3	24.3	14.81	14.53
Zr	172.5	169.6	14.27	14.29
Nb	18.2	18.3	0.54	0.54
Mo	3.6	4.5	0.05	0.04
Ag	0.1	0.1	0.04	0.04
Cd	0.1	0.1	0.06	0.07
Sn	1.7	1.9	0.72	0.94
Sb	0.1	0.1	0.46	0.43
Cs	0.1	0.1	0.00	0.01
Ba	130.2	131.3	6.50	6.46
La	15.1	15.2	0.60	0.60
Ce	37.8	37.8	1.91	1.90
Pr	5.4	5.4	0.38	0.38
Nd	24.3	24.4	2.39	2.38
Sm	6.0	6.1	1.10	1.10
Eu	2.0	2.1	0.52	0.52
Tb	0.9	0.9	0.36	0.36
Gd	6.1	6.2	1.86	1.86
Dy	5.2	5.2	2.52	2.54
Ho	1.0	1.0	0.58	0.58
Er	2.5	2.5	1.69	1.70
Tm	0.3	0.3	0.26	0.26
Yb	2.0	2.0	1.65	1.66
Lu	0.3	0.3	0.25	0.25
Hf	4.2	4.3	0.56	0.57
Ta	1.1	1.1	0.04	0.04
Tl	0.0	0.0	0.00	0.00
Pb	1.6	1.5	2.79	2.96
Th	1.2	1.2	0.03	0.03
U	0.4	0.4	0.01	0.01

*GeoReM preferred values; http://georem.mpch-mainz.gwdg.de/sample_query_pref.asp (09.04.2018); Jochum et al. (2016).

Table A.2.3 The $\delta^{82/76}$Se value of the inter-laboratory standard MH-495 (30 ng mL^{-1} Se) measured together with the samples in this study (*Chapter* 2).

	30 ng mL^{-1} solution	
	$\delta^{82/76}$Se (‰)	2 s.e. (‰)*
	−3.29	0.07
	−3.23	0.06
	−3.27	0.08
	−3.30	0.04
	−3.27	0.04
	−3.23	0.04
	−3.24	0.04
	−3.15	0.05
	−3.21	0.07
	−3.27	0.05
	−3.15	0.07
	−3.24	0.07
	−3.23	0.05
	−3.24	0.04
	−3.20	0.04
	−3.28	0.05
	−3.30	0.05
	−3.23	0.04
	−3.22	0.04
	−3.22	0.04
	−3.29	0.04
	−3.26	0.04
	−3.26	0.05
	−3.27	0.04
	−3.30	0.04
	−3.31	0.04
Average	−3.25	
2 s.d.	0.08	
	n=26	

*Internal precision of a sample run during Se isotope analysis (over 40 cycles) is reported as 2 standard error (2 s.e.).

Table A.2.4 Se isotope and concentration data for multiple digested sample 1880-3 (K2) from the Kasuga seamount measured during different measurement sessions.

sample	location	Rock type		$\delta^{82/76}$Se$_{\text{NIST SRM-3149}}$ (‰)	2 s.e.* (‰)	Se (ng/g)
1880-3 (K2)	arc, Kasuga	basalt		-0.13	0.07	123
				-0.18	0.07	121
				-0.14	0.08	118
				-0.16	0.09	119
				-0.25	0.06	114
				-0.23	0.05	118
			avergage	-0.18		119
			uncertainty (2 s.d.)	0.10	(1 s.d.)	4
1881-4	arc-like	bas. andesite		-0.07	0.07	71
				-0.17	0.05	76
				-0.14	0.06	76
			avergage	-0.13		74
			uncertainty (2 s.d.)	0.10	(1 s.d.)	2

*Internal precision of a sample run during Se isotope analysis (over 40 cycles) is reported as 2 standard error (2 s.e.). Uncertainty of Se concentrations conservatively expressed as 3% r.s.d.

Table A.2.5 Comparison of Tellurium concentrations of GSJ JB-2 and JB-3 acquired during this study with literature data.

	JB-2 (n=6) this study	Terashima (2001)	Hall and Pelchat (1997)	Imai et al. (1995)
Te (ng/g)	3.78	4.10	3.00	4
1 s.d.	0.11*	0.40	1.00	-
	JB-3 (n=2) this study			
Te (ng/g)	1.03	1.8	<1	2
1 s.d.	0.03*	0.2	-	-

*1.s.d. uncertainty of Se and Te concentrations acquired in this study conservatively expressed as 3% relative standard deviation.

Table A.2.6 Comparison of Selenium concentrations of GSJ JB-2 and JB-3 acquired during this study with literature data.

	JB-2 (n=6) this study (ng/g)	Imai et al. (1995) (ng/g)	Hall and Pelchat (1997) (ng/g)	Terashima and Imai (2000) (ng/g)
Se (ng/g)	153	190	150	151
1 s.d.	5*	75	2	8
	JB-3 (n=2) this study			
Se (ng/g)	67	69	54	51
1 s.d.	2*	17	1	2

1.s.d. uncertainty of Se and Te concentrations acquired in this study conservatively expressed as 3% relative standard deviation.

Table A.2.7 Major-, trace element and Se–Se–isotope data of Mariana lavas

Sample	1838-13	1839-3	1841-18	1846-12	1846-9	1881-4
Location	BAB-18°N	BAB-18°N	BAB-18°N	BAB-18°N	BAB-18°N	AL-BAB-22°N
rock type	bas. andesite	basalt	basalt	basalt	basalt	bas. andesite
Latitude	144°44.0'E	144˚42.0'E	144˚43.0'E	144˚41.0'E	144˚41.0'E	143˚15.0'E
Longitude	18°12.0'N	18˚16.0'N	18˚13.0'N	18˚20.0'N	18˚20.0'N	21˚30.0'N
SiO_2 *Major elements (wt.%)*	52.69	*48.52*	50.51	50.75	49.67	53.01
TiO_2	1.12	*0.89*	1.09	1.11	0.57	1.13
Al_2O_3	16.69	*17.42*	17.40	17.30	17.45	16.33
FeO_T	8.68	*6.70*	7.61	7.56	7.03	8.17
MnO	0.19	*0.13*	0.15	0.15	0.16	0.13
MgO	5.68	*7.68*	7.84	7.00	6.95	6.05
CaO	10.22	*11.67*	11.82	11.39	13.46	10.56
Na_2O	3.06	*2.49*	2.81	2.75	2.07	2.89
K_2O	0.52	*0.25*	0.21	0.40	0.71	0.41
P_2O_5	0.2	*0.11*	0.11	0.18	0.13	0.19
Total	99.05	*95.86*	99.55	100.17	100.13	98.87
S* (µg/g)	930	780	620	930	370	280
$\delta^{34}S_{CDT}$ (‰)	0.9	0.9	1.3	1.8	0.7	0.7
Texture	gl	gl	gl	gl	gl	gl
Depth (mbsl)	3600	3700	3600	3600	3600	3250
Se (µg/g)	0.113	0.133	0.132	0.234	0.169	0.074
Te (ng/g)	1.3	3.9	3.8	7.0	4.7	1.8
S/Se	8230	5865	4697	3974	2189	3784
Se/Te	86	34	35	33	36	41
$\delta^{82/76}Se_{NIST\ SRM\text{-}3149}$ (‰)	−0.02	−0.02	−0.05	−0.02	−0.16	−0.13
Li *Trace elements (µg/g)*	6.40	4.85	4.84	5.33	6.32	5.07
Be	0.61	0.48	0.50	0.54	0.46	0.45
Sc	34.0	36.2	33.8	33.8	36.4	35.0
V	262	220	208	224	188	256
Cr	35.3	309	360	284	312	74.8
Co	33.2	35.7	36.6	327	37.6	31.5
Ni	28.4	117	131	122	110	48.6
Cu	43.2	67.2	63.0	67.9	111	53.6
Zn	69.9	56.9	57.4	61.2	52.8	59.7
Ga	16.8	15.1	15.9	15.1	11.8	15.0
As	0.33	0.26	0.22	0.37	0.22	0.63
Rb	9.60	5.60	2.51	6.39	19.5	6.08
Sr	230	227	218	226	328	254
Y	22.9	20.2	21.7	21.8	12.1	18.8
Zr	107	66.1	79.8	79.5	40.1	64.8
Nb	2.95	2.20	2.83	4.83	1.33	3.13
Mo	0.48	0.56	0.47	0.69	0.19	0.51
Ag	0.09	0.20	1.25	0.06	0.05	0.25
Cd	0.10	0.08	0.09	0.09	0.06	0.08
Sn	0.74	1.15	1.45	0.77	0.46	0.64
Sb	0.02	0.02	0.01	0.01	0.02	0.03
Cs	0.15	0.09	0.04	0.10	0.12	0.12
Ba	115	51.0	26.9	60.7	47.7	103
La	7.01	4.83	4.32	5.88	7.65	6.18
Ce	16.2	11.9	11.6	14.2	16.3	13.9
Pr	2.42	1.83	1.85	2.12	2.38	1.98
Nd	11.4	8.92	9.11	10.1	9.94	9.05
Sm	3.25	2.69	2.79	2.95	2.15	2.53
Eu	1.20	1.02	1.05	1.10	0.76	0.96
Tb	0.66	0.58	0.60	0.62	0.36	0.53
Gd	3.92	3.35	3.56	3.65	2.28	3.07
Dy	4.18	3.67	3.86	3.91	2.21	3.37
Ho	0.91	0.79	0.86	0.84	0.47	0.74
Er	2.54	2.23	2.41	2.36	1.31	2.07
Tm	0.38	0.33	0.36	0.36	0.19	0.31
Yb	2.41	2.09	2.29	2.23	1.22	1.97
Lu	0.36	0.31	0.33	0.33	0.18	0.29
Hf	2.66	1.70	1.95	1.95	1.09	1.63
Ta	0.17	0.13	0.17	0.89	0.07	0.18
Tl	0.05	0.03	0.02	0.03	0.08	0.03
Pb	1.21	0.99	0.71	0.91	1.36	1.36
Th	0.68	0.43	0.30	0.57	0.53	0.71
U	0.26	0.17	0.10	0.22	0.21	0.22
V/Sc	7.7	6.1	6.1	6.6	5.2	7.3
Ba/Th	168	118	90	106	90	145
Th/Yb	0.3	0.2	0.1	0.3	0.4	0.4
Ba/Yb	48	24	12	27	39	52

Table A.2.7 continued

Sample	D 65-4	D 67-10	D 68-4	15161	1580
Location	AL-BAB-22°N	AL-BAB-22°N	AL-BAB-22°N	Fukujin	Fukujin
rock type	bas. andesite	basalt	basalt	andesite	andesite
Latitude	143˚12.0'E	143˚00.0'E	143˚10.0'E	143°25.2'E	143°25.2'E
Longitude	22˚00.0'N	21˚ 54.0'N	21˚50.0'N	21°54.6'N	21°54.6'N
SiO_2 *Major elements* (wt.%)	53.90	49.80	50.40	58.04	59.70
TiO_2	1.11	1.11	0.84	1.27	1.10
Al_2O_3	16.36	16.00	15.80	13.50	13.40
FeO_T	8.74	7.54	7.54	10.98	8.87
MnO	n.a.	0.14	0.15	n.a.	0.19
MgO	4.78	8.47	8.89	2.95	2.00
CaO	9.01	10.80	10.30	6.80	5.14
Na_2O	3.27	3.05	2.62	2.84	3.49
K_2O	0.56	0.27	0.54	1.40	1.48
P_2O_5	0.14	0.13	0.14	n.a.	0.22
Total	97.87	97.31	97.22	97.78	95.59
S* (µg/g)	200	930	490	50	40
$\delta^{34}S_{CDT}$ (‰)	1.2	0.3	1.9	5	3
Texture	gl	gl	gl	gly	gly
Depth (mbsl)	2840	3500	3240	1170	1170
Se (µg/g)	0.138	0.182	0.125	0.102	0.077
Te (ng/g)	1.1	3.0	1.6	1.6	0.2
S/Se	1449	5110	3920	490	519
Se/Te	129	60	81	65	481
$\delta^{82/76}Se_{NIST\ SRM\text{-}3149}$ (‰)	−0.24	−0.33	−0.18	−0.24	−0.14
	-0.24	-0.33	-0.18	-0.24	-0.14
Li *Trace elements (µg/g)*	7.13	5.05	4.51	9.07	13.7
Be	0.48	0.52	0.58	0.81	0.94
Sc	35.0	33.4	33.5	38.1	28.1
V	298	230	235	389	76.6
Cr	7.1	341	391	8.0	0.56
Co	80.9	134	120	28.0	101
Ni	11.5	143	178	10.4	1.0
Cu	66.3	53.9	61.9	182	58.5
Zn	77.7	61.6	63.6	101	105
Ga	16.9	14.8	15.1	18.3	16.0
As	0.99	0.27	0.57	4.16	4.23
Rb	5.86	3.80	7.55	25.7	30.3
Sr	237	200	275	440	360
Y	23.8	23.1	20.6	29.8	37.4
Zr	73.9	84.2	78.1	87.5	105
Nb	2.26	2.26	4.73	2.47	2.89
Mo	0.54	0.44	0.66	1.41	1.71
Ag	0.07	0.04	0.06	0.16	0.06
Cd	0.09	0.09	0.09	0.09	0.11
Sn	0.70	1.11	0.76	1.31	1.10
Sb	0.03	0.01	0.02	0.12	0.14
Cs	0.16	0.06	0.13	0.77	0.93
Ba	125	56.4	104	535	654
La	5.90	5.22	7.60	17.7	21.2
Ce	14.2	13.4	17.0	34.7	41.9
Pr	2.12	2.06	2.38	4.53	5.51
Nd	10.2	10.0	10.8	19.5	23.8
Sm	3.03	3.00	3.00	4.78	5.90
Eu	1.16	1.12	1.05	1.45	1.70
Tb	0.66	0.65	0.58	0.86	1.07
Gd	3.76	3.82	3.53	5.25	6.48
Dy	4.25	4.12	3.73	5.37	6.66
Ho	0.94	0.91	0.82	1.17	1.45
Er	2.67	2.57	2.26	3.32	4.10
Tm	0.40	0.38	0.34	0.51	0.63
Yb	2.57	2.40	2.21	3.31	4.03
Lu	0.39	0.36	0.33	0.49	0.61
Hf	1.94	2.05	1.92	2.49	2.97
Ta	0.20	0.31	0.38	0.11	0.23
Tl	0.03	0.02	0.03	0.10	0.12
Pb	1.61	0.91	1.28	5.72	6.89
Th	0.66	0.46	0.89	2.76	3.08
U	0.20	0.14	0.28	0.81	0.95
V/Sc	8.5	6.9	7.0	10.2	2.7
Ba/Th	188	122	116	194	212
Th/Yb	0.3	0.2	0.4	0.8	0.8
Ba/Yb	49	23	47	162	162

Table A.2.7 continued

Sample	15117	15146	D35-1-4	1880-3 (K2)	1883-5 (P)
Location	Fukujin	Fukujin	Fukujin	Kasuga	Kasuga
rock type	andesite	andesite	andesite	basalt	bas. andesite
Latitude	143°25.2'E	143°25.2'E	143°25.2'E	143°34.0E	143˚41.0'E
Longitude	21°54.6'N	21°54.6'N	21°53.4'N	21°39.0'N	21˚27.0'N
SiO_2 *Major elements (wt.%)*	60.60	56.70	56.00	51.18	52.26
TiO_2	1.11	1.28	0.87	0.81	0.77
Al_2O_3	14.00	13.80	17.70	16.45	16.42
FeO_T	8.92	10.29	7.60	7.94	7.21
MnO	0.19	0.18	0.15	0.13	0.13
MgO	1.98	2.86	3.13	5.42	5.46
CaO	5.32	6.99	9.02	10.59	10.46
Na_2O	3.64	3.08	2.63	2.03	2.27
K_2O	1.47	1.29	1.25	2.42	1.61
P_2O_5	0.24	0.15	0.18	0.43	0.29
Total	97.47	96.62	98.53	97.40	96.88
S* (µg/g)	50	30	10	150	120
$\delta^{34}S_{CDT}$ (‰)	4.7	10.3	4.4	5.1	5.5
Texture	gly	gly	mxl	gl	gl
Depth (mbsl)	1170	1170	828	1975	2760
Se (µg/g)	0.083	0.124	0.080	0.119	0.087
Te (ng/g)	0.2	2.0	0.7	4.2	6.4
S/Se	606	242	125	1261	1379
Se/Te	393	61	113	28	14
$\delta^{82/76}Se_{NIST\ SRM\text{-}3149}$ (‰)	−0.16	−0.08	0.03	−0.18	−0.01
	-0.16	-0.08	0.03	-0.18	-0.01
Li *Trace elements (µg/g)*	13.5	10.1	6.17	4.91	3.96
Be	0.93	0.75	0.76	1.76	0.96
Sc	28.8	35.2	34.3	40.7	35.9
V	81.7	402	340	280	242
Cr	0.59	1.1	12.9	592	705
Co	75.3	81.8	69.4	40.1	44.0
Ni	1.0	8.6	15.1	145	271
Cu	61.7	212	159	99.2	79.4
Zn	104	101	86.3	63.8	61.7
Ga	16.0	15.7	18.9	12.8	12.5
As	4.12	3.43	5.51	0.79	0.89
Rb	29.7	26.3	32.5	52.4	26.9
Sr	363	342	450	538	444
Y	36.9	29.8	27.3	19.8	16.9
Zr	102	89.5	96.4	113	74.0
Nb	2.81	2.46	2.85	3.43	3.36
Mo	1.63	1.52	1.75	1.12	0.78
Ag	0.06	0.95	0.15	0.11	0.06
Cd	0.10	0.10	0.09	0.10	0.08
Sn	1.19	1.34	0.91	0.61	0.84
Sb	0.13	0.14	0.18	0.03	0.03
Cs	0.90	0.84	1.03	0.63	0.40
Ba	639	544	623	276	282
La	20.7	17.0	18.5	25.0	20.1
Ce	41.0	33.5	35.3	47.8	37.5
Pr	5.42	4.39	4.52	5.89	4.63
Nd	23.3	19.2	18.9	23.6	18.6
Sm	5.77	4.84	4.53	5.18	3.94
Eu	1.68	1.43	1.34	1.66	1.23
Tb	1.05	0.92	0.79	0.73	0.55
Gd	6.43	5.56	4.90	4.99	3.73
Dy	6.54	5.72	4.89	4.00	3.17
Ho	1.43	1.26	1.07	0.77	0.65
Er	4.03	3.58	3.03	1.94	1.78
Tm	0.62	0.53	0.46	0.27	0.25
Yb	3.98	3.55	3.04	1.67	1.62
Lu	0.61	0.55	0.46	0.24	0.24
Hf	2.89	2.76	2.69	2.46	1.74
Ta	0.20	0.23	0.18	0.13	0.16
Tl	0.12	0.10	0.08	0.16	0.11
Pb	7.00	6.28	6.81	2.81	2.55
Th	3.03	2.55	3.32	2.67	2.65
U	0.91	0.76	0.94	1.07	0.81
V/Sc	2.8	11.4	9.9	6.9	6.7
Ba/Th	211	213	187	103	106
Th/Yb	0.8	0.7	1.1	1.6	1.6
Ba/Yb	161	153	205	166	174

Table A.2.7 continued

Sample	1885-6 (K3)	1884-10 (K3)	D 31-3-1	D 25-3	D 25-1-4
Location	Kasuga	Kasuga	Eifuku	S. Daikoku	S. Daikoku
rock type	bas. andesite	absarokite	bas. andesite	bas. andesite	andesite
Latitude	143˚35.0'E	143˚33.0'E	144°09.0'E	144˚05.0'E	144˚05.0'E
Longitude	21˚27.0'N	21˚23.0'N	21°25.0'N	21˚03.0'N	21˚03.0'N
SiO_2 *Major elements (wt.%)*	54.60	50.29	52.70	54.20	57.50
TiO_2	0.79	0.73	0.89	0.81	0.94
Al_2O_3	16.32	14.62	18.10	16.80	15.60
FeO_T	7.23	7.64	9.36	11.67	11.89
MnO	n.a.	n.a.	0.18	0.20	0.19
MgO	5.80	7.39	3.49	3.89	3.02
CaO	10.25	12.11	9.39	9.02	7.24
Na_2O	2.49	1.45	2.86	3.08	3.33
K_2O	0.98	3.25	1.35	0.73	1.06
P_2O_5	0.20	0.56	0.22	0.13	0.16
Total	98.66	98.04	98.54	100.53	100.93
S* (µg/g)	110	200	20	50	60
$\delta^{34}S_{CDT}$ (‰)	4	0.1	4	1.5	1.4
Texture	gl	gl	mxl	mxl	gly
Depth (mbsl)	2865	2920	1605	1440	1440
Se (µg/g)	0.066	0.142	0.165	0.147	0.134
Te (ng/g)	2.6	4.6	0.8	0.8	1.6
S/Se	1679	1408	121	340	448
Se/Te	25	31	212	186	85
$\delta^{82/76}Se_{NIST\ SRM\text{-}3149}$ (‰)	−0.12	−0.09	−0.09	−0.25	−0.16
	-0.12	-0.09	-0.09	-0.25	-0.16
Li *Trace elements (µg/g)*	5.99	4.61	7.68	4.95	11.4
Be	0.72	2.82	0.92	0.43	0.63
Sc	31.5	38.9	25.7	32.1	28.7
V	237	240	319	204	256
Cr	451	569	7.4	252	0.7
Co	33.5	48.4	58.9	34.8	80.1
Ni	136	289	10.6	114	5.0
Cu	65.4	86.2	162	63.6	166
Zn	63.9	58.6	90.6	53.5	94.8
Ga	14.2	11.0	18.3	14.8	16.3
As	0.64	0.62	1.39	0.31	3.55
Rb	18.6	72.3	26.1	5.28	17.0
Sr	389	557	716	211	318
Y	16.7	21.8	21.3	19.4	29.8
Zr	76.0	156	78.6	63.5	97.1
Nb	3.23	3.57	3.26	2.26	1.96
Mo	0.69	1.65	1.09	0.65	1.80
Ag	0.22	0.11	0.19	0.08	0.21
Cd	0.09	0.11	0.09	0.08	0.10
Sn	0.97	0.71	0.99	0.82	0.92
Sb	0.03	0.03	0.05	0.03	0.09
Cs	0.28	0.77	0.46	0.10	0.67
Ba	254	190	482	46.8	383
La	15.9	28.3	22.8	4.25	8.45
Ce	30.0	55.0	43.7	10.6	19.5
Pr	3.71	6.71	5.47	1.64	2.85
Nd	14.9	27.0	22.1	7.99	13.3
Sm	3.25	6.02	4.82	2.45	3.84
Eu	1.04	1.96	1.46	0.94	1.18
Tb	0.49	0.86	0.67	0.54	0.79
Gd	3.19	5.90	4.51	3.10	4.69
Dy	2.98	4.57	3.95	3.46	5.17
Ho	0.64	0.83	0.83	0.75	1.16
Er	1.82	2.03	2.30	2.12	3.36
Tm	0.27	0.27	0.35	0.32	0.52
Yb	1.74	1.62	2.26	2.02	3.43
Lu	0.27	0.23	0.34	0.30	0.51
Hf	1.86	3.19	2.10	1.63	2.73
Ta	0.17	0.10	0.18	0.14	0.18
Tl	0.08	0.21	0.10	0.03	0.10
Pb	2.73	2.02	4.91	1.17	4.05
Th	2.41	2.63	3.63	0.37	1.13
U	0.70	1.19	1.07	0.15	0.44
V/Sc	7.5	6.2	12.4	6.3	8.9
Ba/Th	105	72	133	126	339
Th/Yb	1.4	1.6	1.6	0.2	0.3
Ba/Yb	146	117	213	23	112

Major element data in italics refer to complemented major element data during this study. All other major element data was obtained by Alt et al. (1993 and references therein). Please note that major element totals do not comprise loss on ignition because of limited sample material. All trace element data was obtained during this study (see text for details). *S concentration data taken from Alt et al. (1993). For location abbreviations see text. gl=glass; gly=glassy; mxl=microcrystalline.

Table A.2.8 Individual Se isotope and Se−Te concentration data of Mariana samples and international rock reference materials (United States Geological Survey, USGS; Geological Survey of Japan, GSJ).

sample	location	Rock type	SiO_2 wt.%	MgO wt.%	$\delta^{82/76}Se_{NIST\ SRM-3149}$ (‰)	2 s.e.† (‰)	Se (ng/g)	1 s.d. (ng/g)	Te (ng/g)	1 s.d. (ng/g)	Se/Te	S (µg/g)
15161	arc, Fukujin	andesite	58.0	2.95	−0.24	0.07	102	3	1.57	0.05	65	50
1580	arc, Fukujin	andesite	59.7	2.00	−0.14	0.04	77	2	0.16	0.00	481	40
15117	arc, Fukujin	andesite	60.6	1.98	−0.16	0.09	83	2	0.21	0.01	393	50
15146	arc, Fukujin	andesite	56.7	2.86	−0.08	0.05	124	4	2.04	0.06	61	30
D35−1−4	arc, Fukujin	andesite	56.0	3.13	0.00	0.05	79	2	0.71	0.02	113	10
					0.06	0.08	82					
1880−3 (K2)*	arc, Kasuga	basalt	51.2	5.42	−0.13	0.07	123	4	4.21	0.13	28	150
					−0.18	0.07	121					
					−0.14	0.08	118					
					−0.16	0.09	119					
					−0.25	0.06	114					
					−0.23	0.05	118					
1883−5 (P)	arc, Kasuga	bas. andesite	52.3	5.46	−0.01	0.07	87	3	6.40	0.19	14	120
1885−6 (K3)	arc, Kasuga	bas. andesite	54.6	5.80	−0.15	0.08	66	2	2.57	0.08	25	110
					−0.10	0.06	65					
1884−10 (K3)	arc, Kasuga	basalt	50.3	7.39	−0.10	0.04	142	4	4.57	0.14	31	200
					−0.08	0.05	142					
D31−3−1	arc, Eifuku	bas. andesite	52.7	3.49	−0.09	0.09	165	5	0.78	0.02	212	20
D25−3	arc, S.Daikoku	bas. andesite	54.2	3.89	−0.25	0.07	147	4	0.79	0.02	186	50
D25−1−4	arc, S.Daikoku	andesite	57.5	3.02	−0.16	0.05	134	4	1.58	0.05	85	60
1838−13	back−arc	bas. andesite	52.7	5.68	−0.12	0.05	112	3	1.31	0.04	86	930
					0.07	0.07	114	3				
1839−3	back−arc	basalt	48.5	7.68	−0.02	0.06	133	4	3.90	0.12	34	780
1841−18	back−arc	basalt	50.5	7.84	−0.05	0.07	132	4	3.79	0.11	35	620
1846−12	back−arc	basalt	50.8	7.00	−0.03	0.08	236	7	7.00	0.21	33	930
					−0.01	0.05	231					
1846−9	arc−like	basalt	49.7	6.95	−0.16	0.08	169	5	4.70	0.14	36	370
1881−4*	arc−like	bas. andesite	53.0	6.05	−0.07	0.07	71	2	1.82	0.05	41	280
					−0.17	0.05	76					
					−0.14	0.06	76					
D65−4	arc−like	bas. andesite	53.9	4.78	−0.31	0.04	135	4	1.07	0.03	129	200
					−0.18	0.07	140					
D67−10	arc−like	basalt	49.8	8.47	−0.33	0.06	182	5	3.03	0.09	60	930
D68−4	arc−like	basalt	50.4	8.89	−0.18	0.05	125	4	1.55	0.05	81	490
USGS BHVO−2**		basalt			0.16	0.06	166	5	14.1	0.42	12	
GSJ JB−2		basalt			−0.18	0.07	154	5	3.78	0.11	40	
					−0.18	0.07	154					
					−0.20	0.05	152					
GSJ JB−3		basalt			0.15	0.06	67	2	1.03	0.03	65	
					0.16	0.08	67					

†Internal precision on a sample run (over 40 cycles) is reported as 2 standard error (2 s.e.). **BHVO-2 was analyzed together with Mariana samples and published by Yierpan et al. (2018) with long-term BHVO-2 reproducibility of 0.18±0.10‰ (2 s.d., n=8, multiple analytical sessions over 6 months). Uncertainty on Se−Te concentrations conservatively expressed as 3% relative standard deviation.

Table A.2.9 Se isotope data from the literature representative of the Se isotope composition of the Mariana pre-subduction mantle wedge.

Reference	Sample	rocktype	$\delta^{82/76}Se_{NIST\ SRM\text{-}3149}$ (‰)
Rouxel et al. (2002)	PCC-1	peridotite	0.24
Yierpan et al. (2018)	BHVO-2	basalt	0.18
	BCR-2	basalt	0.29
	BE-N	basalt	0.15
	BIR-1a	basalt	0.28
		average	0.23
		2 s.d.	0.12

Table A.2.10 Se isotope compositions of marine sediments, hydrothermally altered basalt and hydrothermal sulfides analyzed by Rouxel et al. (2002) and (2004). Original data expressed as $\delta^{82/76}$Se relative to MERCK was converted to $\delta^{82/76}$Se relative to SRM NIST-3149 following the approach of Carignan and Wen (2007).

	Sample	$\delta^{82/76}Se_{MERCK}$ (‰)	2 s.d. (‰)	$\delta^{82/76}Se_{NIST\ SRM\text{-}3149}$ (‰)	2 s.d. (‰)
Marine sediments Site 1149 Leg 185	1149A-10H3,140	-1.19	0.25	0.35	0.32
Rouxel et al. (2002)	1149A-1H1,140	-2.07	0.25	-0.53	0.32
	1149A-4H2,140	-2.62	0.25	-1.08	0.32
	average	-1.96		-0.42	
	2 s.d.	1.44		1.44	
				n=3	
	Hydroth. altered basalt (slab)	-2.76		-1.22	0.32
	Hydroth. altered basalt (slab)	-2.98		-1.44	0.32
	average	-2.87		-1.33	
	2 s.d.	0.31		0.31	
				n=2	
Menez Gwen hydrothermal field	DV-14-06 altB	-2.76	0.25	-1.22	0.32
Rouxel et al. (2002)	DV-16-03 alt B	-2.98	0.25	-1.44	0.32
	DV-16-03 py	-4.88	0.25	-3.34	0.32
Lucky Strike hydrothermal field	DV-1-2- basalte	-1.29	0.25	0.25	0.32
Rouxel et al. (2002)	DV-6-2 basalte	-1.34	0.25	0.20	0.32
	FL-DR py	-1.22	0.25	0.32	0.32
	FL-DR py resampled	-1.18	0.25	0.36	0.32
	FL-DR cpy	-1.38	0.25	0.16	0.32
	FL-DR cpy resampled	-1.44	0.25	0.10	0.32
	FL-19-08 py/mar	-4.34	0.25	-2.80	0.32
	FL-19-08 py/mar	-4.07	0.25	-2.53	0.32
	FL-20-04a cpy	-5.79	0.25	-4.25	0.32
	FL-20-04a cpy resampled	-5.49	0.25	-3.95	0.32
	FL-20-04a cpy resampled	-6.29	0.25	-4.75	0.32
	ALV-2605-3-1 py	-2.01	0.25	-0.47	0.32
	ALV-2608-2-1 cpy	-4.37	0.25	-2.83	0.32
	FL-19-05 py	-1.94	0.25	-0.40	0.32
Rainbow hydrothermal field	FL-07-01 serp	-1.44	0.25	0.10	0.32
Rouxel et al. (2002)	FL-10-07 cpy	-2.69	0.25	-1.15	0.32
	FL-10-07 bn-cv	-2.57	0.25	-1.03	0.32
	FL-07-09 sph	-0.27	0.25	1.27	0.32
	FL-07-09 sph resampled	-0.51	0.25	1.03	0.32
	FL-06-08 cpy	-2.21	0.25	-0.67	0.32
	FL-06-08 cpy resampled	-2.23	0.25	-0.69	0.32
Logatchev hydrothermal field					
Rouxel et al. (2002)	MS-21-08-2/2A bncv	-1.43	0.25	0.11	0.32
	MS-21-08-2/2C cpy	-1.41	0.25	0.13	0.32
	MS-21-08-2/2D cpy	-1.65	0.25	-0.11	0.32
	MS-21-08-2/2E cpy	-1.44	0.25	0.10	0.32
Bairo Alto	FL-19-08	-4.41	0.25	-2.87	0.32
Rouxel et al. (2004)	FL-19-08	-4.34	0.25	-2.80	0.32
	FL-24-01	-3.63	0.25	-2.09	0.32
	FL-24-01	-2.99	0.25	-1.45	0.32
	FL-24-01 resampled	-1.95	0.25	-0.41	0.32
	FL-24-02	-3.18	0.25	-1.64	0.32
	FL-24-02	-3.6	0.25	-2.06	0.32
	FL-29-02	-2.87	0.25	-1.33	0.32
Helene	DV-19-09	-3.28	0.25	-1.74	0.32
Rouxel et al. (2004)	DV-19-09 resampled	-3.71	0.25	-2.17	0.32

Table A.2.10 continued

	Sample	$\delta^{82/76}Se_{MERCK}$ (‰)	2 s.d. (‰)	$\delta^{82/76}Se_{NIST\ SRM\text{-}3149}$ (‰)	2 s.d. (‰)
Bairo Alto	FL-19-08	-4.41	0.25	-2.87	0.32
Rouxel et al. (2004)	FL-19-08	-4.34	0.25	-2.80	0.32
	FL-24-01	-3.63	0.25	-2.09	0.32
	FL-24-01	-2.99	0.25	-1.45	0.32
	FL-24-01 resampled	-1.95	0.25	-0.41	0.32
	FL-24-02	-3.18	0.25	-1.64	0.32
	FL-24-02	-3.6	0.25	-2.06	0.32
	FL-29-02	-2.87	0.25	-1.33	0.32
Helene	DV-19-09	-3.28	0.25	-1.74	0.32
Rouxel et al. (2004)	DV-19-09 resampled	-3.71	0.25	-2.17	0.32
Elisabeth	FL-24-03	-2.68	0.25	-1.14	0.32
Rouxel et al. (2004)	FL-24-03	-2.31	0.25	-0.77	0.32
	FL-29-07A	-3.35	0.25	-1.81	0.32
Y3	DV-01-05	-2.84	0.25	-1.30	0.32
Rouxel et al. (2004)	DV-01-05	-2.77	0.25	-1.23	0.32
	FL-18-04	-2.9	0.25	-1.36	0.32
	FL-21-02	-2.22	0.25	-0.68	0.32
Sintra	ALV-2605-3-1	-2.17	0.25	-0.63	0.32
Rouxel et al. (2004)	ALV-2605-3-1 ditto	-2.01	0.25	-0.47	0.32
	ALV-2605-3-2	-4.24	0.25	-2.70	0.32
	ALV-2605-3-2 ditto	-3.90	0.25	-2.36	0.32
	ALV-2606-4-1J	-4.09	0.25	-2.55	0.32
	ALV-2606-4-1J	-3.75	0.25	-2.21	0.32
	DV-09-04	-3.17	0.25	-1.63	0.32
	DV-09-04 ditto	-2.92	0.25	-1.38	0.32
	FL-24-04	-4.28	0.25	-2.74	0.32
	FL-24-04 ditto	-4.64	0.25	-3.10	0.32
Eiffel Tower	DV-02-01	-2.48	0.25	-0.94	0.32
Rouxel et al. (2004)	DV-02-01	-4.28	0.25	-2.74	0.32
	DV-02-01 ditto	-4.5	0.25	-2.96	0.32
	DV-2	-5.32	0.25	-3.78	0.32
	DV-2 ditto	-5.17	0.25	-3.63	0.32
	L-20-04a	-5.49	0.25	-3.95	0.32
	L-20-04a resampled	-6.29	0.25	-4.75	0.32
Maker US4	ALV-2608-2-1	-4.08	0.25	-2.54	0.32
Rouxel et al. (2004)					
Dredged samples	FL-DR-03	-1.38	0.25	0.16	0.32
Rouxel et al. (2004)	FL-DR-03 resampled	-1.44	0.25	0.10	0.32
	FL-DR-03	-1.22	0.25	0.32	0.32
	FL-DR-03 resampled	-1.18	0.25	0.36	0.32
	FL-DR-03-09	-1.63	0.25	-0.09	0.32
	FL-DR-08	-2.39	0.25	-0.85	0.32
Inactif	DV-05-07	-1.65	0.25	-0.11	0.32
Rouxel et al. (2004)	DV-05-07	-1.89	0.25	-0.35	0.32
	DV-03-04	-3.18	0.25	-1.64	0.32
	DV-03-04 ditto	-3.23	0.25	-1.69	0.32
	FL-19-05	-1.94	0.25	-0.40	0.32
	DV-05-02-2/2	-2.15	0.25	-0.61	0.32
	FL-18-11	-1.87	0.25	-0.33	0.32
	FL-18-11 ditto	-1.66	0.25	-0.12	0.32
	average	2.90		-1.36	
	2 s.d.	2.82		2.82	
				n=77	

Table A.3.1 Compilation of Se concentrations from different sample digestion procedures (Table Top, bomb-, and high-pressure asher digestion).

	Se concentration (ng g^{-1})		
Sample	table top*	high-pressure asher	Bomb§
SEC 47-1	141		128
SEC 50-1	85	87	83
BCR-2	78		72

*Number (n) of table top digestions of all samples is n=4.$^{\$}$Number of bomb digestions is n=4. Sample SEC 50-1 was digested via high-pressure once.

Table A.3.2 The $\delta^{82/76}$Se value of the inter−laboratory standard MH−495 (30 ng mL^{-1} Se) measured together with the samples in this study (*Chapter* 3).

	30 ng mL^{-1} solution	
	$\delta^{82/76}$Se (‰)	2 s.e. (‰)*
	−3.25	0.06
	−3.17	0.06
	−3.30	0.05
	−3.21	0.09
	−3.24	0.08
	−3.25	0.08
	−3.29	0.04
	−3.22	0.03
	−3.26	0.04
	−3.30	0.03
	−3.17	0.03
	−3.30	0.04
	−3.25	0.04
	−3.25	0.04
	−3.22	0.04
	−3.25	0.04
	−3.31	0.05
	−3.30	0.05
	−3.33	0.05
Average	−3.26	
2 s.d.	0.09	
	n=19	

*Internal precision of a sample run during Se isotope analysis (over 40 cycles) is reported as 2 standard error (2 s.e.).

Table A.3.3 Se isotope and Se−Te concentration data of international rock reference material USGS (United States Geological Survey) BCR-2.

sample	rock type	$\delta^{82/76}Se_{NIST\ SRM\text{-}3149}$ (‰)	2 s.e.† (‰)	Se (ng g^{-1})	Te (ng g^{-1})
USGS BCR−2	basalt	0.04	0.07	79	2.5
		0.22	0.06	78	
		0.15	0.05	78	
		0.13	0.05	77	
	average	0.14		78	2.5
	uncertainty	0.15		2	0.08

†Internal precision on a sample run (over 40 cycles) is reported as 2 standard error (2 s.e.).

Table A.3.4 Se isotope and concentration data for multiple digested sample SEC 43-3) measured during different measurement sessions.

sample	Rock type	$\delta^{82/76}Se_{NIST\ SRM\text{-}3149}$ (‰)	2 s.e.* (‰)	Se (ng/g)
SEC 43-3	eclogite	-0.62	0.07	107
		-0.53	0.06	106
		-0.51	0.05	105
		-0.47	0.05	106
	average	-0.53		106
	uncertainty (2 s.d.)	0.13	(1 s.d.)	3

*Internal precision of a sample run during Se isotope analysis (over 40 cycles) is reported as 2 standard error (2 s.e.). Uncertainty of Se concentrations conservatively expressed as 3% r.s.d.

Table A.3.5 Individual Se isotope and Se−Te concentration data of samples from the Raspas complex.

sample	rock type	$\delta^{82/76}Se_{NIST\ SRM\text{-}3149}$ (‰)	2 s.e.† (‰)	Se (ng g^{-1})	Te (ng g^{-1})
SEC 43-3	eclogite	-0.62	0.07	107	2.15
		-0.53	0.06	106	
		-0.51	0.051	105	
		-0.47	0.049	106	
	average	*-0.53*		*106*	*2.15*
	uncertainty	*0.13*		*3*	*0.07*
SEC 44-1	eclogite	0.20	0.10	36	8.55
SEC 46-1	eclogite	-0.90	0.16	6.56	5.54
		-0.85	0.05	6.24	
	average	*-0.88*		*6.40*	*5.54*
	uncertainty	*0.07*		*0.20*	*0.17*
SEC 46-2	eclogite	-1.81	0.09	105	6.33
		-1.96	0.08	102	
	average	*-1.89*		*104*	*6.33*
	uncertainty	*0.21*		*3*	*0.19*
SEC 47-1	eclogite	0.30	0.09	144	6.19
		0.37	0.09	141	6.41
		0.40	0.06	138	
		0.34	0.06	139	
	average	*0.35*		*141*	*6.30*
	uncertainty	*0.08*		*4*	*0.19*
SEC 50-1	eclogite	-1.29	0.09	86	2.63
		-1.18	0.04	86	
		-1.19	0.06	85	
		-1.16	0.05	84	
	average	*-1.21*		*85*	*2.63*
	uncertainty	*0.12*		*3*	*0.08*
SEC 35-2	serpentinized peridoitite	0.11	0.08	45	7.46
		0.02	0.03	46	
	average	0.07		46	7.46
	uncertainty	0.13		1	0.22
SEC 36-2	serpentinized peridoitite	0.39	0.10	37	5.62
SEC 40-1	serpentinized peridoitite	0.35	0.08	69	9.15
		0.24	0.07	67	
	average	*0.30*		*68*	*9.15*
	uncertainty	*0.16*		*2*	*0.27*
SEC 45-3	metapelite	0.14	0.08	22	4.03

†Internal precision on a sample run (over 40 cycles) is reported as 2 standard error (2 s.e.).

Table A.3.6 Selected trace element data of metasediments from The Franciscan Complex and the Western Baja Terrane (Sadofsky and Bebout, 2003).

Site	Sample	Ce	Pb	Rb	Cs	Ce/Pb	Ce/Rb	Ce/Cs
Coast Ranges-Coastal								
97-1	VD-2A	63.1	24	166	14.5	2.6	0.4	4.4
97-1	VD-9B	46.5	14	81	2.6	3.3	0.6	17.9
98-1	KW98-21B	58.5	22	72	1.9	2.7	0.8	30.8
98-1	KW98-1	37.3	11	78	2.1	3.4	0.5	17.8
Coast Ranges-Central								
97-3	EEL4SH	55.9	16	101	5.8	3.5	0.6	9.6
97-3	EEL4GW	29.3	15	77	3.1	2.0	0.4	9.5
97-4	JC-4	44.6	18	90	3.2	2.5	0.5	13.9
97-4	JC-5	42.9	11	54	3.9	3.9	0.8	11.0
97-5	APC5A	51.3	14	39	2.2	3.7	1.3	23.3
97-5	AP8-6	19.5	23	74	4.5	0.8	0.3	4.3
Coast Ranges-Eastern								
97-6	CR-2B	34.4	14	44	2.4	2.5	0.8	14.3
98-5	AS2-B	15.1	15	48	1.8	1.0	0.3	8.4
97-7	ALDER2	30.8	12	48	2.6	2.6	0.6	11.8
97-8	T4	34.8	9	64	3.3	3.9	0.5	10.5
97-8	T8	48.6	22	86	5	2.2	0.6	9.7
Pacheco Pass Area								
	EP4	46.7	21	125	8.9	2.2	0.4	5.2
	EP6	25.5	22	83	3.5	1.2	0.3	7.3
	Q26F	40.4		14	0.5		2.9	80.8
	Q38	14.3	11	58	2.2	1.3	0.2	6.5
Western Baja Terrane-ST1								
	585-1	41.5	7	35	2	5.9	1.2	20.8
	585-14	22.9	15	65	3.8	1.5	0.4	6.0
	585-83A	21.2	11	29	1.4	1.9	0.7	15.1
	585-14B	29.7	12	50	2.3	2.5	0.6	12.9
Western Baja Terrane-ST2								
	585-138	39.7	11	51	1.7	3.6	0.8	23.4
	486-105	19.5	8	106	3.3	2.4	0.2	5.9
	585-71	18.2	21	36	1.7	0.9	0.5	10.7
Western Baja Terrane-ST3								
	585-133	29.3	8	13	0.7	3.7	2.3	41.9
	585-121	38.3	11	15	0.6	3.5	2.6	63.8
	585-179	34.6	9	55	1.7	3.8	0.6	20.4
	486-130	35.6	13	35	1.4	2.7	1.0	25.4
	average	35.7	14.5	63.1	3.15	2.68	0.783	18.1

Chemical Geology 466 (2017) 219–228

Contents lists available at ScienceDirect

Chemical Geology

journal homepage: www.elsevier.com/locate/chemgeo

A method for Se isotope analysis of low ng-level geological samples via double spike and hydride generation MC-ICP-MS

Timon Kurzawa*, Stephan König, Jabrane Labidi, Aierken Yierpan, Ronny Schoenberg

Isotope Geochemistry, Department of Geosciences, Eberhard Karls Universität Tübingen, Wilhelmstraße 56, 72074 Tübingen, Germany

ARTICLE INFO

Keywords:
Selenium isotopes
Heavy stable isotopes
Double spike hydride generation MC-ICP-MS
Mantle geochemistry

ABSTRACT

The isotopic signature of the chalcophile, redox-sensitive and moderately volatile element Se in geological materials may offer valuable new insights into the origin and evolution of volatiles in planetary systems. Here, we report a new method for Se isotope determination of low Se containing samples relevant to the Earth's mantle reservoir. We present a method that combines a double spike and hydride generation sample introduction system with a ThermoFisher Scientific® Neptune*Plus*™ MC-ICP-MS. The measurement routine takes advantage of methane injection in the instrument source during measurement, resulting in enhanced Se signals and suppression of polyatomic interferences. Purification of Se from natural samples was simplified by employing conventional ion exchange chromatography procedures. An external reproducibility of 0.15‰ (2σ) on $\delta^{82/76}$Se values for measurements performed on natural samples with Se abundances down to ~5 ng is obtained. We demonstrate that our technique allows the determination of Se isotope signatures of low Se-bearing geological materials with complex matrices such as mafic igneous rocks, which is essential to extend the Se isotopic investigation to Se-depleted planetary reservoirs such as the Earth's mantle.

1. Introduction

Selenium (Se) is a redox-sensitive element with the valence states −II, 0, +IV, +VI and a total of six stable isotopes (^{74}Se, ^{76}Se, ^{77}Se, ^{78}Se, ^{80}Se and ^{82}Se). The potential for Se isotopes to study low-temperature redox processes on the Earth's surface has been shown in various studies (Clark and Johnson, 2010; Ellis et al., 2003; Johnson and Bullen, 2003; Johnson and Bullen, 2004; Johnson et al., 2000; Johnson et al., 1999; Mitchell et al., 2013; Rouxel et al., 2004; Rouxel et al., 2002; Schilling et al., 2014; Schilling et al., 2011; Schilling et al., 2013; Shore, 2011; Wen and Carignan, 2011; Zhu et al., 2014). In addition, Earth's atmospheric redox evolution has more recently been studied by examining the redox state of the oceans using Se isotopes in the ancient sedimentary record (e.g. Kipp et al., 2017; Mitchell et al., 2016; Pogge von Strandmann et al., 2015; Stüeken et al., 2015a; Wen et al., 2014, and references therein). Moreover, Se isotope systematics have been evaluated as a possible tracer for the volatile evolution of meteoritic material and planetary reservoirs (Vollstaedt et al., 2016a; Vollstaedt et al., 2016b). To this end low Se containing planetary reservoirs such as the Earth's mantle need to be more firmly constrained and require new Se isotopic data which need to be placed in context of its elemental behavior.

In the Earth's mantle, Se is an ultra-trace element, with typical Se content < 100 ng g^{-1} in lherzolites (Lorand and Alard, 2010). Although small fractions of Se can be present in silicates (Tamari et al., 1990), Se mostly is concentrated in micrometric sulfides and is accordingly considered chalcophile (Hattori et al., 2002; König et al., 2014; Lorand et al., 2013; Luguet et al., 2004). In contrast to the highly siderophile elements (HSE, Os, Ir, Ru, Rh, Pt, Pd, Re, Au), studies involving Se in mantle-derived rocks are still relatively rare (Alard et al., 2011; Lorand and Alard, 2010; Lorand et al., 2003; Lorand et al., 2004; Morgan, 1986), although more recent high-precision isotope dilution studies on Se in fertile and depleted peridotites and pyroxenites have emerged (König et al., 2015a; König et al., 2014; König et al., 2012; Wang and Becker, 2013; Wang et al., 2013). These are complemented by geochemical and experimental studies on Se behavior during mantle melting (Brenan, 2015; Lissner et al., 2014; Marchesi et al., 2013).

The Se concentration in the Earth's mantle is estimated to be ~80 ng g^{-1} (McDonough and Sun, 1995; Wang and Becker, 2013). When normalized to a CI chondrite, the Se depletion degree is ~0.0037 × CI (Palme and O'Neill, 2003; Vollstaedt et al., 2016a), similar to but somewhat lower than what is observed for the HSEs (Becker et al., 2006). These elements altogether show a roughly chondritic pattern and an excess abundance in the Earth's mantle compared to those predicted following core-mantle differentiation (Lorand et al., 2008; Morgan et al., 2001; Walker, 2009). This is widely explained by

---

* Corresponding author.
E-mail address: timon.kurzawa@uni-tuebingen.de (T. Kurzawa).

http://dx.doi.org/10.1016/j.chemgeo.2017.06.012
Received 13 March 2017; Received in revised form 6 June 2017; Accepted 7 June 2017

late accretion of chondritic material (e.g. Kimura et al., 1974; Mann et al., 2012; Walker, 2009) shortly after core-mantle differentiation.

Due to its volatile character, Se links late accretion with the origin of other volatiles such as e.g. S, Te, Zn but also highly volatile components like H_2O, C, or N_2 (McDonough and Sun, 1995; Wang and Becker, 2013). Understanding the origin and evolution of Se in the Earth's mantle-crust-atmosphere system may thus help to constrain the origin of volatile components on Earth. However, it remains controversial whether the Se systematics in mantle rocks allow description of late accreted components (Wang and Becker, 2013), or metasomatic processes in the mantle (König et al., 2014; König et al., 2015b; Wang and Becker, 2015). A new perspective provided by the isotopic signature of Se may help in this context. Yet analyses remain challenging because igneous rocks contain orders of magnitudes lower Se concentrations in the range of 10 to 200 ng g^{-1} (König et al., 2014; Lissner et al., 2014) compared to sediments with µg g^{-1} levels of Se. Hence, an analytical technique is needed to precisely and accurately determine the Se isotope ratio of low abundance geological materials including igneous rocks such as basalts. Here we present a method for Se isotope measurements of such samples with Se concentrations of few tens of nanograms, using a double spike technique and a hydride generation introduction system on a Neptune*Plus*™ MC-ICP-MS.

2. Materials and analytical techniques

2.1. Reagents and materials

All sample digestions, chemical purifications and instrumental measurements were performed at the ISO-5 (US FED standards class 100) clean-room facilities of the Isotope Geochemistry Group at the University of Tübingen, Germany. De-ionized water was further purified with a Merck Millipore Milli-Q™ system to 18.2 MΩ × cm at 25 °C. All acids used during digestion, sample preparation and measurements were distilled from MERCK Millipore Emsure™ grade HNO_3 (65%) and HCl (37%) with Savillex™ DST-1000 Acid Purification Systems and diluted to required molarities to ± 0.03 mol L^{-1} as checked by titration. Eichrom® ion exchange resins, beakers, vials for centrifugation and analysis were pre-cleaned with multi-step HCl-HNO_3 treatments.

Two Se standard solutions with different Se isotopic compositions were used. The Se standard reference material SRM-3149 (Lot.-#: 100901; 10.042 ± 0.051 mg g^{-1}) was purchased from the National Institute of Standards and Technology (NIST). NIST SRM-3149 is now widely used as δ-zero reference material for Se isotope measurements (Carignan and Wen, 2007). The second standard solution used in our study is MH-495, previously used as an in-house Se solution at the University of Urbana, Illinois and generously provided by T. M. Johnson (Johnson and Bullen, 2004; Johnson et al., 1999). This standard solution was created from reagent-grade Se^0 pellets at the University of California at Davis by Mitchell Herbel (Johnson et al., 1999) and shows a $\delta^{82/76}$Se isotope ratio lower than the reference value for NIST SRM-3149 by −3.04 ± 0.50‰ (2σ, n = 2) (Carignan and Wen, 2007) to −3.44 ± 0.06‰ (2σ, n = 5) (Zhu et al., 2014).

For comparison to previously published Se isotope results we chose the two US Geological Survey (USGS) shale reference materials SGR-1 and SCo-1 (e.g. Pogge von Strandmann et al., 2014; Rouxel et al., 2002). These shales have relatively high Se concentrations (SGR-1: 3.50 ± 0.28 µg g^{-1}; SCo-1: 0.89 ± 0.06 µg g^{-1}) (Gladney and Roelandts, 1988) and comparison to other studies is possible (Kipp et al., 2017; Mitchell et al., 2012; Pogge von Strandmann et al., 2014; Rouxel et al., 2002; Schilling et al., 2011; Stüeken et al., 2013; Stüeken et al., 2015b; Stüeken et al., 2015c; Vollstaedt et al., 2016a). We also selected the USGS BCR-2 (~77.8 ± 6.4 ng g^{-1}, 2σ, n = 5) (Lissner et al., 2014), which has a factor 50 lower Se concentration compared to the USGS shales, can be compared to data reported by Rouxel et al. (2002) and is suitable as a geological reference to terrestrial basalts.

2.2. Sample digestion and Se purification

Between 10 and 1000 mg of sample powder were weighted into quartz glass vessels (15, 50 or 90 mL) and mixed with an adequate amount of the ^{74}Se-^{77}Se double spike solution. We report accuracy tests where variable amount of in-house standard solution MH-495 was additionally admixed to some samples (section 3.2). Depending on the sample weight 2.5 to 7.5 mL inverse aqua regia (3:1 M ratio; conc. HNO_3: conc. HCl) were added, the vessels were subsequently sealed with Teflon-tape and placed in a high-pressure asher (HPA-S, Anton Paar, Graz). During digestion for 16 h at 220 °C and 100 bar, Se was extracted from the sample material and equilibrated with the Se double-spike.

Several studies emphasize Se loss in the presence of HCl while evaporating at temperatures exceeding 80 to 85 °C (Layton-Matthews et al., 2006; Pogge von Strandmann et al., 2014; Rouxel et al., 2002; Stüeken et al., 2013; Wang et al., 2013). This is because of the formation of volatile Se-species (e.g. Stüeken et al., 2013; Vollstaedt et al., 2016a). Special care was taken during subsequent chemical purification: Se solutions were dried down without exceeding 65 °C and re-dissolved in concentrated HCl to convert all Se^{VI} to Se^{IV} (Elwaer and Hintelmann, 2008; Pogge von Strandmann et al., 2014).

Previous studies have demonstrated that the purification of Se from a sample matrix can be challenging in terms of quantitative recoveries from ion exchange resins and a potentially associated mass-dependent fractionation (e.g. Pogge von Strandmann et al., 2014). Thiol cotton fibre (TCF) or powder (TCP) is one way to separate Se from its sample matrix. This method allows recovering ≥98% of the initial Se (Elwaer and Hintelmann, 2008; Rouxel et al., 2002) and has been used for routine determination of Se concentrations of rock reference materials at low ng levels (e.g. König et al., 2012; Marin et al., 2001; Yu et al., 1983). The relatively high Se yield and the additional advantage of a simultaneous Te purification is considered a good choice for concentration analysis (Yu et al., 1983). The use of TCF/TCP can lead to the formation of insoluble salts and organic-derived interferences on Se masses (Pogge von Strandmann et al., 2014). Thus, TCF-/TCP-handled samples require careful treatment with HNO_3 and H_2O_2 (König et al., 2012; Pogge von Strandmann et al., 2014; Rouxel et al., 2002). In order to test the instrumental capabilities we here describe a simpler technique adapted from Fehr et al. (2004) and Wang et al. (2013). This involves the combination of conventional ion exchange chromatography procedures with hydride generation. The following procedure has been optimized for Se purification and yields.

First, the dried samples obtained after a first evaporation were dissolved with 4 mL 6 mol L^{-1} HCl and centrifuged at 5000 rpm for 10 min. Before loading the sample solutions onto Spectra/Chrom® Disposable MiniColumns containing 3 mL of Eichrom® AG 1-X8 anion resin (100-200 mesh), the resin was washed with 3 mL of 1 mol L^{-1} HNO_3 twice and conditioned with 2 × 3 mL 6 mol L^{-1} HCl. While Fe was retained as $FeCl_4^-$ by the resin, Se was not adsorbed but collected together with other matrix elements in 12 mL 6 mol L^{-1} HCl. The collected Se-containing solutions were evaporated to dryness at T ≤65 °C. The dried down solutions were then taken up in 4 mL 0.06 mol L^{-1} HNO_3 for purification by cation exchange chromatography using Spectra/Chrom® Disposable MiniColumns containing 3 mL of Eichrom® AG 50W-X8 resin (100-200 mesh) (e.g. Wang et al., 2013). The cation exchange resin was washed with 6 mol L^{-1} HCl and H_2O and conditioned with 6 mL 0.06 mol L^{-1} HNO_3 before loading the samples. Se was collected in 12 mL 0.06 mol L^{-1} HNO_3 while other matrix elements were retained on the resin under these conditions. The solutions containing Se were again dried at T ≤65 °C on a hotplate, re-dissolved in 2 mol L^{-1} HCl and heated in closed beakers on a hotplate at 80 °C for several hours to achieve complete reduction of Se^{VI} to Se^{IV} (Elwaer and Hintelmann, 2008; Pogge von Strandmann et al., 2014). Typically our total procedural blanks remain below detection limit and only in some cases show up to 1 ng, likely mirroring randomly

Table 1
Overview of Se double spike compositions used by different working groups.

Se masses	74	76	77	78	80	82
Pogge von Strandmann et al. (2014)[1] $^{74\text{-}78\text{-}77\text{-}82}$Se	**45.89%**	–	0.51%	**53.61%**	–	–
Pogge von Strandmann et al. (2014)[1] $^{78\text{-}82\text{-}76\text{-}77}$Se	**–**	0.14%	–	**15.61%**	–	**84.25%**
Vollstaedt et al. (2016a)[2] $^{74\text{-}77\text{-}78\text{-}82}$Se	**62.42%**	–	**37.56%**	0.02%	–	0.00%
Zhu et al. (2008)[3]; Schilling et al. (2011)[3]; Mitchell et al. (2012)[3]	**51.20%**	0.09%	**48.57%**	0.09%	0.03%	0.01%
This study[4] $^{74\text{-}77\text{-}78\text{-}82}$Se	**52.29%**	0.53%	**47.12%**	0.04%	0.02%	0.01%
Rudge et al. (2009) ideal composition for $^{74\text{-}77\text{-}78\text{-}82}$Se	**51.75%**	–	**48.25%**	–	–	–

Bold numbers indicate spike isotopes. Data acquisition at 1: Bristol Isotope Group, School of Earth Sciences, Bristol University, UK. 2: Institute of Geological Sciences, University of Bern, Switzerland. 3: Department of Geology, University of Illinois at Urbana-Champaign, Urbana. 4 (this study): Isotope Geochemistry, University of Tübingen, Germany.

suboptimal HPA-S glass vial treatment. While this still represents only < 1% of bulk Se for most samples analyzed here, multiple replicate digestions of all samples were performed in order to verify results with different blank levels including for lower Se containing samples. Although blanks are generally too low to determine an isotopic composition, high reproducibility for various blank levels confirms that blanks are negligible.

2.3. The role of the double spike

Enriched ^{74}Se and ^{77}Se tracer material in metal form was obtained from ISOFLEX. Upon dissolution in 2 mol L^{-1} HNO_3, a double spike solution with a composition of ~52% ^{74}Se and ~47% ^{77}Se was prepared taking the error propagation calculations after Rudge et al. (2009) into account. After dilution, the normality of nitric acid in the double-spike solution was 0.1 mol L^{-1}. Other Se isotopes account for < 1% of the double spike solution as shown in Table 1, which also gives a comparison to double spike compositions used in other studies. Provided that sample and spike are well equilibrated prior to chemical purification, double spike methods have already been demonstrated to be suitable for Se stable isotope analyses (Clark and Johnson, 2010; Johnson et al., 1999; Pogge von Strandmann et al., 2014; Vollstaedt et al., 2016a; Zhu et al., 2008).

The spike was calibrated against the NIST SRM-3149 Se solution. Various proportions of spike-sample ratios (f_{spike} from 0.1 to 0.9, n = 9) were tested. To increase the small volumes of NIST SRM-3149 and double spike, an additional 2 mL of 2 mol L^{-1} were added. To achieve equilibration the mixtures were heated at 80 °C in a closed beaker for a minimum of 2 h. The mixtures were then dried down at 65 °C and redissolved in 2 mol L^{-1} HCl, again heated at 80 °C for 2 h to ensure that all Se is reduced and finally measured. All measured mixtures of f_{spike} varying from 0.1 to 0.8 give $\delta^{82/76}$Se within our long-term reproducibility for NIST SRM-3149 of 0.00 ± 0.11‰ (2σ, n = 350) (filled circles in Fig. 1a). Note that the mixture with the lowest f_{spike} = 0.1 has a significantly larger internal uncertainty (2 s.e error bars in Fig. 1a) and the mixture with the highest f_{spike} = 0.9 is outside of the external reproducibility of 0.11‰ given by all other mixtures with f_{spike} between 0.2 and 0.8. This provides a lower and upper limit of acceptable double spike-sample ratios. Within the wide range of f_{spike} between 0.2 and 0.8 the ^{74}Se–^{77}Se double spike used in this study thus allows for accurate Se isotope measurements. A systematic shift to heavier $\delta^{82/76}$Se of 0.18 ± 0.10‰ (2σ, n = 7) is observed for mixtures that were not allowed to equilibrate as described above (open circles in Fig. 1a), but directly dried down after mixing. This may be due to preferential loss of light Se isotopes during evaporation, even at temperatures below 65 °C, prior to full equilibration of standard and spike Se and emphasizes that careful treatment is crucial.

Based on the above observation, we further tested the possibility of Se isotope fractionation during partial Se loss by evaporation from solutions with HCl. For this, NIST SRM-3149 solutions were dried down at 65 °C without spike addition. The Se isotope measurements were then performed with two different analytical approaches, one involving the sample-standard bracketing (SSB) (Stüeken et al., 2013) and the other

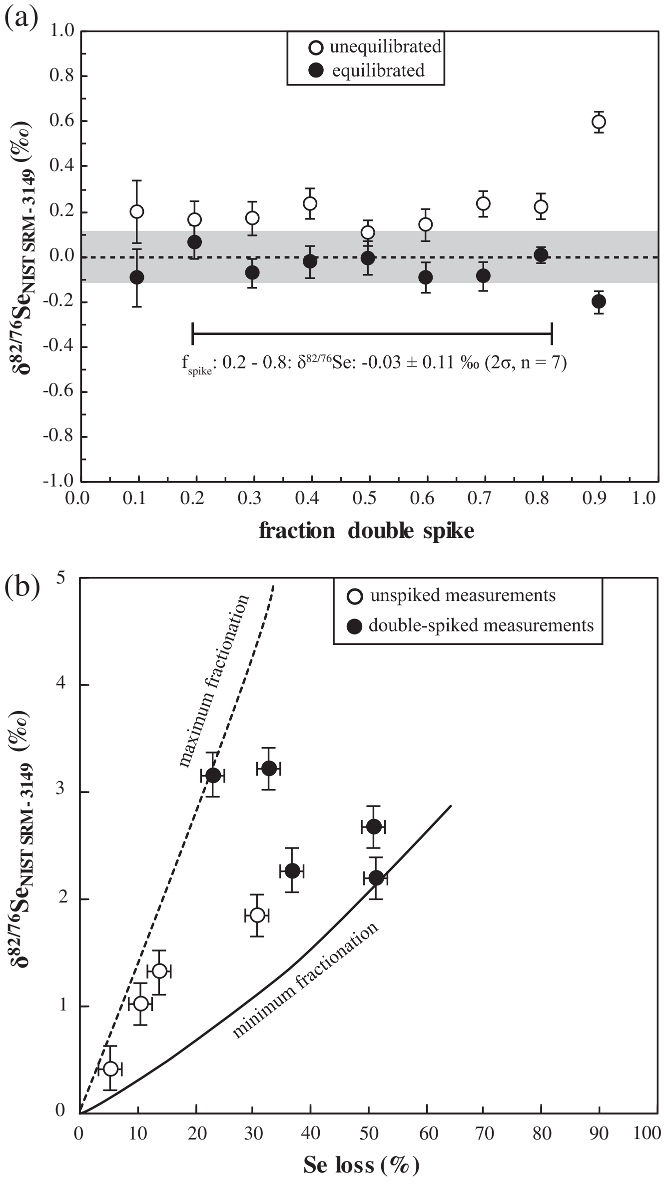

Fig. 1. (a) Measured $\delta^{82/76}Se_{NIST\ SRM-3149}$ as a function of various proportions of double spike (filled circles). The results indicate that even significantly underspiked (f_{spike} = 0.2) or overspiked (f_{spike} = 0.8) standards yield accurate data. Grey box represents the long-term average for $\delta^{82/76}Se_{NIST\ SRM-3149}$ of 0.00 ± 0.11‰ (2σ, n = 350). Unfilled circles show measured $\delta^{82/76}Se_{NIST\ SRM-3149}$ for unequilibrated mixtures of standard and double spike Se, resulting in isotopic shift towards heavier values of 0.10 to 0.60‰. Error bars are internal errors (2 s.e.) for each measurement. (b) $\delta^{82/76}Se_{NIST\ SRM-3149}$ as a function of evaporative loss of light Se isotopes. Results indicate unpredictable loss-induced fractionation between solution and vapor even at 65 °C and thus illustrate the requirement for double spike use in our experimental set up. Unfilled circles represent data from SSB measurements. Filled circles represent double spike measurements (section 2.3). Uncertainty on data is 0.20‰ (2σ). See section 2.3 for details.

the double spike measuring method (e.g. Pogge von Strandmann et al., 2014; Vollstaedt et al., 2016a). For the SSB approach a 50 ng mL^{-1} NIST SRM-3149 Se solution was used as the bracketing standard, yielding ^{82}Se voltages of roughly 1.5 V (using an amplifier resistor of 10^{11} Ω). Sample solutions were then prepared to match the signal intensity of the standard within 10% intensity. Samples and standards were measured for 100 cycles each having an integration time of 4.194 s. Over the measurement session, Se in-house solution (MH-495) was measured versus the NIST SRM-3149 standard solution. These solutions were taken directly out the main batch and were not dried. SSB measurements yielded average $\delta^{82/76}$Se of −3.25 ± 0.03‰ (2σ, n = 4), indistinguishable from our double-spike value (MH-495: −3.27 ± 0.13‰, 2σ, n = 100) (see section 3.1). For the SSB approach, four solutions were processed and Se losses varying between 5 and 30% yielded $\delta^{82/76}$Se values ranging between 0.43 ± 0.31‰ and 1.85 ± 0.31‰ (Fig. 1b, open circles). For the double spike measuring approach, five NIST SRM-3149 solutions were doped with an adequate amount of the double spike after evaporation and prior to mass spectrometric determinations, which were performed on ~15 ng mL^{-1} Se solutions. Evaporative Se losses between 23 and 51% with $\delta^{82/76}$Se values ranging between 2.20 ± 0.20‰ and 3.20 ± 0.20‰ were determined by the double spike measurements (Fig. 1b, filled circles).

The data of our two experiments cannot be explained by a single unidirectional fractionation process as they do not fit a single Rayleigh evaporation function. The data rather indicate Rayleigh distillations with variable isotopic fractionations $\Delta_{\text{vapor-solution}}$ ranging between 3 and 12‰ (Fig. 1b). If the theoretical fractionation associated with evaporation corresponds to the square root of the evaporated molecule masses (Richter, 2004; Young et al., 2002), the inferred fractionations seem consistent with evaporation of pure $SeCl_2$ (fractionation $\Delta_{\text{vapor-solution}}$ of ~13‰) and pure $SeCl_6$ (fractionation $\Delta_{\text{vapor-solution}}$ of ~7‰). Future studies are needed to evaluate the exact speciation of evaporated selenium species. The origin of evaporative loss of Se remains unclear, but our experiments clearly demonstrate a significant loss of preferentially isotopically light Se during evaporation of pure reference materials. However, the double spike approach inherently corrects for such chemistry-induced fractionations.

2.4. Mass spectrometry (MC-ICP-MS)

2.4.1. Instrumental parameters and set up

Isotope measurements were conducted on a ThermoFisher Scientific® Neptune*Plus*™ multi-collector inductively coupled plasma mass spectrometer linked with a CETAC® HGX 200 hydride generator, an ESI MP2-6 peristaltic pump and an ESI SC-μ DX autosampler. To obtain the highest Se sensitivity at high front vacuum a nickel skimmer cone (H-cone) and a Ni-Jet sample cone were employed. Daily tuning included the gas flows and torch positions. Typical parameters and settings are listed in Table 2. Measured masses include interference monitors for hydrides and argon dimers as generated in the plasma (Table 3). Signal intensities given in V were obtained using amplifier resistors of 10^{11} Ω.

2.4.2. Hydride generation

One of the major advantages of a hydride introduction system is the efficient transport of Se into the plasma under dry conditions (Johnson and Bullen, 2004). The hydride generator serves as Se signal booster and as a purification device, because exclusively hydride-forming elements (e.g. Se, As, Ge) are effectively transferred to the plasma (Clark and Johnson, 2008). A sodium borohydride solution is prepared by adding 1 g of $NaBH_4$ (analysis grade) to 250 mL of 18.2 MΩ-grade water. To stabilize the solution, 1 g of sodium hydroxide monohydrate is added. In our setup, constant flows of 2 mol L^{-1} HCl and sodium borohydride ($NaBH_4$; 0.4% (m/m)) are mixed in a coil which results in a steady production of hydrides throughout an entire measurement session. To this constant hydride-generating mixture the sample is then additionally introduced in 2 mol L^{-1} HCl and H_2Se is formed according to reaction (1) that can be ionized efficiently.

Table 2
Operating parameters.

Parameters	
RF power (W)	1200
Acceleration voltage (V)	−10,000
Sample cone	Ni Jet
Skimmer cone	Ni H-type
Ar gas flow rates (L min^{-1})	
Coolant	15
Auxiliary	0.7–1.0
Sample gas	0.24–0.56
Additional gas	0.48–0.56
Methane (mL min^{-1})	2.0–3.5
Analyte matrix	2 mol L^{-1} HCl
$NaBH_4$	0.4% (m/m)
Sample uptake (mL min^{-1})	0.235
Conc. sample solution (ng mL^{-1})	≤15
Sample solution volume (mL)	1
Cycle integration time (s)	4.194
Number of cycles per analysis	40
Intensity ^{82}Se (V)	0.5

$$4\,H_2SeO_{3(aq)} + 3\,HCl_{(aq)} + 3\,NaBH_{4(aq)} \rightarrow 4\,H_2Se_{(g)} + 3\,H_3BO_{3(aq)} + 3\,H_2O_{(aq)} + 3\,NaCl_{(aq)} \quad (1)$$

Residual non-hydride forming matrix elements that remain in the sample solution after chemical purification are fully excluded via a gas/liquid separator while hydrides are carried to the plasma in an argon flux (Fig. 2). In addition to argon for the plasma and to act as the sample carrier gas, we also introduced methane because it enhances the sensitivity for Se as shown in previous studies (e.g. Floor et al., 2011). In our instrumental setup, an increase of the Se signal by a factor two to three was achieved.

2.4.3. Analyses, interference corrections and double spike deconvolution

Instrument parameters were optimized for high Se signal intensities and low Argon dimers before each measurement session. Typical signals on ^{82}Se of a 15 ng mL^{-1} solution with the operating conditions summarized in Table 2 are 0.5 V. Each measurement consists of 40 cycles with 4.194 s integration time. Washout time was generally set to 4 min. All measurements of standards and samples were bracketed by background (on-peak zero) measurements of the same batch of pure 2 mol L^{-1} HCl in which standards and samples were taken up. On-peak zeros were subtracted from measured intensities of standards and samples. Measurements of NIST SRM-3149 standard solutions were performed between each sample to assess potential instrumental drift. Additionally, standard solution MH-495 was measured after every 5th sample. Following acquisition of isotope signal intensities the data was further reduced offline. A major issue of stable Se isotope measurements are the numerous single-mass polyatomic isobaric interferences that typically form in plasma source mass spectrometers in the mass range of Se isotopes and interference monitors (Table 3). These spectral interferences can be divided into (i) plasma induced, (ii) plasma and analyte matrix induced and (iii) analyte and sample matrix induced.

The subtraction of on-peak zero signals determined on pure analyte matrix solutions (i.e. 2 mol L^{-1} HCl) from sample signals adequately accounts for the small interferences of Kr and ArCl. On-peak zero subtraction, however, does not allow accurate correction of the large ArAr interferences due to the considerable fluctuations in the plasma energy between and within sample runs. We typically observe $^{40}Ar^{40}Ar^{+}$ signals of 20–25 V, with variations of this signal from scan to scan of ± 0.15 V due to plasma fluctuations. We therefore employed a two-step strategy for accurate correction of Ar dimer interferences:

(1) We admixed methane to the sample Ar gas carrying the SeH_2 from the hydride generator to the plasma torch (Fig. 2). Enhancement

Table 3
Measured masses and associated isobaric interferences.

Cups	L4	L3	L2			L1	C		H1	H2	H3	H4
Masses	72	73	74	75	76	77	78	79	80	81	82	83
Selenium			^{74}Se		^{76}Se	^{77}Se	^{78}Se		^{80}Se		^{82}Se	
Abundance (%)			0.87		9.36	7.63	23.78		49.61		8.73	
(i) Plasma induced												
Kr							^{78}Kr		^{80}Kr		^{82}Kr	^{83}Kr
	^{36}Ar^{36}Ar		^{38}Ar^{36}Ar		^{40}Ar^{36}Ar		^{40}Ar^{38}Ar		^{40}Ar^{40}Ar			
ArAr					^{38}Ar^{38}Ar							
(ii) Plasma and analyte matrix induced												
		^{36}Ar^{36}ArH		^{38}Ar^{36}ArH		^{40}Ar^{36}ArH		^{40}Ar^{38}ArH		^{40}Ar^{40}ArH		
ArArH						^{38}Ar^{38}ArH						
		^{38}Ar^{35}Cl		^{40}Ar^{35}Cl		^{40}Ar^{37}Cl						
ArCl		^{36}Ar^{37}Cl		^{38}Ar^{37}Cl								
(iii) Analyte and sample matrix induced												
FeO	^{56}Fe^{16}O		^{58}Fe^{16}O									
NiO			^{58}Ni^{16}O		^{60}Ni^{16}O		^{62}Ni^{16}O		^{64}Ni^{16}O			
ZnO									^{64}Zn^{16}O		^{66}Zn^{16}O	^{67}Zn^{16}O
Se-H				^{74}SeH		^{76}SeH	^{77}SeH			^{80}SeH		^{82}SeH
Ge	^{72}Ge	^{73}Ge	^{74}Ge		^{76}Ge							
Br-H									^{79}BrH		^{81}BrH	
As-H					^{75}AsH							

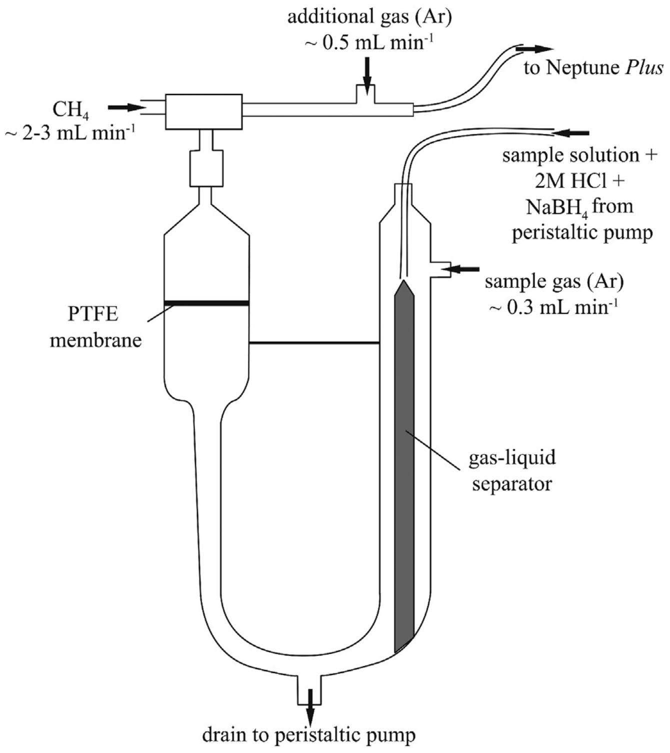

Fig. 2. Schematic set up of the hydride generator system.

of Se signal and suppression of polyatomic interferences by methane addition for Se concentration and isotope ratio measurements has been described in previous studies (Fliegel et al., 2011; Floor et al., 2011; Guo et al., 2013). We indeed observed an approximately two- to three-fold increase in Se signal intensities and a decrease in Ar dimer intensities by a factor of two with an addition of 2.0–3.5 mL min^{-1} methane to the instrument. This significantly suppressed Ar dimer signals allowed more accurate on-peak zero corrections of polyatomic Ar interferences. Furthermore, hydride interferences ($ArArH^+$, SeH^+, GeH^+, BrH^+, AsH^+) dropped to negligible levels by methane addition making subsequent correction of hydrides after on-peak zero subtraction unnecessary.

(2) We employed a secondary correction for Ar dimer interferences as described by Elwaer and Hintelmann (2008), which takes plasma energy fluctuations into account. We used the ^{82}Se signal to predict the ^{80}Se signal of the samples by artificially fractionating the ^{82}Se/^{80}Se ratio using the samples' instrumental mass bias. Assuming IUPAC Se isotope composition (Berglund and Wieser, 2011) the ^{80}Se signal of the sample is estimated and subtracted from the signal measured at m/z = 80 to estimate the excess or deficit in $^{40}Ar^{40}Ar^+$ compared to the on-peak zero measurement. Signals of the minor Ar dimers (i.e. $^{36}Ar^{36}Ar^{+}$, $^{38}Ar^{36}Ar^+$, $^{38}Ar^{38}Ar^+$, $^{40}Ar^{36}Ar^+$ and $^{40}Ar^{38}Ar^+$) are then determined relative to the calculated $^{40}Ar^{40}Ar^+$ signal considering the relative abundance of Ar isotopes (Berglund and Wieser, 2011). For measurements on 15 ng mL^{-1} sample solutions this correction improves the external 2σ reproducibility on $\delta^{82/76}$Se values by 20 to 30%. We tested the necessity to artificially fractionate Ar isotope ratios to account for the instrumental mass bias. We assumed that at a first order, Ar and Se are subject to equal isotope fractionations in the instrument plasma, which per se is not entirely correct. Since this artificial fractionation of Ar isotope ratios only resulted in shifts of 0.001 to 0.002‰ for both sample and standard solutions. This therefore means that the possible occurrence of Ar isotopic fractionation in the plasma has a negligible effect on our Se isotope data correction. Consequently, for routine measurements, possible Ar isotopic fractionations were ignored. The calculated ArAr interferences were arithmetically subtracted from measured Se signal intensities.

The iterative double spike deconvolution calculations used first by Compston and Oversby (1969) for Pb isotopes were applied to correct the measured Se isotope data with the exception that exponential rather than linear law was used as a proxy for the instrumental mass bias. Apart from the two spike isotopes ^{74}Se and ^{77}Se, ^{78}Se and ^{82}Se were used for the deconvolution. All isobaric interferences (e.g. Ge correction, see below) and the fluctuations of Ar dimers were iteratively converged within the double spike deconvolution for accurate corrections. The double spike deconvolution yields three types of information: (i) an exponential fractionation factor (per amu) for the instrumental mass bias, which might also include a mass-dependent Se isotope fractionation during chemical purification of the sample. (ii) An exponential fractionation (per amu) for the samples' natural mass-dependent fractionation compared to NIST SMR-3149 against which the double spike was calibrated. From this factor the samples' natural Se isotope ratios are calculated and can be reported in the δ-notation as the per mil difference in these ratios compared to that of the isotopically certified reference material NIST SRM-3149. The samples' natural isotope ratios are calculated according to eq. (2) and can be converted to any ratio per amu as a function of the exact masses of ^{82}Se, ^{78}Se and

^{76}Se (Young et al., 2002). (iii) The spike-to-sample ratio from which, knowing the Se concentration of the double spike, an accurate Se concentration for the sample can be calculated.

$$\delta^{82/78}Se = [(^{82}Se/^{78}Se)_{sample}/(^{82}Se/^{78}Se)_{NIST\ SRM-3149} - 1] \times 1000 \qquad (2)$$

2.4.4. *Accuracy of isobaric interference correction of ^{74}Ge on ^{74}Se*

Germanium like Se forms hydrides (GeH_4) leading to isobaric interferences of ^{74}Ge on ^{74}Se and ^{76}Ge on ^{76}Se during mass spectrometric analyses. We observed the Ge correction to be unnecessary if the measured Ge/Se ratio is smaller than 0.0001 when measuring 15 ng mL^{-1} sample solutions: below this threshold, Ge signals are below 0.5 mV on mass 72 and appear to be indistinguishable from background noise. Correcting for this signal only adds uncertainty to the internal precision of the $\delta^{82/76}Se$ value without significantly changing it. At Ge/Se ratios above this threshold value, the canonical $^{72}Ge/^{74}Ge$ ratio of 0.7521 (Berglund and Wieser, 2011) was artificially fractionated using the instrumental mass bias determined for Se to correct ^{74}Se from the isobaric interference of ^{74}Ge. However, the instrumental mass bias for Se also includes the mass-dependent Se isotope fractionation induced by the chemical purification when Se recovery is incomplete. Furthermore, the chemically induced mass-dependent isotope fractionation of Ge is likely different from that of Se. As a result, this correction is only applied to Ge/Se ratios < 0.0056. We set this value as it still yields accurate data for Se mass bias corrected data. Above this upper threshold value for the Ge/Se ratio (see. Fig. 3) for 15 ng mL^{-1} measurement solutions, signal intensities of ^{72}Ge and ^{73}Ge become large enough (> 2 mV on mass 72) to accurately determine the mass-dependent instrumental mass bias and chemical fractionation of Ge assuming a canonical $^{72}Ge/^{73}Ge$ of 0.2823 (Berglund and Wieser, 2011). To test the accuracy of our Ge interference correction method, 15 ng mL^{-1} NIST SRM-3149 solutions were mixed with different amounts of a pure Ge in-house standard solution, similar to a previous approach described by Pogge von Strandmann et al. (2014). As illustrated in Fig. 3 the values of the Ge-doped NIST SRM-3149 solutions perfectly lie within the external reproducibility for this standard of 0.00 ± 0.11‰ to Ge/Se ratios of up to 4, showing that this method accurately corrects any Ge interference.

3. Results and discussion

3.1. *Se isotope measurements of matrix-free standard solutions*

Background or "on-peak zero" (OPZ) corrections have been used in Se isotope analytical studies to account for plasma and other instrumental interferences (e.g. Johnson, 2004; Rouxel et al., 2002; Zhu et al., 2008). Previously performed scans on an Element 2 ICP-MS at high resolution (m/Δm = ~10,000, 5–95% peak edge width) resolved Se and ArAr peaks and observed constant voltage on ArAr peaks regardless of whether Se was introduced in the plasma (Pogge von Strandmann et al., 2014). This was argued to justify the use of OPZ correction. We performed Se isotopic measurements while using the OPZ correction on our MC-ICP-MS in low (LR) and medium resolution (MR) mode (m/Δm = ~2000 vs. MR: m/Δm = ~7000, respectively, 5–95% peak edge width). The MR measurements allow crude resolution of Se and ArAr peaks but yielded indistinguishable isotope results than in LR mode. This confirms the validity of the OPZ correction and demonstrates that measurements in LR produce precise and accurate data as previously suggested (Pogge von Strandmann et al., 2014).

Over a period of over 6 months that included LR and MR measurements, a long-term average and reproducibility for MH-495 of $\delta^{82/76}Se = -3.27 \pm 0.13$‰ (2σ, n = 100) is obtained (Fig. 4). This is consistent with recently published values following double-spike measurements (−3.44 ± 0.06‰; 2σ, n = 5) (Zhu et al., 2014) and within uncertainty of an earlier study using standard-sample bracketing measurements (−3.04 ± 0.50‰, 2σ, n = 2) (Carignan and Wen, 2007).

3.2. *Accuracy tests*

Despite a quantitative removal of matrix elements by ion exchange chromatography and hydride generation, potential matrix effects may not be always ruled out because droplets from excess liquid could occasionally pass the PTFE-membrane of the hydride generation system. Although negligible voltages were observed on the masses of chloride

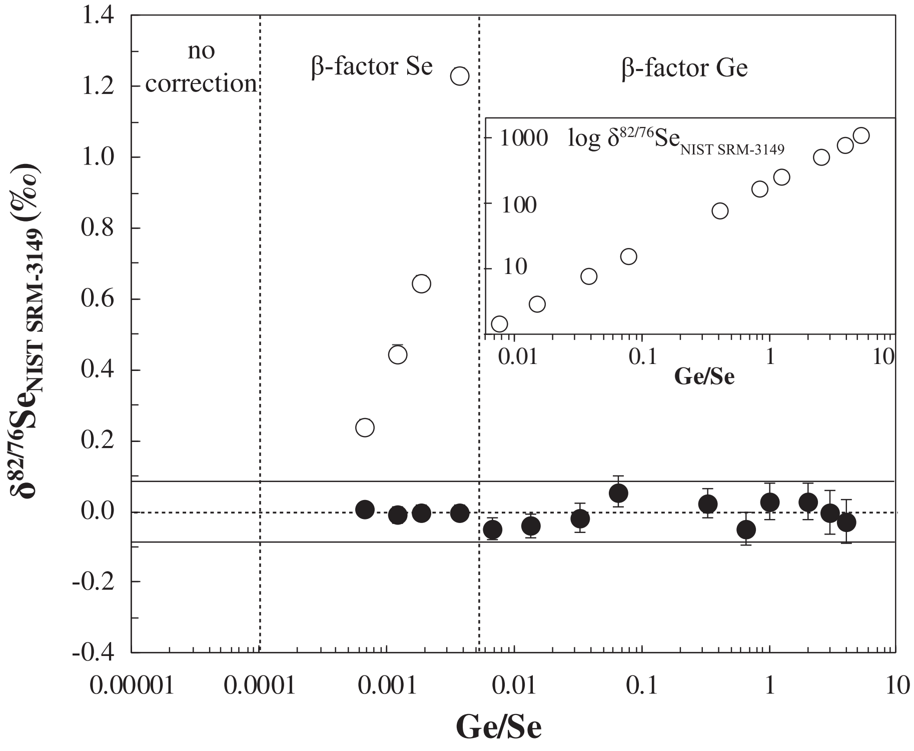

Fig. 3. Results of measurements of Se standard solution NIST SRM-3149 doped with different amounts of Ge. The constant range of $\delta^{82/76}Se$ shows efficient correction even for Ge/Se ratios of up to 4. Grey bar represents 2σ (0.08‰) of obtained $\delta^{82/76}Se_{NIST\ SRM-3149}$ data, whereas error bars are in-run errors (2 s.e.) of single measurements. Dashed lines indicate threshold values for correction with Se or Ge mass bias, respectively. Unfilled symbols indicate uncorrected $\delta^{82/76}Se_{NIST\ SRM-3149}$ (uncorrected data for Ge/Se > 0.0056 given in logarithmic scale as isotopic shift is > 1.3 to 1006‰).

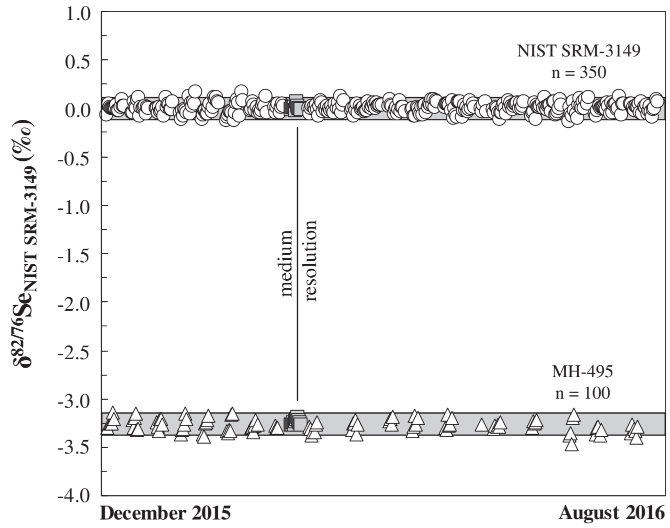

Fig. 4. Long-term reproducibility of NIST SRM-3149 ($\delta^{82/76}Se_{NIST\ SRM\text{-}3149}$: 0.00 ± 0.11‰, n = 350) and MH-495 ($\delta^{82/76}Se_{NIST\ SRM\text{-}3149}$: −3.27 ± 0.13‰; n = 100). Grey bars represent 2σ uncertainties. Measurements in MR yield indistinguishable data compared to data acquired in LR, showing that LR measurements are sufficient for precise and accurate Se isotope data acquisition.

(^{35}Cl and ^{37}Cl), the likely main constituent of such droplets, we tested the effect of variable matrix/Se ratios by adapting a standard addition method employed previously (Nielsen et al., 2004; Schumann et al., 1992; Tipper et al., 2008). Increasing amounts of MH-495 were admixed to constant amounts of NIST SRM-3149, homogenized (see section 2.3), re-dissolved and measured. Unresolved polyatomic interferences from the carrier solutions and/or gases would lead to samples arbitrarily plotting off a two-component mixing line. Here we show that mixtures remain within uncertainty of 0.20‰ (2σ) (Fig. 5a), which argues against the contribution of unresolved interferences.

In addition, we performed accuracy tests involving USGS reference material SGR-1. Increasing amounts of SGR-1 (20 to 40 mg or 70 to 140 ng total Se) were mixed to given amounts of standard solution MH-495. Measured and calculated Se isotope compositions remain within uncertainty of 0.20‰ (2σ) and confirm that potential matrix-induced interferences are negligible (Fig. 5b).

3.3. Exploring the minimum Se required for accurate isotope measurements

A major goal is to determine Se isotope compositions of samples with low Se concentrations such as basalts (< 200 ng g^{-1}, see below). Before this is attempted, the minimum Se required for measurement was evaluated in a first step by analyzing 1 mL solutions of 50 to 3 ng mL^{-1} of MH-495 standard solution (filled circles in Fig. 6). Measured signals on ^{82}Se ranged from 0.1 to 1.5 V and showed no correlation with $\delta^{82/76}$Se of MH-495. It is however observed that the uncertainties vary with signal intensities: Solutions with a minimum of 15 ng mL^{-1} concentrations and > 0.5 V on mass ^{82}Se (lowest abundant mass measured) show internal errors of 0.04‰ (2 s.e., n = 6) and yield an external reproducibility of 0.09‰ (2σ, n = 6). Solutions between 15 and 7.5 ng mL^{-1} show a higher internal error of up to 0.08‰ (2 s.e., n = 5) and the external reproducibility increases to 0.12‰ (2σ, n = 5). When the ^{82}Se signal is below 0.18 V, equivalent to solutions below 7.5 ng mL^{-1}, the internal error increases to 0.12‰ (2 s.e., n = 7) and the external reproducibility becomes > 0.20‰ (2σ, n = 7). Hence, the external reproducibility systematically changes at a concentration of approximately 7.5 ng mL^{-1}. While it is desirable to measure sample solutions with higher than 15 ng total Se, we show the instrumental capability to yield 0.24‰ (2σ, n = 7) external reproducibility for down to 3 ng total Se. This is similar to results of a previous study by Zhu et al. (2008) using a different set up.

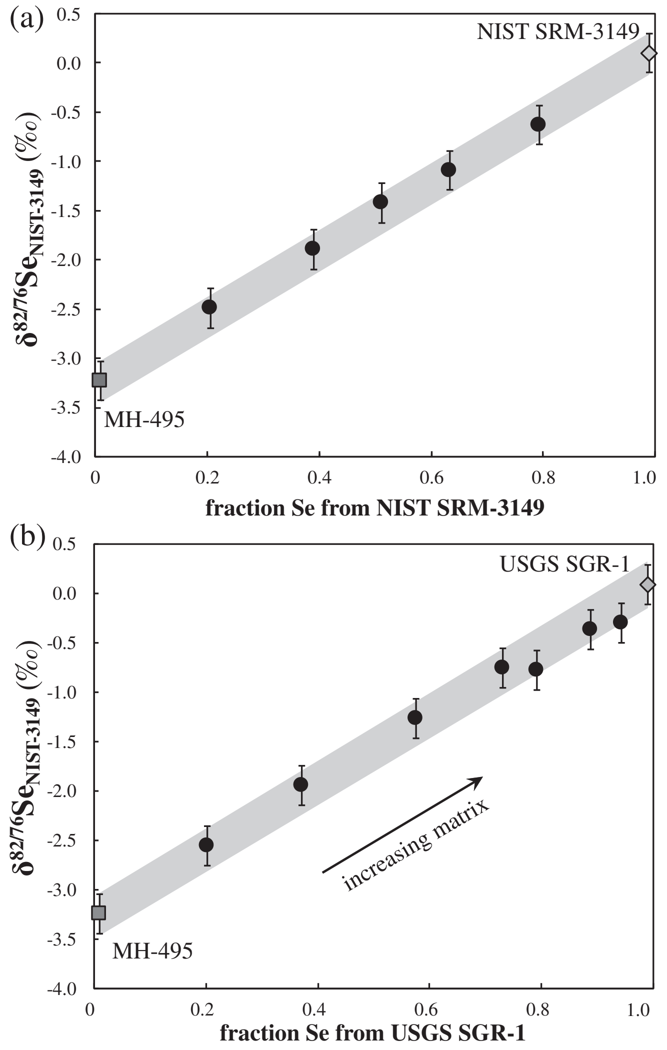

Fig. 5. Results for Se isotope measurements of mixtures between (a) standard solutions MH-495 and NIST SRM-3149 and (b) increasing amounts of sample SGR-1 (20 to 40 mg or 70 to 140 ng total Se) and constant amounts of standard solution MH-495. Doped solutions fall on a mixing line between endmembers within maximum uncertainty of 0.20‰ (2σ), indicating no bias despite increasing matrix over total Se and potential emergence of interferences above background. Endmember data taken from same measurement session.

Analogue to measurements of various amounts of MH-495 we performed tests with USGS reference material SGR-1 (unfilled circles in Fig. 6). This involved the digestion of 100 mg SGR-1 (equivalent to ~350 ng total Se, section 2.2) and dilution to various concentrations (from 50 ng mL^{-1} to 5 ng mL^{-1}). As for standard solution MH-495, the internal errors and the external reproducibility depend on signal intensities. Again, total Se contents with a minimum of 15 ng mL^{-1} yield internal errors of 0.04‰ (2 s.e., n = 4) and an external reproducibility of 0.06‰ (2σ, n = 4), whereas down to 7.5 ng mL^{-1} total Se analyzed yield internal errors of 0.07‰ (2 s.e., n = 4) and an external reproducibility of 0.14‰ (2σ, n = 4). Below 7.5 ng mL^{-1} the ^{82}Se signal intensities are < 0.18 V and the internal error increases to 0.10‰ (2 s.e., n = 6) and the external reproducibility is > 0.14‰.

This reproducibility obtained with a NeptunePlus™ instrument is similar to that previously reported for other instruments where similarly small quantities were analyzed (5 ng total Se analyzed with 0.25‰ (2σ) on $\delta^{82/76}$Se on a Micromass IsoProbe by Rouxel et al. (2002) and on a NuPlasma by Zhu et al. (2008) (4 ng total Se analyzed with 0.10‰ (2σ) for standard solutions MH-495 and NIST SRM-3149 and 0.15–0.20‰ (2σ) for natural samples).

Measurements of USGS reference shales (SGR-1 and SCo-1) allow

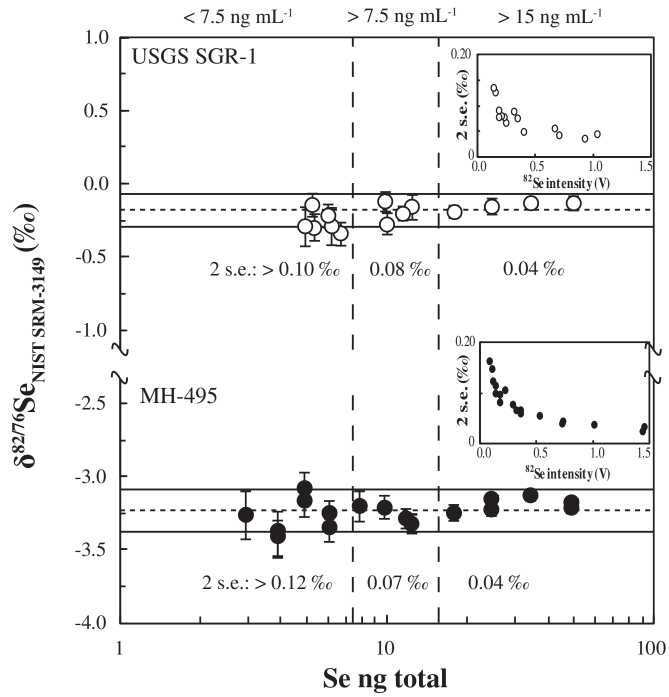

Fig. 6. Results and signal-dependent external reproducibility for measurements of various dilutions of the MH-495 standard solution (filled circles) and 100 mg digested USGS rock reference material SGR-1 (unfilled circles). Error bars represent 2 standard errors (2 s.e.) of the individual measurements. Black dashed horizontal lines represent average value of dilutions > 7.5 ng mL^{-1} as these are characterized by decent internal errors. Black solid horizontal lines are 2σ uncertainties. Vertical dashed lines divide dilutions into < 7.5 ng mL^{-1}, 7.5–15 ng mL^{-1} and > 15 ng mL^{-1}, which are characterized by different internal errors (2 s.e) and external reproducibility (see section 3.3).

comparison to previous studies (Kipp et al., 2017; Mitchell et al., 2012; Pogge von Strandmann et al., 2014; Pogge von Strandmann et al., 2015; Rouxel et al., 2002; Schilling et al., 2011; Stüeken et al., 2013; Stüeken et al., 2015b; Stüeken et al., 2015c; Vollstaedt et al., 2016a) and have relatively high Se abundances (SGR-1: 3.50 ± 0.28 μg g^{-1}; SCo-1: 0.89 ± 0.06 μg g^{-1}) (Gladney and Roelandts, 1988).

Both our obtained concentrations (SGR-1: 3.76 ± 0.32 μg g^{-1}, 2σ, n = 9; SCo-1: 0.84 ± 0.06 μg g^{-1}, 2σ, n = 5) and isotopic compositions (SGR-1: −0.08 ± 0.20‰, 2σ, n = 9; SCo-1: −0.18 ± 0.22‰, 2σ, n = 5) are within error of most previous studies (see Fig. 7) (Kipp et al., 2017; Mitchell et al., 2012; Pogge von Strandmann et al., 2014; Rouxel et al., 2002; Savard et al., 2009; Schilling et al., 2011; Stüeken et al., 2013; Stüeken et al., 2015b; Stüeken et al., 2015c; Vollstaedt et al., 2016a) and demonstrate full homogenization of sample with double spike Se. The USGS SGR-1 batch (USGS SGR-1, Split 25, Position 8) used in this study may be affected by heterogeneity. This may explain better reproducibility for repeated isotope measurements on diluted solutions from the same sample digestion, compared to solutions from separately digested material. Therefore, our values for samples (Fig. 7 and Table 4) that were obtained from separately digested material in different measurement sessions over a period of 9 months provide a long-term external reproducibility.

3.4. *Selenium measurements of samples with concentrations in the ng g^{-1} range*

In order to test our method on low Se containing samples with a matrix relevant to mantle derived rocks, USGS reference basalt BCR-2 is suitable (78 ± 3.2 ng g^{-1}, 1σ, n = 5) (Lissner et al., 2014). For this we weighted, double-spiked and digested 300 mg of BCR-2 (equivalent to ca. 25 ng total Se). Our batch of BCR-2 (3223) yields a Se concentration of 71 ± 4 ng g^{-1} (1σ, n = 3, Table 4), which is within uncertainty to

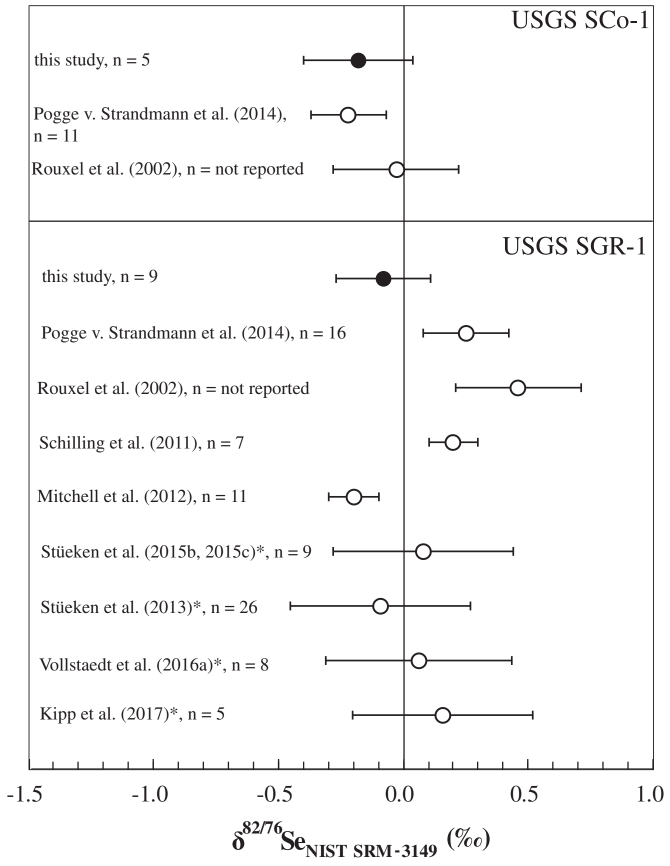

Fig. 7. Compiled Se isotope data for USGS shales SCo-1 and SGR-1. Filled symbols represent results from this study, combining 5 analytical sessions over a period of 9 months (SCo-1: −0.18 ± 0.22‰, n = 5; SGR-1: −0.08 ± 0.19‰, n = 11), providing a long-term external reproducibility for data obtained in our study. Unfilled symbols are data taken from the literature. All error bars indicate 2σ analytical reproducibility; errors where converted to 2σ where data was given in 1σ (e.g. Stüeken et al., 2013, 2015b, 2015c; Kipp et al., 2017). * = Data reported as $\delta^{82/78}$Se was converted to $\delta^{82/76}$Se.

Table 4
Se isotope and concentration data for USGS reference materials SGR-1, SCo-1 and BCR-2.

Sample	Sample type	Se (μg g^{-1})	$\delta^{82/76}$Se (‰)	2 s.e (‰)	$\delta^{82/78}$Se (‰)	2 s.e (‰)
USGS SGR-1	Shale	3.70	0.09	0.04	0.06	0.03
		3.63	−0.08	0.05	−0.05	0.03
		3.49	−0.05	0.05	−0.03	0.03
		3.84	−0.18	0.08	−0.12	0.05
		3.95	−0.17	0.07	−0.11	0.05
		4.03	−0.17	0.07	−0.11	0.05
		3.82	0.04	0.06	0.03	0.04
		3.75	−0.13	0.08	−0.08	0.05
		3.66	−0.16	0.07	−0.10	0.05
	Medium resolution	3.72	0.03	0.03	0.02	0.02
	Average	**3.76**	**−0.08**	**0.06**	**−0.05**	**0.04**
	2 s.d.	**0.32**	**0.20**	**0.03**	**0.13**	**0.02**
USGS SCo-1	Shale	0.88	−0.08	0.07	−0.06	0.04
		0.81	−0.34	0.05	−0.22	0.03
		0.85	−0.15	0.07	−0.10	0.04
		0.86	−0.25	0.08	−0.16	0.05
		0.83	−0.09	0.07	−0.06	0.05
	Average	**0.84**	**−0.18**	**0.07**	**−0.12**	**0.04**
	2 s.d.	**0.06**	**0.22**	**0.02**	**0.14**	**0.01**
USGS BCR-2	Basalt	0.075	0.19	0.06	0.12	0.04
		0.067	0.16	0.05	0.10	0.03
		0.072	0.19	0.06	0.12	0.04
	Average	**0.071**	**0.18**	**0.06**	**0.12**	**0.04**
	2 s.d.	**0.008**	**0.03**	**0.01**	**0.02**	**0.01**

published concentrations (Lissner et al., 2014). The isotopic data acquired is based on measurements of 1 mL sample solution containing ca. 15 ng total Se. Our measurement yields $\delta^{82/76}$Se of 0.18 ± 0.03‰ (2σ, n = 3). This value is also within uncertainty to 0.24 ± 0.25‰ (2σ, n = n. g.) reported by Rouxel et al. (2002). It is important to note that the isotopic composition obtained is unlikely to represent a mantle reference value as mantle processes are not entirely understood yet. The pioneering study by Rouxel et al. (2002) reported a large variety of different geological materials. It is also noteworthy that accurate stable Se isotope measurements down to the lower ng level have been reported by (Zhu et al., 2008). Both groups however reported Se isotope data from analysis on different instruments compared to a Neptune-*Plus*™. While Zhu et al. (2008) and further colleagues of Prof. T. Johnson at the Department of Geology, University of Illinois at Urbana-Champaign (e.g. Mitchell et al., 2012; Schilling et al., 2011) analyzed Se isotopes on a NuPlasma, Rouxel et al. (2002) used a Micromass IsoProbe plasma source instrument with collision/reaction cell technology, which suppressed the formation of polyatomic interferences down to insignificant levels. However, neither this instrument nor another MC-ICP-MS with collision/reaction cell technology is commercially available at the present. The ThermoFisher Scientific® Neptune-*Plus*™ used in this study could be used in medium- or high-mass resolution mode, as a strategy to resolve polyatomic interferences from monoatomic ion beams at a given m/z ratio (Weyer and Schwieters, 2003). Unfortunately, this technique clips the ion beam leading to a significant decrease in ion beam intensity to 15% for medium- and to 8% for high-mass resolution compared to the normal low-mass resolution measurement mode. In medium- or high-resolution modes, it is thus impossible to obtain accurate Se isotope compositions on analytes with lower than 15 ng total Se, even with the efficient sample introduction to the plasma promoted by a hydride generator. At a low-mass resolution measurement mode on the Neptune*Plus*™ MC-ICP-MS, however, background signals mainly from Ar dimers are in the range of tens of mV at m/z of 74, 77, 78 and 82 and are very large (20–25 V) at m/z of 80 (i.e. ^{40}Ar/^{40}Ar^{+}) using amplifier resistors of 10^{11} Ω. In comparison, Rouxel et al. (2002) only report background levels on their Micromass Isoprobe at m/z = 80 to be < 1 mV (using a 10^{11} Ω amplifier resistor). Here, we report the first Se measurement method on the ThermoFisher Scientific® Neptune*Plus*™ MC-ICP-MS that minimizes the problem of major polyatomic interferences on Se isotope masses by introducing methane. Together with a hydride generation system, this additionally increases the Se signal and thus enables the measurement of materials with Se concentrations in the range of 15 ng with a 2σ reproducibility of ca. 0.10‰ and of 5 ng with a reproducibility of 0.20‰. This is significant because it allows a systematic Se isotope investigation of many planetary reservoirs such as the Earth's mantle, which is characterized by low Se concentrations (peridotites: ~1-150 ng g^{-1} (König et al., 2014); MORB: 120-200 ng g^{-1} (Lissner et al., 2014)) as well as different sulfides and minerals (e.g. mantle sulfides range from 20 to 280 μg g^{-1}-Se (e.g. Hattori et al., 2002)).

4. Conclusions

(1) The method presented here allows to employ a ThermoFisher Scientific® Neptune*Plus*™ for the accurate determination of Se isotope ratios. The method is based on a double spike to account for fractionation induced during all stages of sample preparation and combines hydride generation with the introduction of methane, which results in a two- to three-fold Se signal increase and background suppression by a factor of two.
(2) Accurate Se isotope measurements with a reproducibility of < 0.10‰ (2σ) on $\delta^{82/76}$Se are obtained on 1 mL sample solution with a total of 15 ng Se. With lower Se quantities down to 5 ng mL^{-1} a reproducibility of 0.20‰ (2σ) is obtained on $\delta^{82/76}$Se.
(3) Our analytical approach for Se isotope analysis pushes the boundary for the investigation of geological materials and single minerals with low Se concentrations (200 ng g^{-1} down to tens of ng g^{-1}) and thus allows investigating Se-depleted planetary reservoirs such as the terrestrial mantle and other high-temperature environments by employing a commercially available instrument, the ThermoFisher Scientific® Neptune*Plus*™ MC-ICP-MS. As a first result we report a $\delta^{82/76}$Se value of 0.18 ± 0.03‰ (2σ; n = 3) for the USGS reference basalt BCR-2. This value should not be regarded as mantle reference value as processes in the Earth's mantle that might produce Se isotopic fractionations cannot be ruled out.

Acknowledgements

This work was funded by an ERC Starting Grant (O2RIGIN, 636808) to Stephan König. We thank Thomas M. Johnson for providing reference solution MH-495. Elmar Reitter and Martin Wille provided significant laboratory and instrumental support and contributed to fruitful discussions. Eva Stüeken, Hauke Vollstaedt and Philip A. E. Pogge von Strandmann are thanked for constructive reviews which helped to improve the manuscript.

Appendix A. Supplementary data

Supplementary data to this article can be found online at http://dx.doi.org/10.1016/j.chemgeo.2017.06.012.

References

Alard, O., Lorand, J.-P., Reisberg, L., Bodinier, J.-L., Dautria, J.-M., O'Reilly, S.Y., 2011. Volatile-rich metasomatism in Montferrier xenoliths (Southern France): implications for the abundances of chalcophile and highly siderophile elements in the subcontinental mantle. J. Petrol. 52 (10), 2009–2045.
Becker, H., Horan, M.F., Walker, R.J., Gao, S., Lorand, J.P., Rudnick, R.L., 2006. Highly siderophile element composition of the Earth's primitive upper mantle: constraints from new data on peridotite massifs and xenoliths. Geochim. Cosmochim. Acta 70 (17), 4528–4550.
Berglund, M., Wieser, M.E., 2011. Isotopic compositions of the elements 2009 (IUPAC Technical Report). Pure Appl. Chem. 83 (2).
Brenan, J.M., 2015. Se–Te fractionation by sulfide–silicate melt partitioning: implications for the composition of mantle-derived magmas and their melting residues. Earth Planet. Sci. Lett. 422, 45–57.
Carignan, J., Wen, H., 2007. Scaling NIST SRM 3149 for Se isotope analysis and isotopic variations of natural samples. Chem. Geol. 242 (3–4), 347–350.
Clark, S.K., Johnson, T.M., 2008. Effective isotopic fractionation factors for solute removal by reactive sediments: a laboratory microcosm and slurry study. Environ. Sci. Technol. 42 (21), 7850–7855.
Clark, S.K., Johnson, T.M., 2010. Selenium stable isotope investigation into selenium biogeochemical cycling in a lacustrine environment: Sweitzer Lake, Colorado. J. Environ. Qual. 39 (6), 2200.
Compston, W., Oversby, V., 1969. Lead isotopic analysis using a double spike. J. Geophys. Res. 74 (17), 4338–4348.
Ellis, A.S., Johnson, T.M., Herbel, M.J., Bullen, T.D., 2003. Stable isotope fractionation of selenium by natural microbial consortia. Chem. Geol. 195 (1), 119–129.
Elwaer, N., Hintelmann, H., 2008. Selective separation of selenium (IV) by thiol cellulose powder and subsequent selenium isotope ratio determination using multicollector inductively coupled plasma mass spectrometry. J. Anal. At. Spectrom. 23 (5), 733–743.
Fehr, M.A., Rehkämper, M., Halliday, A.N., 2004. Application of MC-ICPMS to the precise determination of tellurium isotope compositions in chondrites, iron meteorites and sulfides. Int. J. Mass Spectrom. 232 (1), 83–94.
Fliegel, D., Frei, C., Fontaine, G., Hu, Z., Gao, S., Günther, D., 2011. Sensitivity improvement in laser ablation inductively coupled plasma mass spectrometry achieved using a methane/argon and methanol/water/argon mixed gas plasma. Analyst 136 (23), 4925–4934.
Floor, G.H., Millot, R., Iglesias, M., Négrel, P., 2011. Influence of methane addition on selenium isotope sensitivity and their spectral interferences. J. Mass Spectrom. 46 (2), 182–188.
Gladney, E.S., Roelandts, I., 1988. 1987 compilation of elemental concentration data for USGS BHVO-1, MAG-1, QLO-1, RGM-1, SCo-1, SDC-1, SGR-1 and STM-1. Geostand. Newslett. 12 (2), 253–362.
Guo, W., Hu, S., Wang, Y., Zhang, L., Hu, Z., Zhang, J., 2013. Trace determination of selenium in biological samples by CH 4-Ar mixed gas plasma DRC-ICP-MS. Microchem. J. 108, 106–112.
Hattori, K.H., Arai, S., Clarke, D.B., 2002. Selenium, tellurium, arsenic and antimony contents of primary mantle sulfides. Can. Mineral. 40 (2), 637–650.
Johnson, T.M., 2004. A review of mass-dependent fractionation of selenium isotopes and implications for other heavy stable isotopes. Chem. Geol. 204 (3), 201–214.
Johnson, T.M., Bullen, T.D., 2003. Selenium isotope fractionation during reduction by Fe (II)-Fe(III) hydroxide-sulfate (green rust). Geochim. Cosmochim. Acta 67 (3), 413–419.
Johnson, T.M., Bullen, T.D., 2004. Mass-dependent fractionation of selenium and

chromium isotopes in low-temperature environments. Rev. Mineral. Geochem. 55 (1), 289–317.

Johnson, T.M., Herbel, M.J., Bullen, T.D., Zawislanski, P.T., 1999. Selenium isotope ratios as indicators of selenium sources and oxyanion reduction. Geochim. Cosmochim. Acta 63 (18), 2775–2783.

Johnson, T.M., Bullen, T.D., Zawislanski, P.T., 2000. Selenium stable isotope ratios as indicators of sources and cycling of selenium: results from the northern reach of San Francisco Bay. Environ. Sci. Technol. 34 (11), 2075–2079.

Kimura, K., Lewis, R.S., Anders, E., 1974. Distribution of gold and rhenium between nickel-iron and silicate melts: implications for the abundance of siderophile elements on the Earth and Moon. Geochim. Cosmochim. Acta 38 (5), 683–701.

Kipp, M.A., Stüeken, E.E., Bekker, A., Buick, R., 2017. Selenium isotopes record extensive marine suboxia during the Great Oxidation Event. Proc. Natl. Acad. Sci. 114 (5), 875–880.

König, S., Luguet, A., Lorand, J.-P., Wombacher, F., Lissner, M., 2012. Selenium and tellurium systematics of the Earth's mantle from high precision analyses of ultra-depleted orogenic peridotites. Geochim. Cosmochim. Acta 86, 354–366.

König, S., Lorand, J.-P., Luguet, A., Pearson, D.G., 2014. A non-primitive origin of near-chondritic S–Se–Te ratios in mantle peridotites; implications for the Earth’s late accretionary history. Earth Planet. Sci. Lett. 385, 110–121.

König, S., Lissner, M., Lorand, J.-P., Bragagni, A., Luguet, A., 2015a. Mineralogical control of selenium, tellurium and highly siderophile elements in the Earth's mantle: evidence from mineral separates of ultra-depleted mantle residues. Chem. Geol. 396, 16–24.

König, S., Luguet, A., Lorand, J.-P., Lissner, M., Graham Pearson, D., 2015b. Reply to the comment on “A non-primitive origin of near-chondritic S–Se–Te ratios in mantle peridotites: implications for the Earth's late accretionary history” by König S. et al. [Earth Planet. Sci. Lett. 385 (2014) 110–121]. Earth Planet. Sci. Lett. 417, 167–169.

Layton-Matthews, D., Leybourne, M.I., Peter, J.M., Scott, S.D., 2006. Determination of selenium isotopic ratios by continuous-hydride-generation dynamic-reaction-cell inductively coupled plasma-mass spectrometry. J. Anal. At. Spectrom. 21 (1), 41–49.

Lissner, M., König, S., Luguet, A., le Roux, P., Schuth, S., Heuser, A., le Roex, A., 2014. Selenium and tellurium systematics in MORBs from the southern Mid-Atlantic Ridge (47–50 S). Geochim. Cosmochim. Acta 144, 379–402.

Lorand, J.-P., Alard, O., 2010. Determination of selenium and tellurium concentrations in Pyrenean peridotites (Ariege, France): new insight into S/Se/Te systematics of the upper in mantle samples. Chem. Geol. 278 (1), 120–130.

Lorand, J.-P., Alard, O., Luguet, A., Keays, R.R., 2003. Sulfur and selenium systematics of the subcontinental lithospheric mantle: inferences from the Massif Central xenolith suite (France). Geochim. Cosmochim. Acta 67 (21), 4137–4151.

Lorand, J.-P., Delpech, G., Grégoire, M., Moine, B., O'Reilly, S.Y., Cottin, J.-Y., 2004. Platinum-group elements and the multistage metasomatic history of Kerguelen lithospheric mantle (South Indian Ocean). Chem. Geol. 208 (1–4), 195–215.

Lorand, J.-P., Luguet, A., Alard, O., Bezos, A., Meisel, T., 2008. Abundance and distribution of platinum-group elements in orogenic lherzolites; a case study in a Fontete Rouge lherzolite (French Pyrénées). Chem. Geol. 248 (3–4), 174–194.

Lorand, J.-P., Luguet, A., Alard, O., 2013. Platinum-group element systematics and petrogenetic processing of the continental upper mantle: a review. Lithos 164–167, 2–21.

Luguet, A., Lorand, J.-P., Alard, O., Cottin, J.-Y., 2004. A multi-technique study of platinum group element systematic in some Ligurian ophiolitic peridotites, Italy. Chem. Geol. 208 (1–4), 175–194.

Mann, U., Frost, D.J., Rubie, D.C., Becker, H., Audétat, A., 2012. Partitioning of Ru, Rh, Pd, Re, Ir and Pt between liquid metal and silicate at high pressures and high temperatures-implications for the origin of highly siderophile element concentrations in the Earth's mantle. Geochim. Cosmochim. Acta 84, 593–613.

Marchesi, C., Garrido, C.J., Harvey, J., González-Jiménez, J.M., Hidas, K., Lorand, J.-P., Gervilla, F., 2013. Platinum-group elements, S, Se and Cu in highly depleted abyssal peridotites from the Mid-Atlantic Ocean ridge (ODP Hole 1274A): influence of hydrothermal and magmatic processes. Contrib. Mineral. Petrol. 166 (5), 1521–1538.

Marin, L., Lhomme, J., Carignan, J., 2001. Determination of selenium concentration in sixty five reference materials for geochemical analysis by GFAAS after separation with thiol cotton. Geostand. Newslett. 25 (2–3), 317–324.

McDonough, W.F., Sun, S.-S., 1995. The composition of the Earth. Chem. Geol. 120, 223–253.

Mitchell, K., Mason, P.R., Van Cappellen, P., Johnson, T.M., Gill, B.C., Owens, J.D., Diaz, J., Ingall, E.D., Reichart, G.-J., Lyons, T.W., 2012. Selenium as paleo-oceanographic proxy: a first assessment. Geochim. Cosmochim. Acta 89, 302–317.

Mitchell, K., Couture, R.-M., Johnson, T.M., Mason, P.R., Van Cappellen, P., 2013. Selenium sorption and isotope fractionation: iron (III) oxides versus iron (II) sulfides. Chem. Geol. 342, 21–28.

Mitchell, K., Mansoor, S.Z., Mason, P.R.D., Johnson, T.M., Van Cappellen, P., 2016. Geological evolution of the marine selenium cycle: insights from the bulk shale δ82/76Se record and isotope mass balance modeling. Earth Planet. Sci. Lett. 441, 178–187.

Morgan, J.W., 1986. Ultramafic xenoliths: clues to Earth's late accretionary history. J. Geophys. Res. Solid Earth 91 (B12), 12375–12387.

Morgan, J., Walker, R., Brandon, A., Horan, M., 2001. Siderophile elements in Earth's upper mantle and lunar breccias: data synthesis suggests manifestations of the same late influx. Meteorit. Planet. Sci. 36 (9), 1257–1275.

Nielsen, S.G., Rehkämper, M., Baker, J., Halliday, A.N., 2004. The precise and accurate determination of thallium isotope compositions and concentrations for water samples by MC-ICPMS. Chem. Geol. 204 (1–2), 109–124.

Palme, H., O'Neill, H.S.C., 2003. Cosmochemical estimates of mantle composition. Treatise on geochemistry 2, 568.

Pogge von Strandmann, P.A., Coath, C.D., Catling, D.C., Poulton, S.W., Elliott, T., 2014. Analysis of mass dependent and mass independent selenium isotope variability in black shales. J. Anal. At. Spectrom. 29 (9), 1648–1659.

Pogge von Strandmann, P.A., Stüeken, E.E., Elliott, T., Poulton, S.W., Dehler, C.M., Canfield, D.E., Catling, D.C., 2015. Selenium isotope evidence for progressive oxidation of the Neoproterozoic biosphere. Nat. Commun. 6.

Richter, F.M., 2004. Timescales determining the degree of kinetic isotope fractionation by evaporation and condensation. Geochim. Cosmochim. Acta 68 (23), 4971–4992.

Rouxel, O., Ludden, J., Carignan, J., Marin, L., Fouquet, Y., 2002. Natural variations of Se isotopic composition determined by hydride generation multiple collector inductively coupled plasma mass spectrometry. Geochim. Cosmochim. Acta 66 (18), 3191–3199.

Rouxel, O., Fouquet, Y., Ludden, J.N., 2004. Subsurface processes at the lucky strike hydrothermal field, Mid-Atlantic ridge: evidence from sulfur, selenium, and iron isotopes 1. Geochim. Cosmochim. Acta 68 (10), 2295–2311.

Rudge, J.F., Reynolds, B.C., Bourdon, B., 2009. The double spike toolbox. Chem. Geol. 265 (3), 420–431.

Savard, D., Bédard, L.P., Barnes, S.-J., 2009. Selenium concentrations in twenty-six geological reference materials: new determinations and proposed values. Geostand. Geoanal. Res. 33 (2), 249–259.

Schilling, K., Johnson, T.M., Wilcke, W., 2011. Selenium partitioning and stable isotope ratios in urban topsoils. Soil Sci. Soc. Am. J. 75 (4), 1354–1364.

Schilling, K., Johnson, T.M., Wilcke, W., 2013. Isotope fractionation of selenium by biomethylation in microcosm incubations of soil. Chem. Geol. 352, 101–107.

Schilling, K., Johnson, T.M., Mason, P.R.D., 2014. A sequential extraction technique for mass-balanced stable selenium isotope analysis of soil samples. Chem. Geol. 381, 125–130.

Schumann, G., Klauke, R., Büttner, J., 1992. 036 Standard addition in HPLC: a calibration method for the determination of reference method values. Fresenius J. Anal. Chem. 343 (1), 89–90.

Shore, A.J.T., 2011. Selenium Geochemistry and Isotopic Composition of Sediments from the Cariaco Basin and the Bermuda Rise: A Comparison between a Restricted Basin and the Open Ocean over the Last 500 Ka. University of Leicester.

Stüeken, E., Foriel, J., Nelson, B., Buick, R., Catling, D., 2013. Selenium isotope analysis of organic-rich shales: advances in sample preparation and isobaric interference correction. J. Anal. At. Spectrom. 28 (11), 1734–1749.

Stüeken, E.E., Buick, R., Anbar, A.D., 2015a. Selenium isotopes support free O2 in the latest Archean. Geology 43 (3), 259–262.

Stüeken, E.E., Buick, R., Bekker, A., Catling, D., Foriel, J., Guy, B.M., Kah, L.C., Machel, H.G., Montanez, I.P., Poulton, S.W., 2015b. The evolution of the global selenium cycle: secular trends in Se isotopes and abundances. Geochim. Cosmochim. Acta 162, 109–125.

Stüeken, E.E., Foriel, J., Buick, R., Schoepfer, S.D., 2015c. Selenium isotope ratios, redox changes and biological productivity across the end-Permian mass extinction. Chem. Geol. 410, 28–39.

Tamari, Y., Ogawa, H., Fukumoto, Y., Tsuji, H., Kusaka, Y., 1990. Selenium content and its oxidation-state in igneous rocks, rock-forming minerals, and a reservoir sediment. Bull. Chem. Soc. Jpn. 63 (9), 2631–2638.

Tipper, E.T., Louvat, P., Capmas, F., Galy, A., Gaillardet, J., 2008. Accuracy of stable Mg and Ca isotope data obtained by MC-ICP-MS using the standard addition method. Chem. Geol. 257 (1–2), 65–75.

Vollstaedt, H., Mezger, K., Leya, I., 2016a. The isotope composition of selenium in chondrites constrains the depletion mechanism of volatile elements in solar system materials. Earth Planet. Sci. Lett. 450, 372–380.

Vollstaedt, H., Mezger, K., Nagler, T., Leya, I., Trinquier, A., 2016b. Selenium isotope analysis by N-TIMS: potential and challenges. Int. J. Mass Spectrom. 401, 55–63.

Walker, R.J., 2009. Highly siderophile elements in the Earth, Moon and Mars: update and implications for planetary accretion and differentiation. Chemie der Erde - Geochemistry 69 (2), 101–125.

Wang, Z., Becker, H., 2013. Ratios of S, Se and Te in the silicate Earth require a volatile-rich late veneer. Nature 499 (7458), 328–331.

Wang, Z., Becker, H., 2015. Comment on “A non-primitive origin of near-chondritic SSeTe ratios in mantle peridotites: implications for the Earth's late accretionary history” by König S. et al. [Earth Planet. Sci. Lett. 385 (2014) 110–121]. Earth Planet. Sci. Lett. 417, 164–166.

Wang, Z., Becker, H., Gawronski, T., 2013. Partial re-equilibration of highly siderophile elements and the chalcogens in the mantle: a case study on the Baldissero and Balmuccia peridotite massifs (Ivrea Zone, Italian Alps). Geochim. Cosmochim. Acta 108, 21–44.

Wen, H., Carignan, J., 2011. Selenium isotopes trace the source and redox processes in the black shale-hosted Se-rich deposits in China. Geochim. Cosmochim. Acta 75 (6), 1411–1427.

Wen, H., Carignan, J., Chu, X., Fan, H., Cloquet, C., Huang, J., Zhang, Y., Chang, H., 2014. Selenium isotopes trace anoxic and ferruginous seawater conditions in the Early Cambrian. Chem. Geol. 390, 164–172.

Weyer, S., Schwieters, J., 2003. High precision Fe isotope measurements with high mass resolution MC-ICPMS. Int. J. Mass Spectrom. 226 (3), 355–368.

Young, E.D., Galy, A., Nagahara, H., 2002. Kinetic and equilibrium mass-dependent isotope fractionation laws in nature and their geochemical and cosmochemical significance. Geochim. Cosmochim. Acta 66 (6), 1095–1104.

Yu, M.Q., Liu, G.Q., Jin, Q., 1983. Determination of trace arsenic, antimony, selenium and tellurium in various oxidation states in water by hydride generation and atomic-absorption spectrophotometry after enrichment and separation with thiol cotton. Talanta 30 (4), 265–270.

Zhu, J.-M., Johnson, T.M., Clark, S.K., Xiang-Kun, Z., 2008. High precision measurement of selenium isotopic composition by hydride generation multiple collector inductively coupled plasma mass spectrometry with a 74 Se-77 Se double spike. Chin. J. Anal. Chem. 36 (10), 1385–1390.

Zhu, J.-M., Johnson, T.M., Clark, S.K., Zhu, X.-K., Wang, X.-L., 2014. Selenium redox cycling during weathering of Se-rich shales: a selenium isotope study. Geochim. Cosmochim. Acta 126, 228–249.

Chemical Geology 513 (2019) 239–249

Contents lists available at ScienceDirect

Chemical Geology

journal homepage: www.elsevier.com/locate/chemgeo

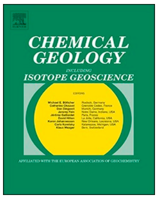

The role of subduction recycling on the selenium isotope signature of the mantle: Constraints from Mariana arc lavas

Timon Kurzawa[a,*], Stephan König[a], Jeffrey C. Alt[b], Aierken Yierpan[a], Ronny Schoenberg[a,c]

[a] Isotope Geochemistry, Department of Geosciences, Eberhard Karls University of Tübingen, Wilhelmstraße 56, 72074 Tübingen, Germany
[b] Department of Earth and Environmental Sciences, The University of Michigan, 1100 North University Avenue, Ann Arbor, MI 48109-1005, USA
[c] Department of Geology, University of Johannesburg, P.O. Box 524, Auckland Park 2006, South Africa

ARTICLE INFO

Editor: Catherine Chauvel

Keywords:
Mariana arc
Selenium isotopes
Selenium
Tellurium
Subduction zone
Chalcophile element recycling

ABSTRACT

Investigating the isotope systematics and behavior of selenium in subduction zones provides valuable insights into mechanisms that contribute to chalcophile and moderately volatile element distribution between terrestrial reservoirs. In this study, we present high-precision Se isotope and Se–Te elemental data on subduction zone lavas from the Mariana arc system. Our results indicate that Se–Te concentrations are unaffected by submarine degassing but are affected by magmatic differentiation. In contrast, Se isotopes of submarine lavas are unaffected by both magmatic differentiation and degassing and thus may preserve their magmatic source signature. Compared to the average Se isotope composition previously obtained for mantle-derived samples ($\delta^{82/76}$Se = 0.23 ± 0.12‰, 2 s.d., n = 5), suitable to represent the Mariana pre-subduction wedge, Mariana lavas show a larger overall range ($\delta^{82/76}$Se from 0.03 to −0.33‰, n = 21) with a clear tendency towards lighter Se isotope compositions. The variable Se isotope signatures within the Mariana suite can further be attributed to different slab-derived fluid and melt-like subduction components. This provides evidence for a significant role of subduction recycling of hydrothermal sulfide-containing altered oceanic crust and pelagic sediments with possible implications for the Se isotope evolution of the crust-mantle system throughout geological time.

1. Introduction

Constraining the behavior of elements in subduction zones provides valuable insights into their distribution and (re)cycling between surface and igneous reservoirs throughout Earth's evolution. The distribution of the chalcophile and moderately volatile elements sulfur (S), selenium (Se) and tellurium (Te) are of particular interest because they provide insights into Earth's volatile origin and evolution (König et al., 2014; Wang and Becker, 2013). Selenium and Te are ultra-trace elements with two orders of magnitude lower abundances in Earth's mantle compared to CI chondrites. Their abundances however, are still higher than expected from metal-silicate partitioning experiments (Rose-Weston et al., 2009), which predict S, Se and Te to be very effectively scavenged from Earth's mantle into its core during metal core formation. This may be reconciled with a late accretion of chondritic material (late veneer hypothesis; e.g. Kimura et al., 1974) following core-mantle differentiation. The relative abundances of S–Se–Te in mantle rocks believed to represent the primitive upper mantle (PUM) signature are near-chondritic, which was interpreted as evidence for replenishment of Earth's mantle by accretion of chondritic late veneer material (Wang and Becker, 2013). However, this interpretation conflicts with the non-chondritic sulfur isotopic composition of the Earth's mantle (Labidi et al., 2013), which has been attributed to partial incorporation of S into the Earth's core and thus substantial pre-Late Veneer existence of volatiles (Labidi et al., 2016). Alternatively, the observed near-chondritic Se/Te ratios in fertile peridotites might be the result of refertilization and thus represent secondary magmatic processes (Harvey et al., 2015; König et al., 2014; Lorand and Alard, 2010; Luguet et al., 2015). The fertile peridotite signature for adequate representation of a PUM model composition remains therefore controversially debated (König et al., 2015a; König et al., 2014; König et al., 2015b; Wang and Becker, 2013; Wang and Becker, 2015).

Investigation of the Se isotopic composition of the Earth's mantle offers a novel approach to investigate the origin and evolution of volatiles. This requires firm constraints on the Se isotopic composition of the different terrestrial reservoirs. Within this scope, the role of subduction zone processes on the Se isotope composition of the mantle is relevant because of large concentration and isotope differences between Earth's mantle and crust (Jenner, 2017; Jenner et al., 2012; Lissner et al., 2014; Rouxel et al., 2002; Yierpan et al., 2018). As in mid-ocean

---

[*] Corresponding author.
E-mail address: timon.kurzawa@uni-tuebingen.de (T. Kurzawa).

https://doi.org/10.1016/j.chemgeo.2019.03.011
Received 13 September 2018; Received in revised form 15 February 2019; Accepted 7 March 2019

ridge settings, Se elemental signatures of subduction zone lavas are affected by sulfide segregation during magma differentiation (Brenan, 2015; Hamlyn et al., 1985; Jenner, 2017; Lissner et al., 2014) and these processes must therefore be considered in order to adequately interpret the Se isotope composition of arc lavas. Due to the different partitioning behavior of Se and Te in sulfides (i.e. partitioning into distinct sulfide phases), Se–Te systematics are a valuable tracer of the relative influence of the different sulfide populations involved during magmatic differentiation and partial melting (Brenan, 2015; Yierpan et al., 2019). Interpretation of the Se isotope composition of subduction zone lavas therefore benefits significantly from combined Se isotope and Se–Te elemental investigations. Recently, Kurzawa et al. (2017) and Yierpan et al. (2018) presented refined analytical techniques for both chemical purification and high-precision analyses of Se–Te concentrations and Se isotope compositions on samples with low total amounts of Se and Te. These analytical advancements provide the potential to investigate the Se isotope signature of low ng Se-bearing silicate rocks in the context of their Se–Te elemental signatures. This helps to evaluate the different petrogenetic processes involved in mantle melt evolution and ultimately to decipher the role of subduction recycling on the Se isotope composition of the mantle.

Studies on V, Fe and Tl isotopes (Prytulak et al., 2013; Prytulak et al., 2017; Williams et al., 2018) have been conducted on samples from the Mariana arc system to (i) investigate the oxygen fugacity of the mantle source (using V isotopes), to (ii) explore the interplay of sulfide saturation and segregation as well as crystal fractionation on the isotope composition of arc lavas (Fe and V isotopes) and to (iii) trace subduction zone inputs (using Tl isotopes). These studies concluded that Fe and V isotope signatures of magmatic rocks cannot directly be used as redox proxies without considering the influence of magmatic processes such as partial melting and differentiation. Yet, the timing of sulfide saturation and magnetite crystallization and associated isotope fractionations could be constrained.

In this study we focus on a suite of well-characterized, submarine arc lavas dredged from the Mariana subduction system (Fig. 1), which already have been the focus of a pioneering work on S isotopes (Alt et al., 1993). This suite may hence provide the geochemical background for first Se isotope constraints on chalcophile element recycling in subduction zones.

2. Geodynamic and geochemical context of sample materials

The Mariana arc-basin magmatic system (herein referred to as the Mariana system) extends over a distance of 2800 km (N–S) and constitutes the southern extension of the Izu-Bonin-Mariana subduction zone. The Mariana system is the result of westward subduction of the Pacific Plate along the Mariana trench beneath the Philippine Sea Plate initiated in the early Eocene (e.g. Stern and Bloomer, 1992; Stern et al., 2003). It can be subdivided into the Mariana island arc, which is an arcuate alignment of ~40 subaerial and submarine volcanoes, and the Mariana trough, an actively spreading back-arc basin (e.g. Pearce et al., 2005).

A total of 21 glassy samples from the submarine Mariana arc and trough sections (Fig. 1) were analyzed in this study. Among these are 12 samples from the active Mariana arc. These samples were either dredged (Fukujin, Eifuku and S. Daikoku) or collected by submersible (Kasuga) at collection depths of ~800–2900 mbsl (Alt et al., 1993). Additionally, 9 samples from two trough localities (18°N and 22°N) were analyzed, that were obtained by submersible or dredging at collection depths of ~2800–3700 mbsl. The samples are mainly basalts, basaltic andesites and andesites (Alt et al., 1993). Samples were petrographically classified into three groups: (i) ‘glass’, (ii) ‘glassy’ and (iii) ‘microcrystalline’ (see Alt et al., 1993). Some materials analyzed here have previously been analyzed including for S, Sr and Nd isotopes and major and trace element systematics (Alt et al., 1993 and references therein). These studies showed that back-arc lavas from 22°N and a single trough rock from 18°N (1846-9; Alt et al. (1993)) carry a strong arc signature, as inferred from trace element and Sr–Nd–Pb isotope systematics, which can be explained by addition of an arc component to a MORB mantle (e.g. Stern et al., 1990). Based on this observation, we suggest the subdivision of the following groups among the samples analyzed: back-arc samples at 18°N, arc-like samples at 22°N (and sample 1846-9 from 18°N) (where the back-arc basin intersects the arc) and arc samples from submarine volcanoes (Kasuga, Fukujin, Eifuku, S.Daikoku). These subdivisions also account for different subduction components that comprise shallow, deep and total slab-derived contributions as expressed by Ba/Th, Th/Yb and Ba/Yb, respectively (Pearce et al., 2005). The shallow subduction contribution results from early dehydration of the slab and migration of fluids from the slab-mantle interface into the sub-arc mantle wedge (arc and back-arc). Deep subduction additions are explained as sediment-derived melt-like components (mainly arc). The flux of subduction components in not limited to vertical transport but also includes lateral transport (Stolper and Newman, 1994 and references therein). In previous studies, the sub-arc mantle wedge has been interpreted to act as chromatographic column diluting the subduction input in arc-distal areas. However, assessing these mechanisms in these arc-distal areas is not the aim of this study and we rather focus on how the different and variable subduction components influence the Se isotope systematics of arc-related melts.

3. Analytical techniques

3.1. Reagents, materials, major- and trace element analyses

Glass free of coatings and alteration was carefully handpicked from each sample, followed by multiple washing steps in dilute HCl and distilled water and were finally ground to powder (Alt et al., 1993). Sulfur concentrations of these samples were already published by Alt et al. (1993). In addition to Se isotope measurements and Se–Te concentration analyses, selected samples were also analyzed for major and trace element concentrations. All analyses were performed in the ISO-5 (US FED standards class 100) clean-room facilities of the Isotope Geochemistry at the University of Tübingen, Germany. All reagents used during digestion, sample preparation and measurements were distilled from MERCK Millipore Emsure™ grade HCl (37%) and HNO_3 (65%) using Savillex™ DST-1000 Acid Purification Systems. Reagents were diluted to required molarities to ± 0.03 $\mathrm{mol\,L^{-1}}$ as checked by titration. Ion exchange resins, beakers, pipette tips and centrifuge vials were pre-cleaned with multi-step HCl and HNO_3 treatments. A Merck Millipore Milli-Q™ system was employed to further purify de-ionized water to 18.2 MΩ·cm at 25 °C.

Previously determined major element data was complemented and trace elements were measured for the entire Mariana sample suite (Alt et al., 1993) during this study using a ThermoFisher Scientific iCAP Qc quadrupole ICP-MS housed at the Isotope Geochemistry Laboratory at the University of Tübingen following the analytical procedure by Albut et al. (2018). Due to limited sample material, all major and trace element concentrations of samples were determined together with rock reference materials AGV-2 (for major element data, n = 2) and BHVO-2 and BIR-1a (for trace element data, n = 2 and 1, respectively). Analytical precision for most analyzed trace elements is better than 2% r.s.d. except for Be, As, W and U with analytical precisions better than 5% r.s.d. Obtained trace element concentrations of rock reference materials match those reported by Jochum et al. (2016) (see Supplemental Information). For major element analysis, 0.1 g of homogenized sample material was fused together with 0.5 g of Spectromelt® to produce a fused glass bead, which was subsequently dissolved in 0.45 $\mathrm{mol\,L^{-1}}$ HNO_3 in a Teflon beaker agitated in an ultrasonic bath and diluted by addition of an internal standard solution before final measurement. For determination of trace element concentrations, 0.02 g homogenized powder of each sample were weighted into Teflon beakers and digested at 120 °C in a mixture of concentrated HF and HNO_3 (5:1, v/v). After

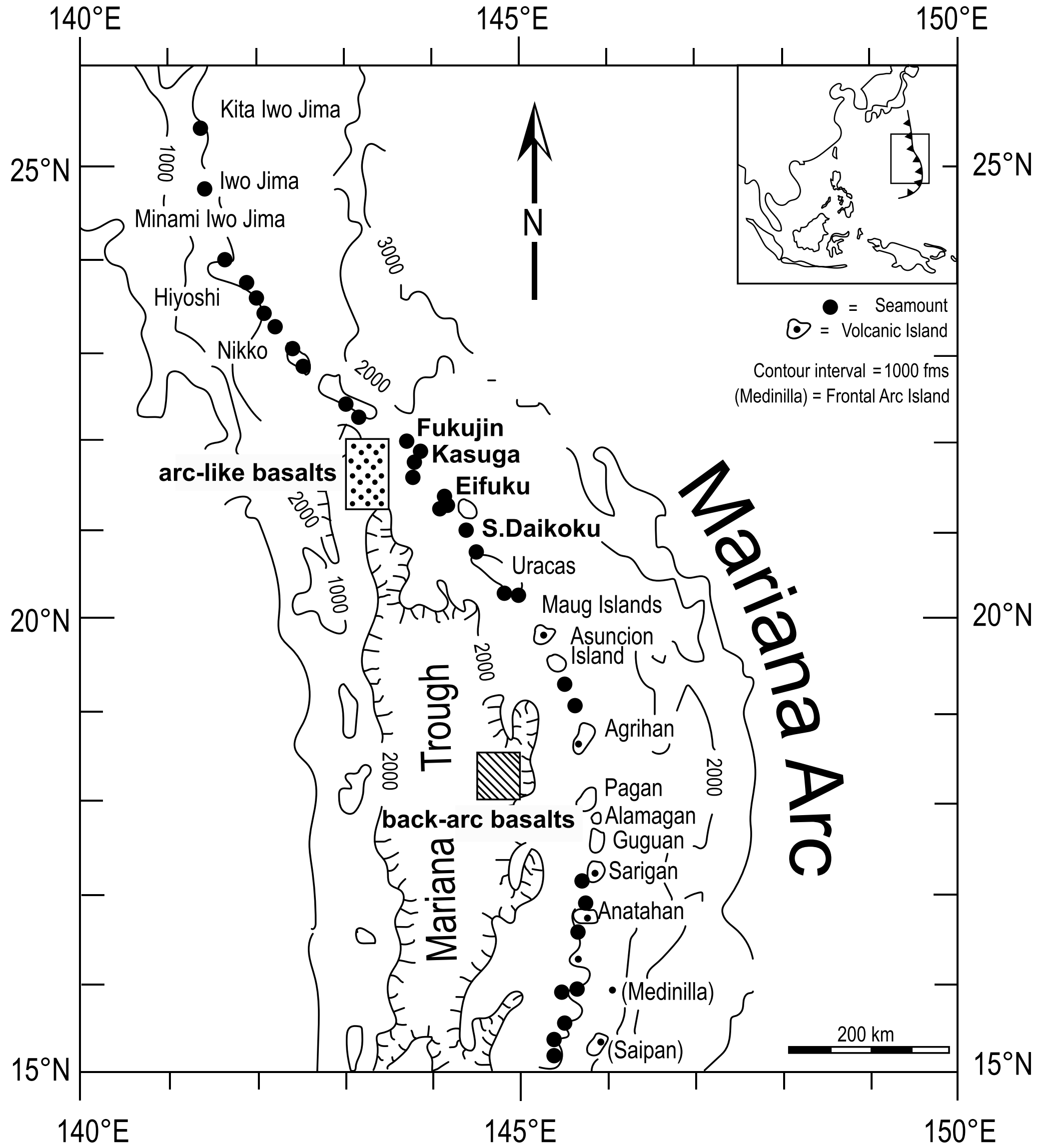

Fig. 1. Locality map for the Mariana arc system and locations of samples. Analyzed samples are from submarine seamounts (bold labels) and from two back-arc regions (shaded rectangular boxes). Modified after Alt et al. (1993 and references therein).

dry down, the samples were taken up in 6 mol L^{-1} HCl and heated in closed beakers to break up existing fluoride complexes. The sample solutions were again evaporated to dryness, converted to nitrite form and subsequently diluted with an internal standard solution before final measurement.

3.2. Se concentration analyses

Pre-determination of Se concentration of an unknown sample is required in order to know the amount of double spike to be added to the sample for precise Se isotope analysis with ideal double spike-sample ratio of ~1:1 (Kurzawa et al., 2017). For the pre-determination of Se concentrations via isotope dilution, we followed the procedure described by Yierpan et al. (2018). For this, we weighed 0.02 g sample material (equivalent to 2 ng total Se assuming a Se concentration of 100 ng g^{-1}) in Teflon beakers, added an adequate amount of ^{74}Se–^{77}Se double spike and digested the mix with an acid mixture of 5:1 (v/v) conc. HF: conc. HNO_3 in closed Teflon beakers at 85 °C. The digested samples were then dried at 65 °C followed by conversion, heating and dry down steps (see Yierpan et al., 2018) in 6 mol L^{-1} HCl before Fe was removed by means of anion exchange chromatography. Fe-free cuts were then diluted to 0.5–1 ng mL^{-1} Se and finally measured on the iCAP Qc ICP-MS using hydride generation following the protocol of Yierpan et al. (2018).

3.3. Se isotope and Te concentration analyses

Chemical purification of Se and Te for subsequent Se isotope and Se–Te concentration analyses was achieved following the protocol by Yierpan et al. (2018) as it allows to simultaneously purify Se and Te from a single sample digest with high yields. Briefly, this involves weighing sample material equivalent to ~30 ng Se (exact Te amount uncritical) into conventional perfluoralkoxy (PFA) beakers, adding adequate amounts of ^{74}Se–^{77}Se double spike (1:1; sample Se: double spike Se) and ^{125}Te single spike (exact single spike amount less critical) and digesting the sample-spike mixtures in an acid mixture of 5:1 (v/v) conc. HF: conc. HNO_3 in closed beakers on a hotplate at 85 °C for 48 h. Se and Te were purified from sample solutions by a two-step ion exchange chromatography. In a first step, we employed an anion exchange column to remove Fe and collect purified Te. In a second step, Se was purified using a cation exchange column to remove remaining cations. Te concentrations were then determined by hydride generator

Table 1

Combined Se isotope compositions and Se—Te concentrations of Mariana samples and international rock reference materials (United States Geological Survey, USGS; Geological Survey of Japan, GSJ).

Sample	Location	Rock type	SiO_2 wt%	MgO wt%	analyses n	$\delta^{82/76}$Se (‰)	2 s.d.† (‰)	Se ($ng\,g^{-1}$)	1 s.d. ($ng\,g^{-1}$)	Te ($ng\,g^{-1}$)	1 s.d. ($ng\,g^{-1}$)	Se/Te	S^{π} ($\mu g\,g^{-1}$)
15161	arc, Fukujin	andesite	58.0	2.95	1	−0.24	0.10	102	3	1.57	0.05	65	50
1580	arc, Fukujin	andesite	59.7	2.00	1	−0.14	0.10	77	2	0.16	< 0.01	481	40
15117	arc, Fukujin	andesite	60.6	1.98	1	−0.16	0.10	83	2	0.21	< 0.01	393	50
15146	arc, Fukujin	andesite	56.7	2.86	1	−0.08	0.10	124	4	2.04	0.06	61	30
D35-1-4	arc, Fukujin	andesite	56.0	3.13	2	0.03	0.10	81	2	0.71	0.02	113	10
1880-3 (K2)*	arc, Kasuga	basalt	51.2	5.42	6	−0.18	0.10	119	4	4.21	0.13	28	150
1883-5 (P)	arc, Kasuga	bas. Andesite	52.3	5.46	1	−0.01	0.10	87	3	6.40	0.19	14	120
1885-6 (K3)	arc, Kasuga	bas. Andesite	54.6	5.80	2	−0.13	0.10	66	2	2.57	0.08	25	110
1884-10 (K3)	arc, Kasuga	basalt	50.3	7.39	2	−0.09	0.10	142	4	4.57	0.14	31	200
D31-3-1	arc, Eifuku	bas. Andesite	52.7	3.49	1	−0.09	0.10	165	5	0.78	0.02	212	20
D25-3	arc, S.Daikoku	bas. Andesite	54.2	3.89	1	−0.25	0.10	147	4	0.79	0.02	186	50
D25-1-4	arc, S.Daikoku	andesite	57.5	3.02	1	−0.16	0.10	134	4	1.58	0.05	85	60
1838-13	back-arc, 18°N	bas. Andesite	52.7	5.68	2	−0.03	0.10	113	3	1.31	0.04	86	930
1839-3	back-arc, 18°N	basalt	48.5	7.68	1	−0.02	0.10	133	4	3.90	0.12	34	780
1841-18	back-arc, 18°N	basalt	50.5	7.84	1	−0.05	0.10	132	4	3.79	0.11	35	620
1846-12	back-arc, 18°N	basalt	50.8	7.00	2	−0.02	0.10	234	7	7.00	0.21	33	930
1846-9	arc-like, 18°N	basalt	49.7	6.95	1	−0.16	0.10	169	5	4.70	0.14	36	370
1881-4*	arc-like, 22°N	bas. Andesite	53.0	6.05	3	−0.13	0.10	74	2	1.82	0.05	41	280
D65-4	arc-like, 22°N	bas. Andesite	53.9	4.78	2	−0.25	0.10	138	4	1.07	0.03	129	200
D67-10	arc-like, 22°N	basalt	49.8	8.47	1	−0.33	0.10	182	5	3.03	0.09	60	930
D68-4	arc-like, 22°N	basalt	50.4	8.89	1	−0.18	0.10	125	4	1.55	0.05	81	490
USGS BHVO-2**		basalt			1	0.16	0.10	166	5	14.1	0.42	12	
GSJ JB-2		basalt			3	−0.19	0.10	153	5	3.78	0.11	40	
GSJ JB-3		basalt			2	0.16	0.10	67	2	1.03	0.03	65	

Se isotope data reported relative to Se reference solution NIST SRM-3149. *Samples 1881-4 and 1880-3 (K2) were used to assess external reproducibility, see Supplementary Information. †Uncertainty on Se isotope compositions is conservatively set to be 0.10‰ as derived from multiple digested and analyzed samples during different measurement sessions. **BHVO-2 was analyzed together with Mariana samples and published by Yierpan et al. (2018) with long-term BHVO-2 reproducibility of 0.18 ± 0.10‰ (2 s.d., n = 8, multiple analytical sessions over 6 months). Uncertainty on Se–Te concentrations conservatively expressed as 3% relative standard deviation. $^{\pi}$S concentrations from Alt et al. (1993). For reference concentration data of GSJ JB-2 and JB-3 see Supplementary Information.

quadrupole ICP-MS on the iCAP Qc instrument and Se isotopes and concentrations were measured by hydride generation multi-collector ICP-MS on the ThermoFisher Scientific Neptune*Plus*™ instrument of the Isotope Geochemistry laboratory, University of Tübingen. Typical signals on ^{82}Se (using an amplifier resistor of 10^{11} Ω) on a 30 ng mL^{-1} Se solution with operating parameters similar to those reported by Kurzawa et al. (2017) generally are 0.8–0.9 V. During Te concentration measurements on the iCAP Qc ICP-MS using similar operating parameters to those of Yierpan et al. (2018), ~55000cps on ^{126}Te were obtained for a Te standard solution of 0.5 ng mL^{-1}. Se isotopes and Te concentrations of samples were determined at similar signal intensities compared to those of standard solutions. For detailed descriptions of analytical techniques employed see Kurzawa et al. (2017) and Yierpan et al. (2018). All Se isotope compositions obtained during this study are reported relative to the NIST-3149 Se reference solution. Measurements of the inter-laboratory standard solution MH-495 yielded an average value of $\delta^{82/76}$Se of −3.25 ± 0.08‰ (2 s.d., n = 26, 30 ng mL^{-1} solutions, see Supplemental Information), in agreement with previous studies (Kurzawa et al., 2017; Labidi et al., 2018; Yierpan et al., 2019; Yierpan et al., 2018 and references therein). The external reproducibility for sample materials was derived from two multiple digested samples (arc-like 1881-4; Kasuga 1880-3 (K2)) during different measurement sessions and is 0.10‰ (2 s.d., n = 3 and n = 6, respectively; Supplemental Information). All samples were measured together with the international rock reference material USGS BHVO-2 that has been published by Yierpan et al. (2018). Further, we provide Se isotope and Se–Te concentration data for the international rock reference materials JB-2 and JB-3 (Geological Survey of Japan). Obtained Se–Te concentrations are in agreement with data reported in the literature (see Supplemental Information). Long-term analytical reproducibility for both Se and Te concentration determinations are ~3% r.s.d. The main advantage of the procedure by Yierpan et al. (2018) followed here is that it yields very low blanks. Accurate isotopic compositions of procedural blanks cannot be determined because blank levels are always insignificant (at background level; e.g., ~0.05 and 0.01 ng for Se and Te, respectively; see Yierpan et al. (2019)). However, Kurzawa et al. (2017) showed high accuracy for low Se-containing solutions with various blank levels (up to 1 ng) that confirms a negligible blank contribution for a given isotopic composition.

4. Results

4.1. Major and trace elements

All samples show 48 to 61 wt% SiO_2 and 2 to 9 wt% MgO (Table 1) and are classified as basalts, basaltic andesites, andesites. Relative to the back-arc samples (MgO between 5 and 9 wt%) and with the exception of the Kasuga samples, the arc samples are more differentiated showing MgO contents of 2 to 4 wt%. The Kasuga samples are more primitive as indicated by lower SiO_2 and higher MgO contents of < 55 wt% and > 5 wt%, respectively. The samples from S.Daikoku, Eifuku, Fukujin and both back-arc localities follow the tholeiitic fractionation trend whereas samples from Kasuga follow calc-alkaline to shoshonitic fractionation trends (Alt et al., 1993). In terms of major element composition samples from both back-arc localities (18°N and 22°N) are indistinguishable from each other. Our new trace element data are in accordance with previous observations (Stern et al., 2003 and references therein) in that primitive mantle normalized trace element diagrams (after Palme and O'Neill, 2014) for the Mariana arc and trough samples all show marked enrichments in large ion lithophile elements and light rare earth elements such as Rb, Ba, U, K, Pb, Sr, La and Ce, show arc-typical relative depletions in high field strength elements (HFSE) (e.g. Nb, Ta, Zr, Hf) and relatively low heavy rare earth element concentrations (e.g. Tb, Er, Yb) (Fig. A.1). They share these characteristics with other arc volcanic rocks from the Mariana arc (e.g. Elliott et al., 1997). In addition, our new trace element data are in agreement with the previous observation (see Section 2 and references therein, e.g Pearce et al., 2005) that the back-arc samples are dominated by slab-derived fluid enrichment (elevated Ba/Th compared to primitive mantle) and the arc samples additionally contain a marked sediment-melt subduction component (similar Ba/Th but higher Th/Yb and Ba/Yb than the back-arc suite).

4.2. S–Se–Te concentrations

The arc samples exhibit S contents in the range of 10 to 200 $\mu g\, g^{-1}$. Compared to those, back-arc and arc-like samples are characterized by higher S contents between 200 and 930 $\mu g\, g^{-1}$ (Alt et al., 1993). Selenium concentrations of back-arc samples are on average 153 ± 55 $ng\, g^{-1}$ (1 s.d., n = 4), similar to those from arc-like samples with an average of 138 ± 42 $ng\, g^{-1}$ (1 s.d., n = 5) (Fig. 4a). In contrast, the arc samples show lower Se contents with an average of 111 ± 32 $ng\, g^{-1}$ (1 s.d., n = 12) (Table 1) and can vary significantly between volcanoes and even within one individual volcano (e.g. Kasuga). Sulfur/Selenium ratios of back-arc and arc-like samples range from 2190 to 8230 and 1450 to 5110, respectively (Fig. 3d). The arc samples show generally lower S/Se ratios in the range of 120 to 1680 (Fig. 3d).

Tellurium concentrations of back-arc and arc-like samples show average concentrations of 4.0 ± 2.3 $ng\, g^{-1}$ (1 s.d., n = 4) and 2.4 ± 1.5 $ng\, g^{-1}$ (1 s.d., n = 5), respectively (Fig. 4b). The arc samples are characterized by Te concentrations with an average of 2.1 ± 2.0 $ng\, g^{-1}$ (1 s.d., n = 12). The Te concentrations of some arc samples (n = 5, e.g. back-arc sample 1846-9) analyzed by Yi et al. (2000) are in good agreement with those obtained in this study. The Se—Te ratios are controlled by variable Te concentrations and are most variable within the arc samples ranging from 14 to 481. It is noteworthy, that the Se/Te ratios of the Kasuga volcano are among the lowest of all arc samples with typical Se/Te between 14 and 31. Two samples from Fukujin are characterized by very low Te concentrations (< 1 $ng\, g^{-1}$; see Table 1) and thus have the highest Se/Te ratios (393 and 481, respectively).

4.3. Se isotope composition

The average $\delta^{82/76}$Se of the back-arc samples is −0.03 ± 0.03‰ (2 s.d., n = 4) whereas the average $\delta^{82/76}$Se of the arc-like samples is −0.21 ± 0.16‰ (2 s.d., n = 5) (Figs. 2 and 5a). The arc samples exhibit Se isotopic compositions that average at −0.13 ± 0.17‰ (2 s.d., n = 12) (Figs. 2 and 5a). The Se isotope compositions of the samples are not related to silicate differentiation as inferred from the absence of covariation of MgO and $\delta^{82/76}$Se (Fig. 5a). Furthermore, the $\delta^{82/76}$Se of the samples are unrelated to the collection depths (Fig. 3b).

Interestingly, the back-arc samples are isotopically heavier than the arc and arc-like samples, which overlap in their Se isotope composition with recent Se isotope data of MORBs from the Pacific Antarctic Ridge (PAR; Yierpan et al., 2019). However, it is very important to note that, Mariana samples originate from a different mantle domain than Pacific-type MORBs. Volpe et al. (1990) concluded from Sr, Nd and Pb isotope ratios of Mariana Trough basalts (equivalent to back-arc samples analyzed in this study), that the mantle beneath the back-arc region of the Mariana arc is isotopically similar to average Indian-type MORB. Most likely, this also applies to the mantle wedge beneath the Mariana arc, similar to complex dynamics revealed for other SW Pacific arcs (e.g. König et al., 2007; Schuth et al., 2011). In contrast, PAR basalts originate from the Pacific mantle domain that is isotopically depleted compared to the Indian mantle domain (Ito et al., 1987). Thus, the Indian mantle domain resembles an enriched mantle reservoir compared to the Pacific mantle domain, which precludes a direct comparison of the PAR data and our Mariana data. Given the absence of literature $\delta^{82/76}$Se data for the Indian mantle domain, the Mariana pre-subduction wedge may be best represented by melts that originate from enriched reservoirs that are isotopically heavier as indicated also by the heavier back-arc compared to arc lavas analyzed here (Fig. 2). Hence, a suitable Mariana pre-subduction background is provided by the most recent data of worldwide, non-subduction-related basalts (BHVO-2, BCR-2, BIR-1a and BE-N) by Yierpan et al. (2018) and the reported peridotite (PCC-1) value of Rouxel et al. (2002), which yield an average $\delta^{82/76}$Se of 0.23 ± 0.12‰ (2 s.d., n = 5). Compared to this value, all Mariana samples, including for the back-arc, show isotopically lighter Se isotope compositions (Fig. 2). Note, that especially the arc and arc-like samples display a greater variability in their $\delta^{82/76}$Se (e.g. Fig. 2) compared to the more homogeneous and slightly isotopically heavier back-arc lavas. We conducted *t*-tests to evaluate the statistical significance of the different averages of the distinct sample suites relative to the pre-subduction mantle. The three obtained two-tailed *p* values for the back-arc, the arc-like and the arc samples each relative to the pre-subduction mantle equal $t(7) = 4.18$, $p = 0.0042$, $t(8) = 4.92$, $p = 0.0012$ and $t(15) = 4.27$, $p = 0.0007$, which are all statistically very significant.

5. Discussion

5.1. No effect of degassing on Se isotope signatures of submarine Mariana lavas

Previous work on Mariana arc lavas showed heavier S isotope signatures compared to the mantle, which was suggested to mirror recycling of subducted sediments (Alt et al., 1993). A trend of decreasing S contents (Fig. 3a) and low S concentrations in highly vesicular Mariana lavas suggests that partial extrusive degassing of S can occur in submarine environments despite the great pressures of overlying water columns (Alt et al., 1993; Davis et al., 1991). Considerable differences in S concentrations of lavas erupted under submarine conditions may result from partial eruptive degassing, the degree of crystal fractionation, different conditions and percentages of partial melting and variations in source conditions (Davis et al., 1991). An assessment of these processes and their role on S isotope compositions is beyond the scope of this study. Importantly, Se contents and Se isotope compositions of our samples do not systematically change with water depths (Fig. 3b, c), nor do Se contents correlate with Se isotope compositions (Fig. 5b). Moreover, Se concentrations of our samples are independent from S as inferred from a lack of covariation between these elements (Fig. 3d) in contrast to a correlation of S/Se ratios controlled by S (not shown). Therefore, irrespective of the process affecting S, we rule out Se loss and Se isotope fractionation due to eruption-related degassing.

Recently, Jenner et al. (2010) reported similar Se concentrations in volcanic rocks derived from the Manus back-arc basin (north-east of Papua New Guinea) compared to MORB and concluded, that the Se contents remain unchanged during eruption associated degassing, which is in accordance with our conclusion. The decoupling of Se from S in terms of their degassing potential might be due to the fact that Se becomes oxidized only at elevated fO_2, or Eh, compared to S as earlier proposed by Jenner et al. (2010 and references therein). This implies that Se is retained whereas S (oxidized at given Eh) is lost.

5.2. Magmatic differentiation

Although submarine Mariana arc lavas from the shallowest depths contain the lowest S contents (Table 1), back-arc lavas from rather constant and great depths ($>$ 3000 mbsl) also show very variable S contents (~200–1000 $\mu g/g^{-1}$). This suggests that a process unrelated to changing water column pressure (such as potential degassing and magmatic differentiation) also affected the S contents of the lavas. Since all our samples show MgO contents between ~9 and 2 wt% (Table 1) the effect of magmatic differentiation and potential sulfide segregation needs to be considered when interpreting chalcophile element concentrations and in particular potential Se isotope variations.

Geochemical evidence for sulfide segregation stems from trends of chalcophile element concentrations (Cu, Se and Te) and V/Sc versus

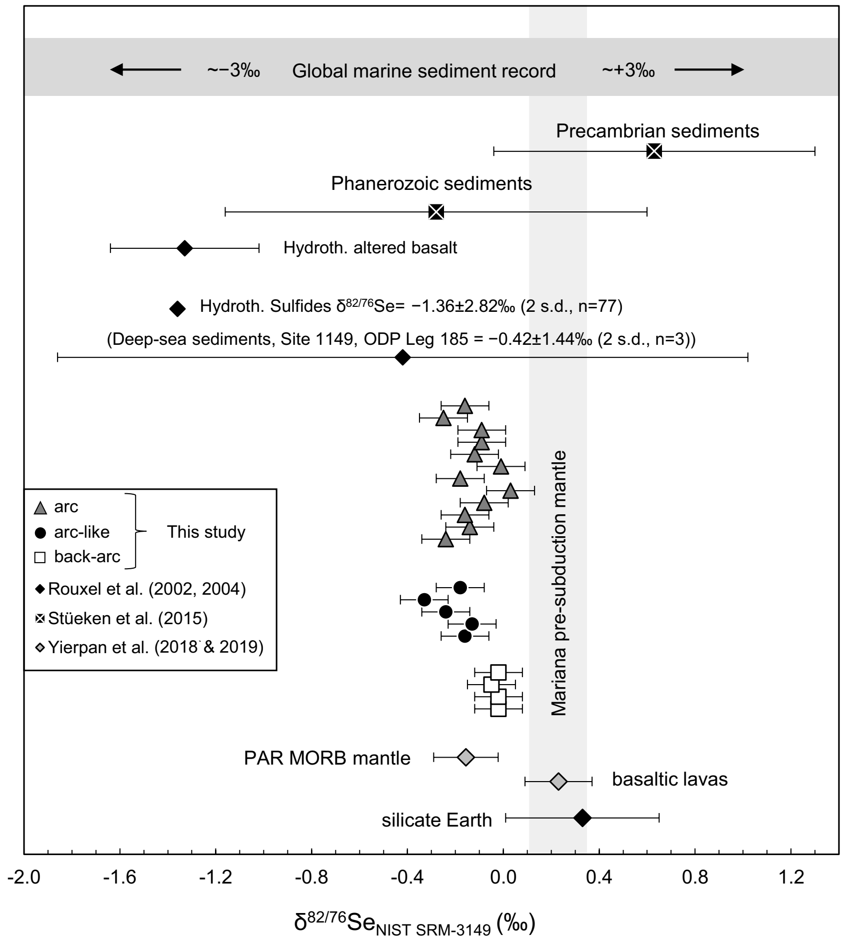

Fig. 2. Compilation of Se isotope compositions of Mariana lavas analyzed in this study and literature data. Data for deep-sea sediments, hydrothermal sulfides, hydrothermally altered basalts and the silicate Earth from Rouxel et al., (2002) are averaged values. Additional data for hydrothermal sulfides from Rouxel et al. (2004). Silicate Earth value by Rouxel et al. (2002) comprises a peridotite (PCC-1) and five basalts (BHVO-1, BCR-1, BE-N and BR). 'basaltic lavas' (BHVO-2, BCR-2, BIR-1a, BE-N) from Yierpan et al. (2018). The vertical grey box indicates range of the Mariana pre-subduction mantle value that comprises basalts without any subduction-related origin measured by Yierpan et al. (2018) and the peridotite analyzed by Rouxel et al., (2002). PAR mantle represented by Pacific Antarctic Ridge MORBs (n = 27) from Yierpan et al. (2019). Average values for Phanerozoic and Precambrian sediments from Stüeken et al. (2015). Range of global marine sediments from Mitchell et al., (2016) and references therein. All error bars given as 2 s.d. uncertainty, for details see Section 3.3. No error bars displayed for hydrothermal sulfides as uncertainties exceed the diagram range (instead values are given).

MgO (Fig. 4) (Jenner, 2017 and references therein). Before ~7 wt% MgO the concentrations of Se, Te (and some Cu) increase, followed by a drop in concentrations (Fig. 4a-c). A different phase than sulfide has to account for the observed changes in Se–Te–Cu concentrations, because the melt is under-saturated in sulfides at this stage of melt differentiation (Jenner et al., 2015; Jenner et al., 2010). In the case of the platinum group elements (PGEs), a Pt-rich alloy has been identified to be the most likely source of PGE depletion during early stages of fractional crystallization before the magnetite crisis and segregation of sulfides (Jenner et al., 2015; Park et al., 2013). Thus, it is likely that Se and (especially) Te are concentrated in alloys (e.g. tellurides; König et al., 2015a) that crystallize from sulfide under-saturated melts.

From ~6 to ~3 wt% MgO, Se and Cu concentrations increase whereas Te concentrations still decrease, which might be due to incorporation of Te into Pt-Te-alloys (Fig. 4b). Note, that the observed trend seen for Cu concentrations (Fig. 4c) is also evident from Cu data reported in the literature (Jenner et al., 2015; Williams et al., 2018). At ~3 wt% MgO and contents of Cu, Se and Te in the melt show a pronounced scatter, possibly related to appearance of sulfides, which are not fully segregating (previously inferred by Williams et al. (2018)).

At 2.8 wt% MgO, magnetite appears on the liquidus as inferred from the onset of decreasing V/Sc that is accompanied with a decrease in the $Fe^{3+}/\Sigma Fe$ ratio leading to a decline in fO_2 (Jenner et al., 2010). At this stage sulfide becomes saturated in the melt and finally segregates, thus scavenging Se, Te and Cu, albeit to different extents (more pronounced decrease of Cu and Te contents compared to Se; Fig. 4). This is related to a lower sulfide-silicate melt partition coefficient of Se compared to Cu.

Whereas the exact processes responsible for the unsystemtic variations in Cu, Se and Te concentrations remain to be constrained, it is important to investigate potential correlations between Se concentrations and an index of differentiation, such as MgO, with Se isotope variations. Previous studies (Prytulak et al., 2017; Williams et al., 2018) involving Mariana arc lavas showed that for both V and Fe, significant isotope fractionation is induced as a consequence of magnetite fractionation and sulfide segregation, respectively. Both studies identified heavier isotope compositions following the 'magnetite-crisis' at ~2.8 wt % MgO, consistent with preferential scavenging of isotopically light V and Fe into magnetite and sulfide phases.

Such a link between sulfide saturation and Se isotope fractionation is not observed in our study. No trend between the Se isotope composition and MgO or Se is seen (Fig. 5a,b), which suggests that magmatic differentiation processes significantly affect both Se and other chalcophile element contents of the samples analyzed (Fig. 4), but do not result in Se isotope fractionation. This is in agreement with observations and conclusions based on a dry magmatic suite from the PAR (Yierpan et al., 2019). As neither degassing nor magmatic differentiation affect the Se isotope compositions of our samples, the isotopic variations among Mariana samples, particularly systematic differences between back-arc and arc samples are most likely related to their respective source composition.

5.3. *Different subduction components and their influence on the Se isotope composition of arc lavas*

The $\delta^{82/76}$Se signatures of Mariana lavas show a relatively large range and overall lower values compared to a rather confined range for the Mariana pre-subduction mantle, represented by basaltic melts and peridotite from intraplate and ridge settings, but without any subduction-related origin. Thus, $\delta^{82/76}$Se signatures of Mariana lavas seem

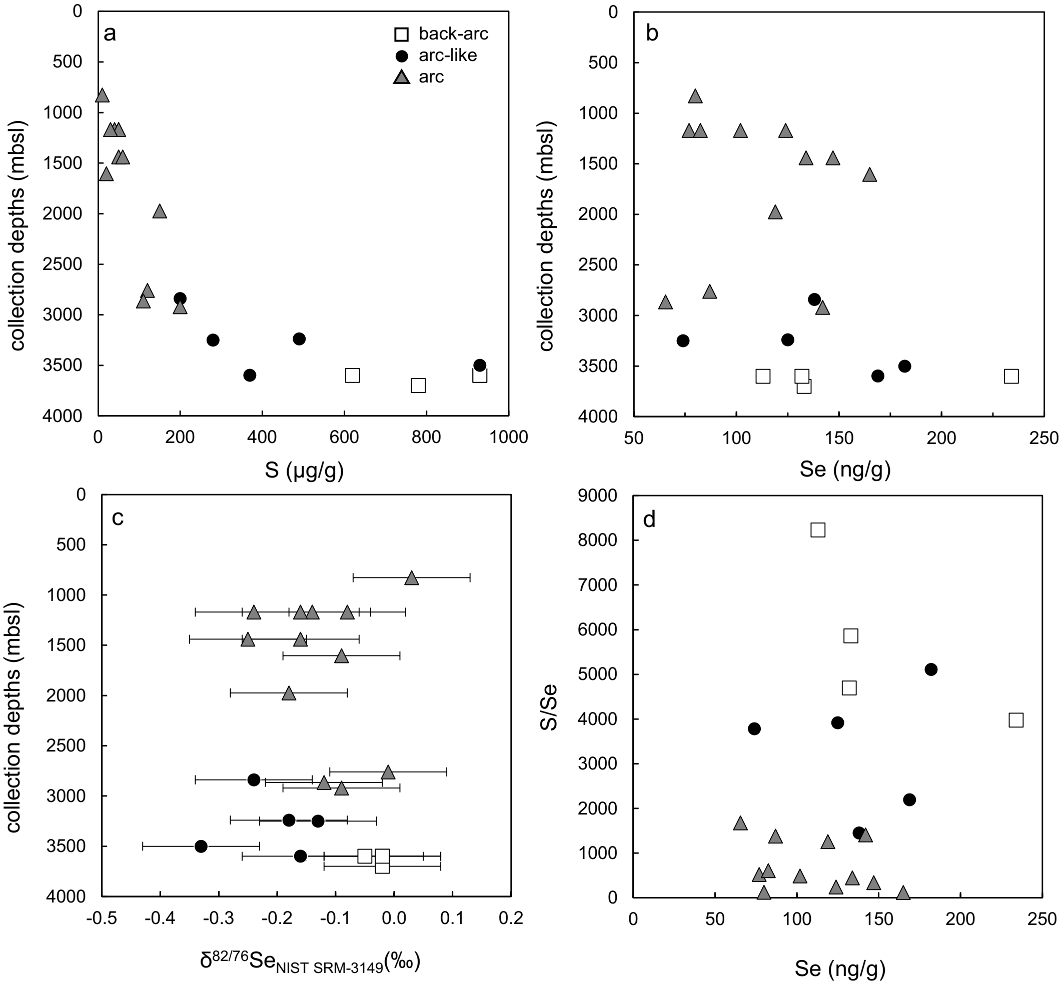

Fig. 3. (a) Apparent covariation of collection depth and S concentrations, (b) no indication of eruption-related degassing of Se. (c) No covariation of collection depth and Se isotope composition, (d) S/Se vs. Se concentrations indicating S/Se not controlled by Se concentrations. All error bars given as 2 s.d.

indeed intrinsic to their subduction zone origin (Fig. 2). The Se isotope compositions of the Mariana lavas represent that of their mantle sources in contrast to their elemental budget that is compromised by magmatic differentiation (see Section 5.2). Se isotopes of Mariana lavas may thus trace the slab-derived contribution and be related to potential recycling of Se in subduction zones. Although the Mariana system is highly complex, the natures of subduction components (i.e. fluid-like and melt-like components, see Sections 2 and 4.1) added to the sub-arc mantle are broadly classified via different incompatible trace element systematics (Pearce et al., 2005). Any covariations between these proxies of subduction components and Se isotope compositions could therefore help to assess potential subduction recycling of Se. Slab-derived fluids and sediment melts may influence the Se isotope compositions of Mariana lavas to different extents. Fig. 6a shows variable Ba/Th and Th/Yb ratios indicating that Mariana arc lavas are affected by both subduction components as has been documented in the literature (e.g. Elliott et al., 1997). Fig. 6b shows the Se isotope compositions of all Mariana samples relative to Ba/Th, indicating slab-derived fluid enrichments (termed shallow subduction component by Pearce et al. (2005)). It can be observed that Mariana lavas all show lower $\delta^{82/76}$Se at somewhat higher Ba/Th compared to the Mariana pre-subduction mantle albeit some scatter exists in the dataset (Fig. 6b). Slab-derived sediment melts were termed deep subduction component by Pearce et al. (2005) and are indicated for instance by elevated Th/Yb in arc samples. Interestingly, these arc samples also extend to slightly heavier Se isotope compositions relative to slab-fluid dominated back-arc and arc-like samples (Fig. 6c). The influence of a sediment melt on the arc samples is also expressed by high La/Sm ratios (Elliott, 2003), which indeed show a positive trend with $\delta^{82/76}$Se but no trend with indicators for magmatic differentiation such as MgO contents (Fig. A.2).

Although back-arc and arc-like samples mostly overlap in their relatively low Th/Yb, they can be distinguished based on their respective $\delta^{82/76}$Se (Fig. 6c). In particular the back-arc samples with their highest relative $\delta^{82/76}$Se do not match the tendencies observed for the other sample suites, which could be attributed to their rather distinct origin within the subduction zone. Indeed, the location of the back-arc samples lies ~350 km away from that of the arc-like samples (Fig. 1). In contrast, arc and arc-like samples originate from relatively restricted areas, respectively. These two groups however share the same subtle tendency between $\delta^{82/76}$Se and Th/Yb (Fig. 6c), which is in agreement with a strong arc signature previously found in back-arc lavas from 22°N (see Section 2; Stern et al. (1990)). The back-arc samples fall off this trend, possibly reflecting a different source due to the remote setting. It seems clear however, that all samples experienced slab fluid addition revealed by increased Ba/Th and offset to lower $\delta^{82/76}$Se compared to the pre-subduction mantle. Again, the distinction between shallow and deep subduction contribution based on Ba–Th–Yb systematics and the observation that sediment melts are more dominant in the arc samples compared to the back-arc samples is entirely based on a previous classification (Pearce et al., 2005). Reasons for a similar shallow and less pronounced deep subduction signature in back-arc lavas may be a chromatographic effect and dilution by back-arc melts

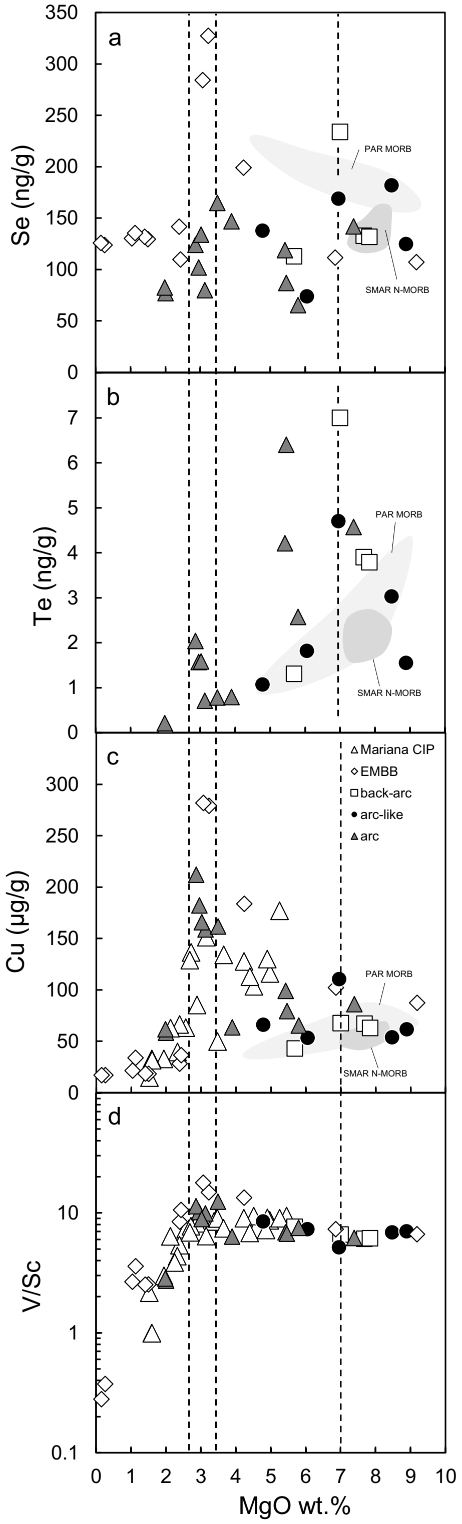

Fig. 4. (a) Se, (b) Te and (c) Cu concentrations vs. MgO content show variation of chalcophile element concentrations as a function of their bulk partition coefficients during magmatic differentiation. (d) V/Sc ratio vs. MgO content, indicates V partitioning into magnetite and onset of the 'magnetite crisis' at ~3–4 wt% MgO. Data for the Eastern Manus back-arc basin (EMBB) from Jenner et al., (2015 and references therein). PAR MORB data (light grey fields) from Yierpan et al. (2019). SMAR N-MORB (dark grey fields) data from Lissner et al. (2014). Copper concentration data of samples from the Central Island Province (CIP) of the Mariana system from Williams et al. (2018). Dashed vertical lines represent important stages during magmatic differentiation, see text for interpretation of the data.

(Stolper and Newman, 1994). Overall, it seems that shallow slab fluids can explain lower $\delta^{82/76}$Se, whereas deep-derived sediment melts may carry a heavier Se isotope signature that raises the $\delta^{82/76}$Se again (i.e. buffer the initial slab-fluid signature). Hence, slab-derived fluids and sediment melts (Fig. 6a, Ba/Th vs. Th/Yb) may shift $\delta^{82/76}$Se in arc lavas to opposing directions, where the relative proportion of these subduction components ultimately determines the direction of tendencies among suites. As a result, the total subduction addition, expressed by Ba/Yb (Fig. 6d), may be the best approximation of a net recycling signature (Pearce et al., 2005) that seems to produce lower overall $\delta^{82/76}$Se compared to the Mariana pre-subduction mantle. Further studies that examine in more detail the effects of different types of subduction components are clearly required. Moreover, it remains to be investigated if and how a net contribution of subduction components to arc lavas relate to the Se isotope signature of the subduction input. In the case of S, the heavier δ^{34}S of Mariana lavas compared to the mantle has been linked to recycling of subducted sediments (Alt et al., 1993). Sediments in addition to altered oceanic crust containing hydrothermal sulfides indeed show variable Se isotope compositions (e.g. Mitchell et al., 2016; Rouxel et al., 2004; Rouxel et al., 2002). Therefore, it is necessary to assess if recycling of these materials might in principle account for the Se isotope compositions observed in subduction zone magmas.

5.4. Recycling of subducted surface material as possible source for Se isotope variability in Mariana arc lavas

Marine sediments have been the focus of numerous Se isotope studies (e.g. Mitchell et al., 2016 and references therein). So far, available data from the literature comprises shales of various ages (Archean to present day) and depositional environments (open marine and marine basins) with distinct conditions (euxinic, anoxic, suboxic and oxic) (Mitchell et al., 2016). Stüeken et al. (2015) identified a statistically significant shift in the Se isotope composition from predominantly positive (0.63 ± 0.67‰; 2 s.d., n = 169) to negative (−0.28 ± 0.88‰; 2 s.d., n = 240) $\delta^{82/76}$Se values from Precambrian to Phanerozoic samples (Fig. 2; see also Fig. 3a in Stüeken et al., 2015). Taken together, the Se isotope compositions of all these samples combined with other published $\delta^{82/76}$Se data (e.g. Mitchell et al., 2016) are in the range of −3 to +3‰ (Fig. 2; see also Mitchell et al., 2016). This suggests that not the entire Se isotope variation of all hitherto analyzed sediments qualify as endmembers to constrain potential sediment recycling in a modern subduction zone system. Instead, a narrower isotopic range of only modern sediments can be considered to begin with. In addition to age, the depositional setting may also be critical. Isotope fractionations in low-temperature environments can be large as inferred from laboratory experiments (Johnson and Bullen, 2004) and the wide range of reported $\delta^{82/76}$Se of sediments (e.g. Mitchell et al., 2016; Rouxel et al., 2002; Stüeken et al., 2015). Even these modern surface Se isotope variations exceed that identified in Mariana lavas by far but all show average $\delta^{82/76}$Se that are distinctly negative (Fig. 2). Thus, subduction recycling of surface material may indeed account for the isotopic offset of Mariana lavas compared to the Mariana pre-subduction mantle range.

Deep-sea sediments of the uppermost stratigraphic section from Site 1149 ODP 129, which are subducted beneath the Izu-Bonin-Arc as part of the Izu-Bonin-Mariana subduction system, have been analyzed for Se isotopes (Rouxel et al., 2002). These sediments have an average Se isotope composition of −0.42 ± 1.44‰ (2 s.d., n = 3, Rouxel et al., 2002), in agreement with input of, on average, isotopically light Se during subduction. However, in addition to pelagic sediments, subducted volcaniclastic turbidites have been identified as another major source of melt-like subduction components affecting the geochemistry of arc lavas in the northern part of the Mariana arc (Tollstrup and Gill, 2005). Moreover, isotopically light, hydrothermally altered basalt may also contribute to an isotopically light subduction input

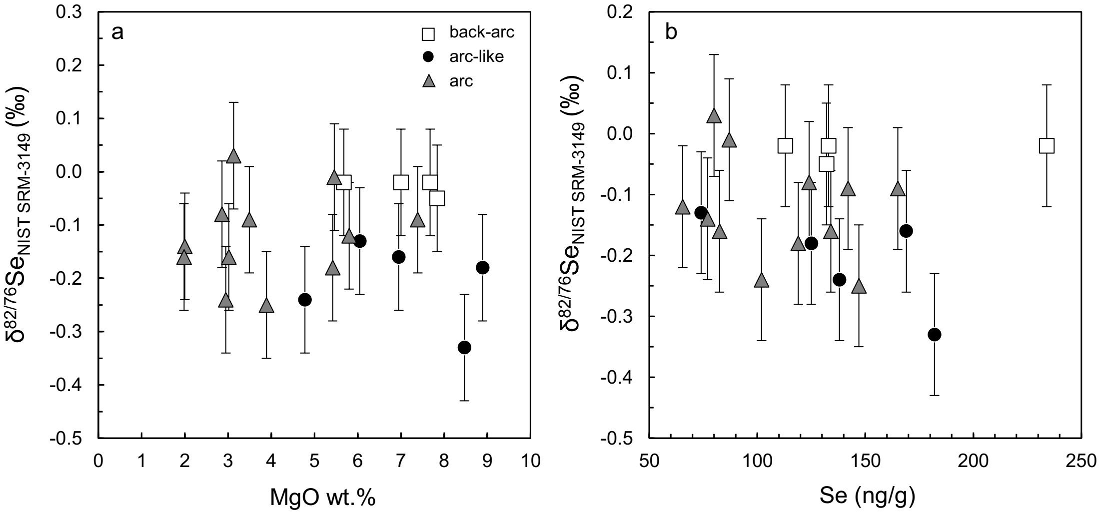

Fig. 5. (a) Se isotope compositions of Mariana lavas vs. MgO contents shows no covariation with index of alteration indicating absence of isotope fractionation during magmatic differentiation. (b) Se isotope composition of Mariana lavas vs. Se concentrations indicates no isotope fractionation during magmatic differentiation (i.e. sulfide segregation, alloy fractionation; see text for details).

(-1.33 ± 0.31‰, 2 s.d., n = 2; Rouxel et al., 2002). Overall, although the proportion of altered versus unaltered oceanic crust to a net subduction input is difficult to constrain, the role of subducted sulfides need to be considered.

Due to its chalcophile behavior Se is predominantly hosted by sulfides both in the mantle and slab (e.g. Guo et al., 1999; Hattori et al., 2002; König et al., 2015a; König et al., 2014). Thus, hydrothermal sulfides may constitute important subduction input material and published data show an average Se isotope composition of -1.36 ± 2.82‰ (2 s.d., n = 77; Rouxel et al., 2004; Rouxel et al., 2002) with the most extreme values up to -4.75‰. This is in agreement with recent analyses of hydrothermal pyrite minerals, albeit from a continental setting, showing a record of $\delta^{82/76}$Se ranging from -4.48 ± 0.09‰ to -0.39 ± 0.09‰ (2 s.d., n = 10) with an average of -2.73 ± 0.09‰, altogether confirming the pronounced, isotopically light hydrothermal sulfide signatures for Se (König et al., 2019). Hydrothermal sulfides together with pelagic clays may be among the first phases to destabilize during subduction and therefore significantly contribute to slab-derived fluid signatures. The importance of sulfides in the recycling of chalcophile elements is supported by the observation of migrating S-bearing fluids up the subduction interface after liberation of sulfide from sediments and altered basalt at shallower depth (Mottl et al., 2004). It has further been suggested that S is released from magmatic sulfides in sediments and the oceanic crust itself by extensive recrystallization during high-pressure metamorphism (Li et al., 2016), possibly amplifying Se recycling. However, some S enters deeper parts of the subduction zone as indicated by sulfide inclusions in garnets from eclogites that grew during prograde metamorphism (Li et al., 2016). This sulfur might be liberated by subduction components that contribute to enrichment of the deeper sub-arc mantle wedge. In summary, the complex combination of pelagic and volcaniclastic sediments, altered and unaltered oceanic crust and sulfides altogether could account for the relatively lighter Se isotope signatures of Mariana lavas compared to the pre-subduction mantle (Fig. 2).

A pronounced shift in the average Se isotope composition of marine sediments before and after ca. 550 Ma ($\Delta_{\text{Precambrian}-\text{Phanerozoic}} \approx 0.91$‰; Stüeken et al. (2015)) was recently reported. This shift was interpreted to be the result of increased oxidative weathering and more pronounced continental mobilization of Se following Earth's second atmospheric oxygen increase ca. 550 Ma ago (Neoproterozoic Oxygenation Event, NOE). Progressive subduction of this isotopically lighter average Se isotope input may have had an impact on the secular Se isotope composition of the Earth's upper mantle after ca. 550 Ma, possibly mirroring the NOE. Such a link between stepwise atmospheric oxygenation and mantle evolution has previously been invoked for redox-sensitive uranium isotope systematics (Andersen et al., 2015). Subduction recycling of Se may not only produce larger and systematic Se isotope variations in Mariana lavas compared to the Mariana pre-subduction mantle but also, make Se isotopes a tool to investigate links between Earth's interior and atmospheric oxygenation throughout geological history.

6. Conclusions

The first case study involving stable Se isotopes in arc and back-arc lavas provides significant new insights into the systematics of this chalcophile and moderately volatile element in subduction zones. The Se isotope signature of submarine Mariana lavas is not affected by degassing and, unlike the elemental Se budget, not affected by magmatic differentiation. Therefore, the $\delta^{82/76}$Se of submarine arc lavas may retain its source signature. This signature is likely enriched by melt-like and fluid-like subduction components derived from the subducting Pacific crust and overlying sedimentary cover. Mariana samples show a tendency to become isotopically lighter from the back-arc to arc(-like) lavas, possibly reflecting a decreasing chromatographic effect of the overlying mantle wedge and increasing influence of a fluid signature. Addition of a sediment melt-like subduction component seems to buffer this fluid-induced signature as observed in Mariana arc samples. Due to these complex contributions of subduction components, Se isotope compositions of Mariana lavas show a larger range and are overall lighter than the pre-subduction mantle range that comprises peridotite and non-subduction related worldwide mantle melts. Possible slab-derived contributions may be traced back to subduction recycling of isotopically light Se input such as modern sediments and altered sulfide-bearing oceanic crust. Subduction recycling of Se may also have had an impact on the secular Se isotope composition of the Earth's upper mantle, because of a considerable shift to lighter average $\delta^{82/76}$Se in sediments that was attributed to the Neoproterozoic Oxygenation Event ca. 550 Ma ago. Further work on Se isotope systematics in arc lavas should therefore be dedicated to the different roles of variable subduction components and the possible links between atmospheric oxygenation, Se recycling and isotopic evolution of the mantle through geological time.

Supplementary data to this article can be found online at https://doi.org/10.1016/j.chemgeo.2019.03.011.

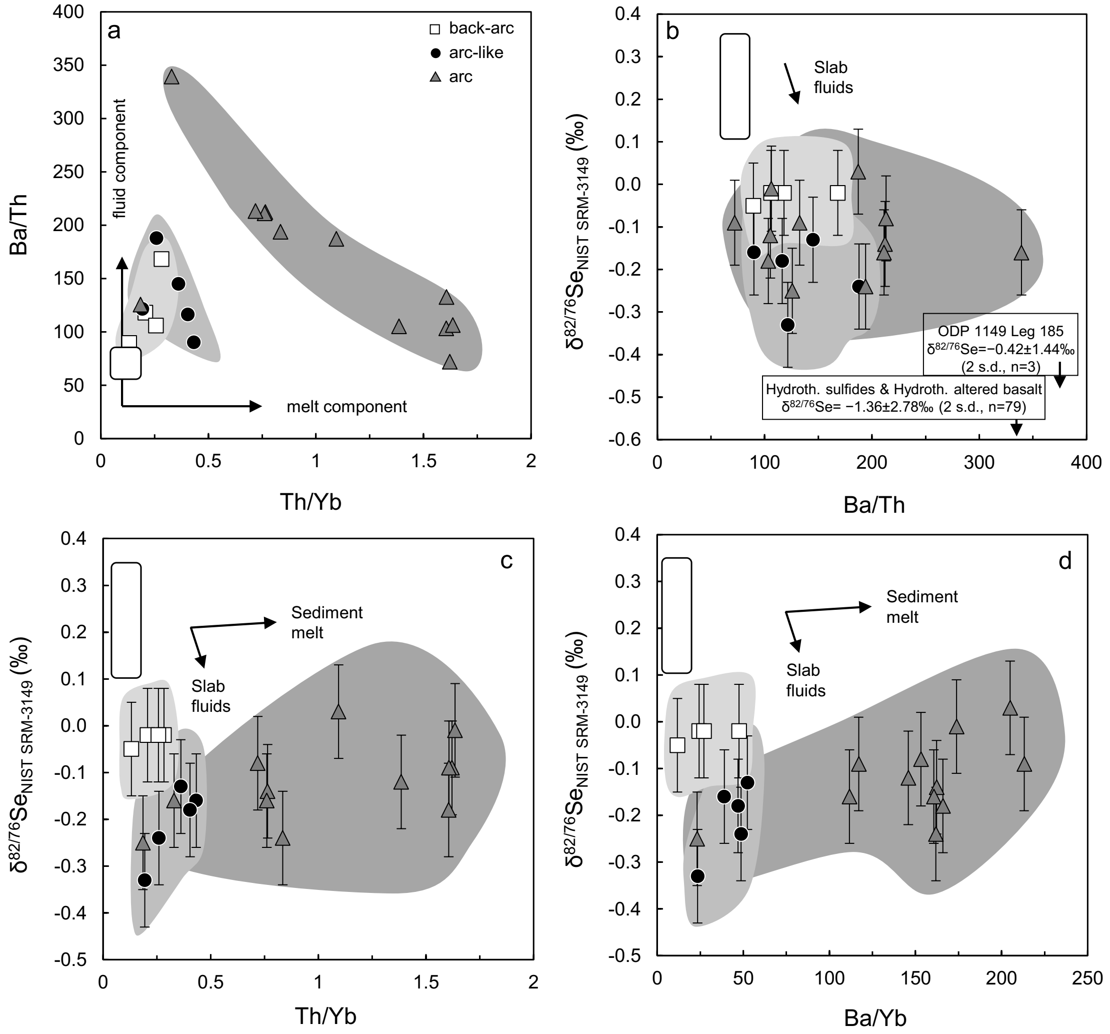

Fig. 6. (a) Ba/Th vs. Th/Yb indicating different proportions of slab-derived components. Se isotope composition vs. (b) Ba/Th and (c) Th/Yb indicating the influence of slab-derived fluid and melt-like components. (d) Se isotope composition vs. Ba/Yb demonstrates Se isotope composition as function of total subduction addition. See Section 5.3 for details. Labelled boxes in (b) point to Se isotope compositions of deep-sea sediments (ODP 1149 Leg 185), hydrothermally altered basalt and hydrothermal sulfides analyzed by Rouxel et al., (2002, 2004). White box indicates Mariana pre-subduction mantle wedge value (0.23 ± 0.12‰, 2 s.d., n = 5) represented by non-subduction-related mantle melts (basalts, Yierpan et al., 2018; peridotite, Rouxel et al., 2002) and. Ba/Th, Th/Yb and Ba/Yb ratios for the (sub-arc) mantle taken from Gale et al. (2013). All error bars given as 2 s.d.

Acknowledgements

This work was funded by an ERC Starting Grant (O2RIGIN, 636808) to Stephan König. We acknowledge laboratory support by Ilka Kleinhanns and Elmar Reitter and help with major and trace element analyses by Bernd Steinhilber. This study benefited from constructive reviews by Frances Jenner, an anonymous reviewer and Catherine Chauvel, who also is thanked for editorial handling.

References

Albut, G., Babechuk, M.G., Kleinhanns, I.C., Benger, M., Beukes, N.J., Steinhilber, B., Smith, A.J., Kruger, S.J., Schoenberg, R., 2018. Modern rather than Mesoarchaean oxidative weathering responsible for the heavy stable Cr isotopic signatures of the 2.95 Ga old Ijzermijn iron formation (South Africa). Geochim. Cosmochim. Acta 228, 157–189.

Alt, J.C., Shanks, W.C., Jackson, M.C., 1993. Cycling of sulfur in subduction zones: the geochemistry of sulfur in the Mariana Island Arc and back-arc trough. Earth Planet. Sci. Lett. 119 (4), 477–494.

Andersen, M.B., Elliott, T., Freymuth, H., Sims, K.W., Niu, Y., Kelley, K.A., 2015. The terrestrial uranium isotope cycle. Nature 517 (7534), 356–359.

Brenan, J.M., 2015. Se–Te fractionation by sulfide–silicate melt partitioning: implications for the composition of mantle-derived magmas and their melting residues. Earth Planet. Sci. Lett. 422, 45–57.

Davis, A.S., Clague, D.A., Schulz, M.S., Hein, J.R., 1991. Low sulfur content in submarine lavas: an unreliable indicator of subaerial eruption. Geology 19 (7), 750–753.

Elliott, T., 2003. Tracers of the Slab. Inside the Subduction Factory. pp. 23–45.

Elliott, T., Plank, T., Zindler, A., White, W., Bourdon, B., 1997. Element transport from slab to volcanic front at the Mariana arc. J. Geophys. Res. Solid Earth 102 (B7), 14991–15019.

Gale, A., Dalton, C.A., Langmuir, C.H., Su, Y., Schilling, J.G., 2013. The mean composition of ocean ridge basalts. Geochem. Geophys. Geosyst. 14 (3), 489–518.

Guo, J.F., Griffin, W.L., O'Reilly, S.Y., 1999. Geochemistry and origin of sulphide minerals in mantle xenoliths: Qilin, southeastern China. J. Petrol. 40 (7), 1125–1149.

Hamlyn, P.R., Keays, R.R., Cameron, W.E., Crawford, A.J., Waldron, H.M., 1985. Precious metals in magnesian low-ti lavas - implications for metallogenesis and sulfur saturation in primary magmas. Geochim. Cosmochim. Acta 49 (8), 1797–1811.

Harvey, J., König, S., Luguet, A., 2015. The effects of melt depletion and metasomatism on highly siderophile and strongly chalcophile elements: S–Se–Te–Re–PGE systematics of peridotite xenoliths from Kilbourne Hole, New Mexico. Geochim. Cosmochim. Acta 166, 210–233.

Hattori, K.H., Arai, S., Clarke, D.B., 2002. Selenium, tellurium, arsenic and antimony contents of primary mantle sulfides. Can. Mineral. 40 (2), 637–650.

Ito, E., White, W.M., Göpel, C., 1987. The O, Sr, Nd and Pb isotope geochemistry of MORB. Chem. Geol. 62 (3), 157–176.

Jenner, F.E., 2017. Cumulate causes for the low contents of sulfide-loving elements in the continental crust. Nat. Geosci. 10 (7), 524–529.

Jenner, F.E., O'Neill, H.S.C., Arculus, R.J., Mavrogenes, J.A., 2010. The magnetite crisis in the evolution of arc-related magmas and the initial concentration of Au, Ag and Cu. J. Petrol. 51 (12), 2445–2464.

Jenner, F.E., Arculus, R.J., Mavrogenes, J.A., Dyriw, N.J., Nebel, O., Hauri, E.H., 2012.

Chalcophile element systematics in volcanic glasses from the northwestern Lau Basin. Geochem. Geophys. Geosyst. 13 (6).

Jenner, F.E., Hauri, E.H., Bullock, E.S., Konig, S., Arculus, R.J., Mavrogenes, J.A., Mikkelson, N., Goddard, C., 2015. The competing effects of sulfide saturation versus degassing on the behavior of the chalcophile elements during the differentiation of hydrous melts. Geochem. Geophys. Geosyst. 16 (5), 1490–1507.

Jochum, K.P., Weis, U., Schwager, B., Stoll, B., Wilson, S.A., Haug, G.H., Andreae, M.O., Enzweiler, J., 2016. Reference values following ISO guidelines for frequently requested rock reference materials. Geostand. Geoanal. Res. 40 (3), 333–350.

Johnson, T.M., Bullen, T.D., 2004. Mass-dependent fractionation of selenium and chromium isotopes in low-temperature environments. Rev. Mineral. Geochem. 55 (1), 289–317.

Kimura, K., Lewis, R.S., Anders, E., 1974. Distribution of gold and rhenium between nickel-iron and silicate melts: implications for the abundance of siderophile elements on the Earth and Moon. Geochim. Cosmochim. Acta 38 (5), 683–701.

König, S., Schuth, S., Münker, C., Qopoto, C., 2007. The Role of Slab Melting in the Petrogenesis of High-Mg Andesites: Evidence from Simbo Volcano, Solomon Islands. 153. pp. 85–103.

König, S., Lorand, J.-P., Luguet, A., Pearson, D.G., 2014. A non-primitive origin of near-chondritic S–Se–Te ratios in mantle peridotites; implications for the Earth's late accretionary history. Earth Planet. Sci. Lett. 385, 110–121.

König, S., Lissner, M., Lorand, J.-P., Bragagni, A., Luguet, A., 2015a. Mineralogical control of selenium, tellurium and highly siderophile elements in the Earth's mantle: evidence from mineral separates of ultra-depleted mantle residues. Chem. Geol. 396, 16–24.

König, S., Luguet, A., Lorand, J.-P., Lissner, M., Graham Pearson, D., 2015b. Reply to the comment on "a non-primitive origin of near-chondritic S–Se–Te ratios in mantle peridotites: Implications for the Earth's late accretionary history" by König S. Et al. [Earth Planet. Sci. Lett. 385 (2014) 110–121]. Earth Planet. Sci. Lett. 417, 167–169.

König, S., Eickmann, B., Zack, T., Yierpan, A., Wille, M., Taubald, H., Schoenberg, R., 2019. Redox induced sulfur-selenium isotope decoupling recorded in pyrite. Geochim. Cosmochim. Acta 244, 24–39.

Kurzawa, T., Konig, S., Labidi, J., Yierpan, A., Schoenberg, R., 2017. A method for Se isotope analysis of low ng-level geological samples via double spike and hydride generation MC-ICP-MS. Chem. Geol. 466, 219–228.

Labidi, J., Cartigny, P., Moreira, M., 2013. Non-chondritic Sulphur isotope composition of the terrestrial mantle. Nature 501 (7466), 208–211.

Labidi, J., Shahar, A., Le Losq, C., Hillgren, V.J., Mysen, B.O., Farquhar, J., 2016. Experimentally determined sulfur isotope fractionation between metal and silicate and implications for planetary differentiation. Geochim. Cosmochim. Acta 175, 181–194.

Labidi, J., König, S., Kurzawa, T., Yierpan, A., Schoenberg, R., 2018. The selenium isotopic variations in chondrites are mass-dependent; Implications for sulfide formation in the early solar system. Earth Planet. Sci. Lett. 481, 212–222.

Li, J.L., Gao, J., Klemd, R., John, T., Wang, X.S., 2016. Redox processes in subducting oceanic crust recorded by sulfide-bearing high-pressure rocks and veins (SW Tianshan, China). Contrib. Mineral. Petrol. 171, 72(8–9.

Lissner, M., König, S., Luguet, A., le Roux, P., Schuth, S., Heuser, A., le Roex, A., 2014. Selenium and tellurium systematics in MORBs from the southern Mid-Atlantic Ridge (47–50 S). Geochim. Cosmochim. Acta 144, 379–402.

Lorand, J.-P., Alard, O., 2010. Determination of selenium and tellurium concentrations in Pyrenean peridotites (Ariege, France): new insight into S/Se/Te systematics of the upper in mantle samples. Chem. Geol. 278 (1), 120–130.

Luguet, A., Behrens, M., Pearson, D.G., König, S., Herwartz, D., 2015. Significance of the whole rock Re–Os ages in cryptically and modally metasomatised cratonic peridotites: Constraints from HSE–Se–Te systematics. Geochim. Cosmochim. Acta 164, 441–463.

Mitchell, K., Mansoor, S.Z., Mason, P.R.D., Johnson, T.M., Van Cappellen, P., 2016. Geological evolution of the marine selenium cycle: insights from the bulk shale δ82/76Se record and isotope mass balance modeling. Earth Planet. Sci. Lett. 441, 178–187.

Mottl, M.J., Wheat, C.G., Fryer, P., Gharib, J., Martin, J.B., 2004. Chemistry of springs across the Mariana forearc shows progressive devolatilization of the subducting plate. Geochim. Cosmochim. Acta 68 (23), 4915–4933.

Palme, H., O'Neill, H.S.C., 2014. 3.1 - cosmochemical estimates of mantle composition. In: Holland, H.D., Turekian, K.K. (Eds.), Treatise on Geochemistry, Second edition. Elsevier, Oxford, pp. 1–39.

Park, J.-W., Campbell, I.H., Arculus, R.J., 2013. Platinum-alloy and sulfur saturation in an arc-related basalt to rhyolite suite: evidence from the Pual Ridge lavas, the Eastern Manus Basin. Geochim. Cosmochim. Acta 101, 76–95.

Pearce, J.A., Stern, R.J., Bloomer, S.H., Fryer, P., 2005. Geochemical mapping of the Mariana arc-basin system: Implications for the nature and distribution of subduction components. Geochem. Geophys. Geosyst. 6.

Prytulak, J., Nielsen, S., Plank, T., Barker, M., Elliott, T., 2013. Assessing the utility of thallium and thallium isotopes for tracing subduction zone inputs to the Mariana arc. Chem. Geol. 345, 139–149.

Prytulak, J., Sossi, P.A., Halliday, A.N., Plank, T., Savage, P.S., Woodhead, J.D., 2017. Stable vanadium isotopes as a redox proxy in magmatic systems? Geochem. Perspect. Lett. 3 (0), 75–84.

Rose-Weston, L., Brenan, J.M., Fei, Y., Secco, R.A., Frost, D.J., 2009. Effect of pressure, temperature, and oxygen fugacity on the metal-silicate partitioning of Te, Se, and S: Implications for earth differentiation. Geochim. Cosmochim. Acta 73 (15), 4598–4615.

Rouxel, O., Ludden, J., Carignan, J., Marin, L., Fouquet, Y., 2002. Natural variations of Se isotopic composition determined by hydride generation multiple collector inductively coupled plasma mass spectrometry. Geochim. Cosmochim. Acta 66 (18), 3191–3199.

Rouxel, O., Fouquet, Y., Ludden, J.N., 2004. Subsurface processes at the lucky strike hydrothermal field, Mid-Atlantic ridge: evidence from sulfur, selenium, and iron isotopes 1. Geochim. Cosmochim. Acta 68 (10), 2295–2311.

Schuth, S., König, S., Münker, C., 2011. Subduction zone dynamics in the SW Pacific plate boundary region constrained from high-precision Pb isotope data. Earth Planet. Sci. Lett. 311 (3), 328–338.

Stern, R.J., Bloomer, S.H., 1992. Subduction Zone Infancy - examples from the Eocene Izu-Bonin-Mariana and Jurassic California Arcs. Geol. Soc. Am. Bull. 104 (12), 1621–1636.

Stern, R.J., Lin, P.-N., Morris, J.D., Jackson, M.C., Fryer, P., Bloomer, S.H., Ito, E., 1990. Enriched back-arc basin basalts from the northern Mariana Trough: implications for the magmatic evolution of back-arc basins. Earth Planet. Sci. Lett. 100 (1), 210–225.

Stern, R.J., Fouch, M.J., Klemperer, S.L., 2003. An Overview of the Izu-Bonin-Mariana Subduction Factory. Inside the Subduction Factory. vol. 138. pp. 175–222.

Stolper, E., Newman, S., 1994. The role of water in the petrogenesis of Mariana trough magmas. Earth Planet. Sci. Lett. 121 (3), 293–325.

Stüeken, E.E., Buick, R., Bekker, A., Catling, D., Foriel, J., Guy, B.M., Kah, L.C., Machel, H.G., Montanez, I.P., Poulton, S.W., 2015. The evolution of the global selenium cycle: secular trends in Se isotopes and abundances. Geochim. Cosmochim. Acta 162, 109–125.

Tollstrup, D.L., Gill, J.B., 2005. Hafnium systematics of the Mariana arc: evidence for sediment melt and residual phases. Geology 33 (9), 737–740.

Volpe, A.M., Douglas Macdougall, J., Lugmair, G.W., Hawkins, J.W., Lonsdale, P., 1990. Fine-scale isotopic variation in Mariana Trough basalts: evidence for heterogeneity and a recycled component in backarc basin mantle. Earth Planet. Sci. Lett. 100 (1), 251–264.

Wang, Z., Becker, H., 2013. Ratios of S, Se and Te in the silicate Earth require a volatile-rich late veneer. Nature 499 (7458), 328–331.

Wang, Z., Becker, H., 2015. Comment on "a non-primitive origin of near-chondritic SSeTe ratios in mantle peridotites: Implications for the Earth's late accretionary history" by König S. et al. [Earth Planet. Sci. Lett. 385 (2014) 110–121]. Earth Planet. Sci. Lett. 417, 164–166.

Williams, H.M., Prytulak, J., Woodhead, J.D., Kelley, K.A., Brounce, M., Plank, T., 2018. Interplay of crystal fractionation, sulfide saturation and oxygen fugacity on the iron isotope composition of arc lavas: an example from the Marianas. Geochim. Cosmochim. Acta 226, 224–243.

Yi, W., Halliday, A.N., Alt, J.C., Lee, D.C., Rehkamper, M., Garcia, M.O., Langmuir, C.H., Su, Y.J., 2000. Cadmium, indium, tin, tellurium, and sulfur in oceanic basalts: Implications for chalcophile element fractionation in the Earth. J. Geophys. Res. Solid Earth 105 (B8), 18927–18948.

Yierpan, A., König, S., Labidi, J., Kurzawa, T., Babechuk, M.G., Schoenberg, R., 2018. Chemical sample processing for combined selenium isotope and selenium-tellurium elemental investigation of the earth's igneous reservoirs. Geochem. Geophys. Geosyst. 19 (2), 516–533.

Yierpan, A., König, S., Labidi, J., Schoenberg, R., 2019. Selenium isotope and S-Se-Te elemental systematics along the Pacific-Antarctic ridge: role of mantle processes. Geochim. Cosmochim. Acta 249, 199–224.

References

Ague, J.J., 2011. Extreme channelization of fluid and the problem of element mobility during Barrovian metamorphism. Am. Mineral., 96(2-3): 333-352.

Alard, O., Lorand, J.-P., Reisberg, L., Bodinier, J.-L., Dautria, J.-M., O'Reilly, S.Y., 2011. Volatile-rich Metasomatism in Montferrier Xenoliths (Southern France): Implications for the Abundances of Chalcophile and Highly Siderophile Elements in the Subcontinental Mantle. J. Petrol., 52(10): 2009-2045.

Albut, G., Babechuk, M.G., Kleinhanns, I.C., Benger, M., Beukes, N.J., Steinhilber, B., Smith, A.J., Kruger, S.J., Schoenberg, R., 2018. Modern rather than Mesoarchaean oxidative weathering responsible for the heavy stable Cr isotopic signatures of the 2.95 Ga old Ijzermijn iron formation (South Africa). Geochim. Cosmochim. Acta, 228: 157-189.

Alt, J.C., Shanks, W.C., Jackson, M.C., 1993. Cycling of sulfur in subduction zones: The geochemistry of sulfur in the Mariana Island Arc and back-arc trough. Earth Planet. Sci. Lett., 119(4): 477-494.

Andersen, M.B., Elliott, T., Freymuth, H., Sims, K.W., Niu, Y., Kelley, K.A., 2015. The terrestrial uranium isotope cycle. Nature, 517(7534): 356-359.

Arculus, R.J., Lapierre, H., Jaillard, E., 1999. Geochemical window into subduction and accretion processes: Raspas metamorphic complex, Ecuador. Geology, 27(6): 547-550.

Aulbach, S., Stachel, T., Seitz, H.-M., Brey, G.P., 2012. Chalcophile and siderophile elements in sulphide inclusions in eclogitic diamonds and metal cycling in a Paleoproterozoic subduction zone. Geochim. Cosmochim. Acta, 93: 278-299.

Bebout, G.E., 2007. Metamorphic chemical geodynamics of subduction zones. Earth Planet. Sci. Lett., 260(3-4): 373-393.

Becker, H., Horan, M.F., Walker, R.J., Gao, S., Lorand, J.P., Rudnick, R.L., 2006. Highly siderophile element composition of the Earth's primitive upper mantle: Constraints from new data on peridotite massifs and xenoliths. Geochim. Cosmochim. Acta, 70(17): 4528-4550.

Berglund, M., Wieser, M.E., 2011. Isotopic compositions of the elements 2009 (IUPAC Technical Report). Pure and Applied Chemistry, 83(2).

Bosch, D., Gabriele, P., Lapierre, H., Malfere, J.L., Jaillard, E., 2002. Geodynamic significance of the Raspas Metamorphic Complex (SW Ecuador): geochemical and isotopic constraints. Tectonophysics, 345(1-4): 83-102.

Boynton, W.V., 1984. Chapter 3 - Cosmochemistry of the Rare Earth Elements: Meteorite Studies. In: Henderson, P. (Ed.), Dev. Geochem. Elsevier, pp. 63-114.

Brenan, J.M., 2015. Se–Te fractionation by sulfide–silicate melt partitioning: implications for the composition of mantle-derived magmas and their melting residues. Earth Planet. Sci. Lett., 422: 45-57.

Bulanova, G.P., Griffin, W.L., Ryan, C.G., Shestakova, O.Y., Barnes, S.J., 1996. Trace elements in sulfide inclusions from Yakutian diamonds. Contrib. Mineral. Petrol., 124(2): 111-125.

Carignan, J., Wen, H., 2007. Scaling NIST SRM 3149 for Se isotope analysis and isotopic variations of natural samples. Chem. Geol., 242(3–4): 347-350.

Chaussidon, M., Albarede, F., Sheppard, S., 1987. Sulphur isotope heterogeneity in the mantle from ion microprobe measurements of sulphide inclusions in diamonds. Nature, 330(6145): 242.

Chiaradia, M., 2014. Copper enrichment in arc magmas controlled by overriding plate thickness. Nat. Geosci., 7(1): 43.

Clark, S.K., Johnson, T.M., 2008. Effective isotopic fractionation factors for solute removal by reactive sediments: A laboratory microcosm and slurry study. Environmental science & technology, 42(21): 7850-7855.

Clark, S.K., Johnson, T.M., 2010. Selenium Stable Isotope Investigation into Selenium Biogeochemical Cycling in a Lacustrine Environment: Sweitzer Lake, Colorado. Journal of Environment Quality, 39(6): 2200.

Compston, W., Oversby, V., 1969. Lead isotopic analysis using a double spike. J. Geophys. Res., 74(17): 4338-4348.

Cruz-Uribe, A., Walters, J., Marschall, H., 2018. Trace element redistribution during rehydration of eclogite via sulfide-silicate reactions, AGU Fall Meeting Abstracts.

Davis, A.S., Clague, D.A., Schulz, M.S., Hein, J.R., 1991. Low sulfur content in submarine lavas: An unreliable indicator of subaerial eruption. Geology, 19(7): 750-753.

De Hoog, J., Mason, P., van Bergen, M.m., 2001a. Sulfur and chalcophile elements in subduction zones: constraints from a laser ablation ICP-MS study of melt inclusions from Galunggung Volcano, Indonesia. Geochim. Cosmochim. Acta, 65(18): 3147-3164.

De Hoog, J., Taylor, B., Van Bergen, M., 2001b. Sulfur isotope systematics of basaltic lavas from Indonesia: implications for the sulfur cycle in subduction zones. Earth Planet. Sci. Lett., 189(3): 237-252.

Dreibus, G., Palme, H., Spettel, B., Zipfel, J., Wänke, H., 1995. Sulfur and selenium in chondritic meteorites. Meteoritics, 30(4): 439-445.

Elliott, T., 2003. Tracers of the slab. Inside the subduction factory: 23-45.

Elliott, T., Plank, T., Zindler, A., White, W., Bourdon, B., 1997. Element transport from slab to volcanic front at the Mariana arc. Journal of Geophysical Research-Solid Earth, 102(B7): 14991-15019.

Ellis, A.S., Johnson, T.M., Herbel, M.J., Bullen, T.D., 2003. Stable isotope fractionation of selenium by natural microbial consortia. Chem. Geol., 195(1): 119-129.

Elwaer, N., Hintelmann, H., 2008. Selective separation of selenium (IV) by thiol cellulose powder and subsequent selenium isotope ratio determination using multicollector inductively coupled plasma mass spectrometry. J. Anal. At. Spectrom., 23(5): 733-743.

Evans, K., Tomkins, A., Cliff, J., Fiorentini, M., 2014. Insights into subduction zone sulfur recycling from isotopic analysis of eclogite-hosted sulfides. Chem. Geol., 365: 1-19.

Farquhar, J., Wing, B.A., McKeegan, K.D., Harris, J.W., Cartigny, P., Thiemens, M.H., 2002. Mass-Independent Sulfur of Inclusions in Diamond and Sulfur Recycling on Early Earth. Science, 298(5602): 2369-2372.

Fehr, M.A., Rehkämper, M., Halliday, A.N., 2004. Application of MC-ICPMS to the precise determination of tellurium isotope compositions in chondrites, iron meteorites and sulfides. International Journal of Mass Spectrometry, 232(1): 83-94.

Feininger, T., 1980. Eclogite and Related High-Pressure Regional Metamorphic Rocks from the Andes of Ecuador. J. Petrol., 21(1): 107-&.

Feininger, T., 1982. Glaucophane Schist in the Andes at Jambalo, Colombia. Can. Mineral., 20(Feb): 41-48.

Fliegel, D., Frei, C., Fontaine, G., Hu, Z., Gao, S., Günther, D., 2011. Sensitivity improvement in laser ablation inductively coupled plasma mass spectrometry achieved using a methane/argon and methanol/water/argon mixed gas plasma. Analyst, 136(23): 4925-4934.

Floor, G.H., Millot, R., Iglesias, M., Négrel, P., 2011. Influence of methane addition on selenium isotope sensitivity and their spectral interferences. Journal of Mass Spectrometry, 46(2): 182-188.

Gabriele, P., 2002. HP terranes exhumation in an active margin setting: Geology, petrology and geochemistry of the Raspas Complex in SW Ecuador [Ph. D. thesis]: Lausanne. Switzerland, University of Lausanne.

Gabriele, P., Ballevre, M., Jaillard, E., Hernandez, J., 2003. Garnet-chloritoid-kyanite metapelites from the Raspas Complex (SW Ecuador): a key eclogite-facies assemblage. Eur. J. Mineral., 15(6): 977-989.

Gale, A., Dalton, C.A., Langmuir, C.H., Su, Y., Schilling, J.G., 2013. The mean composition of ocean ridge basalts. Geochem. Geophys. Geosyst., 14(3): 489-518.

Gladney, E.S., Roelandts, I., 1988. 1987 Compilation of Elemental Concentration Data for USGS BHVO-1, MAG-1, QLO-1, RGM-1, SCo-1, SDC-1, SGR-1 and STM-1. Geostand. Newslett., 12(2): 253-362.

Green, D.H., 1973. Experimental melting studies on a model upper mantle composition at high pressure under water-saturated and water-undersaturated conditions. Earth Planet. Sci. Lett., 19(1): 37-53.

Guo, J.F., Griffin, W.L., O'Reilly, S.Y., 1999. Geochemistry and origin of sulphide minerals in mantle xenoliths: Qilin, southeastern China. J. Petrol., 40(7): 1125-1149.

Guo, W., Hu, S., Wang, Y., Zhang, L., Hu, Z., Zhang, J., 2013. Trace determination of selenium in biological samples by CH 4-Ar mixed gas plasma DRC-ICP-MS. Microchemical Journal, 108: 106-112.

Halama, R., Bebout, G.E., John, T., Schenk, V., 2010. Nitrogen recycling in subducted oceanic lithosphere: The record in high- and ultrahigh-pres sure metabasaltic rocks. Geochim. Cosmochim. Acta, 74(5): 1636-1652.

Halama, R., John, T., Herms, P., Hauff, F., Schenk, V., 2011. A stable (Li, O) and radiogenic (Sr, Nd) isotope perspective on metasomatic processes in a subducting slab. Chem. Geol., 281(3-4): 151-166.

Halama, R., Savov, I.P., Garbe-Schonberg, D., Schenk, V., Toulkeridis, T., 2013. Vesuvianite in high-pressure-metamorphosed oceanic lithosphere (Raspas Complex, Ecuador) and its role for transport of water and trace elements in subduction zones. Eur. J. Mineral., 25(2): 193-219.

Hall, G.E., Pelchat, J.C., 1997. 1 Determination of As, Bi, Sb, Se and Te in Fifty Five Reference Materials by Hydride Generation ICP-MS. Geostand. Newslett., 21(1): 85-91.

Hamlyn, P.R., Keays, R.R., Cameron, W.E., Crawford, A.J., Waldron, H.M., 1985. Precious Metals in Magnesian Low-Ti Lavas - Implications for Metallogenesis and Sulfur Saturation in Primary Magmas. Geochim. Cosmochim. Acta, 49(8): 1797-1811.

Harvey, J., König, S., Luguet, A., 2015. The effects of melt depletion and metasomatism on highly siderophile and strongly chalcophile elements: S–Se–Te–Re–PGE systematics of peridotite xenoliths from Kilbourne Hole, New Mexico. Geochim. Cosmochim. Acta, 166: 210-233.

Hattori, K.H., Arai, S., Clarke, D.B., 2002. Selenium, tellurium, arsenic and antimony contents of primary mantle sulfides. The Canadian Mineralogist, 40(2): 637-650.

Hedenquist, J.W., Lowenstern, J.B., 1994. The role of magmas in the formation of hydrothermal ore deposits. Nature, 370(6490): 519-527.

Hermann, J., Spandler, C., Hack, A., Korsakov, A.V., 2006. Aqueous fluids and hydrous melts in high-pressure and ultra-high pressure rocks: implications for element transfer in subduction zones. Lithos, 92(3-4): 399-417.

Hofmann, A.W., 1988. Chemical Differentiation of the Earth - the Relationship between Mantle, Continental-Crust, and Oceanic-Crust. Earth Planet. Sci. Lett., 90(3): 297-314.

Imai, A., Listanco, E.L., Fujii, T., 1993. Petrologic and sulfur isotopic significance of highly oxidized and sulfur-rich magma of Mt. Pinatubo, Philippines. Geology, 21(8): 699-702.

Imai, N., Terashima, S., Itoh, S., Ando, A., 1995. 1994 Compilation of analytical data for minor and trace elements in seventeen GSJ geochemical reference samples, 'Igenous Rock Series'. Geostand. Newslett., 19(2): 135-213.

Ito, E., White, W.M., Göpel, C., 1987. The O, Sr, Nd and Pb isotope geochemistry of MORB. Chem. Geol., 62(3): 157-176.

Jenner, F.E., 2017. Cumulate causes for the low contents of sulfide-loving elements in the continental crust. Nat. Geosci., 10(7): 524-529.

Jenner, F.E., Arculus, R.J., Mavrogenes, J.A., Dyriw, N.J., Nebel, O., Hauri, E.H., 2012. Chalcophile element systematics in volcanic glasses from the northwestern Lau Basin. Geochem. Geophys. Geosyst., 13(6).

Jenner, F.E., Hauri, E.H., Bullock, E.S., Konig, S., Arculus, R.J., Mavrogenes, J.A., Mikkelson, N., Goddard, C., 2015. The competing effects of sulfide saturation versus degassing on the behavior of the chalcophile elements during the differentiation of hydrous melts. Geochemistry Geophysics Geosystems, 16(5): 1490-1507.

Jenner, F.E., O'Neill, H.S.C., Arculus, R.J., Mavrogenes, J.A., 2010. The Magnetite Crisis in the Evolution of Arc-related Magmas and the Initial Concentration of Au, Ag and Cu. J. Petrol., 51(12): 2445-2464.

Jochum, K.P., Weis, U., Schwager, B., Stoll, B., Wilson, S.A., Haug, G.H., Andreae, M.O., Enzweiler, J., 2016. Reference Values Following ISO Guidelines for Frequently Requested Rock Reference Materials. Geostand. Geoanal. Res., 40(3): 333-350.

John, T., Gussone, N., Podladchikov, Y.Y., Bebout, G.E., Dohmen, R., Halama, R., Klemd, R., Magna, T., Seitz, H.-M., 2012. Volcanic arcs fed by rapid pulsed fluid flow through subducting slabs. Nat. Geosci., 5: 489.

John, T., Scherer, E.E., Haase, K., Schenk, V., 2004. Trace element fractionation during fluid-induced eclogitization in a subducting slab: trace element and Lu-Hf-Sm-Nd isotope systematics. Earth Planet. Sci. Lett., 227(3-4): 441-456.

John, T., Scherer, E.E., Schenk, V., Herms, P., Halama, R., Garbe-Schonberg, D., 2010. Subducted seamounts in an eclogite-facies ophiolite sequence: the Andean Raspas Complex, SW Ecuador. Contrib. Mineral. Petrol., 159(2): 265-284.

Johnson, T.M., 2004. A review of mass-dependent fractionation of selenium isotopes and implications for other heavy stable isotopes. Chem. Geol., 204(3): 201-214.

Johnson, T.M., Bullen, T.D., 2003. Selenium isotope fractionation during reduction by Fe(II)-Fe(III) hydroxide-sulfate (green rust). Geochim. Cosmochim. Acta, 67(3): 413-419.

Johnson, T.M., Bullen, T.D., 2004. Mass-dependent fractionation of selenium and chromium isotopes in low-temperature environments. Rev. Mineral. Geochem., 55(1): 289-317.

Johnson, T.M., Bullen, T.D., Zawislanski, P.T., 2000. Selenium stable isotope ratios as indicators of sources and cycling of selenium: Results from the northern reach of San Francisco Bay. Environmental science & technology, 34(11): 2075-2079.

Johnson, T.M., Herbel, M.J., Bullen, T.D., Zawislanski, P.T., 1999. Selenium isotope ratios as indicators of selenium sources and oxyanion reduction. Geochim. Cosmochim. Acta, 63(18): 2775-2783.

Kimura, K., Lewis, R.S., Anders, E., 1974. Distribution of gold and rhenium between nickel-iron and silicate melts: implications for the abundance of siderophile elements on the Earth and Moon. Geochim. Cosmochim. Acta, 38(5): 683-701.

Kipp, M.A., Stüeken, E.E., Bekker, A., Buick, R., 2017. Selenium isotopes record extensive marine suboxia during the Great Oxidation Event. Proceedings of the National Academy of Sciences, 114(5): 875-880.

König, S., Eickmann, B., Zack, T., Yierpan, A., Wille, M., Taubald, H., Schoenberg, R., 2019. Redox induced sulfur-selenium isotope decoupling recorded in pyrite. Geochim. Cosmochim. Acta, 244: 24-39.

König, S., Lissner, M., Lorand, J.-P., Bragagni, A., Luguet, A., 2015a. Mineralogical control of selenium, tellurium and highly siderophile elements in the Earth’s mantle: Evidence from mineral separates of ultra-depleted mantle residues. Chem. Geol., 396: 16-24.

König, S., Lorand, J.-P., Luguet, A., Pearson, D.G., 2014. A non-primitive origin of near-chondritic S–Se–Te ratios in mantle peridotites; implications for the Earth’s late accretionary history. Earth Planet. Sci. Lett., 385: 110-121.

König, S., Luguet, A., Lorand, J.-P., Lissner, M., Graham Pearson, D., 2015b. Reply to the comment on “A non-primitive origin of near-chondritic S–Se–Te ratios in mantle peridotites: Implications for the Earth's late accretionary history” by König S. et al. [Earth Planet. Sci. Lett. 385 (2014) 110–121]. Earth Planet. Sci. Lett., 417: 167-169.

König, S., Luguet, A., Lorand, J.-P., Wombacher, F., Lissner, M., 2012. Selenium and tellurium systematics of the Earth's mantle from high precision analyses of ultra-depleted orogenic peridotites. Geochim. Cosmochim. Acta, 86: 354-366.

König, S., Schuth, S., Münker, C., Qopoto, C., 2007. The role of slab melting in the petrogenesis of high-Mg andesites: Evidence from Simbo Volcano, Solomon Islands, 153, 85-103 pp.

König, S., Wille, M., Voegelin, A., Schoenberg, R., 2016. Molybdenum isotope systematics in subduction zones. Earth Planet. Sci. Lett., 447: 95-102.

Kurzawa, T., König, S., Alt, J.C., Yierpan, A., Schoenberg, R., 2019. The role of subduction recycling on the selenium isotope signature of the mantle: Constraints from Mariana arc lavas. Chem. Geol., 513: 239-249.

Kurzawa, T., Konig, S., Labidi, J., Yierpan, A., Schoenberg, R., 2017. A method for Se isotope analysis of low ng-level geological samples via double spike and hydride generation MC-ICP-MS. Chem. Geol., 466: 219-228.

Labidi, J., Cartigny, P., Moreira, M., 2013. Non-chondritic sulphur isotope composition of the terrestrial mantle. Nature, 501(7466): 208-211.

Labidi, J., König, S., Kurzawa, T., Yierpan, A., Schoenberg, R., 2018. The selenium isotopic variations in chondrites are mass-dependent; Implications for sulfide formation in the early solar system. Earth Planet. Sci. Lett., 481: 212-222.

Labidi, J., Shahar, A., Le Losq, C., Hillgren, V.J., Mysen, B.O., Farquhar, J., 2016. Experimentally determined sulfur isotope fractionation between metal and silicate and implications for planetary differentiation. Geochim. Cosmochim. Acta, 175: 181-194.

Layton-Matthews, D., Leybourne, M.I., Peter, J.M., Scott, S.D., 2006. Determination of selenium isotopic ratios by continuous-hydride-generation dynamic-reaction-cell inductively coupled plasma-mass spectrometry. J. Anal. At. Spectrom., 21(1): 41-49.

Layton-Matthews, D., Leybourne, M.I., Peter, J.M., Scott, S.D., Cousens, B., Eglington, B.M., 2013. Multiple sources of selenium in ancient seafloor hydrothermal systems: Compositional and Se, S, and Pb isotopic evidence from volcanic-hosted and volcanic-sediment-hosted massive sulfide deposits of the Finlayson Lake District, Yukon, Canada. Geochim. Cosmochim. Acta, 117: 313-331.

Lee, C.-T.A., Erdman, M., Yang, W., Ingram, L., Chin, E.J., DePaolo, D.J., 2018. Sulfur isotopic compositions of deep arc cumulates. Earth Planet. Sci. Lett., 500: 76-85.

Li, J.-L., Gao, J., John, T., Klemd, R., Su, W., 2013. Fluid-mediated metal transport in subduction zones and its link to arc-related giant ore deposits: constraints from a sulfide-bearing HP vein in lawsonite eclogite (Tianshan, China). Geochim. Cosmochim. Acta, 120: 326-362.

Li, J.L., Gao, J., Klemd, R., John, T., Wang, X.S., 2016. Redox processes in subducting oceanic crust recorded by sulfide-bearing high-pressure rocks and veins (SW Tianshan, China). Contrib. Mineral. Petrol., 171:72(8-9).

Lissner, M., König, S., Luguet, A., le Roux, P., Schuth, S., Heuser, A., le Roex, A., 2014. Selenium and tellurium systematics in MORBs from the southern Mid-Atlantic Ridge (47–50 S). Geochim. Cosmochim. Acta, 144: 379-402.

Liu, S.-A., Huang, J., Liu, J., Wörner, G., Yang, W., Tang, Y.-J., Chen, Y., Tang, L., Zheng, J., Li, S., 2015. Copper isotopic composition of the silicate Earth. Earth Planet. Sci. Lett., 427: 95-103.

Lorand, J.-P., Alard, O., 2001. Platinum-group element abundances in the upper mantle: new constraints from in situ and whole-rock analyses of Massif Central xenoliths (France). Geochim. Cosmochim. Acta, 65(16): 2789-2806.

Lorand, J.-P., Alard, O., 2010. Determination of selenium and tellurium concentrations in Pyrenean peridotites (Ariege, France): new insight into S/Se/Te systematics of the upper in mantle samples. Chem. Geol., 278(1): 120-130.

Lorand, J.-P., Alard, O., Luguet, A., Keays, R.R., 2003. Sulfur and selenium systematics of the subcontinental lithospheric mantle: inferences from the Massif Central xenolith suite (France). Geochim. Cosmochim. Acta, 67(21): 4137-4151.

Lorand, J.-P., Delpech, G., Grégoire, M., Moine, B., O'Reilly, S.Y., Cottin, J.-Y., 2004. Platinum-group elements and the multistage metasomatic history of Kerguelen lithospheric mantle (South Indian Ocean). Chem. Geol., 208(1–4): 195-215.

Lorand, J.-P., Luguet, A., Alard, O., 2013. Platinum-group element systematics and petrogenetic processing of the continental upper mantle: A review. Lithos, 164–167: 2-21.

Lorand, J.-P., Luguet, A., Alard, O., Bezos, A., Meisel, T., 2008. Abundance and distribution of platinum-group elements in orogenic lherzolites; a case study in a Fontete Rouge lherzolite (French Pyrénées). Chem. Geol., 248(3–4): 174-194.

Luguet, A., Behrens, M., Pearson, D.G., König, S., Herwartz, D., 2015. Significance of the whole rock Re–Os ages in cryptically and modally metasomatised cratonic peridotites: Constraints from HSE–Se–Te systematics. Geochim. Cosmochim. Acta, 164: 441-463.

Luguet, A., Lorand, J.-P., Alard, O., Cottin, J.-Y., 2004. A multi-technique study of platinum group element systematic in some Ligurian ophiolitic peridotites, Italy. Chem. Geol., 208(1–4): 175-194.

Macgregor, I.D., Manton, W.I., 1986. Roberts-Victor Eclogites - Ancient Oceanic-Crust. Journal of Geophysical Research-Solid Earth and Planets, 91(B14): 14063-14079.

Mann, U., Frost, D.J., Rubie, D.C., Becker, H., Audétat, A., 2012. Partitioning of Ru, Rh, Pd, Re, Ir and Pt between liquid metal and silicate at high pressures and high temperatures-Implications for the origin of highly siderophile element concentrations in the Earth's mantle. Geochim. Cosmochim. Acta, 84: 593-613.

Marchesi, C., Garrido, C.J., Harvey, J., González-Jiménez, J.M., Hidas, K., Lorand, J.-P., Gervilla, F., 2013. Platinum-group elements, S, Se and Cu in highly depleted abyssal peridotites from the Mid-Atlantic Ocean Ridge (ODP Hole 1274A): Influence of hydrothermal and magmatic processes. Contrib. Mineral. Petrol., 166(5): 1521-1538.

Marin, L., Lhomme, J., Carignan, J., 2001. Determination of selenium concentration in sixty five reference materials for geochemical analysis by GFAAS after separation with thiol cotton. Geostand. Newslett., 25(2-3): 317-324.

McDonough, W.F., Sun, S.-S., 1995. The composition of the Earth. Chemical Geology, 120: 223-253.

Métrich, N., Schiano, P., Clocchiatti, R., Maury, R.C., 1999. Transfer of sulfur in subduction settings: an example from Batan Island (Luzon volcanic arc, Philippines). Earth Planet. Sci. Lett., 167(1): 1-14.

Mitchell, K., Couture, R.-M., Johnson, T.M., Mason, P.R., Van Cappellen, P., 2013. Selenium sorption and isotope fractionation: Iron (III) oxides versus iron (II) sulfides. Chem. Geol., 342: 21-28.

Mitchell, K., Mansoor, S.Z., Mason, P.R.D., Johnson, T.M., Van Cappellen, P., 2016. Geological evolution of the marine selenium cycle: Insights from the bulk shale δ82/76Se record and isotope mass balance modeling. Earth Planet. Sci. Lett., 441: 178-187.

Mitchell, K., Mason, P.R., Van Cappellen, P., Johnson, T.M., Gill, B.C., Owens, J.D., Diaz, J., Ingall, E.D., Reichart, G.-J., Lyons, T.W., 2012. Selenium as paleo-oceanographic proxy: A first assessment. Geochim. Cosmochim. Acta, 89: 302-317.

Morgan, J., Walker, R., Brandon, A., Horan, M., 2001. Siderophile elements in Earth's upper mantle and lunar breccias: data synthesis suggests manifestations of the same late influx. Meteorit. Planet. Sci., 36(9): 1257-1275.

Morgan, J.W., 1986. Ultramafic xenoliths: clues to Earth's late accretionary history. Journal of Geophysical Research: Solid Earth, 91(B12): 12375-12387.

Mottl, M.J., Wheat, C.G., Fryer, P., Gharib, J., Martin, J.B., 2004. Chemistry of springs across the Mariana forearc shows progressive devolatilization of the subducting plate. Geochim. Cosmochim. Acta, 68(23): 4915-4933.

Nielsen, S.G., Rehkämper, M., Baker, J., Halliday, A.N., 2004. The precise and accurate determination of thallium isotope compositions and concentrations for water samples by MC-ICPMS. Chem. Geol., 204(1-2): 109-124.

Niu, Y.L., 2004. Bulk-rock major and trace element compositions of abyssal peridotites: Implications for mantle melting, melt extraction and post-melting processes beneath mid-ocean ridges. J. Petrol., 45(12): 2423-2458.

Noll Jr, P., Newsom, H., Leeman, W., Ryan, J.G., 1996. The role of hydrothermal fluids in the production of subduction zone magmas: evidence from siderophile and chalcophile trace elements and boron. Geochim. Cosmochim. Acta, 60(4): 587-611.

Palme, H., O'Neill, H.S.C., 2003. Cosmochemical estimates of mantle composition. Treatise on geochemistry, 2: 568.

Palme, H., O'Neill, H.S.C., 2014. 3.1 - Cosmochemical Estimates of Mantle Composition. In: Holland, H.D., Turekian, K.K. (Eds.), Treatise on Geochemistry (Second Edition). Elsevier, Oxford, pp. 1-39.

Park, J.-W., Campbell, I.H., Arculus, R.J., 2013. Platinum-alloy and sulfur saturation in an arc-related basalt to rhyolite suite: Evidence from the Pual Ridge lavas, the Eastern Manus Basin. Geochim. Cosmochim. Acta, 101: 76-95.

Pearce, J.A., Stern, R.J., Bloomer, S.H., Fryer, P., 2005. Geochemical mapping of the Mariana arc-basin system: Implications for the nature and distribution of subduction components. Geochemistry Geophysics Geosystems, 6.

Perfit, M.R., Gust, D.A., Bence, A.E., Arculus, R.J., Taylor, S.R., 1980. Chemical characteristics of island-arc basalts: Implications for mantle sources. Chem. Geol., 30(3): 227-256.

Plümper, O., John, T., Podladchikov, Y.Y., Vrijmoed, J.C., Scambelluri, M., 2016. Fluid escape from subduction zones controlled by channel-forming reactive porosity. Nat. Geosci., 10: 150.

Pogge von Strandmann, P.A., Coath, C.D., Catling, D.C., Poulton, S.W., Elliott, T., 2014. Analysis of mass dependent and mass independent selenium isotope variability in black shales. J. Anal. At. Spectrom., 29(9): 1648-1659.

Pogge von Strandmann, P.A., Stüeken, E.E., Elliott, T., Poulton, S.W., Dehler, C.M., Canfield, D.E., Catling, D.C., 2015. Selenium isotope evidence for progressive oxidation of the Neoproterozoic biosphere. Nature communications, 6.

Prytulak, J., Nielsen, S., Plank, T., Barker, M., Elliott, T., 2013. Assessing the utility of thallium and thallium isotopes for tracing subduction zone inputs to the Mariana arc. Chem. Geol., 345: 139-149.

Prytulak, J., Sossi, P.A., Halliday, A.N., Plank, T., Savage, P.S., Woodhead, J.D., 2017. Stable vanadium isotopes as a redox proxy in magmatic systems? Geochemical Perspectives Letters, 3(0): 75-84.

Puchelt, H., Prichard, H., Berner, Z., Maynard, J., 1996. Sulfide mineralogy, sulfur content, and sulfur isotope composition of mafic and ultramafic rocks from Leg 147, PROCEEDINGS-OCEAN DRILLING PROGRAM SCIENTIFIC RESULTS. NATIONAL SCIENCE FOUNDATION, pp. 91-102.

Ranero, C.R., Phipps Morgan, J., McIntosh, K., Reichert, C., 2003. Bending-related faulting and mantle serpentinization at the Middle America trench. Nature, 425: 367.

Ribeiro, J.M., Stern, R.J., Kelley, K.A., Shaw, A.M., Martinez, F., Ohara, Y., 2015. Composition of the slab-derived fluids released beneath the Mariana forearc: Evidence for shallow dehydration of the subducting plate. Earth Planet. Sci. Lett., 418: 136-148.

Richards, J.P., 2015. The oxidation state, and sulfur and Cu contents of arc magmas: implications for metallogeny. Lithos, 233: 27-45.

Richter, F.M., 2004. Timescales determining the degree of kinetic isotope fractionation by evaporation and condensation. Geochim. Cosmochim. Acta, 68(23): 4971-4992.

Rose-Weston, L., Brenan, J.M., Fei, Y., Secco, R.A., Frost, D.J., 2009. Effect of pressure, temperature, and oxygen fugacity on the metal-silicate partitioning of Te, Se, and S: Implications for earth differentiation. Geochim. Cosmochim. Acta, 73(15): 4598-4615.

Rouxel, O., Fouquet, Y., Ludden, J.N., 2004. Subsurface processes at the lucky strike hydrothermal field, Mid-Atlantic ridge: evidence from sulfur, selenium, and iron isotopes 1. Geochim. Cosmochim. Acta, 68(10): 2295-2311.

Rouxel, O., Ludden, J., Carignan, J., Marin, L., Fouquet, Y., 2002. Natural variations of Se isotopic composition determined by hydride generation multiple collector inductively coupled plasma mass spectrometry. Geochim. Cosmochim. Acta, 66(18): 3191-3199.

Rudge, J.F., Reynolds, B.C., Bourdon, B., 2009. The double spike toolbox. Chem. Geol., 265(3): 420-431.

Sadofsky, S.J., Bebout, G.E., 2003. Record of forearc devolatilization in low-T, high-P/T metasedimentary suites: Significance for models of convergent margin chemical cycling. Geochem. Geophys. Geosyst., 4(4).

Savard, D., Bédard, L.P., Barnes, S.-J., 2009. Selenium Concentrations in Twenty-Six Geological Reference Materials: New Determinations and Proposed Values. Geostand. Geoanal. Res., 33(2): 249-259.

Scambelluri, M., Bottazzi, P., Trommsdorff, V., Vannucci, R., Hermann, J., Gòmez-Pugnaire, M.T., Lòpez-Sànchez Vizcaìno, V., 2001. Incompatible element-rich fluids released by antigorite breakdown in deeply subducted mantle. Earth Planet. Sci. Lett., 192(3): 457-470.

Scambelluri, M., Philippot, P., 2001. Deep fluids in subduction zones. Lithos, 55(1): 213-227.

Schilling, K., Johnson, T.M., Mason, P.R.D., 2014. A sequential extraction technique for mass-balanced stable selenium isotope analysis of soil samples. Chem. Geol., 381: 125-130.

Schilling, K., Johnson, T.M., Wilcke, W., 2011. Selenium partitioning and stable isotope ratios in urban topsoils. Soil Sci. Soc. Am. J., 75(4): 1354-1364.

Schilling, K., Johnson, T.M., Wilcke, W., 2013. Isotope fractionation of selenium by biomethylation in microcosm incubations of soil. Chem. Geol., 352: 101-107.

Schmidt, M.W., Poli, S., 2003. 3.17 - Generation of Mobile Components during Subduction of Oceanic Crust. In: Holland, H.D., Turekian, K.K. (Eds.), Treatise on Geochemistry. Pergamon, Oxford, pp. 567-591.

Schumann, G., Klauke, R., Büttner, J., 1992. 036 Standard addition in HPLC: A calibration method for the determination of reference method values. Fresenius' Journal of Analytical Chemistry, 343(1): 89-90.

Schuth, S., König, S., Münker, C., 2011. Subduction zone dynamics in the SW Pacific plate boundary region constrained from high-precision Pb isotope data. Earth Planet. Sci. Lett., 311(3): 328-338.

Shore, A.J.T., 2011. Selenium geochemistry and isotopic composition of sediments from the Cariaco Basin and the Bermuda Rise: a comparison between a restricted basin and the open ocean over the last 500 ka, University of Leicester.

Sillitoe, R.H., 1972. Relation of Metal Provinces in Western America to Subduction of Oceanic Lithosphere. GSA Bulletin, 83(3): 813-818.

Stern, R.J., Bloomer, S.H., 1992. Subduction Zone Infancy - Examples from the Eocene Izu-Bonin-Mariana and Jurassic California Arcs. Geol. Soc. Am. Bull., 104(12): 1621-1636.

Stern, R.J., Fouch, M.J., Klemperer, S.L., 2003. An overview of the Izu-Bonin-Mariana subduction factory. Inside the subduction factory, 138: 175-222.

Stern, R.J., Lin, P.-N., Morris, J.D., Jackson, M.C., Fryer, P., Bloomer, S.H., Ito, E., 1990. Enriched back-arc basin basalts from the northern Mariana Trough: implications for the magmatic evolution of back-arc basins. Earth Planet. Sci. Lett., 100(1): 210-225.

Stolper, E., Newman, S., 1994. The role of water in the petrogenesis of Mariana trough magmas. Earth Planet. Sci. Lett., 121(3): 293-325.

Stüeken, E., Foriel, J., Nelson, B., Buick, R., Catling, D., 2013. Selenium isotope analysis of organic-rich shales: Advances in sample preparation and isobaric interference correction. J. Anal. At. Spectrom., 28(11): 1734-1749.

Stüeken, E.E., Buick, R., Anbar, A.D., 2015a. Selenium isotopes support free O2 in the latest Archean. Geology, 43(3): 259-262.

Stüeken, E.E., Buick, R., Bekker, A., Catling, D., Foriel, J., Guy, B.M., Kah, L.C., Machel, H.G., Montanez, I.P., Poulton, S.W., 2015b. The evolution of the global selenium cycle: Secular trends in Se isotopes and abundances. Geochim. Cosmochim. Acta, 162: 109-125.

Stüeken, E.E., Foriel, J., Buick, R., Schoepfer, S.D., 2015c. Selenium isotope ratios, redox changes and biological productivity across the end-Permian mass extinction. Chem. Geol., 410: 28-39.

Tamari, Y., Ogawa, H., Fukumoto, Y., Tsuji, H., Kusaka, Y., 1990. Selenium Content and Its Oxidation-State in Igneous Rocks, Rock-Forming Minerals, and a Reservoir Sediment. Bulletin of the Chemical Society of Japan, 63(9): 2631-2638.

Terashima, S., 2001. Determination of Indium and Tellurium in Fifty Nine Geological Reference Materials by Solvent Extraction and Graphite Furnace Atomic Absorption Spectrometry. Geostand. Newslett., 25(1): 127-132.

Terashima, S., Imai, N., 2000. Determination of Selenium in Fifty Two Geochemical Reference Materials by Hydride Generation Atomic Absorption Spectrometry. Geostand. Newslett., 24(1): 83-86.

Thomassot, E., Cartigny, P., Harris, J.W., Lorand, J.P., Rollion-Bard, C., Chaussidon, M., 2009. Metasomatic diamond growth: A multi-isotope study (C-13, N-15, S-33, S-34) of sulphide inclusions and their host diamonds from Jwaneng (Botswana). Earth Planet. Sci. Lett., 282(1-4): 79-90.

Timm, C., de Ronde, C.E., Leybourne, M.I., Layton-Matthews, D., Graham, I.J., 2012. Sources of chalcophile and siderophile elements in Kermadec arc lavas. Econ. Geol., 107(8): 1527-1538.

Tipper, E.T., Louvat, P., Capmas, F., Galy, A., Gaillardet, J., 2008. Accuracy of stable Mg and Ca isotope data obtained by MC-ICP-MS using the standard addition method. Chem. Geol., 257(1-2): 65-75.

Tollstrup, D.L., Gill, J.B., 2005. Hafnium systematics of the Mariana arc: Evidence for sediment melt and residual phases. Geology, 33(9): 737-740.

Ueda, A., Sakai, H., 1984. Sulfur Isotope Study of Quaternary Volcanic-Rocks from the Japanese Islands Arc. Geochim. Cosmochim. Acta, 48(9): 1837-1848.

Vollstaedt, H., Mezger, K., Leya, I., 2016a. The isotope composition of selenium in chondrites constrains the depletion mechanism of volatile elements in solar system materials. Earth Planet. Sci. Lett., 450: 372-380.

Vollstaedt, H., Mezger, K., Nagler, T., Leya, I., Trinquier, A., 2016b. Selenium isotope analysis by N-TIMS: Potential and challenges. International Journal of Mass Spectrometry, 401: 55-63.

Volpe, A.M., Douglas Macdougall, J., Lugmair, G.W., Hawkins, J.W., Lonsdale, P., 1990. Fine-scale isotopic variation in Mariana Trough basalts: evidence for heterogeneity and a recycled component in backarc basin mantle. Earth Planet. Sci. Lett., 100(1): 251-264.

Walker, R.J., 2009. Highly siderophile elements in the Earth, Moon and Mars: Update and implications for planetary accretion and differentiation. Chem. Erde Geochem., 69(2): 101-125.

Wang, Z., Becker, H., 2013. Ratios of S, Se and Te in the silicate Earth require a volatile-rich late veneer. Nature, 499(7458): 328-331.

Wang, Z., Becker, H., 2015. Comment on “A non-primitive origin of near-chondritic SSeTe ratios in mantle peridotites: Implications for the Earth's late accretionary history” by König S. et al. [Earth Planet. Sci. Lett. 385 (2014) 110–121]. Earth Planet. Sci. Lett., 417: 164-166.

Wang, Z., Becker, H., Gawronski, T., 2013. Partial re-equilibration of highly siderophile elements and the chalcogens in the mantle: A case study on the Baldissero and Balmuccia peridotite massifs (Ivrea Zone, Italian Alps). Geochim. Cosmochim. Acta, 108: 21-44.

Wen, H., Carignan, J., 2011. Selenium isotopes trace the source and redox processes in the black shale-hosted Se-rich deposits in China. Geochim. Cosmochim. Acta, 75(6): 1411-1427.

Wen, H., Carignan, J., Chu, X., Fan, H., Cloquet, C., Huang, J., Zhang, Y., Chang, H., 2014. Selenium isotopes trace anoxic and ferruginous seawater conditions in the Early Cambrian. Chem. Geol., 390: 164-172.

Weyer, S., Schwieters, J., 2003. High precision Fe isotope measurements with high mass resolution MC-ICPMS. International Journal of Mass Spectrometry, 226(3): 355-368.

Wilkinson, J.J., 2013. Triggers for the formation of porphyry ore deposits in magmatic arcs. Nat. Geosci., 6: 917.

Williams, H.M., Prytulak, J., Woodhead, J.D., Kelley, K.A., Brounce, M., Plank, T., 2018. Interplay of crystal fractionation, sulfide saturation and oxygen fugacity on the iron isotope composition of arc lavas: An example from the Marianas. Geochim. Cosmochim. Acta, 226: 224-243.

Woodhead, J.D., Harmon, R.S., Fraser, D.G., 1987. O, S, Sr, and Pb isotope variations in volcanic rocks from the Northern Mariana Islands: implications for crustal recycling in intra-oceanic arcs. Earth Planet. Sci. Lett., 83(1): 39-52.

Yi, W., Halliday, A.N., Alt, J.C., Lee, D.C., Rehkamper, M., Garcia, M.O., Langmuir, C.H., Su, Y.J., 2000. Cadmium, indium, tin, tellurium, and sulfur in oceanic basalts: Implications for chalcophile element fractionation in the Earth. Journal of Geophysical Research-Solid Earth, 105(B8): 18927-18948.

Yierpan, A., König, S., Labidi, J., Kurzawa, T., Babechuk, M.G., Schoenberg, R., 2018. Chemical Sample Processing for Combined Selenium Isotope and Selenium-Tellurium Elemental Investigation of the Earth's Igneous Reservoirs. Geochem. Geophys. Geosyst., 19(2): 516-533.

Yierpan, A., Konig, S., Labidi, J., Schoenberg, R., 2019. Selenium isotope and S-Se-Te elemental systematics along the Pacific-Antarctic ridge: Role of mantle processes. Geochim. Cosmochim. Acta, 249: 199-224.

Young, E.D., Galy, A., Nagahara, H., 2002. Kinetic and equilibrium mass-dependent isotope fractionation laws in nature and their geochemical and cosmochemical significance. Geochim. Cosmochim. Acta, 66(6): 1095-1104.

Yu, M.Q., Liu, G.Q., Jin, Q., 1983. Determination of trace arsenic, antimony, selenium and tellurium in various oxidation states in water by hydride generation and atomic-absorption spectrophotometry after enrichment and separation with thiol cotton. Talanta, 30(4): 265-70.

Zack, T., John, T., 2007. An evaluation of reactive fluid flow and trace element mobility in subducting slabs. Chem. Geol., 239(3-4): 199-216.

Zhu, J.-M., Johnson, T.M., Clark, S.K., Xiang-Kun, Z., 2008. High precision measurement of selenium isotopic composition by hydride generation multiple collector inductively coupled plasma mass spectrometry with a 74 Se-77 Se double spike. Chinese Journal of Analytical Chemistry, 36(10): 1385-1390.

Zhu, J.-M., Johnson, T.M., Clark, S.K., Zhu, X.-K., Wang, X.-L., 2014. Selenium redox cycling during weathering of Se-rich shales: A selenium isotope study. Geochim. Cosmochim. Acta, 126: 228-249.

Acknowledgements

Stephan König designed this project and gave me the opportunity to do my doctorate on it. Thanks to the European Research Council (ERC) for funding Stephan König (ERC Starting Grant; O$_2$RIGIN, 636808). Stephan König prepared and calibrated the ^{125}Te single spike solution, set up the Se–Te measurement method on the iCAP Qc ICP-MS together with Michael Babechuk, and was intensively involved in Se test measurements during initial set up of the isotope measurements on the Netune*Plus* MC-ICP-MS before I started my PhD study. I am very grateful for his guidance, motivation, expertise and liberties he gave me during my time in Tübingen. Thank you for that, Stephan!

I am deeply thankful to Ronny Schoenberg, who always had his mind set to improve analytical procedures, always contributed his expertise and never failed to motivate. I also want to thank him for preliminary work that involves preparation and calibration of the Se double spike, thorough tests and writing the spreadsheet for Se isotope data evaluation without which no data would have been obtained at all. Thank you Ronny for your advice and enriching conversations during numerous lunch breaks!

Further I want to thank Aierken Yierpan (a PhD student of Stephan König), who helped me gain understanding on Se-Te elemental systematics and always had an open ear for discussion on systematics out of his own expertise. He also was involved in calibrating the ^{125}Te single spike and further modified the existing Se–Te measurement set-up on the iCAP Qc ICP MS. Most importantly, than you for your companionship; it was a great time!

I also want to thank Jabrane Labidi (former post-doctoral researcher of Stephan König) for sharing his expertise on isotope systematics that helped to improve the method paper. Thank you for conducting part of the evaporation experiments and the standard-sample-bracketing measurements (C*hapter* 1). In addition, thank you for your motivation and spending the numerous lunch breaks with me. It was great fun having you around!

Thank you Bernd Steinhilber and Michael Babechuk for help with major and trace element analysis. Thank you Michael for your help setting up the Se–Te measurements on the iCAP Qc ICP-MS.

I am very grateful to Martin Wille and Elmar Reitter for their significant trouble shooting skills that many times helped to gather data during measurement sessions. Without you guy, many data points would be missing in this thesis.

Maria Varas-Reus (post-doctoral researcher of Stephan König) and Aierken Yierpan are thanked for their support during Se–Te measurements on the iCAP Qc and for help with high-pressure asher digestions.

Thank you Jeffrey C. Alt for providing the submarine volcanic glass samples from the Mariana trench that were the basis of my analyses and interpretations made to understand Se recycling in subduction zones.

Further thanks to Timm John for providing the samples from the Raspas metamorphic Complex that significantly contributed to our current understanding on geochemical processes that affect the Se isotope composition of slab lithologies within subduction zones.

Thank you Johannes Redlinger for your intensive help with numerous high-pressure asher digestions and lab work. Without your help some days would not have ended at all.

Thank you Alena Wawra for your preliminary Se concentrations obtained during your Bachelor study. These data were the basis for further studies. In addition thank you for all your assistance during lab work.

Further I want to thank Mona Schiller for her assistance during lab work and Felix Brey for preparing fused glass beads.

The last 4 years in the Isotope Geochemistry Group in Tübingen were an enrichment of both knowledge and wisdom and I really enjoyed it. Having met all of you guys and spending time with you either science-related or during the ‘Kaffeerunde’ was great pleasure. Special thanks to Elmar Reitter, Bernd Steinhilber, Doro Mühlbayer-Renner, Martin Wille, Mike Bacbechuk, Daniel Schöckle, Ilka Kleinhanns, Benjamin Eickmann, Maria Varas-Reus, Heinrich Taubald, Gülüm Albut, Luise Wagner, Lucile Roué, Carolina Rosca, Barbara Maier and Simone Schafflick for their advice and help during analytical work. Especially Elmar always tried to help and solved several analytical difficulties we came across even though this is not his field of activity. Also, thanks to several guests (Claudio Marchesi, Gabriel Sindol and Carolina Rosca) who shared an office with me and never failed to lighten the mood. Thanks to all of you guys for your support, fruitful discussions and suggestions during the isotope seminars and overall for your great personalities and lots of fun we had together.

Last but most important, I want to thank my wife, my daughter and my entire family who were always there for me with their support, warmth, love and sunshine. Thank you!